

Elamin, Ahmed Mohamed Elamin Ahmed (2014) The face bending behaviour of blind-bolted connections to concrete-filled hollow sections. PhD thesis, University of Nottingham.

Access from the University of Nottingham repository:

http://eprints.nottingham.ac.uk/13938/1/Ahmed_Elamin_PhD_Thesis.pdf

Copyright and reuse:

The Nottingham ePrints service makes this work by researchers of the University of Nottingham available open access under the following conditions.

- Copyright and all moral rights to the version of the paper presented here belong to the individual author(s) and/or other copyright owners.
- To the extent reasonable and practicable the material made available in Nottingham ePrints has been checked for eligibility before being made available.
- Copies of full items can be used for personal research or study, educational, or not-for-profit purposes without prior permission or charge provided that the authors, title and full bibliographic details are credited, a hyperlink and/or URL is given for the original metadata page and the content is not changed in any way.
- Quotations or similar reproductions must be sufficiently acknowledged.

Please see our full end user licence at:

http://eprints.nottingham.ac.uk/end_user_agreement.pdf

A note on versions:

The version presented here may differ from the published version or from the version of record. If you wish to cite this item you are advised to consult the publisher's version. Please see the repository url above for details on accessing the published version and note that access may require a subscription.

For more information, please contact eprints@nottingham.ac.uk



The University of
Nottingham

UNITED KINGDOM • CHINA • MALAYSIA

THE FACE BENDING BEHAVIOUR OF BLIND-BOLTED CONNECTIONS TO CONCRETE-FILLED HOLLOW SECTIONS

Ahmed Mohamed Elamin Ahmed Elamin

BEng (Hons), MSc

Thesis submitted to the University of Nottingham for the degree of
Doctor of Philosophy

October 2013

Centre for Structural Engineering and Construction
Materials, Mechanics and Structures Division
Faculty of Engineering

Abstract

Structural Hollow Sections have superior structural performance over open sections and are currently available as circular, elliptical or rectangular sections. However, the practical use of these sections is limited due to complexities involved in their connections. The lack of access to the interior of the section makes it almost impossible to use standard bolted connections. The so-called Blind Bolts are therefore used as fasteners to alleviate these complexities by allowing for bolted rather than, the-not-so-popular, welded connections to hollow sections. Lindapter's Holo-Bolt is one of the Blind Bolts used for hollow sections connections. However its established use is currently restricted to transferring tensile forces and vertical shear only. Filling Square Hollow Sections (SHS) with concrete, when utilising Holo-Bolts, was found to improve the connections' performance in resisting moments, but there is currently no guidance available for the design of such connections.

Many methods are used to model connections behaviour. The so-called component method has emerged to be the most favourite and has been adopted in the Eurocode 3. In this method, the connection is divided into basic components. Each component has a contribution to the structural behaviour of the connection. For Holo-Bolted moment resisting connections, the behaviour of two of the components, fastener in tension and concrete-filled SHS face in bending, are not available. The application of the component method is therefore not possible. This research aims to devise a model to predict the behaviour of the concrete-filled SHS face in bending.

A novel analytical model of the concrete-filled SHS face bending has been proposed in this work. The model has three parts: Initial Stiffness, Yield Force and Post-Yield Stiffness. The Initial Stiffness was formulated by theoretically substituting the face of the concrete-filled SHS with a beam element. The beam is assumed to be loaded by a rigid strip and fixed at its ends. Yield line analysis was used to investigate possible failure mechanisms and associated strengths. The model adopted the mechanism which theoretically led to the

critical yield force. The Post-Yield Stiffness was taken as a percentage of the Initial Stiffness in line with other work from the literature.

An extensive full-scale experimental programme was undertaken to calibrate the aforementioned analytical model, and to examine the effects of varying parameters on the SHS face bending behaviour. Typical experiments involved one row of two bolts pulled out of concrete-filled SHS. A special dummy bolts were manufactured to the exact size and geometry of open Holo-Bolts, and were used in the experimental programme to remove the influence of any deformation associated with the real Holo-Bolts, and thus isolate the face bending behaviour. Non-contact video-based equipment was used to record the SHS face deformation. Three parameters were varied: the SHS face slenderness ratio, the bolts gauge to SHS width ratio and the concrete in-fill compressive strength.

A finite element model was also developed to complement the experimental programme. The model was developed using the ANSYS Parametric Design Language (APDL) to allow for easy parametric analysis and knowledge transfer. Dimensions, parameters and materials properties could be easily altered in the fully parametric model script.

The outcomes of the experimental programme and the finite element model were used to formulate design charts for two calibration factors: k_{fs} for the calculation of Initial Stiffness, k_{yf} for the calculation of Yield Force. A chart was also formulated for the Post-Yield stiffness ratio.

The proposed analytical model (semi-analytical after calibration) was compared with the results of experimental programme and finite element modelling. The model was found to capture the behaviour of concrete-filled SHS face bending with sufficient accuracy, lying between 90% prediction lines derived from the experimental results. This is considered sufficient for the proposed model to capture the concrete-filled SHS face bending component for connection design purposes.

List of Contents

Abstract	i
List of Contents.....	iii
List of Figures.....	vii
List of Tables.....	xiii
List of Notation.....	xiv
Roman symbols.....	xiv
Capital roman symbols.....	xv
Greek symbols.....	xv
Abbreviations	xvi
Trademarks.....	xvi
Acknowledgements	xvii
Declaration	xviii
Chapter 1: Introduction.....	1
1.1 Background	1
1.2 Research Aim and Objectives.....	4
1.3 Research Methodology	5
1.4 Overview of the Thesis.....	6
Chapter 2: Literature Review.....	8
2.1 Introduction	8
2.2 Beam-to-Column joints.....	9
2.2.1 Joints Classification.....	10
2.2.2 Methods of modelling Joints Behaviour.....	13
2.2.3 The Component Method.....	15
2.3 SHS Joints	19
2.4 The Holo-Bolt	21
2.5 Why concrete-filled SHS?.....	23
2.6 The concrete-filled SHS face bending	24
2.6.1 Initial Stiffness	25
2.6.2 Yield Force (Resistance).....	30
2.6.3 Post-Yield Stiffness	32
2.7 Summary	32
Chapter 3: Analytical Modelling	34
3.1 Introduction	34
3.2 The Initial Stiffness Component.....	35
3.3 The Resistance	38
3.3.1 Mechanism 1	41
3.3.2 Mechanism 2	43

3.3.3	Mechanism 3	45
3.3.4	Mechanism 4	47
3.3.5	Comparison of Mechanisms	49
3.4	Post-yield Stiffness	51
3.5	Proposed Model	52
3.6	Summary	53
Chapter 4: Experimental Programme.....		54
4.1	Introduction	54
4.2	Design of Experimental Programme	55
4.2.1	Parameters.....	55
4.2.2	Range	56
4.2.3	Test Matrix.....	61
4.3	Description of the Samples	62
4.4	Test set-up.....	65
4.4.1	Testing Rig and Layout.....	66
4.4.2	Actuator and Control Program	70
4.5	Instrumentation A: The Video Gauge	72
4.5.1	Introduction	72
4.5.2	Targets Identification.....	74
4.5.3	Calibration.....	75
4.5.4	Accuracy.....	75
4.6	Instrumentation B: The Digital Image Correlation.....	76
4.7	Material Properties	78
4.7.1	Structural Hollow Sections	78
4.7.2	Dummy Bolts.....	79
4.7.3	Concrete in-fill	81
4.8	Test Procedure	83
4.9	Summary	85
Chapter 5: Experimental Results.....		86
5.1	Introduction	86
5.2	Errors & Corrections.....	87
5.3	Failure Criteria.....	88
5.4	Visual Observations.....	90
5.5	Force-Displacement Results.....	95
5.5.1	Raw Force-Displacement Results	95
5.5.2	Possible Sources of Variation in Repeated Tests.....	102
5.5.3	Normalised Force-Displacement Results.....	107
5.5.4	Parametric Analysis	114
5.6	Digital Image Correlation Results (DIC).....	120
5.7	Summary	125

Chapter 6: Finite Element Modelling	126
6.1 Introduction	126
6.2 Description of the Model	128
6.2.1 Element Types	130
6.2.2 Concrete Failure Criteria in ANSYS	136
6.2.3 Material Models	137
6.2.4 Boundary Conditions	142
6.2.5 Loading and Solution	143
6.2.6 Model Mesh.....	144
6.2.7 Model Illustration	147
6.3 General Behaviour of the Finite Element Model	150
6.3.1 SHS Face Bending.....	150
6.3.2 Observations.....	151
6.3.3 Strain Distribution on SHS Face	153
6.4 Results and Validation (force-displacement curves)	153
6.5 Parameters Variation Analysis	159
6.5.1 The effect of SHS slenderness	161
6.5.2 The effect of bolt gauge.....	163
6.6 Proposed Charts for SHS 200x200	167
6.7 Summary	169
 Chapter 7: Semi-Analytical Model	 170
7.1 Introduction	170
7.2 Experimental Linear Data-Fit	171
7.3 Calibration Factor k	175
7.3.1 Background	176
7.3.2 Initial Stiffness calibration factor (k_{is}).....	178
7.3.3 Yield Force calibration factor (k_{yf}).....	182
7.3.4 Discussion	186
7.4 Post-Yield Stiffness.....	188
7.4.1 Effect of SHS face slenderness ratio (μ).....	188
7.4.2 Effect of bolt gauge to SHS width ratio (β).....	190
7.4.3 Effect of concrete in-fill compressive strength	192
7.5 Proposed Semi-Analytical Model.....	195
7.5.1 Part 1: Initial Stiffness	195
7.5.2 Part 2: Yield Force	196
7.5.3 Part 3: Post-Yield Stiffness ratio	196
7.5.4 How to use the proposed charts	197
7.6 Statistical Analysis.....	201
7.7 Prediction of Yield Force in the proposed model	209
7.8 Proposed Semi-Analytical Model limitations.....	214

7.9	Summary	215
Chapter 8: Conclusions and Recommendations		216
8.1	Introduction	216
8.2	Observations and Conclusions	218
8.3	Contribution of this work	222
8.4	Application of the proposed Semi-Analytical model	223
8.5	Recommendations for Future Work	224
References		228

List of Figures

Figure 1.1	Typical beam-to-hollow section column connections	2
Figure 1.2	Some of the Blind Bolts.....	3
Figure 2.1	Joint configurations	9
Figure 2.2	Typical joint $M-\phi$ behaviour	10
Figure 2.3	Joints classification by stiffness	11
Figure 2.4	Joints classification by strength	12
Figure 2.5	Comparison of joints ductility	12
Figure 2.6	Basic components in bolted end-plate connection (SCI/BCSA, 2005) .	16
Figure 2.7	Actual and idealised bi-linear behaviour of a component.....	17
Figure 2.8	Bi-linear components in-series / in-parallel (Kurobane et al., 2004)...	17
Figure 2.9	Typical open section-to-SHS column connections.....	20
Figure 2.10	3-Part Hollo-Bolt (Lindapter, 2013c).....	21
Figure 2.11	5-Part Hollo-Bolt (Lindapter, 2013c).....	22
Figure 2.12	Hollo-Bolt Installation steps (Lindapter, 2013b).....	22
Figure 2.13	Hollo-Bolt with and without concrete (Tizani and Ridley-Ellis, 2003) .	24
Figure 2.14	Bi-linear idealisation of the component	25
Figure 2.15	Comparison of Initial Stiffness of SHS face bending	28
Figure 2.16	Web/face loaded by equivalent strip (Simões da Silva et al, 2004)	29
Figure 2.17	Equivalent fixed beam loaded by rigid strip	29
Figure 2.18	Assumed failure pattern of SHS face (SCI/BCSA, 2002)	31
Figure 3.1	Web/face loaded by equivalent strip (Simões da Silva et al, 2004)	36
Figure 3.2	Typical hexagon nut layout (BSI, 2012).....	36
Figure 3.3	Assumed load transfer mechanism from Hollo-Bolts to SHS face.....	37
Figure 3.4	Possible failure mechanisms (using yield line analysis).....	39
Figure 3.5	Mechanism 1 yield-lines pattern	41
Figure 3.6	Mechanism 2 yield-lines pattern	43
Figure 3.7	Mechanism 3 yield-lines pattern	46
Figure 3.8	Mechanism 4 yield-lines pattern	47
Figure 3.9	Yield force theoretically calculated for SHS 200x200x10	50
Figure 3.10	Yield force theoretically calculated for SHS 300x300x10	50
Figure 3.11	Yield force theoretically calculated for SHS 200x200x5	51

Figure 3.12	Proposed Bi-Linear analytical model	52
Figure 4.1	Minimum Gauge and Edge distances	58
Figure 4.2	Illustration of minimum SHS width requirement	60
Figure 4.3	Test ID description	62
Figure 4.4	Typical SHS sample layout	65
Figure 4.5	Dummy Bolt	66
Figure 4.6	Test layout CAD drawing (Elevation)	68
Figure 4.7	Test layout CAD drawing (Plan)	69
Figure 4.8	Testing rig	70
Figure 4.9	Zoom-in of Test lay-out (Push-out).....	70
Figure 4.10	A screen snap-shot of actuator control program	72
Figure 4.11	A screen snap-shot of actuator control program during test.....	72
Figure 4.12	Video Gauge Components	75
Figure 4.13	Video Gauge calibration	76
Figure 4.14	CAD drawing and testing process of mechanical pieces	79
Figure 4.15	Handling SHS 300x300 samples	84
Figure 5.1	Accuracy and Precision	87
Figure 5.2	Dummy-bolt push-out of SHS hole	89
Figure 5.3	Experiment b200t8g100C40-1 failure.....	90
Figure 5.4	Different SHS face bending behaviour.....	91
Figure 5.5	Sample b200t8g80C40-2 after the concrete-infill was exposed.....	92
Figure 5.6	Concrete attachment to dummy-bolts in sample b200t8g60C40-3	93
Figure 5.7	Strain distribution on SHS face	94
Figure 5.8	Force-Displacement relationship of b200t8g80C20-1&2 (raw).....	96
Figure 5.9	Force-Displacement relationship of b200t8g80C50-1,2&3 (raw).....	96
Figure 5.10	Force-Displacement relationship of b200t8g80C80-1&2 (raw).....	97
Figure 5.11	Force-Displacement relationship of b200t8g60C40-1,2&3 (raw).....	97
Figure 5.12	Force-Displacement relationship of b200t8g80C40-1,2,3&4 (raw).....	98
Figure 5.13	Force-Displacement relationship of b200t8g100C40-1&2 (raw).....	98
Figure 5.14	Force-Displacement relationship of b200t10g80C40-1&2 (raw).....	99
Figure 5.15	Force-Displacement relationship of b200t6.3g80C40-1&2 (raw).....	99
Figure 5.16	Force-Displacement relationship of b200t5g80C40-1&2 (raw).....	100
Figure 5.17	Force-Displacement relationship of b300t12g120C40-1&2 (raw).....	100

Figure 5.18	Force-Displacement relationship of b300t16g120C40-1&2 (raw).....	101
Figure 5.19	Proper and improper dummy bolts alignment.....	103
Figure 5.20	The weld-seam in tested face of Sample b200t8g100C40-2	104
Figure 5.21	Updated Test ID description	107
Figure 5.22	b200t8g80C20-1&2 Normalised F-D relationships	108
Figure 5.23	b200t8g80C50-2&3 Normalised F-D relationships	108
Figure 5.24	b200t8g80C80-1&2 Normalised F-D relationships	109
Figure 5.25	b200t8g60C40-2&3 Normalised F-D relationships	109
Figure 5.26	b200t8g80C40-3&4 Normalised F-D relationships	110
Figure 5.27	b200t8g100C40-1&2 Normalised F-D relationships	110
Figure 5.28	b200t10g80C40-1&2 Normalised F-D relationships	111
Figure 5.29	b200t6.3g80C40-1&2 Normalised F-D relationships	111
Figure 5.30	b200t5g80C40-1&2 Normalised F-D relationships	112
Figure 5.31	b300t12.5g120C40-1&2 Normalised F-D relationships.....	112
Figure 5.32	b300t16g120C40-1&2 Normalised F-D relationships.....	113
Figure 5.33	The effect of bolt gauge on SHS face bending.....	115
Figure 5.34	The effect of bolt gauge on SHS face bending (zoom-in)	115
Figure 5.35	The effect of SHS face slenderness on SHS face bending	117
Figure 5.36	The effect of SHS face slenderness on face bending (zoom-in).....	117
Figure 5.37	The effect concrete strength on SHS face bending	118
Figure 5.38	Speckle pattern disturbed in b200t8g80C40-DIC	121
Figure 5.39	Strain development on SHS face captured using DIC	122
Figure 5.40	SHS face deformation across a section-line passing over bolts.....	123
Figure 5.41	SHS face deformation across a section-line passing over one bolt ...	124
Figure 6.1	Numerical model Flowchart	129
Figure 6.2	SOLID185 Geometry (ANSYS, 2010c)	131
Figure 6.3	SOLID65 Geometry (ANSYS, 2010c)	132
Figure 6.4	CONTA173 Geometry ((ANSYS, 2010c).....	134
Figure 6.5	TARGE170 Geometry (ANSYS, 2010c).....	135
Figure 6.6	Stress-Strain relationship for different concrete grades	142
Figure 6.7	Finite element model Boundary Conditions.....	143
Figure 6.8	The direction of applied displacement in the finite element model.	144
Figure 6.9	Meshed dummy bolts	145
Figure 6.10	Mesh sensitivity analysis.....	146

Figure 6.11	The finite element model fully meshed.....	147
Figure 6.12	Typical SHS in the finite element model.....	147
Figure 6.13	Typical Dummy Bolts in the finite element model	148
Figure 6.14	Typical concrete-infill in the finite element model	148
Figure 6.15	Contact surfaces between SHS and concrete-infill.....	149
Figure 6.16	Contact surfaces between bolt sleeves and concrete-infill.....	149
Figure 6.17	Contact surfaces between bolt sides and concrete-infill	149
Figure 6.18	Contact surfaces between back of bolts and concrete-infill	149
Figure 6.19	Typical SHS face bending	150
Figure 6.20	General behaviour cross-checks	151
Figure 6.21	von Mises plastic strain of SHS face.....	152
Figure 6.22	von Mises stresses of SHS face and Bolt sleeves	152
Figure 6.23	Strain development on SHS face	154
Figure 6.24	Analytical yield-lines pattern and Finite Element strains	155
Figure 6.25	Positions where force and displacement are calculated	155
Figure 6.26	FE vs. Experiment of b200t6.3g80C40.....	156
Figure 6.27	FE vs. Experiment of b200t8g60C40	157
Figure 6.28	FE vs. Experiment of b200t8g80C40.....	157
Figure 6.29	FE vs. Experiment of b200t8g100C40.....	158
Figure 6.30	FE vs. Experiment of b200t10g80C40	158
Figure 6.31	The face bending of concrete-filled SHS 200x200 when $\beta = 0.3$	161
Figure 6.32	The face bending of concrete-filled SHS 200x200 when $\beta = 0.4$	162
Figure 6.33	The face bending of concrete-filled SHS 200x200 when $\beta = 0.5$	162
Figure 6.34	The face bending of concrete-filled SHS 200x200 when $\mu = 40$	164
Figure 6.35	The face bending of concrete-filled SHS 200x200 when $\mu = 31.75$...	164
Figure 6.36	The face bending of concrete-filled SHS 200x200 when $\mu = 25$	165
Figure 6.37	The face bending of concrete-filled SHS 200x200 when $\mu = 20$	165
Figure 6.38	The face bending of concrete-filled SHS 200x200 when $\mu = 16$	166
Figure 6.39	The face bending of concrete-filled SHS 200x200 when $\mu = 12.5$	166
Figure 6.40	The face bending of concrete-filled SHS 200x200 ($\beta=0.3$).....	167
Figure 6.41	The face bending of concrete-filled SHS 200x200 ($\beta=0.4$).....	168
Figure 6.42	The face bending of concrete-filled SHS 200x200 ($\beta=0.5$).....	168
Figure 7.1	Vertical deviation from data point to best-fit line.....	171
Figure 7.2	Example of linear fit: test b300t16g120C40-2N	173

Figure 7.3	Example of linear fit: test b200t8g80C40-2	174
Figure 7.4	k_{is} for experiments which vary SHS face slenderness	179
Figure 7.5	k_{is} for experiments which vary Bolt gauge to SHS width ratio	180
Figure 7.6	k_{is} for experiments which vary Concrete in-fill strength	181
Figure 7.7	k_{yf} for experiments which vary SHS face slenderness	183
Figure 7.8	k_{yf} for experiments which vary Bolt gauge to SHS width ratio	184
Figure 7.9	k_{yf} for experiments which vary Concrete in-fill strength	185
Figure 7.10	Min. & Max. calculated angles of assumed concrete cone	187
Figure 7.11	Post-Yield Stiffness ratio when varying SHS face slenderness	189
Figure 7.12	Post-Yield Stiffness ratio when varying Bolt gauge	191
Figure 7.13	Post-Yield Stiffness ratio when varying Bolt gauge (FE+Exp)	192
Figure 7.14	Post-Yield Stiffness ratio when varying concrete strength	193
Figure 7.15	Post-Yield Stiffness ratio when varying concrete strength (FE+Exp)	194
Figure 7.16	Illustration of how to use k_{is} , k_{yf} or Post-Yield Stiffness ratio charts	197
Figure 7.17	Calibration factor k_{is} charts	198
Figure 7.18	Calibration factor k_{yf} charts	199
Figure 7.19	Post-Yield Stiffness ratio charts	200
Figure 7.20	Proposed Model for the concrete-filled SHS face in bending	201
Figure 7.21	Proposed Semi-Analytical Model and b200t8g80C20-1&2	202
Figure 7.22	Proposed Semi-Analytical Model and b200t8g80C50-1,2&3	203
Figure 7.23	Proposed Semi-Analytical Model and b200t8g80C80-1&2	203
Figure 7.24	Proposed Semi-Analytical Model and b200t8g60C40-1,2&3	204
Figure 7.25	Proposed Semi-Analytical Model and b200t8g80C40-1,2,3&4	204
Figure 7.26	Proposed Semi-Analytical Model and b200t8g100C40-1&2	205
Figure 7.27	Proposed Semi-Analytical Model and b200t10g80C40-1&2	205
Figure 7.28	Proposed Semi-Analytical Model and b200t6.3g80C40-1&2	206
Figure 7.29	Proposed Semi-Analytical Model and b200t5g80C40-1&2	206
Figure 7.30	Proposed Semi-Analytical Model and b300t12.5g120C40-1&2	208
Figure 7.31	Proposed Semi-Analytical Model and b300t16g120C40-1&2	209
Figure 7.32	Proposed Model using Eq. (7-13) for b200t8g80C20-1&2	210
Figure 7.33	Proposed Model using Eq. (7-13) for b200t8g80C50-1,2&3	211
Figure 7.34	Proposed Model using Eq. (7-13) for b200t8g80C80-1&2	211
Figure 7.35	Proposed Model using Eq. (7-13) for b200t8g60C40-1,2&3	212
Figure 7.36	Proposed Model using Eq. (7-13) for b200t8g80C40-1,2,3&4	212
Figure 7.37	Proposed Model using Eq. (7-13) for b200t8g100C40-1&2	213

Figure 7.38	Proposed Model using Eq. (7-13) for b200t10g80C40-1&2	213
Figure 7.39	Proposed Model using Eq. (7-13) for b200t6.3g80C40-1&2	214
Figure 7.40	Proposed Model using Eq. (7-13) for b200t5g80C40-1&2	214
Figure 8.1	Simple component-based models for Hollo-Bolted connection	224
Figure 8.2	Possible load transfer mechanism of EHB (right) and HB (left)	225
Figure 8.3	Possible failure mechanisms of a two-row connection	226

List of Tables

Table 4.1	Hollo-Bolt HB16 main properties (Extracted from Lindapter Manual)	56
Table 4.2	Test Matrix.....	63
Table 4.3	Video Gauge lens specification (Imetrum ¹)	74
Table 4.4	Digital Image Correlation Q-400 Technical Data (Dantec).....	78
Table 4.5	Structural Hollow Sections material properties	80
Table 4.6	Stresses range for Structural Hollow Sections grade S355.....	80
Table 4.7	Mechanical Properties of EN24U.....	81
Table 4.8	Concrete in-infill Mix Design.....	81
Table 4.9	Cube Compressive Strength of Concrete-infill.....	82
Table 4.10	Experimental programme ranges and limitations	85
Table 5.1	Variation in Concrete-infill Compressive Strength	105
Table 6.1	Concrete mixes theoretical Cube and Cylinder strength.....	141
Table 6.2	Comparison between FE and experimental outcomes.....	159
Table 6.3	Test Matrix for the finite element modelling	160
Table 6.4	Finite element modelling ranges and limitations	169
Table 7.1	Linear data-fit estimations.....	175
Table 7.2	k_{fs} for experiments which vary SHS face slenderness.....	178
Table 7.3	k_{fs} for experiments which vary Bolt gauge to SHS width ratio.....	179
Table 7.4	k_{fs} for experiments which vary Concrete in-fill strength.....	181
Table 7.5	k_{yf} for experiments which vary SHS face slenderness.....	182
Table 7.6	k_{yf} for experiments which vary Bolt gauge to SHS width ratio	183
Table 7.7	k_{yf} for experiments which vary Concrete in-fill strength	185
Table 7.8	Post-Yield Stiffness ratio when varying SHS face slenderness.....	189
Table 7.9	Post-Yield Stiffness ratio when varying Bolt gauge	190
Table 7.10	Post-Yield Stiffness ratio when varying concrete in-fill strength.....	193

List of Notation

Roman symbols

c	dimension on hollow section face
c_{is}	dimension on hollow section face determined from Initial Stiffness equation
c_{yf}	dimension on hollow section face determined from Yield Force equation
b	hollow section width
d_g	max diameter of aggregate
d_h	bolt hole diameter
e	bolt head diameter
f_{ck}	cylinder compressive strength of concrete
f_{cu}	cube concrete compressive strength
f_y	Steel yield strength
g	bolts gauge (horizontal)
g_{max}	maximum bolt gauge
g_{min}	minimum bolt gauge
k_1, k_2	numerical calibration coefficients (or factors)
k_{is}	proposed initial stiffness calibration factor
k_{yf}	proposed yield force calibration factor
l	length
l_{eff}	effective length
n	number of samples, number of rows
p	bolts pitch (vertical)
r	radius of circular yield line (or radius)
r^2	coefficient of determination
s	standard deviation (or bolt head diameter)
t	thickness of hollow section face
t_c	thickness of Hollo-Bolt collar
$t_{critical\ value}$	determined from statistical tables
t_{wc}	column thickness
\bar{x}	mean
z	lever arm

Capital roman symbols

A	area
B	hollow section width
C	calibration coefficient
E	Young's modulus of elasticity
F, F_y	Yield Force
H_o	outer dimension of steel tube
I	second moment of area
K	Stiffness (or Flexural Rigidity)
K_i	Stiffness
L	length of bolt shank (or length)
L_r	length bolt shank from head to end of sleeves
M	moment
N	axial load
$PYSr$	Post-Yield Stiffness ratio
R^*	reduction factor
S, S_i	Initial Stiffness
T	tightening torque
U_x, U_y, U_z	displacement/transition in x, y and z axis
V	shear load
W	clamping thickness

Greek symbols

α	geometrical parameter = c/L
β	bolts gauge to hollow section width ratio
γ_f, γ_s	deflection coefficient
δ	deflection/displacement
ϵ	strain
θ	angle
μ	hollow section face slenderness ratio
ν	Poisson's ratio
σ	stress
ϕ	rotation angle

Abbreviations

CHS Circular Hollow Section

DIC Digital Image Correlation

FOV Camera lens's Field of View

HB Hollo-Bolt

EHB Extended Hollo-Bolt

LVDT Linear variable differential transformers

RHS Rectangular Hollow Section

SHS Square Hollow Section

WD Camera lens's Working Distance

Trademarks

Blind Bolt is a trademark of Blind Bolt Company Limited.

DIC is a trademark of Dantec Dynamics.

Flowdrill is a trademark of Flowdrill Limited.

Hollo-Bolt is a trademark of Lindapter International.

Molabolt is a trademark of Advanced Bolting Solutions Limited.

ONESIDE is a trademark of Ajax Engineered Fasteners Limited.

Video Gauge is a trademark of Imetrum Limited.

Acknowledgements

This thesis would have not been possible without the help and support of many people and I would like to thank them profoundly.

Firstly, I would like to express my deep gratitude and thanks to my supervisor Dr Walid Tizani for his kind support, invaluable guidance, full support and patience throughout the research period.

The generous financial fund provided by the University of Nottingham through the Dean of Engineering Research Scholarship for International Excellence is gratefully appreciated. Also, I would like extend my appreciation to Sudan University of Science and Technology and Gordon Memorial Trust for the generous financial support.

I would like to thank Mr Trevor Mustard and Mr Andrew Orton of TATA Steel (formerly known as Corus Tubes) and Mr Neil Gill of Lindapter International for supporting this work.

I would like to acknowledge the assistance provided in the laboratory to conduct the experimental work in this thesis. Sincere thanks are extended to Mr Thomas Buss from Department of Mechanical Engineering, Mr Nigel Rook, Mr Balbir Loyla and Mr Michael Langford from Department of Civil Engineering. Special thanks go to Mr Gordon Hardy the former Director of Facilities, Mr Damien Goy and Mr Jim Bellis who left the university during the experimental work.

Special thanks go to my colleagues in the Centre for Structural Engineering and Construction. I particularly enjoy my time with Amged, Aras, Dimitrios, Henry, Justin, Mohammed, Samuel, Sean, Shida, Theo, Waleed and Yagoub.

Also, my deepest gratitude and affection go to my family for their support and blessing.

Finally, heartfelt thanks go to my wife and my sons who without their support, encouragement, understanding and patience I would have never been able to present this thesis.

Declaration

I declare that, except for commonly understood and accepted ideas or where specific reference has been made to the work of others, I am the sole author of this thesis. The research work presented in this thesis was conducted at the University of Nottingham, under the guidance of my supervisor, between November 2009 and October 2013. This thesis has not been submitted to any institution other than the University of Nottingham for the degree of Doctor of Philosophy.

Ahmed Mohamed Elamin Ahmed Elamin
BEng (Honours), MSc

Chapter 1

Introduction

1.1 Background

Structures have benefited from the use of steel as a building material in modern ages. It allowed for higher buildings with longer spans. This is because structural steel has superiority over other materials like structural concrete and timber. In general, the steel is a well behaved material which its properties can be predicted with high degree of certainty. Additionally, its high strength-to-weight ratio and re-usability allow for better and more sustainable utilisation of material. It also has high suitability for mass production and prefabrication. While structural steel has its shortcomings such as; strength reduction when it is heated and its susceptibility to corrosion when exposed to surrounding weathering conditions (as it reacts to air and moisture), fire and weather proofing products that are capable of eliminating these problems are widely available.

There are two main types of structural steel sections: open sections and hollow sections. Currently, due to the easy access to the open sections, they are more common and are used in most steel structures as beams and columns. Nonetheless, hollow sections have several advantages over open sections as they are better suited - structurally - to withstand axial forces, in addition to being architecturally more appealing. These sections are currently available as circular, elliptical, rectangular and square sections and commonly known as Structural Hollow Sections. Complexities involved in connecting these sections hamper their practical application, particularly for moment-resisting structures. The lack of access to the interior of the section makes it impossible to use the standard bolted beam-to-column connections. Various alternatives have been used usually such as the ones shown in Figure 1.1.

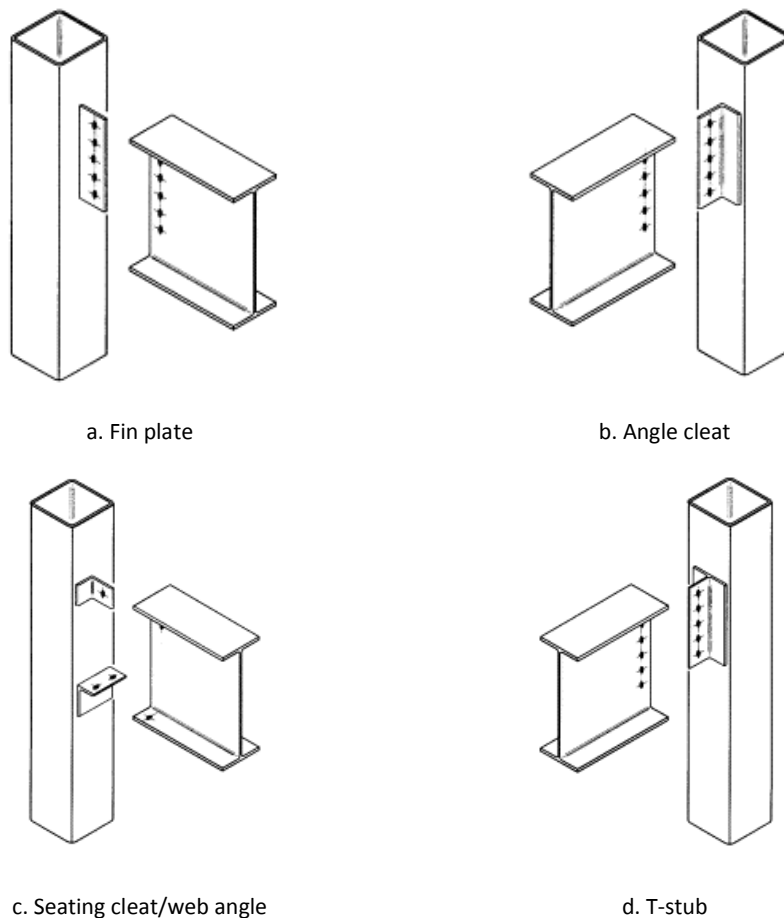


Figure 1.1 Typical beam-to-hollow section column connections

In these connections, Plates, Cleats or T-stubs are fully welded to Square Hollow Sections to form beam-to-column connections. Design guidance for such welded connections can be found in many publications such as BCSA (2011). However, welding is a complex and time-consuming process and is therefore unfavourable on-site in the construction industry. In addition, though the welding process can take place off-site, this introduces more complications in terms of storing, transporting and assembling the steel members.

The lack of access to the interior of hollow sections was behind the development of the so-called Blind-Bolts. They are new fasteners that can connect steel members to hollow sections, and be installed from the outside of the hollow sections without having access to the inner of the section, hence, the name blind. Many types of these fasteners are currently available in the market such as the Hollo-Bolts®, the Blind Bolt™, ONESIDE™, Molabolt® and Flowdrill®. Some of these fasteners are shown in Figure 1.2.

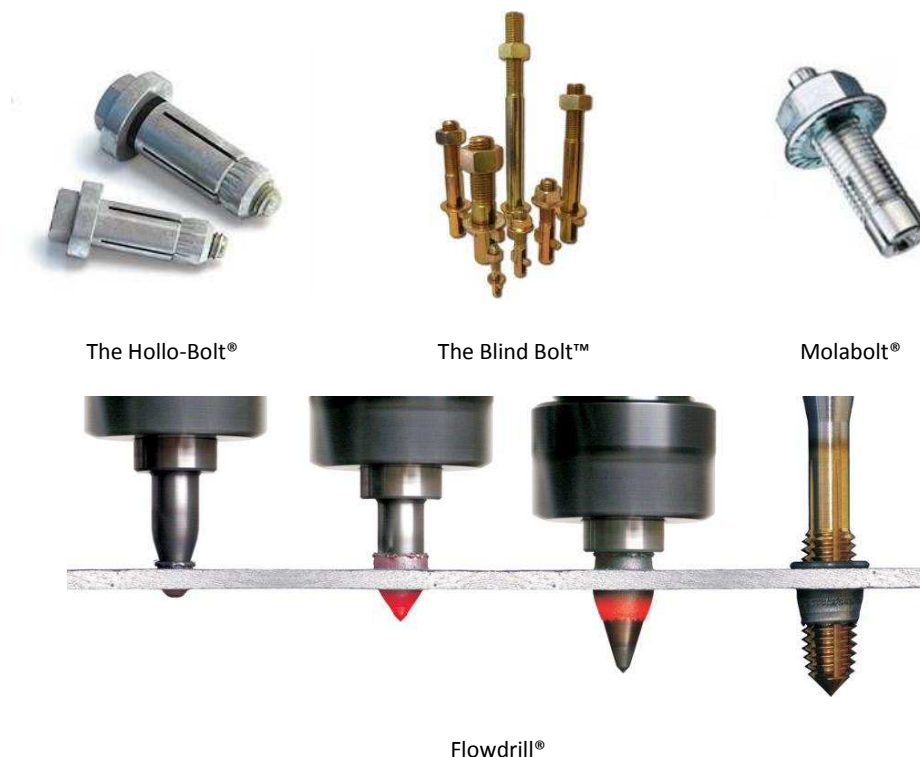


Figure 1.2 **Some of the Blind Bolts**

The Holo-Bolt® is manufactured by Lindapter® and is available in a range of sizes and shapes. Specifications and working mechanisms of these bolts can be found in its manufacturing brochures which can be obtained from its website. In addition, the brochures provide safe tensile and single shear working loads of these bolt based on 5 to 1 safety factor. This information might be sufficient for the utilization of these bolts for simple connection purposes. However, it is not sufficient for utilising them for moment-resisting connections. This has been the subject of an on-going research at the University of Nottingham. In this research, it was found that filling the hollow section with concrete significantly improves the behaviour of the Holo-Bolted connection (Tizani and Ridley-Ellis, 2003). In Eurocode 3, beam-to-column connections are assessed using the component method which assesses each connection's components separately to determine the overall behaviour. If this method is to be used to assess Holo-Bolted connections, some components need further examination. These components are the Holo-Bolt in tension and the concrete-filled hollow section face in bending (when using Holo-Bolts). Many investigations have examined specific Holo-Bolted connection such as Tizani et al. (2013a) and Tizani et al. (2013b), yet up to the present time, no models for these components exist. The component method can be used to develop advanced models of Holo-Bolted connections to concrete-filled hollow sections if these two components are determined. This work focuses on the concrete-filled hollow section face in bending.

1.2 Research Aim and Objectives

The aim of this research is 'to devise an analytical model for the structural behaviour of the face bending of concrete-filled Square Hollow Sections when connected to other structural members using Holo-Bolts'.

It focuses on connections where one row of Holo-Bolts, i.e. two Holo-Bolts, is subjected to tension. It is part of an on-going research in the University of Nottingham aiming to establish a design guidance of Holo-Bolted connections.

The objectives of the research are to:

1. Study the available state-of-the-art literature that involves blind bolted connections especially the ones which consider Square Hollow Sections face bending behaviour to understand the research question and tools used in similar studies.
2. Develop an analytical model for the face bending behaviour of concrete-filled Square Hollow Sections when connected to other structural members using Holo-bolts.
3. Determine the parameters which may influence the analytical model and investigate their effects.
4. Design and conduct an experimental programme to determine the behaviour and evaluate the effects of varying parameters.
5. Develop and validate a finite element model to complement the experimental programme outcomes.
6. Calibrate the analytical model using the data collected from the experiments and the finite element model.
7. Establish a simplified approach from the analytical model that can be used for connections design.

1.3 Research Methodology

The investigation done in this research is planned to consist of analytical modelling, finite element modelling and experimental testing.

In the analytical part, a model for the face bending behaviour of concrete-filled Square Hollow Sections is to be formulated. The model is

thought to have three parts: Initial Stiffness, Yield Force and Post-Yield Stiffness.

As the full scale testing is the most reliable way to determine any behaviour, an experimental programme is needed to determine the behaviour and calibrate the analytical model. The slenderness of hollow section face, the bolt gauge to section width ratio and the concrete in-fill properties are identified from the literature as the parameters that may affect the behaviour. The experimental programme is also used to evaluate the effect of varying these parameters on the model.

Experiments are often costly and time-consuming. Therefore, a finite element model which predicts the face bending behaviour of concrete-filled Square Hollow Sections is planned to be developed and validated. The model is to be developed using parametric design language of the finite element analysis package ANSYS. This is done to ensure that the model is fully parametric and to enable the possibility of its use for future work. The outcomes of the model are to be used to complement the experimental programme outcomes.

The outcomes of the experimental work and finite element analysis are to be used to calibrate the analytical model leading to the introduction of a novel Semi-Analytical Model. The model is to compose of analytical equations for Initial Stiffness and Yield Force and complemented by charts for calibration factors and a ratio to determine the Post-Yield Stiffness.

1.4 Overview of the Thesis

The thesis consists of eight chapters:

Chapter One (this chapter) briefly introduces background of the research area and justifies this research. It also presents the research

Aim and Objectives and describes the Research Methodology. The overview of the thesis is highlighted in this chapter.

Chapter Two is the literature review. This chapter reviews previous investigations focused on the hollow sections face bending. It also provides a review of the topics necessary to understand the work carried out in the subsequent chapters.

Chapter Three describes the development of the analytical model proposed in this work to predict the face bending behaviour of concrete-filled Square Hollow Sections.

Chapter Four details the experimental testing programme designed to calibrate the analytical model and defines its ranges. This chapter also describes the testing setup, testing matrix, instrumentation and equipment used to acquire data during tests.

Chapter Five presents the raw experimental results and highlights the effect of varying the hollow section face slenderness, the bolt gauge to section width ratio and the concrete in-fill properties on the behaviour.

Chapter Six describes the finite element model developed in this work and presents its outcomes.

Chapter Seven details the calibration of the analytical model done by analysing results and comparing it with the model. It also demonstrates how the charts for calibration factors and Post-Yield Stiffness ratio were developed.

Chapter Eight summarises the main findings of this work and suggests recommendation for future work.

Chapter 2

Literature Review

2.1 Introduction

This chapter presents a review of the state-of-the-art investigations focusing on the face bending of hollow sections. It starts by describing the main characteristics of Beam-to-Column joints and how their connections are classified. This is followed by a description of current Square Hollow Section (SHS) connections and the limitation which led to the introduction of Blind Bolts. It also presents the Hollo-Bolt and details its components. Information on the performance of the Hollo-Bolt are also summarised herein.

This chapter also provides a brief review of the topics necessary to understand the work carried out in the subsequent chapters i.e. the component method and Yield Line analysis, and concludes with the justification for this work and the gap in the knowledge in the area.

2.2 Beam-to-Column joints

Loads in most structures are usually applied on roofs, slabs and/or walls. It is then transferred through structural members to the ground. These members are connected with each other in joints. In the Eurocode 3 part 1-8 (BS EN 1993-1-8:2005), a joint is defined as the zone where two or more members are interconnected (CEN, 2005). It could be beam-to-beam, beam-to-column, column-to-column or column-to-base as shown in Figure 2.1.

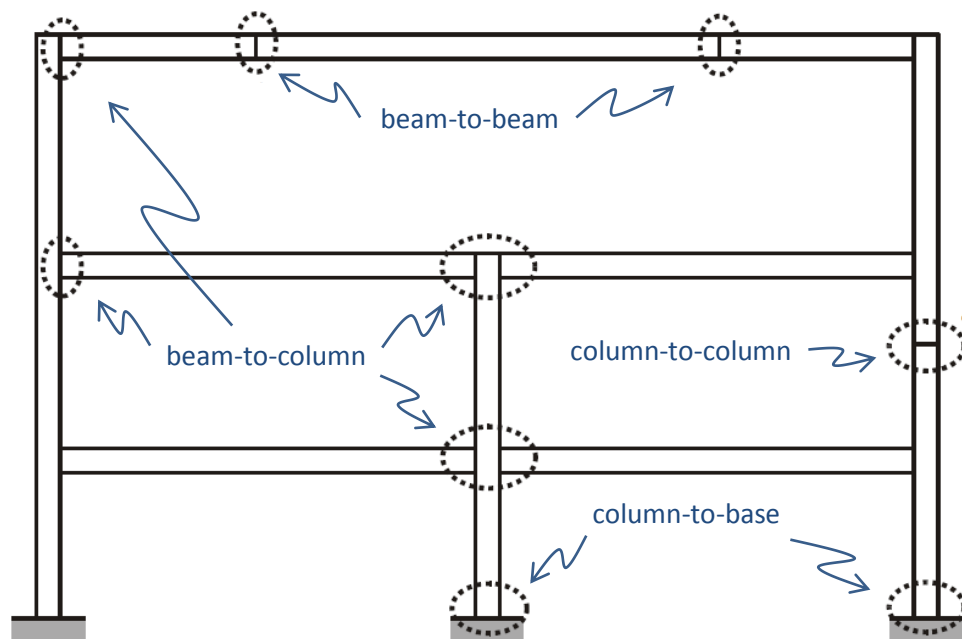


Figure 2.1 Joint configurations

The beam-to column joints typically have two configurations (in 2D frames):

- Single-sided joints
- Double-sided joints

In the single sided joints, only one beam is connected to a column i.e. one connection. Two beams are connected to a column in the double sided joints i.e. two connections. The location where two or more

element meet is called the connection (CEN, 2005). The main structural requirement of any connection is to safely transfer the internal forces and moments between the members. There are many ways in the literature in which joints could be classified and modelled. Some of these ways are described next.

2.2.1 Joints Classification

The behaviour of a joint is commonly characterised by its moment-rotation behaviour. This behaviour is represented by the relation of the moment applied on the joint (M) and the rotation angle resulting from this moment commonly known as (ϕ). Typical M - ϕ behaviour of a joint is shown in Figure 2.2.

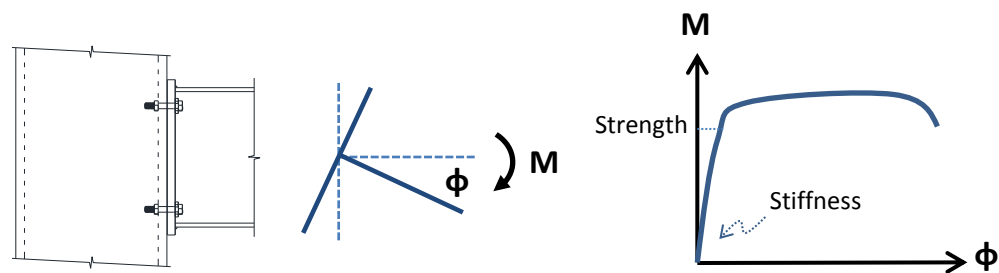


Figure 2.2 Typical joint M - ϕ behaviour

The Eurocode 3 part 1-8 uses the M - ϕ behaviour of a joint for its classification in two ways:

- Classification by Stiffness
- Classification by Strength

Classification by Stiffness

In This classification, joint behaviour is used to classify joint as rigid, semi-rigid or nominally pinned as shown in Figure 2.3. This is done by comparing the joint's initial rotational stiffness with classification boundaries directly related to the bending stiffness

of the connected elements (presented in section 5.2.2.5 of Eurocode 3 part 1-8).

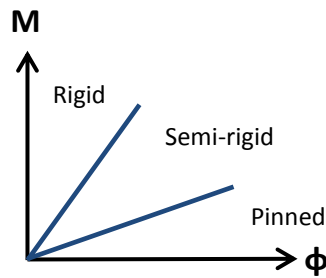


Figure 2.3 Joints classification by stiffness

Rigid joints are assumed to have sufficient rotational stiffness to transmit internal forces and moments between members to maintain continuity in the structure without rotation. Nominally pinned joints are capable of transferring internal forces between members without developing moments that is significant enough to affect the behaviour of the structure. Joints which behave in between the requirements of rigid and nominally pinned are classified as semi-rigid joints.

Classification by Strength

The second classification adopted by the Eurocode 3 part 1-8 compares the design moment resistance of the joint to the design moment resistances of the members it connects. In this classification the joints are classified as full-strength, partial-strength or nominally pinned as shown in Figure 2.4.

The joint is classified as full-strength joint if its design moment resistance is not less than the design moment resistances of the connected members. Similarly, if the joint's design moment resistance is less than 0.25 of that required for a full-strength

joint, it classified as nominally pinned. The joint which its design moment resistances fall between the boundaries of full-strength and nominally pinned is classified as partial-strength joints.

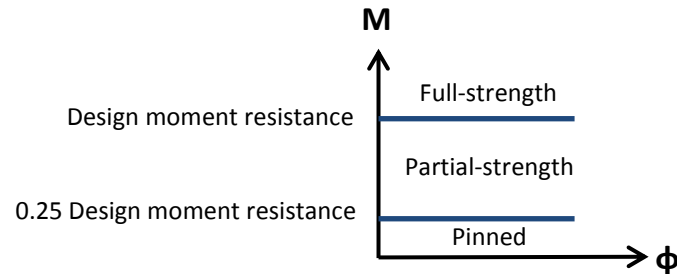


Figure 2.4 Joints classification by strength

The ductility of the joints might be considered as essential characteristic to determine whether it can provide sufficient rotation capacity for the plastic analysis. Joints with different ductility are shown in Figure 2.5 where for the same moment each joint exhibits different rotation capacity. Some investigations have considered joints ductility in joints modelling and classification such as Simões da Silva et al. (2002) as well as some design guidance such as (SCI/BCSA, 2005), yet it is not presented in Eurocode 3 as classification method.

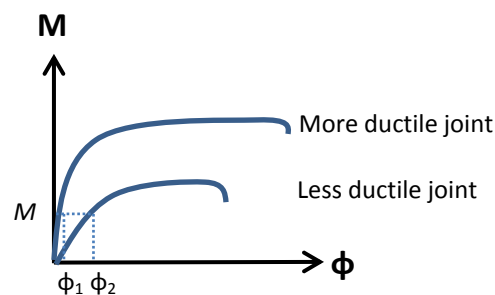


Figure 2.5 Comparison of joints ductility

The effect of joints behaviour on the forces/moment transfer between elements and on the deformation of the overall structure is generally

taken into account when analysing any structure. However, it may be possible to neglect these effects if they are significantly small. This is generally identified by the method of global analysis which used to analyse the structure. Four global methods of analysis are presented in part 1-8 of Eurocode 3:

- Elastic
- Rigid-Plastic
- Elastic-Plastic
- Type of joint model.

The classification of joint is used to select the appropriate method where the moment-rotation characteristic of the joint is used in the analysis.

The Eurocode 3 part 1-8 also allows for the use of simplified moment-rotation characteristic of joints including a linearized approximation (e.g. bi-linear or tri-linear), provided that the approximated curve lies wholly below the actual moment-rotation characteristic (CEN, 2005).

2.2.2 Methods of modelling Joints Behaviour

Different methods are used to model joints behaviour. Currently, four methods stand as most common:

Experimental method

Joints could be experimentally tested to determine their behaviour. The first investigation in which a beam-to-column was tested experimentally could be traced to Wilson and Moore (1917). This method developed over the years as more group investigation allowed for more experiments as done by Nethercort (1985) where he collected more than 700 experimental results from experiments done by his research group. The Experimental method is very reliable as it determines the

actual behaviour of joints. Yet, it is not always possible to examine joints experimentally. This is in addition to the time and resources involved in experimental investigations which limit the possibility of utilising this method to examine every joint.

Curve fitting

The large amount of moment-rotation curves available in the literature enabled some researchers to fit these curves to mathematical expressions. The work done by Jones et al. (1983) and Nethercot and Zandonini (1989) are examples where this method was used with success. The moment-rotation curves are often fitted to linear, bi-linear, tri-linear or polynomial functions depending on their shapes. Linear and bi-linear curve fitting generally provide an approximation of moment-rotation curves, where polynomial curves could represent the moment-rotation curves more accurately. This method could be highly efficient in representing large amount of experimental data. However, it can only be used for the range of parameters experimentally tested. More experiments will be needed if any change in geometry and mechanical properties of any parameters occurs.

Numerical modelling

Finite element modelling could be and has been used to determine joints behaviour as well as to predict joints behaviour. In fact, these models are used to examine detailed stresses and strains distribution in joints. It is also beneficial to use this method to create conditions which are not simply created experimentally such as the ones in the joints exposed to fire. Nevertheless, experimental results are often required to validate these models i.e. cannot be a stand-alone method. Also, the complexities involved in developing finite element models limit the use of this method to researchers and large engineering firms.

Mechanical modelling

This method assumes that each joint could be divided into its basic components. The properties of each component, commonly force-displacement relation, are then determined by means of experimental testing, finite element modelling and/or analytical modelling. The overall behaviour of the joints is then determined by adding properties of its basic components together. The main advantage of this method is that the properties of basic components could be determined independently regardless of joint configuration. This makes it relatively simple to assemble the overall behaviour of joints for design purposes. This method is commonly referred to as the component method. It has been adopted in the Eurocode 3 part 1-8 and will be described in more detail in the following sub-section.

2.2.3 The Component Method

Background

In this method, the connection is divided into basic components. Each component has a contribution to the structural behaviour of the connections. For example, in a bolted connection, the bolt in tension is one of the basic components. This method has emerged to be the most favourite as it has the flexibility to deal with any changes in connection details, yet it is simple enough to be implemented in practical design. This method is adopted by the Eurocode 3 part 1-8. It is also the main platform for the majority of research on joints characterisation.

The use of this method could be traced back to (Wales and Rossow, 1983) where they developed a mechanical model for double web cleat connections using the component-based approach. Since then, the component-based approach has been used in numerous investigations such as in Simões da Silva et al. (2001), Bayo et al. (2006), Málaga-

Chuquitaype and Elghazouli (2010b), Liu et al. (2012b), Park and Wang (2012) and Pitrakkos and Tizani (2013).

Application of the Method

In principle, application of the component method generally involves three steps:

1. Identification of component involved in the considered joint. An example of the active components in endplate connection is shown in Figure 2.6.

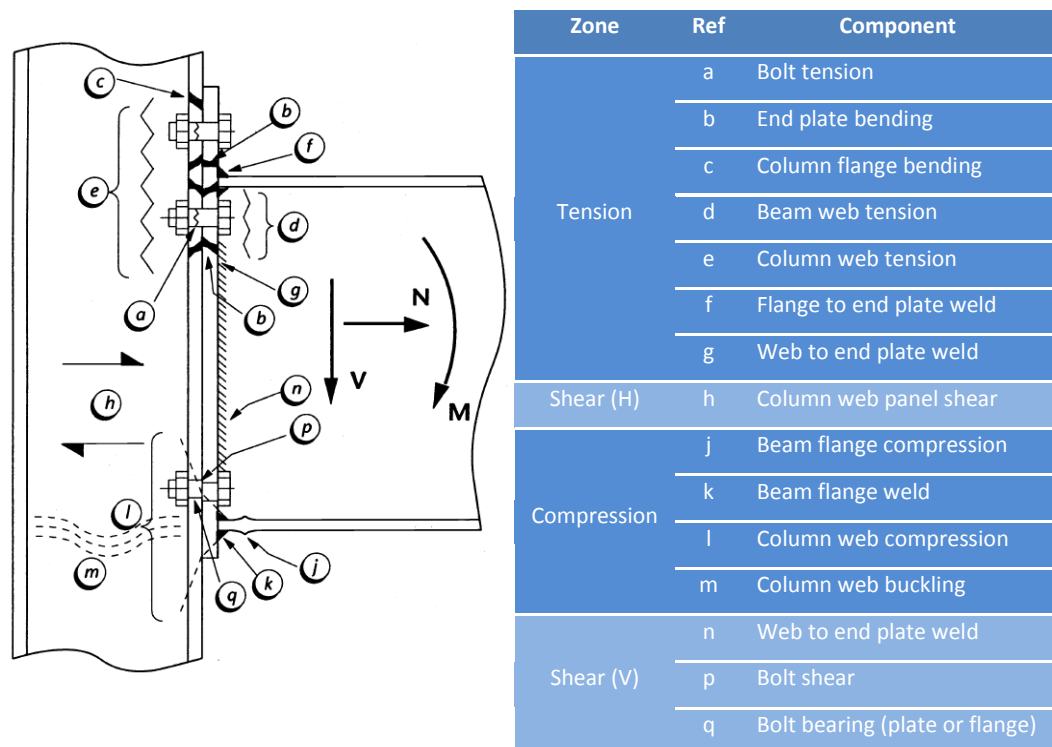


Figure 2.6 Basic components in bolted end-plate connection (SCI/BCSA, 2005)

2. Evaluation of the mechanical properties of each component. This is done to each component regardless of its interaction with other components usually by determining its non-linear force-displacement relation. It is also permissible to use linear idealisation of the non-linear force-displacement relation. An example of bi-linear idealisation of a component is shown in Figure 2.7. In this

figure, the component properties are initial stiffness, yield force or resistance and post-yield stiffness. The relation between the initial stiffness S_i and yield force F_y in this case is represented linearly using the following expression in which E is Young's modulus of elasticity and δ_y is the displacement at yield:

$$F_y = E S_i \delta_y \quad (2-1)$$

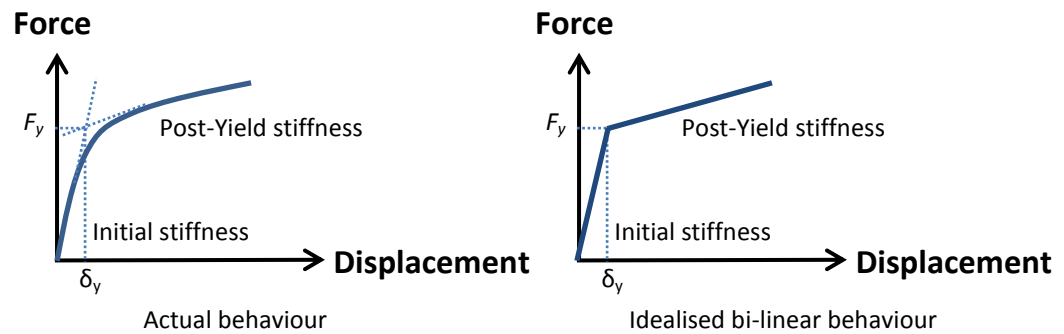


Figure 2.7 Actual and idealised bi-linear behaviour of a component

3. Assembly of the overall behaviour of the joints using components properties. To do this, the components properties are added to each other either in-series or in-parallel. An example of two Bi-Linear components added in-series and in-parallel is shown in Figure 2.8. The identification of the appropriate way depends on how components interact with each other.

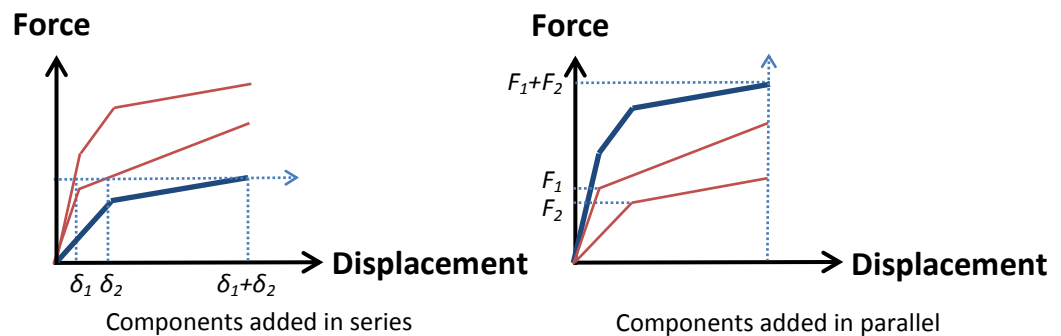


Figure 2.8 Bi-linear components in-series / in-parallel (Kurobane et al., 2004)

Advanced models which use component behaviour to determine the joint behaviour exist in the literature such as the one proposed by Jaspart (1997). The moment-rotation characteristic of a joint that has a lever arm z and i number of components could be assembled using the following expressions:

Rotation of joint ϕ_j is calculated using:

$$\phi_j = \begin{cases} \frac{\sum \delta_i}{z} & \text{if components are added in – series} \\ \frac{\sum \frac{1}{\delta_i}}{z} & \text{if components are added in – parallel} \end{cases} \quad (2-2)$$

Resistance moment of joint M is calculated using:

$$M = \min F_i \cdot z \quad (2-3)$$

Initial Stiffness of joint $S_{j,i}$ is calculated using:

$$S_{j,i} = \frac{M_j}{\phi_i} = \frac{F \cdot z}{\phi_i} \quad (2-4)$$

This expression could be simplified further by substituting the Equations (2-1) and (2-2) as:

$$S_{j,i} = \begin{cases} \frac{E \cdot z^2}{\sum \frac{1}{S_i}} & \text{if components are added in series} \\ \frac{E \cdot z^2}{\sum S_i} & \text{if components are added in parallel} \end{cases} \quad (2-5)$$

Limitation of the Method

The use of the component method to examine any joints requires that the behaviour of all components involved in the joint to be pre-determined i.e. the use of the method is limited to known components. Also, the interaction between components to assemble the overall joint behaviour could be complicated.

Concluding Remarks

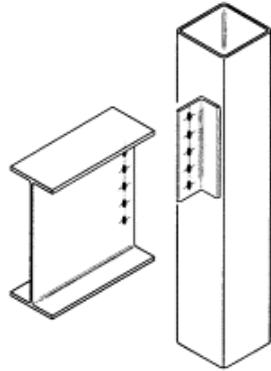
As the Eurocode 3 part 1-8 adopts this method, it recommends that the design moment-rotation characteristic of a joint should depend on the properties of its basic components. The basic components of joints connecting H or I sections are identified in Table 6.1 of Eurocode 3 part 1-8 (BS EN 1993-1-8:2005). The table summarises the performance of each basic component by describing its resistance, stiffness and/or rotation capacity. However, no such information is available for joints connecting SHS as only welded hollow sections joints are presented in the Eurocode 3 part 1-8 to date. This limits the possibility of using the component method to assemble the behaviour of joints to hollow sections. Some of connections currently used in joints to SHS columns are described next.

2.3 SHS Joints

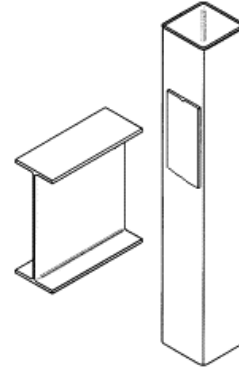
SHS have several advantages over open sections as they structurally better withstand axial forces due to their symmetrical shape and architecturally are more appealing. However, complexities involved in their connections hamper their practical application, particularly for moment-resisting structures. The lack of access to the interior of the section makes it almost impossible to use the standard bolted connections.

In practice, various ways to connect open sections to SHS which involve welding are available (examples are shown in Figure 2.9). Likewise, hollow sections are fully welded to SHS to form beam-to-column connections. Design guidance for such welded connections can be found in many publications such as (SCI/BCSA, 2002, SCI/BCSA, 2005, SCI/BCSA, 2011). However, welding is a complex and time-consuming process and is therefore unfavourable in the construction industry. In

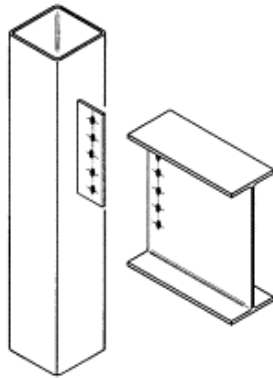
addition, although the welding process can take place off-site, this introduces more complications in terms of storing, transporting and assembling the materials.



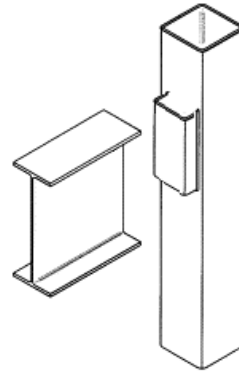
a. Angle cleat



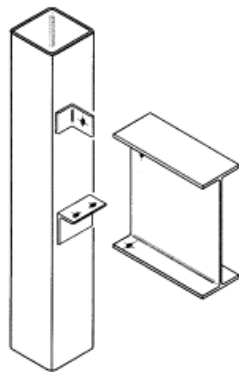
b. End plate



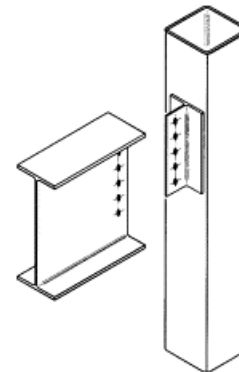
c. Fin plate



c. Reverse channel



d. Seating cleat/web angle



e. T-stub

Figure 2.9 Typical open section-to-SHS column connections

Alternatives to welding in SHS connection are investigated for some time now. Currently, there are available practical solutions on the

market, as shown in (BSTP, 2003) and (TATA-Steel, 2010). Most practical solutions adopt mechanical fasteners, which can connect steel members to SHS, and be installed from the outside of the SHS. These types of fasteners are called the 'Blind Bolts'. These include Holo-Bolts®, the Blind Bolt™, ONESIDE™, Molabolt® and Flowdrill®. The Holo-Bolt is the focus of this study.

2.4 The Holo-Bolt

Lindapter's Holo-Bolts are one of the Blind Bolts currently available in the market. It is available in two versions: the original 3-part design for general hollow section connections and the larger size 5-part version for higher strength structural connections. The 3-part version is available in the sizes M8, M10 and M12 while the 5-part version is available in sizes M16 and M20. The 3-part version consists of standard bolt encased in a collar-and-sleeve as one part and threaded cone attached to the bolt at the end of the sleeve. The bottom part of the sleeve is divided into 4 legs which expand during installation as shown in Figure 2.10. In the 5-part version, the collar and the sleeve are separated with a washer that compresses to allow for more clamping force compared to the 3-part version (shown in Figure 2.11).

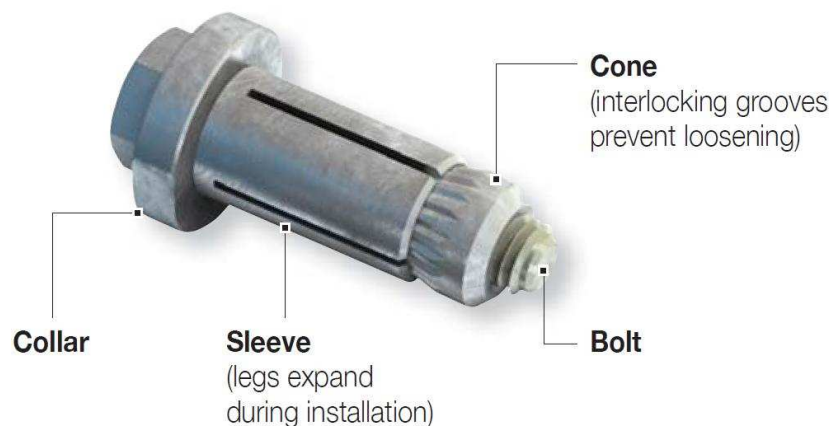


Figure 2.10 3-Part Holo-Bolt (Lindapter, 2013c)



Figure 2.11 5-Part Holo-Bolt (Lindapter, 2013c)

The installation of Holo-Bolt involves three stages which are described in Figure 2.12. Sizes, geometry requirements and recommended torques are provided in Lindapter's Holo-Bolt brochure (Lindapter, 2013b).

1. Align pre-drilled fixture and hollow section and insert Holo-Bolt.



2. Grip the Holo-Bolt collar with an open ended spanner.



3. Using a calibrated torque wrench, tighten the central bolt to the recommended torque.



Figure 2.12 Holo-Bolt Installation steps (Lindapter, 2013b)

The Hollo-Bolt brochures also provide safe tensile and single shear working loads based on 5:1 safety factor (Lindapter, 2013a). In fact, design guidance for pin joints that involve Hollo-Bolts is available in SCI/BCSA's Joints in Steel Construction: Simple Connections (SCI/BCSA, 2002), and the recently published Joints in Steel Construction: Simple Joints to Eurocode 3 (SCI/BCSA, 2011). However, neither safe working load, nor component behaviour are available for other structural components required for Hollo-Bolted moment connection, e.g. the SHS face bending. Although, the capability of specific Hollo-Bolted connections to transfer moment has been investigated such as in the work of Málaga-Chuquitaype and Elghazouli (2010a) and Liu et al. (2012a), yet, to date, there is no sufficient data available to design such connections. All investigations conducted in the course of this study involved the 5-Part Hollo-Bolt which has M16 bolt, commonly referred to as HB16.

2.5 Why concrete-filled SHS?

In general, large SHS wall deformation is observed in SHS connections. This is due to the high slenderness of SHS walls which allow for more flexibility in SHS connection. This flexibility decreases the performance of Hollo-Bolted connections (Pitrakkos, 2012). One of the practical solutions for this is to fill the SHS with concrete after installing Hollo-Bolts. In fact, Tizani and Ridley-Ellis (2003) reported significant improvement in Hollo-Bolts performance after filling SHS with concrete. In this investigation, 8 Hollo-Bolts HB16 were pulled out of two adjacent sides of SHS 200x200x10 using rigid T-Stubs (4 bolts in each side). The bolts had a gauge of 120mm and a pitch of 100mm. A comparison of the average separation of the T-stub from SHS face is shown in Figure 2.13. Significant improvement in stiffness, resistance and ductility of the system can be observed in this figure.

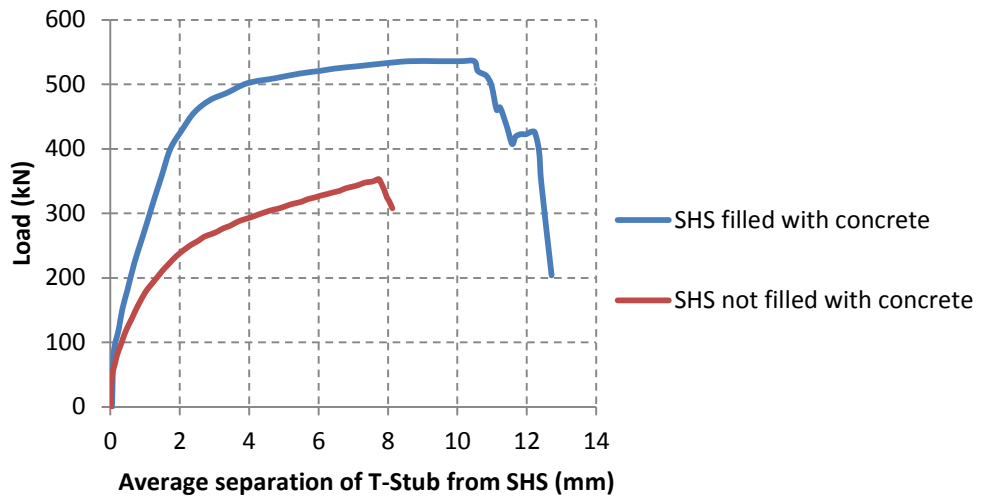


Figure 2.13 Hollo-Bolt with and without concrete (Tizani and Ridley-Ellis, 2003)

Since then filling SHS with concrete to improve Hollo-Bolted connection performance was adopted in many investigation like in the work done by Ellison and Tizani (2004), Wang et al. (2009b), Al-Mughairi et al. (2010), Wang and Chen (2012) and Tizani et al. (2013). The SHS are filled with concrete in this investigation for the same purpose.

2.6 The concrete-filled SHS face bending

Previous brief investigations done by (Elamin, 2009, Richards, 2009) showed that the concrete-filled SHS face bending behaviour could be bilinearly idealised. The bilinear idealisation (shown in Figure 2.14) is determined by evaluating:

- Initial Stiffness
- Yield force
- Post yield stiffness

This section examines how each of these three parts for similar behaviours, or when Hollo-Bolts or other blind bolts, is evaluated in previous investigations.

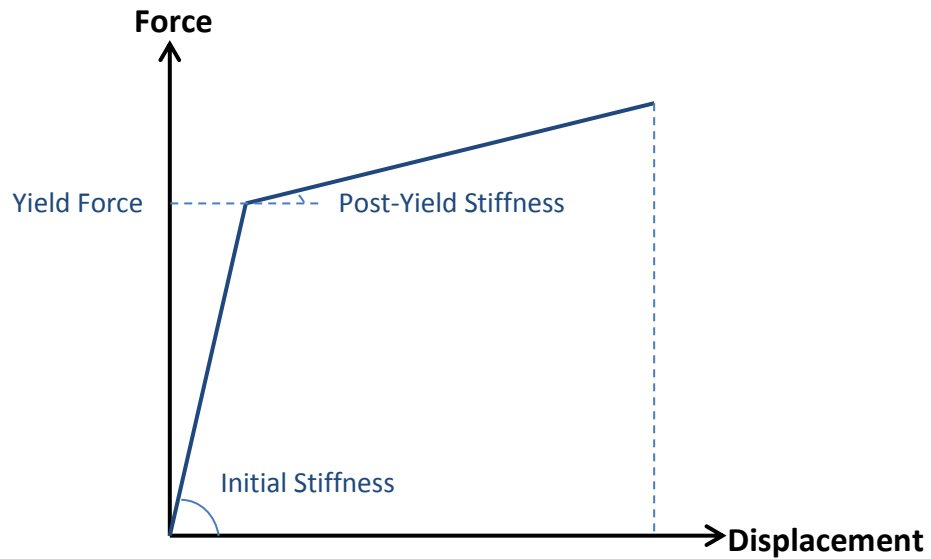


Figure 2.14 Bi-linear idealisation of the component

2.6.1 Initial Stiffness

In mechanics of materials, the bending stiffness, often called Flexural Rigidity, of a plate with a unit width is represented by:

$$K = \frac{E t^3}{12(1 - \nu^2)} \quad (2-6)$$

where E is Young's modulus, t is plate thickness, and ν is Poisson's ratio. The derivation of Equation 1 is available in a number of textbooks such as Timoshenko and Goodier (1952) and Landau and Lifshitz (1986). In many investigations of Blind Bolted connections, a modified version of this equation was used to describe the stiffness of the SHS face-bending component. This section describes and compares some of the recent versions to highlights the need of a unique representation for the stiffness of the SHS face-bending component.

In the work of Elghazouli et al. (2009), where a component-based model was used to examine the stiffness characteristic of an angle connection using Hollo-Bolts, the stiffness of the SHS face bending component was represented by:

$$K_c = \frac{\pi E_s t_c^3}{6(1 - \nu^2)C \alpha^2} \quad (2-7)$$

where E_s is steel young's modulus, t_c is hollow section thickness, α is half of the column face width, and C is a coefficient which assumed as 0.18 based on calibration studies using detailed continuum finite element models. The SHS were not filled with concrete in this work. Similar representation was also used in (Málaga-Chuquitaype and Elghazouli, 2010b) and (Málaga-Chuquitaype and Elghazouli, 2010a).

Similar equation was also used by Wang et al. (2009a) to develop a mechanical model of flush end-plate joint to concrete-filled SHS and Circular Hollow Section (CHS) columns which is:

$$K_4 = \frac{\frac{t^3}{12(1 - \nu^2)}}{\gamma_f (H_o - 2t)^2} \quad (2-8)$$

in which, H_o is the outer dimension of steel tube, and γ_f is the deflection coefficient for concrete-filled hollow sections. This coefficient is obtained from design charts compiled using finite element analysis in Ghobarah et al. (1996). These charts were based on finite element modelling performed by Mourad (1994), who investigated the face-deflection and bending stiffness of SHS and CHS. The term $\gamma_f (H_o - 2t)^2$ was introduced to account for the hollow sections face deflection at the bolts location.

The same approach has also been adopted by Lee et al. (2010) using the Ajax ONSIDE® - a different type of Blind Bolts. The stiffness of the SHS was described by:

$$K_{col} = \frac{\frac{E t_c^3}{12(1 - \nu^2)}}{R^* \gamma_s (b_c - 2t_c)^2} \quad (2-9)$$

where b_c is the width of column, R^* is the reduction factor due to corner restraints and γ_s is the deflection coefficient. Again, both R^* and γ_s are based on the work done in (Ghobarah et al., 1996, Mourad, 1994) and obtained from design charts presented in these studies. However, as unfilled hollow sections were used in this study, both R^* and γ_s are different from the ones in Equation (2-8).

When comparing Equation (2-7) with Equation (2-8), the similarity between these equations became very clear when re-arranging Equation (2-8) in the order shown in Equation (2-10) i.e. the term $\gamma_f (H_o - 2t)^2$ in Equation (2-10) is equivalent to the term $\pi/C\alpha^2$ in Equation (2-7).

$$K_4 = \frac{t^3}{12(1 - \nu^2) \gamma_f (H_o - 2t)^2} \quad (2-10)$$

Also, Equation (2-9) from Lee et al. (2010) work can be re-arranged to the form:

$$K_{col} = \frac{E t_c^3}{12(1 - \nu^2) R^* \gamma_s (b_c - 2t_c)^2} \quad (2-11)$$

The SHS in the case of Lee et al. (2010) work were unfilled, yet the similarities between Equations (2-7), (2-10) and (2-11) is clear. How these equations compare to Equation (2-6) is also clear as the term $t^3/12(1-\nu^2)$ from Equation (2-6) is present in all these equations. The use of Young's Modulus in these equations depends on each model characteristics.

To compare these three equations, the predicted Force-Displacement curves of SHS face bending component evaluated using these equations are plotted in Figure 2.15. This was done for the same SHS (SHS 300x300x10) for a load range from 0kN to 10kN. In theory, though the three equations are used to within different models, investigators will

expect minimal variation in the predicted curves. This is due to the fact that there is no parameter related to concrete-infill or bolt type exists in any of the equations, and each equation worked well within the model presented in each study. Yet predicted force-displacement curves do vary as shown in the figure. This highlights the lack of a unique representation for the SHS face bending component.

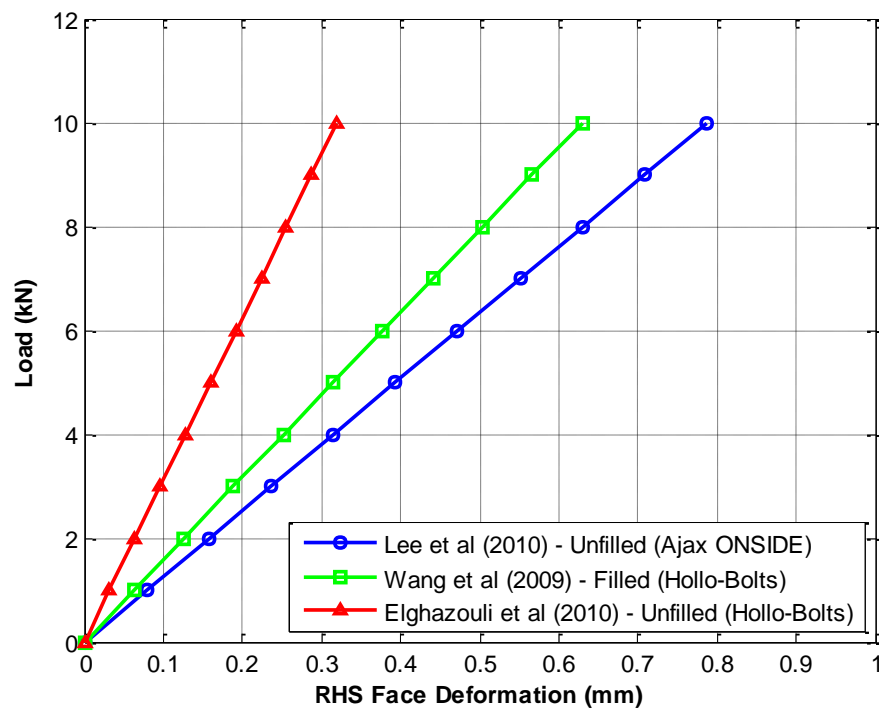


Figure 2.15 Comparison of Initial Stiffness of SHS face bending

A more comprehensive work was carried out by Simões da Silva et al. (2004) which aimed to develop a model for the bending of columns web or face. In this work, it was assumed that the web of I section is loaded by a rigid area describing bolts head/nut and gauge dimensions for the case of bolted connections, or welded strip dimensions for the case of welded connections as shown in Figure 2.16. The same assumption was also applied when the face of concrete-filled SHS was considered. The SHS face was represented by a plate, whereas its boundary conditions were defined based on the concrete-filled SHS. The plate was assumed

to be fixed at the two parallel ends as the concrete-infill restrains the two SHS faces perpendicular to the connected face from deforming.

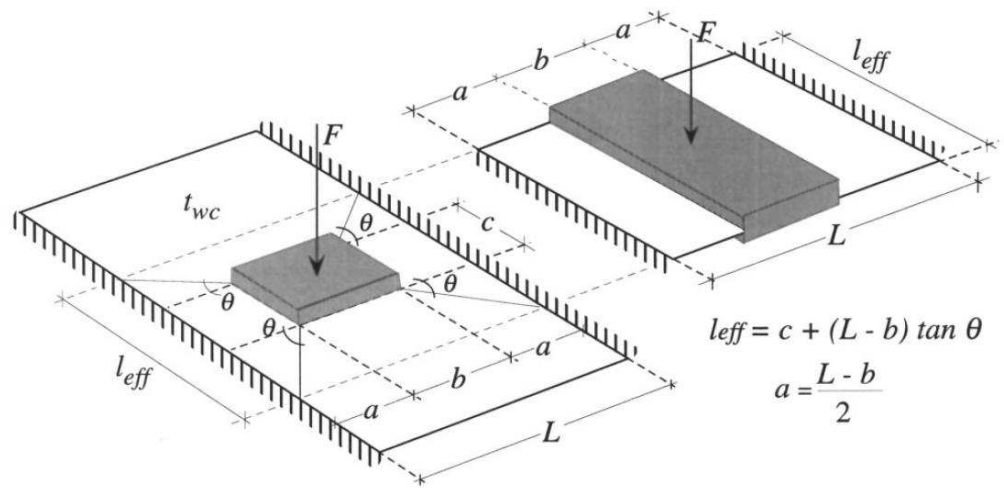


Figure 2.16 Web/face loaded by equivalent strip (Simões da Silva et al., 2004)

For bolted connections to SHS face, it was assumed that the loaded rigid strip has a height equivalent to bolt nut/head diameter (denoted as c in Figure 2.16), and width equivalent to the gauge between bolts plus bolt nut/head diameter (denoted as b in Figure 2.16). Since the length of the plate (i.e. SHS column height) is very long compared to its width (SHS column width), the problem was simplified to a fixed beam loaded by a rigid strip as shown in Figure 2.17.

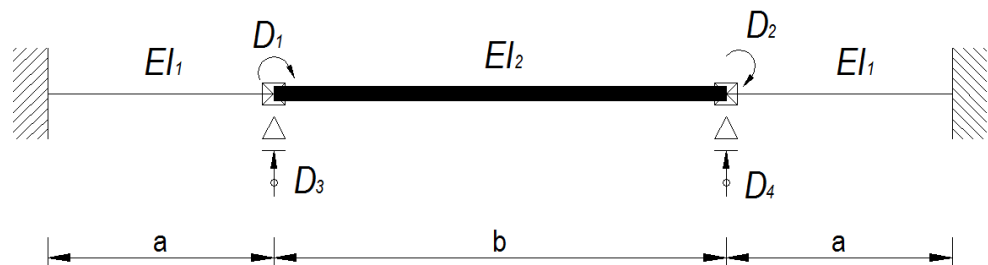


Figure 2.17 Equivalent fixed beam loaded by rigid strip

The stiffness matrix in (Simões da Silva et al., 2004) system is assembled in the form:

$$K = E \begin{bmatrix} 4\left(\frac{I_1}{a} + \frac{I_2}{b}\right) & 2\frac{I_2}{b} & 6\left(\frac{I_1}{a^2} - \frac{I_2}{b^2}\right) & 6\frac{I_2}{b^2} \\ 2\frac{I_2}{b} & 4\left(\frac{I_1}{a} + \frac{I_2}{b}\right) & -6\frac{I_2}{b^2} & -6\left(\frac{I_1}{a^2} - \frac{I_2}{b^2}\right) \\ 6\left(\frac{I_1}{a^2} - \frac{I_2}{b^2}\right) & -6\frac{I_2}{b^2} & 12\left(\frac{I_1}{a^3} - \frac{I_2}{b^3}\right) & -12\frac{I_2}{b^3} \\ 6\frac{I_2}{b^2} & -6\left(\frac{I_1}{a^2} - \frac{I_2}{b^2}\right) & -12\frac{I_2}{b^3} & 12\left(\frac{I_1}{a^3} + \frac{I_2}{b^3}\right) \end{bmatrix} \quad (2-12)$$

in which E is Young's modules, a and b are dimensions shown in Figure 2.17 and I_1 and I_2 are the second moment of area of the beam parts 1 and 2 shown in Figure 2.17. As a result, Simões da Silva et al. (2004) proposed and validated the following expression:

$$S_i = \frac{Et_{wc}^3}{L^2} 16 \frac{\alpha + (1 - \beta) \tan \theta}{(1 - \beta)^3 + \frac{10.4(k_1 - k_2\beta)}{\mu^2}} \quad (2-13)$$

in which E is the steel young's modulus, t_{wc} is the column thickness, α , β and μ are dimensional parameter equal to c/L , b/L and L/t_{wc} respectively. K_1, K_2 are numerical calibration coefficients and θ is the angle that defines l_{eff} (shown in Figure 2.16) and equal to $35-10 [(g+c)/(b-t)]$ as suggested in (Jaspart, 1997). The dimensions c , b and L are shown in Figure 2.16. In fact, Simões da Silva et al. (2004) recommended the expression shown in Equation (2-13) to be added to table 6.1 of Eurocode 3 to represent the stiffness of column web or face in bending component. Nonetheless, it must be noted that Hollo-Bolts were not considered in this study.

2.6.2 Yield Force (Resistance)

Yield Line analysis/method has been used to calculate the resistance of SHS faces for some time. This is done by determining possible failure mechanisms of SHS face and evaluating their corresponding failure

loads. Yield Line analysis was successfully utilised by Gomes et al. (1996), Simões da Silva et al. (2004), Park (2012) and Li (2012) to calculate the resistance of web, flange or face of steel elements. In effect, it is used by some design guides to determine the structural capacity of SHS face for structural integrity purpose. For instance, Figure 2.18 show the assumed failure pattern used to calculate the tying capacity of SHS face in SCI/BCSA (2002) guide.

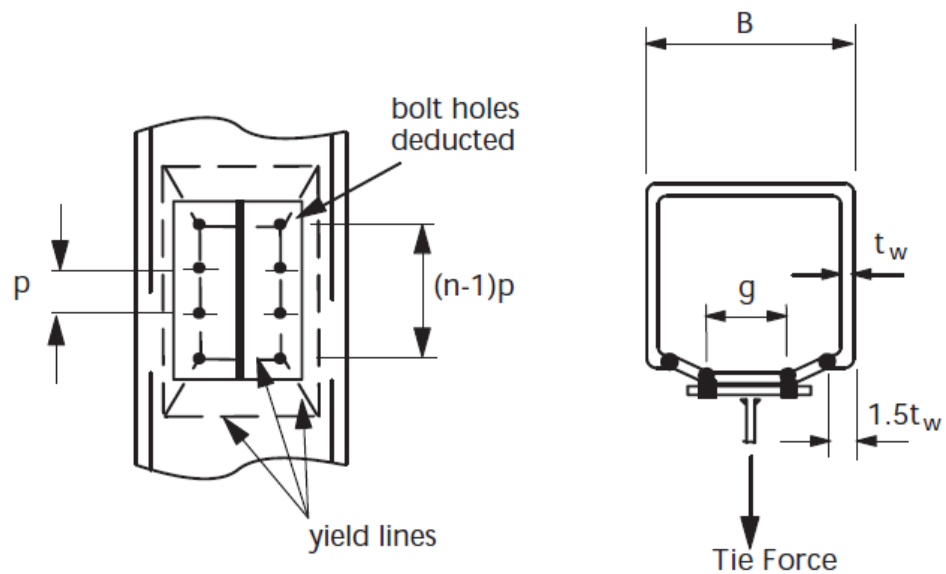


Figure 2.18 Assumed failure pattern of SHS face (SCI/BCSA, 2002)

The Yield Line theory was originally pioneered by K. W. Johansen in 1940s to calculate the capacity of reinforced concrete slabs and was supported with extensive testing (Johansen, 1962b, Johansen, 1962a). The main principle of the theory is '*the work done in yield lines rotating is equal to the work done in loads moving*' (Kennedy and Goodchild, 2003). The practical application of the theory involves the followings:

- Step 1 Assumption a collapse mechanism by choosing a pattern of yield lines.
- Step 2 Calculation of the load capacity corresponding to that yield line pattern.

- Step 3 Repetition of Steps 1 and 2 for all possible yield line patterns.
- Step 4 Actual failure occurs at collapse mechanism which produces the lower load capacity.

2.6.3 Post-Yield Stiffness

Traditionally, it was suggested Post-Yield stiffness could be assumed zero for bolted connections except the ones which exhibit web shear or web buckling (Yee and Melcher, 1986). However, it was observed that the Post-Yield Stiffness to be between 5% and 9% of the Initial Stiffness in an investigation involved Blind-Bolted connection (Ghobarah et al., 1996). In fact, Ghobarah et al. (1996) adopted a ratio of 7% of the initial stiffness. Since then it was accepted in the research community to assume Post-Yield Stiffness equal a percentage of the Initial Stiffness. In recent study involved Holo-Bolted connections to RHS and SHS columns, Málaga-Chuquitaype and Elghazouli (2010b) assumed a ratio of 10% of the Initial Stiffness for the Post-Yield Stiffness for the column face component. In this study, the post yield stiffness will be assumed to be a percentage of the Initial stiffness in line with the literature.

2.7 Summary

Holo-Bolts are one of the Blind Bolts currently available in the market for use in hollow sections joints as an alternative to welding e.g. SHS joints, but its use is currently restricted to transferring tensile forces and vertical shear. Filling SHS with concrete, when utilising Holo-Bolts in SHS joints, was found to improve the joints performance. However, to date, there is no guidance available for how to model and design Holo-Bolted concrete-filled SHS joints i.e. lack of knowledge exists.

In the component-based framework, if Holo-Bolts are to be used in beam-to-column joint where concrete-filled SHS are used as column, some of the basic components described in Table 6.1 of Eurocode 3 part 1-8 could be used to determine the behaviour of such joint. These include End-plate in bending, Beam web in tension and/or Beam flange and web in compression. Nonetheless, the behaviour of other components which are required and not described in that table is yet to be determined. These components are the Holo-Bolt in tension and the concrete-filled SHS face in bending when using Holo-Bolts. This research aims to devise a model to predict the behaviour of the concrete-filled SHS face in bending when using Holo-Bolts. Providing a model for the concrete-filled SHS face in bending component, along with Holo-Bolt in tension component, will allow for the use of the component method to model Holo-Bolted joints. This will also pave the way of these joints to be utilised by the main stream designers in buildings where SHS are used as column.

The work done to develop an analytical model for the concrete-filled SHS face in bending component is presented in the next chapter. This is followed by a description of full-scale experimental work and numerical modelling which are used to calibrate the aforementioned analytical model.

Chapter 3

Analytical Modelling

3.1 Introduction

This chapter presents the work done to develop a new analytical model for the structural behaviour of the face bending of concrete-filled SHS. This is done for SHS which are connected to other structural members, e.g. beams, using Hollo-Bolts.

Structural behaviour can be generally described by specifying stiffness and resistance. In this chapter, firstly, a description of how an analytical representation of the concrete-filled SHS face bending initial stiffness has been developed, for Hollo-Bolted connections, is presented. This is followed by yield-line analysis used to investigate possible failure mechanisms of such connections and their associated strengths. The mechanism which theoretically led to the critical yield force was adopted for the proposed model.

The Proposed model is considered novel in that it is based on a different controlling failure mechanisms than considered in other studies, and that is computed to produce a critical yield force.

3.2 The Initial Stiffness Component

In beam to SHS column bolted connections, the load is transferred from the beam to the column through the bolts. For concrete-filled SHS, Simões da Silva et al. (2004) validated the following expression to predict the initial stiffness of the SHS face bending (background in section 2.6.1 of this thesis):

$$S_i = \frac{Et_{wc}^3}{L^2} 16 \frac{\alpha + (1 - \beta) \tan \theta}{(1 - \beta)^3 + \frac{10.4(k_1 - k_2\beta)}{\mu^2}} \quad (3-1)$$

in which E is the steel young's modulus, t_{wc} is the column thickness, α , β and μ are dimensional parameters equal to c/L , b/L and L/t_{wc} respectively. K_1 , K_2 are numerical calibration coefficients equal to 1.5 and 1.6, and θ is the angle that defines l_{eff} (shown in Figure 3.1) and equal to $35-10\beta$ as suggested in both Simões da Silva et al. (2003) and (2004). The dimensions c and b are shown in Figure 3.1. L is equal to width of the SHS minus t_{wc} . By substituting all the dimensional parameters, this equation could be re-written as:

$$S = \frac{16Et^3}{(b-t)^2} \frac{\frac{c}{(b-t)} + \left(1 - \frac{g+c}{b-t}\right) \tan \theta}{\left(1 - \frac{g+c}{b-t}\right)^3 + \frac{10.4 \left[1.5 - 1.6 \left(\frac{g+c}{b-t}\right)\right]}{\left(\frac{b-t}{t}\right)^2}} \quad (3-2)$$

in which g is the distance between the centrelines of bolts commonly known as the bolts gauge. In Simões da Silva et al. (2004) work, the SHS face was represented by a plate loaded by a rigid strip. The plate boundary conditions were defined based on the concrete-filled SHS

geometry. The plate was assumed to be fixed at the two parallel ends as the concrete infill restrains the two SHS faces perpendicular to the connected face from deforming. The rigid strip is assumed to have a height equivalent to c which is calculated using (with reference to Figure 3.2):

$$c = \frac{s + e}{2} \quad (3-3)$$

Furthermore, the width of the rigid strip is assumed equivalent to b which is calculated using:

$$b = g + c \quad (3-4)$$

Since the length of the plate (i.e. SHS column height) is very long compared to its width (i.e. SHS column width), the problem was simplified to a fixed beam loaded by a rigid area. Detailed description of how Equation (3-1) was reached is presented in Chapter 2 of this thesis.

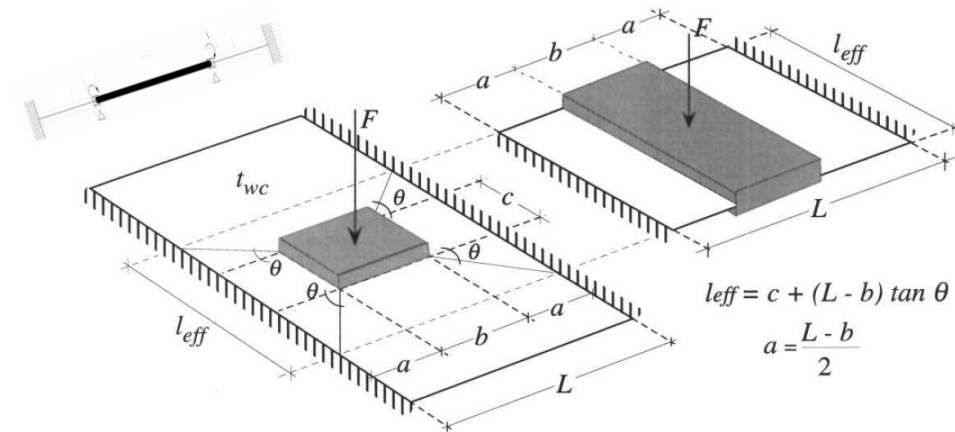


Figure 3.1 Web/face loaded by equivalent strip (Simões da Silva et al., 2004)

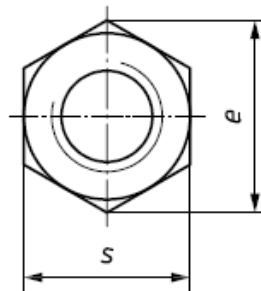


Figure 3.2 Typical hexagon nut layout (BSI, 2012)

In this work, when the Hollo-Bolt is utilised in SHS connection, the load transfer mechanism differs from that of the conventional bolt. In the case of conventional bolt, the load is directly applied on SHS column face through bolt nut in contact. However, in the case of the Hollo-Bolts, the opened sleeves apply the load on the SHS column face through the concrete-infill, where a concrete cone is assumed to develop as shown in Figure 3.3.

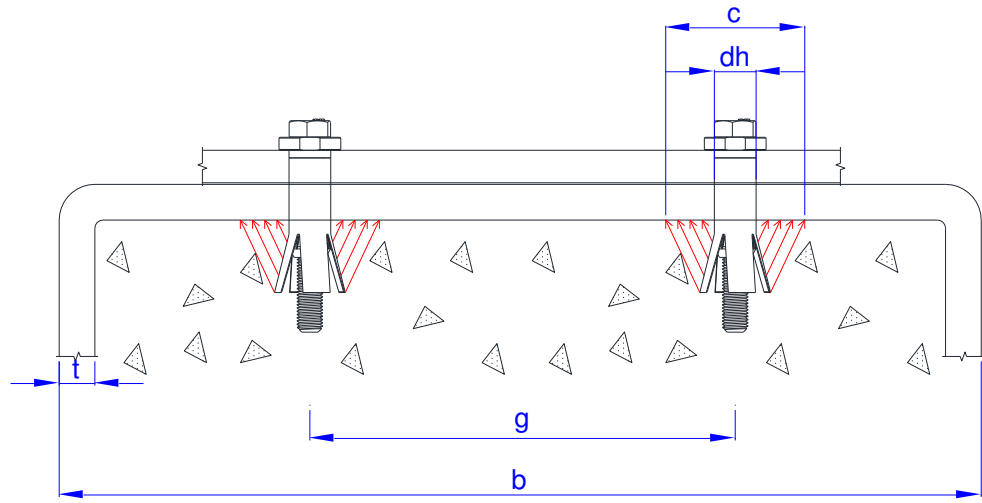


Figure 3.3 Assumed load transfer mechanism from Hollo-Bolts to SHS face

This load transfer mechanism (shown in the figure above) results in a larger loaded area on the SHS face compared with the conventional bolt loaded area. In order to use Equation (3-2) for the initial stiffness, the height (c) and width (b) of the loaded rigid area should be modified to account for Hollo-Bolt utilisation. This is done by introducing the following expression to calculate the height of the loaded rigid area (c) instead of using Equation (3-3):

$$c = k d_h \quad (3-5)$$

in which k is a calibration factor and d_h is the hole diameter which is equal to Hollo-Bolt sleeve diameter.

The calibration factor (k) in Equation (3-5) has been introduced to account for the geometry of opened/tightened Holo-Bolts and how it will transfer the load to the SHS face.

The load transfer mechanism (as shown in Figure 3.3) is affected by the width of Holo-Bolt's opened sleeves which is directly affected by the Holo-Bolt embedded length inside the RHS/concrete in-fill. This embedded length is in turn affected by the plate/RHS thickness which the Holo-Bolt clamps i.e. the clamping thickness. The load transfer mechanism would be also affected by the properties of the concrete-infill and the connection configuration. Equation (3-4) can still be used to calculate the width b . The work done to determine the calibration factor k is presented in Chapter 7 of this thesis after presenting the testing programme designed and conducted to calibrate the proposed model (in Chapter 4) and its outcomes (in Chapter 5).

3.3 The Resistance

This section describes how the yield force in the proposed model is formulated.

In a connection to concrete-filled SHS, and where a single row of bolts is in tension, the connected SHS face can be assumed as a plate loaded with two point loads. To assess the bending behaviour of this plate, the edges degrees of freedom (i.e. boundary conditions) need to be defined. The two parallel edges of the plate, along the length of SHS, are assumed fixed due to the concrete-infill restraint following what is mentioned in the previous section. The remaining two edge restraints - along the width of SHS column - are assumed to not influence the behaviour of the plate as the restraints are relatively far from the load. The result is a long plate fixed in two edges and loaded with two internal point loads. Using Yield-line analysis, the possible failure

mechanisms for this loading arrangement were evaluated. These mechanisms are shown in Figure 3.4.

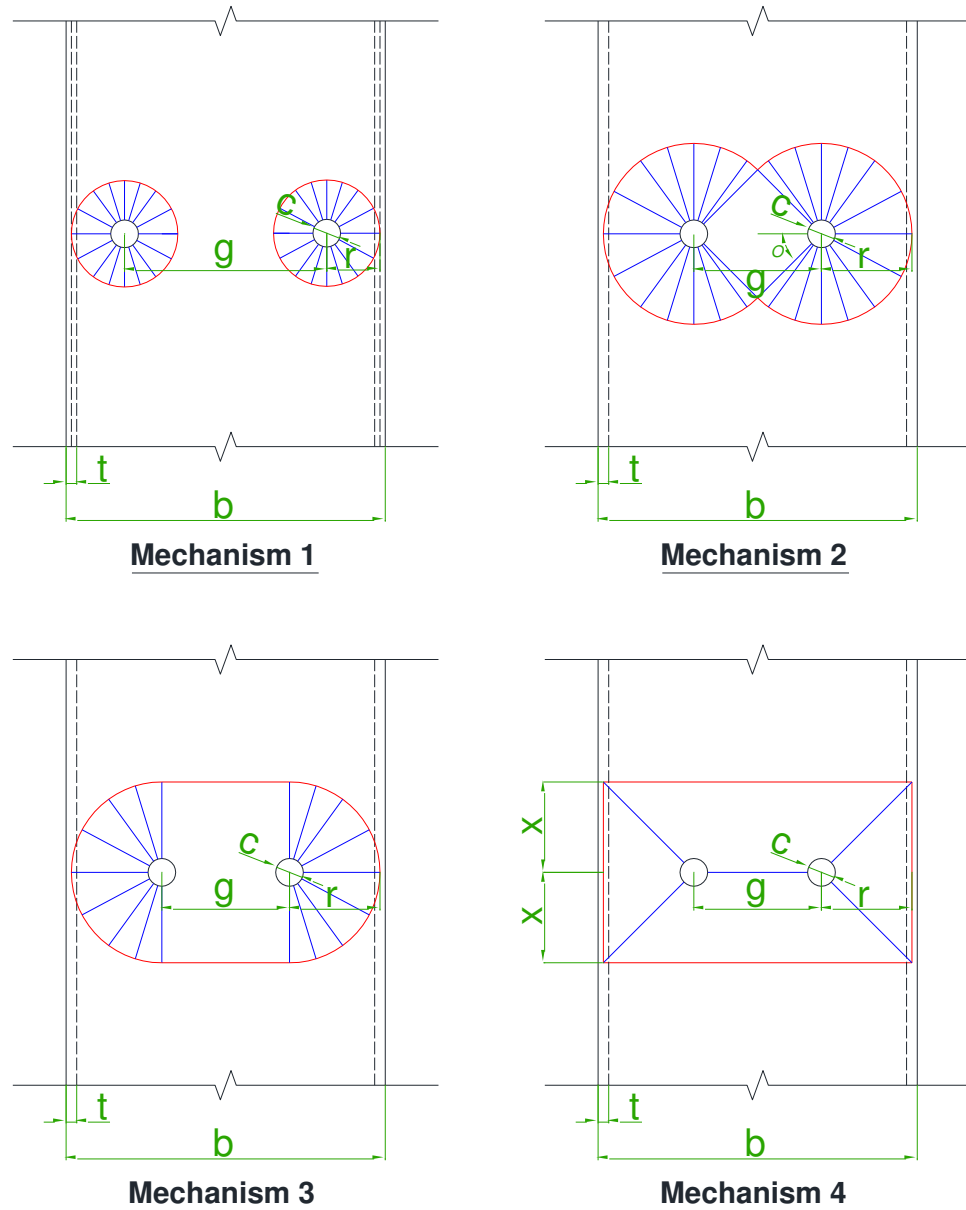


Figure 3.4 Possible failure mechanisms (using yield line analysis)

The first three mechanisms are the possible variations of developing the typical circular yield area, while the fourth assume the simplified yield lines pattern currently assumed in the design of tie forces in the literature (SCI/BCSA, 2002, SCI/BCSA, 2011).

The punching shear of the SHS face was not considered in these mechanisms nor was the axial compression on the SHS.

Mechanisms 1 and 2 depend on g . If g is greater than the $2r$ then two separate yield line circles can occur i.e. Mechanism 1 can develop, otherwise, Mechanism 2 will develop instead. In other words, Mechanisms 1 & 2 complement each other geometrically as mechanism 1 is possible when $r \geq g/2$, while mechanism 2 is possible only when $r < g/2$.

To evaluate the capacity of each mechanism, the moment required to yield a unit length of the SHS face is assumed equal to the yield moment and is equal to:

$$M = \frac{f_y t^2}{4} \quad (3-6)$$

where f_y and t are the yield stress of the SHS steel and the thickness of the SHS face respectively.

Evaluation of the area enclosed by the curved yield lines in mechanisms 1, 2 and 3 is also needed. These yield lines are assumed to propagate up to the centreline of any fixed edge. This is because the fixed edge will restrain any further propagation as mention in the literature (Johansen, 1962b, Johansen, 1962a). Therefore, referring to Figure 3.4, the radius of the curved line for Mechanisms 1, 2 and 3, which equal to the distance r in mechanism 4, will be taken as:

$$r = \frac{b - g - t}{2} \quad (3-7)$$

In all mechanisms, the load from the Hollo-Bolts/concrete-infill is assumed to be applied on the SHS face on a circle. This circle is assumed to have a diameter equal to c (as shown in Figure 3.4).

The force required to yield a small length of a yield line is calculated using the work method. This is done using the following expression:

$$\begin{aligned} & \text{Force} \times \text{Displacement} \\ &= \text{Moment} \times \text{Rotation angle} \times \text{Yield lines length} \end{aligned} \quad (3-8)$$

The following sections show how the yield force is calculated for the possible failure mechanisms shown in Figure 3.4:

3.3.1 Mechanism 1

For Mechanisms 1, the force required to yield a small part of the circular yielded area (i.e. yielded circle) is calculated using Equation (3-8). This force is then integrated to determine the yield force of the mechanism. Figure 3.5 shows a small part of the yielded area that has a length of ds .

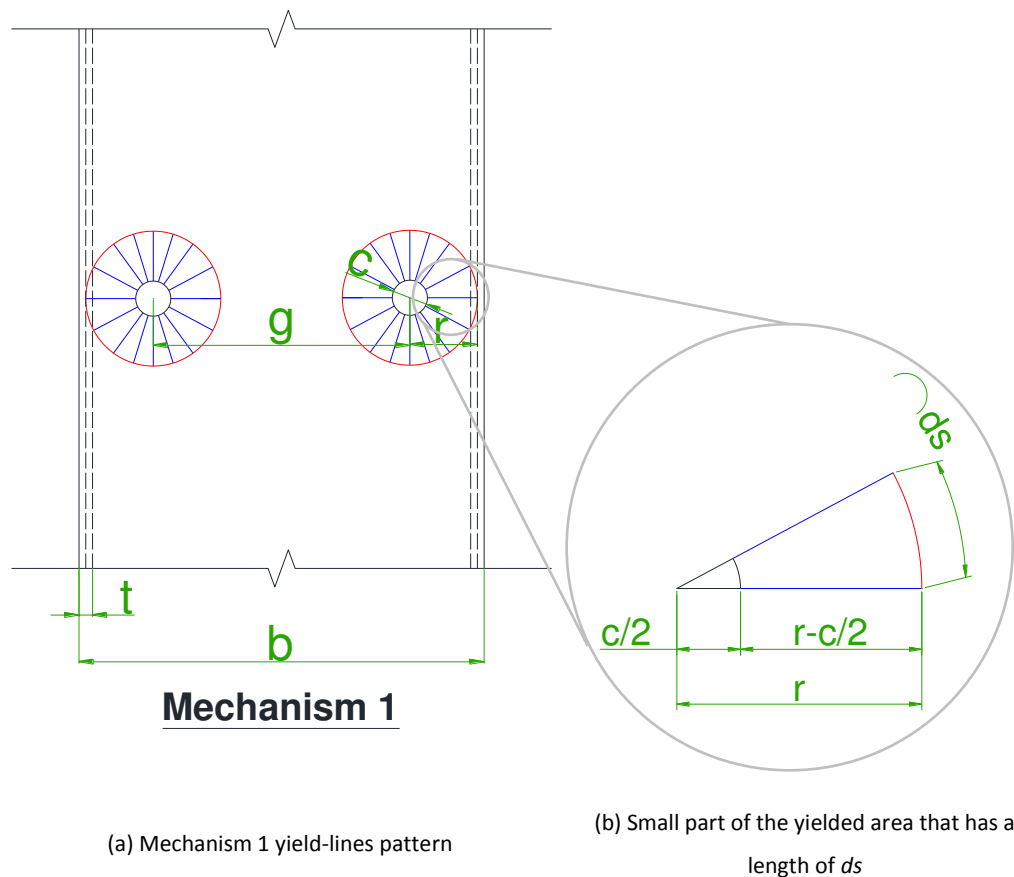


Figure 3.5 Mechanism 1 yield-lines pattern

The moment required to yield a unit length of the SHS face is assumed equal to M as in Equation (3-6). The rotation angle is calculated assuming that the SHS face has displaced one unit where the load is applied i.e. at the circle which has the diameter c . This angle can be calculated as:

$$\theta_{circle} = \frac{1}{r - \frac{c}{2}} \quad (3-9)$$

Using Equations (3-6), (3-7), (3-8) and (3-9), the force required for the part shown in Figure 3.5 (b) can be calculated as:

$$\partial F \cdot 1 = M \frac{1}{r - \frac{c}{2}} \partial s + M \frac{1}{r - \frac{c}{2}} r - \frac{c}{2} \frac{\partial s}{r} \quad (3-10)$$

The first part of Equation (3-10) represents *moment x angle x length* for the circular yield lines (drawn in red in Figure 3.5), where the second part represent the same for the straight lines (drawn in blue in Figure 3.5). The expression in Equation (3-10) can be integrated to calculate the yield force of one circular area i.e. for one bolt, and doubled to calculate the yield force for the full mechanism as:

$$F = 2 \times \int_0^{2\pi r} M \frac{1}{r - \frac{c}{2}} \partial s + M \frac{1}{r - \frac{c}{2}} \frac{r - \frac{c}{2}}{r} \partial s \quad (3-11)$$

This can be simplified as:

$$F = 2 \times \int_0^{2\pi r} M \left(\frac{1}{r - \frac{c}{2}} + \frac{1}{r} \right) \partial s \quad (3-12)$$

$$F = 2 \times 2 \pi M r \left(\frac{1}{r - \frac{c}{2}} + \frac{1}{r} \right) \quad (3-13)$$

Which lead to the following expression to calculate the force of Mechanism 1:

$$F_{Mec. 1} = 4 \pi M \left(1 + \frac{r}{r - \frac{c}{2}} \right) \quad (3-14)$$

3.3.2 Mechanism 2

In this mechanism, the circular areas intersect in the middle as shown in Figure 3.6. The intersection depends on the gauge between the bolts and for the purpose of the following calculations is defined by an angle called α (also shown in Figure 3.6).

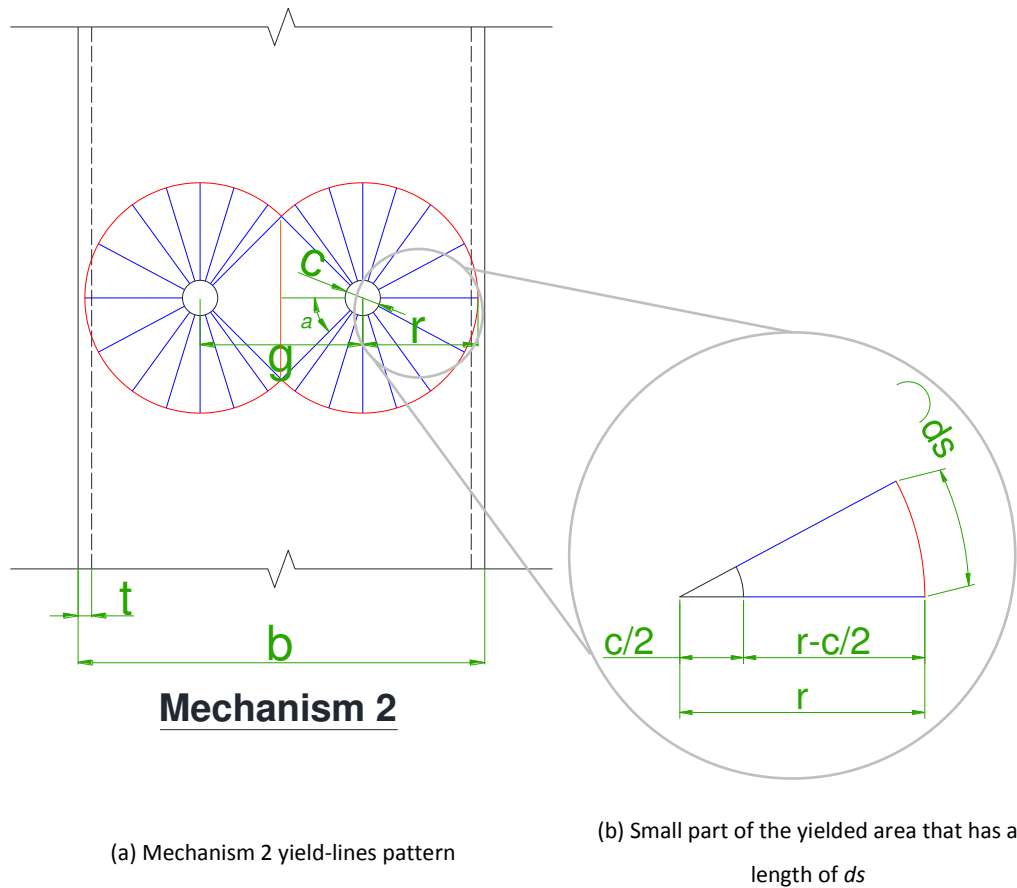


Figure 3.6 Mechanism 2 yield-lines pattern

The moment required to yield a unit length of the SHS face is assumed equal to M as in Equation (3-6). The rotation angles are calculated assuming that the SHS face has displaced one unit where the load is applied i.e. at the circle which has the diameter c . These angles can be calculated as:

$$\begin{aligned}\theta_{circle} &= \frac{1}{r - \frac{c}{2}} \\ \theta_{tringle} &= \frac{1}{\frac{g}{2} - \frac{c}{2}} = \frac{1}{\frac{g - c}{2}}\end{aligned}\tag{3-15}$$

Similar to Mechanism 1, the force required to yield a small part of the circular yielded area in Mechanism 2 is calculated using Equation (3-8). This force is then integrated to determine the yield force of the mechanism.

The angle a is used to define the limits for the integration. This angle is calculated as:

$$a = \cos^{-1}\left(\frac{g}{2r}\right)\tag{3-16}$$

The force which results from the linear yield-lines is calculated using Equation (3-8). This is done as:

$$\begin{aligned}F &= 2 \int_0^{\left(1 - \frac{2a}{360}\right) 2\pi r} M \left(\frac{1}{r - \frac{c}{2}} + \frac{1}{r} \right) ds \\ &\quad + 2 M \frac{1}{\frac{g - c}{2}} \sqrt{r^2 - \left(\frac{g}{2}\right)^2}\end{aligned}\tag{3-17}$$

Equation (3-17) is then simplified as:

$$F = 4 \left(1 - \frac{2\alpha}{360} \right) \pi M r \left(\frac{1}{r - \frac{c}{2}} + \frac{1}{r} \right) + 2 M \frac{\sqrt{r^2 - \left(\frac{g}{2} \right)^2}}{\frac{g - c}{2}} \quad (3-18)$$

which lead to the following expression to calculate the force of Mechanism 2:

$$F_{Mec. 2} = 2M \left[2\pi \left(1 - \frac{\alpha}{180} \right) \left(1 + \frac{r}{r - \frac{c}{2}} \right) + \left(\frac{\sqrt{r^2 - \left(\frac{g}{2} \right)^2}}{\frac{g - c}{2}} \right) \right] \quad (3-19)$$

3.3.3 Mechanism 3

In this mechanism, the circular areas of yield lines only exist towards the walls of the SHS as half circles. Linear yield lines forms between the two half circles as shown in Figure 3.7.

The moment required to yield a unit length of the SHS face is assumed equal to M as in Equation (3-6).

The rotation angles are calculated assuming that the SHS face has displaced one unit where the load is applied i.e. at the circle which has the diameter c . These angles can be calculated using Equation (3-20).

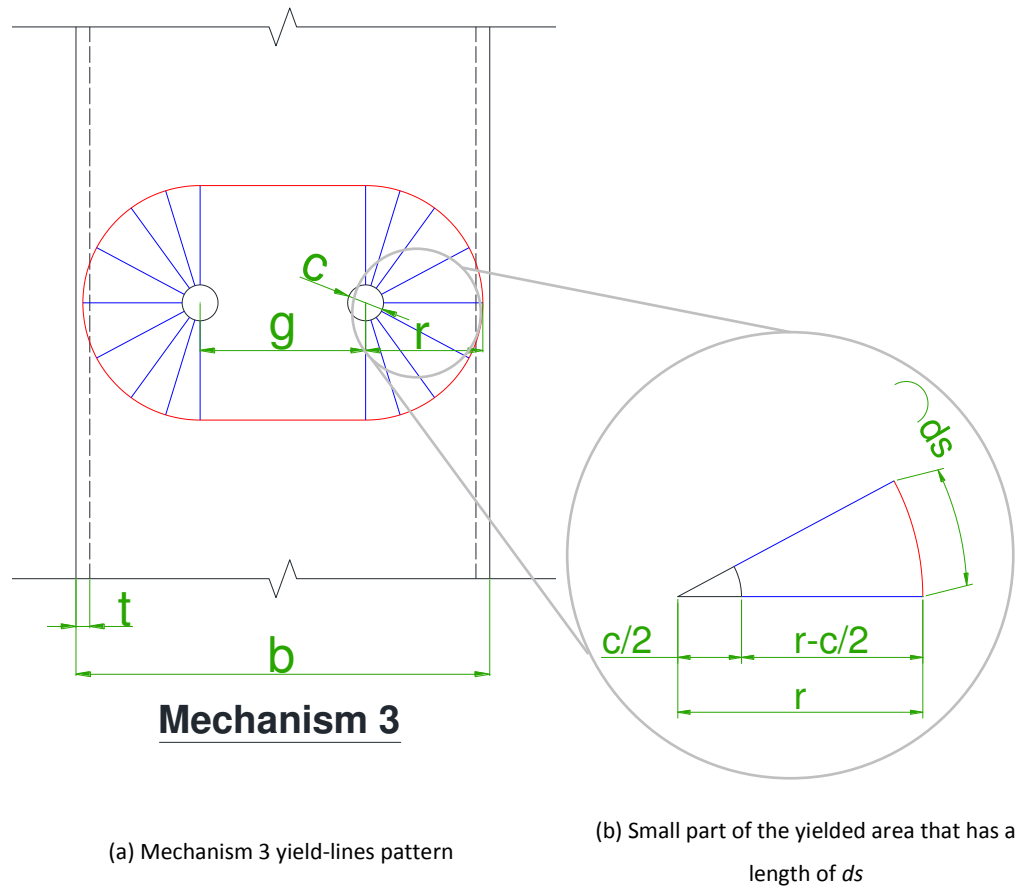


Figure 3.7 Mechanism 3 yield-lines pattern

$$\theta_{circle} = \frac{1}{r - \frac{c}{2}} \quad (3-20)$$

$$\theta_{linear} = \frac{1}{r}$$

The force required to yield a small part of the circular yielded area in Mechanism 3 is calculated using Equation (3-8). This force is then integrated to determine the yield force of the mechanism. Similarly, the force which results from the linear yield-lines is calculated using Equation (3-8). This is done as:

$$F = 2 \int_0^{2\pi r} M \left(\frac{1}{r - \frac{c}{2}} + \frac{1}{r} \right) \partial s + 2 M g \frac{1}{r} \quad (3-21)$$

The above equation is simplified as:

$$F = 2 \pi M r \left(\frac{1}{r - \frac{c}{2}} + \frac{1}{r} \right) + 2 M \frac{g}{r} \quad (3-22)$$

which lead to the following expression to calculate the force of Mechanism 3:

$$F_{Mec. 3} = 2 \pi M \left(1 + \frac{r}{r - \frac{c}{2}} \right) + 2 M \frac{g}{r} \quad (3-23)$$

3.3.4 Mechanism 4

In this mechanism, no circular lines exist. The yield-lines pattern is shown in Figure 3.8 below.

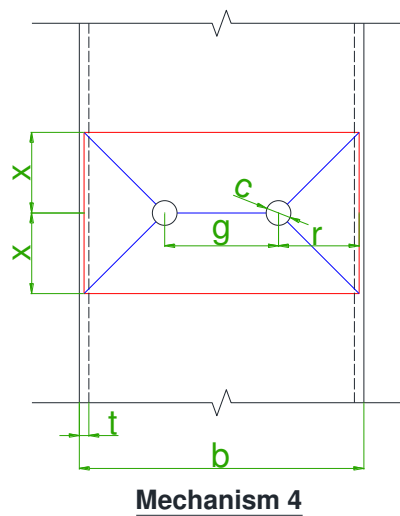


Figure 3.8 Mechanism 4 yield-lines pattern

The moment required to yield a unit length of the SHS face is assumed equal to M as in Equation (3-6). The rotation angles are calculated assuming that the SHS face has displaced one unit where the load is applied i.e. at the circle which has the diameter c . These angles can be calculated as:

$$\theta_{triangle} = \frac{1}{r} \quad (3-24)$$

$$\theta_{rectangular} = \frac{1}{x}$$

Using Equation (3-8), the yield force which results from this mechanism is calculated as:

$$F = 2 \left[M 2x \frac{1}{r} + M (2x - c) \frac{1}{r} \right] + 2 \left[M (g + 2r) \frac{1}{x} + M (g + 2r - 2c) \frac{1}{x} \right] \quad (3-25)$$

The above equation is simplified as:

$$F = 4 \frac{M}{r} \left(x + x - \frac{c}{2} \right) + 4 \frac{M}{x} (g + 2r - c) \quad (3-26)$$

which lead to the following expression to calculate the force of Mechanism 4:

$$F_{Mec. 4} = 4 M \left(\frac{2x - \frac{c}{2}}{r} + \frac{g + 2r - c}{x} \right) \quad (3-27)$$

The unknown dimension x is determined using first derivative test on Equation (3-27) to find the minima/maxima of the function as:

$$\begin{aligned} F_{Mec. 4}'(x) &= 4M \left(\frac{\partial}{\partial x} \left[\frac{1}{r} \left(2x - \frac{c}{2} \right) + (g + 2r - c) \frac{1}{x} \right] \right) \\ &= 4M \left(\frac{2}{r} + (-1)(g + 2r - c) \frac{1}{x^2} \right) = 0 \end{aligned} \quad (3-28)$$

which lead to the x to be calculated as:

$$x = \sqrt{\frac{r(g + 2r - c)}{2}} \quad (3-29)$$

3.3.5 Comparison of Mechanisms

All the possible mechanisms are varied to determine the critical mechanism. Practical range of SHS is considered. This range is described in detail and justified in section 4.2.2 of this thesis. The yield forces calculated using all four mechanisms are compared for all possible geometries across the range. The comparison is shown in Figure 3.9 to Figure 3.11 below.

Three slenderness ratios of the SHS face (width to thickness ratio) are shown in the figures: 20 (in Figure 3.9), 30 (in Figure 3.10) and 40 (in Figure 3.11). The gauge has been varied to all possible values for all of the aforementioned three slenderness ratios. This is shown as the ratio β which is equal to gauge to width ratio. The figures plot the yield force resulting from all of the four mechanisms.

Figure 3.9 shows a comparison of how each mechanism evaluates the yield force for a SHS, which has a slenderness ratio of 20. The force is plotted against β . Figure 3.10 and Figure 3.11 show the same comparison for SHS, which has a slenderness ratio of 30 and 40, correspondingly.

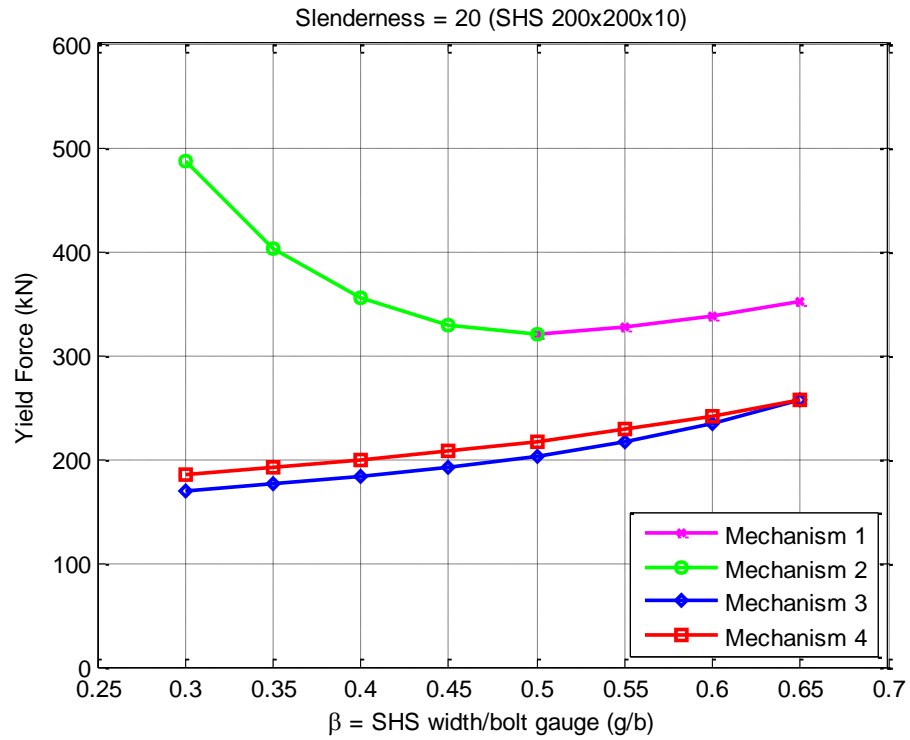


Figure 3.9 Yield force theoretically calculated for SHS 200x200x10

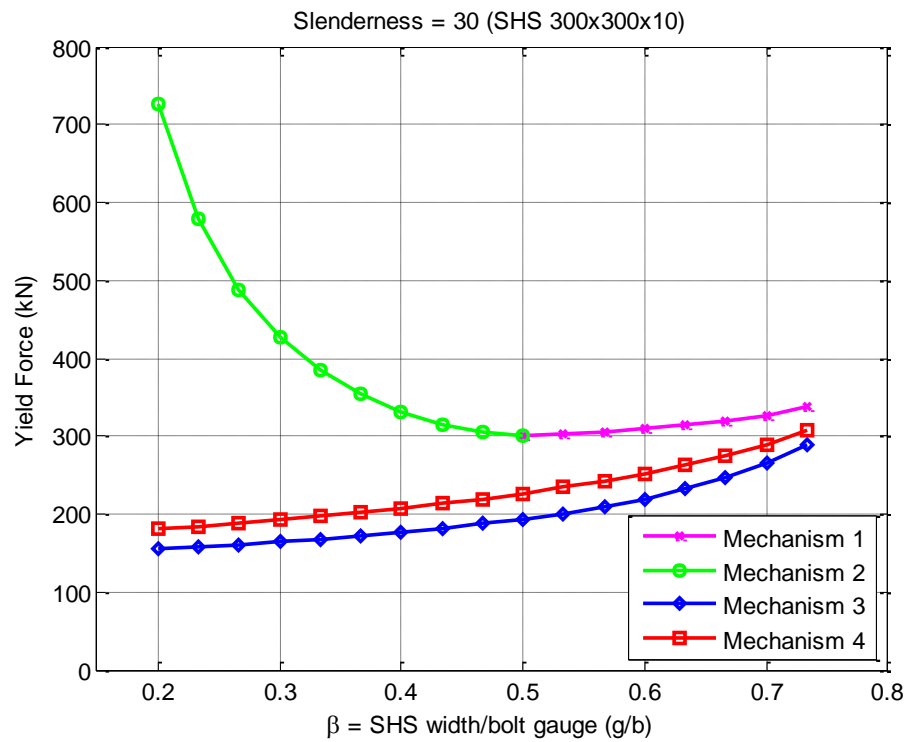


Figure 3.10 Yield force theoretically calculated for SHS 300x300x10

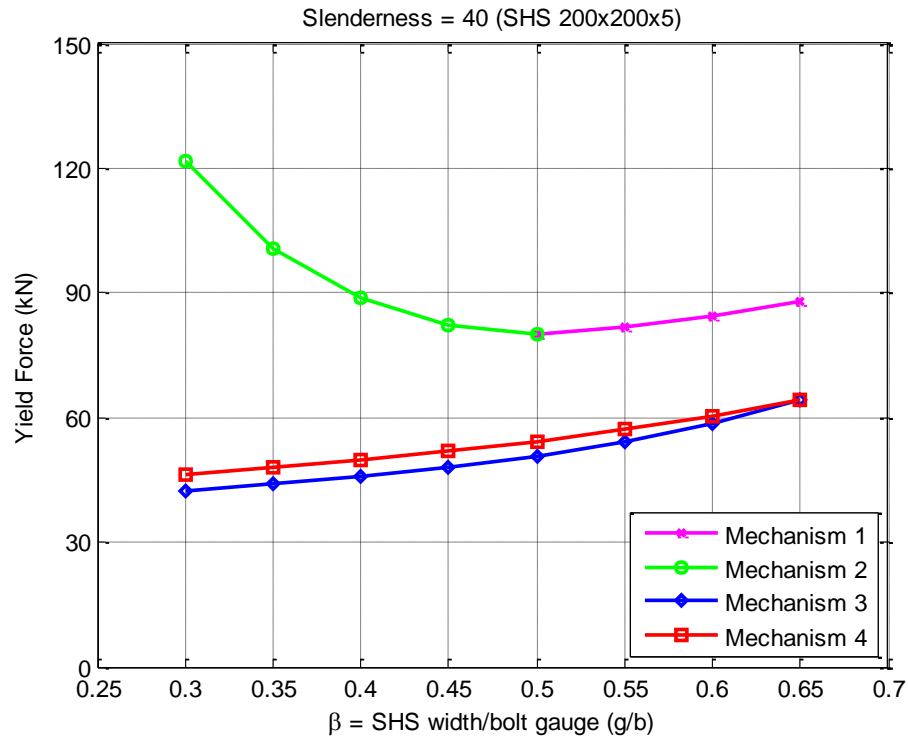


Figure 3.11 Yield force theoretically calculated for SHS 200x200x5

It is apparent from Figure 3.9, Figure 3.10 and Figure 3.11 that the yield force calculated assuming Mechanism 3 is the lowest for the range considered. This conclusion was found for all the possible geometries within the range. Therefore, based on the Yield line theory, Mechanism 3 is the critical mechanism in this loading arrangement. Mechanism 3 is also found to be less conservative than the idealisation commonly used in practice for this loading arrangement that is typically represented by Mechanism 4. This mechanism is adopted for the analytical model.

3.4 Post-yield Stiffness

In many studies in the literature, the post-yield stiffness is taken as a percentage of the initial stiffness such as in the work of Málaga-Chuquitaype and Elghazouli (2010) and Ghobarah et al. (1996). The work done to determine this percentage is presented in Chapter 7 of this thesis.

3.5 Proposed Model

Following the work which has been described in this chapter, the introduced bi-linear model consists of three parts. The first part is the initial stiffness which is calculated using Equation (3-2). The parameter c in this equation is calculated using Equation (3-5) in which the calibration factor k is introduced. The second part is the Yield force calculated using Equation (3-23) assuming Mechanism 3 to be critical. Finally, the third part is the post-yield stiffness, which is considered to be a percentage of the initial stiffness. The work done to calculate the calibration factor k in Equation (3-5) and the post-yield stiffness is described in details in Chapter 7 of this thesis which analyse the outcomes of an experimental programme designed and conducted to calibrate the proposed model. The proposed model is shown in Figure 3.12.

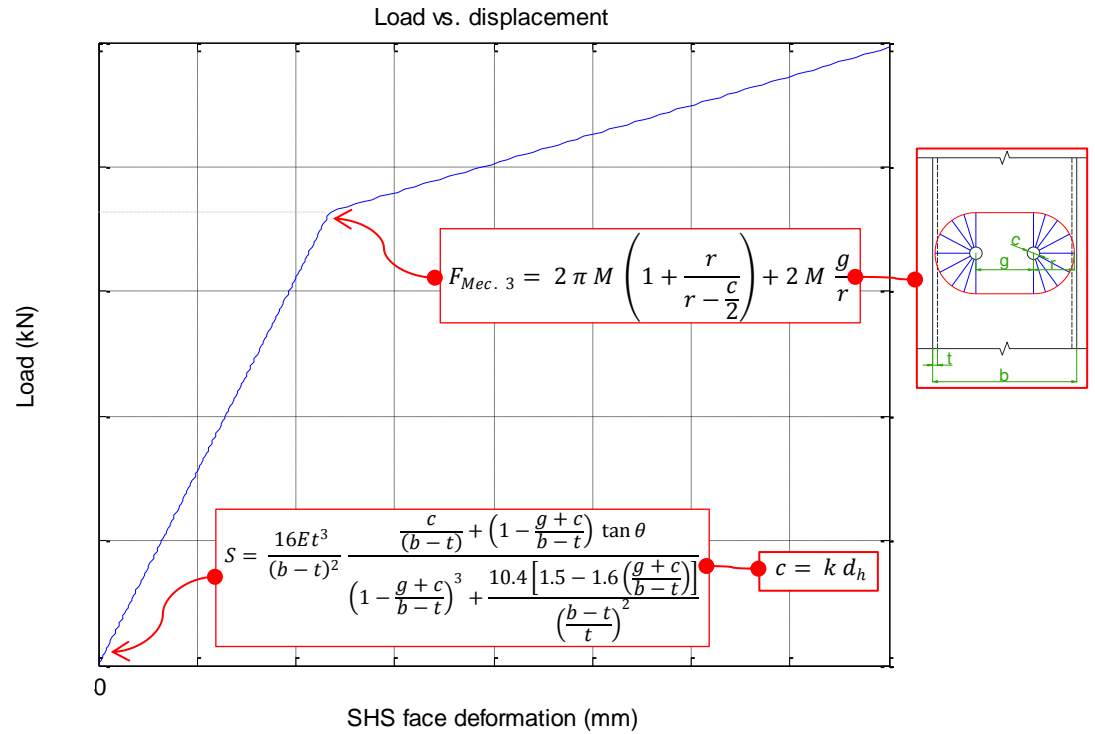


Figure 3.12 Proposed Bi-Linear analytical model

3.6 Summary

This chapter proposes a new Bi-Linear analytical model to predict the face bending behaviour of concrete-filled Square Hollow Sections when connected to other structural members using Hollo-Bolts. The model has three parts; initial stiffness, resistance (in a form of yield force) and post-yield stiffness.

The initial stiffness is formulated by theoretically substituting the concrete-filled Square Hollow Section face with a beam loaded by a rigid strip while fixed at its ends. The Yield Line Theory is used to investigate possible failure mechanisms. The critical mechanism is adopted to evaluate the resistance part of the model. Post-yield stiffness is to be considered as a percentage of the Initial stiffness.

The Bi-Linear analytical model is limited to SHS where just one row of Hollo-bolts (i.e. two bolts) is subjected to tension. The punching shear of the SHS face and the axial compression on the SHS were not considered in the development of this model.

An experimental programme is designed and conducted to calibrate the proposed model i.e. calculate the calibration factor k and determine the Post-Yield Stiffness. This programme is detailed in the next chapter.

Chapter 4

Experimental Programme

4.1 Introduction

As part of this research, an experimental programme was designed and carried out to investigate the face bending behaviour of concrete filled SHS, when connected to other structural elements, via Hollo-Bolts.

The aim of the programme is to verify the analytical model. It also investigates how several parameter variations affect the behaviour. This chapter details the programme, and describes how the Test Matrix was formulated.

The chapter includes the description of the samples and the testing rig. It also provides a detailed description of instruments used in the course of the programme to measure the SHS face bending, as force-displacement response. Actual properties of the materials used during the programme along with testing procedure are also reported herein.

4.2 Design of Experimental Programme

To meet the aim of this experimental programme the following objectives were set:

- Define the parameters which may affect the face bending behaviour of concrete-filled SHS.
- Investigate the effect of varying parameters across their appropriate range.
- Use a suitable test setup which enables the isolation and capture of the face bending behaviour of concrete-filled SHS.

The following sections highlight what are the parameters that affect the face bending behaviour of concrete-filled SHS. A description of how the appropriate range for each parameter was determined is also presented.

The outcome of each experiment of this programme is a force-displacement curve. This was decided to enable the comparison between the outcomes of the programme and the theoretical model which relates force to displacement. The instruments used to capture and produce force-displacement curves are described in sections 4.6 and 4.7 of this chapter.

4.2.1 Parameters

The experimental programme considers concrete-filled SHS connections where only one row of bolts is in tension (the row consist two bolts only). The programme utilises Lindapter HB16 Hollo-Bolt. HB16 has three types: HB16-1, HB16-2 and HB16-3. The main properties of HB16 are described in Table 4.1. Concrete-filled SHS and Lindapter HB16 Hollo-Bolt are controlled parameters throughout this testing programme.

Table 4.1 **Hollo-Bolt HB16 main properties (Extracted from Lindapter Manual)**

Type	Bolt	Clamping	Sleeve		Collar		Tightening
		Thickness	Length	Outer Diameter	Height	Diameter	Torque
		(mm)	(mm)	(mm)	(mm)	(mm)	(Nm)
HB16-1	M16x75	12-29	41.5	25.75	8	38	190
HB16-2	M16x100	29-50	63	25.75	8	38	190
HB16-3	M16x120	50-71	84	25.75	8	38	190

When considering such connections, the following parameters can affect the SHS face bending behaviour:

- SHS outside width (b)
- SHS thickness (t)
- The distance between Hollo-Bolts in the row i.e. gauge (g)
- SHS mechanical properties
- Concrete-infill mechanical properties

During this experimental programme, the geometrical properties listed above are combined into the following dimension-less parameters:

- SHS slenderness ratio (μ) = SHS width (b) / SHS thickness (t)
- β = gauge (g) / SHS width (b)

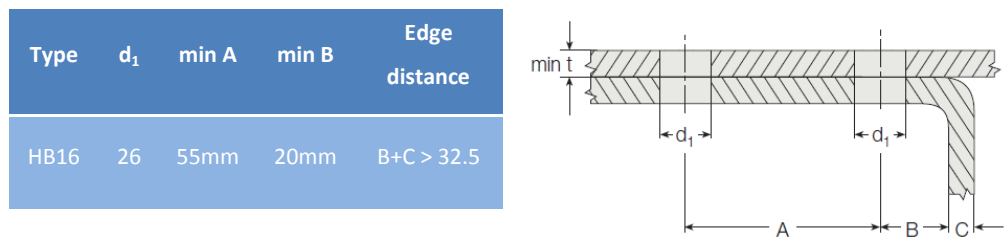
These non-dimensional parameters are commonly used in practice in the design of Hollow Sections connections.

4.2.2 Range

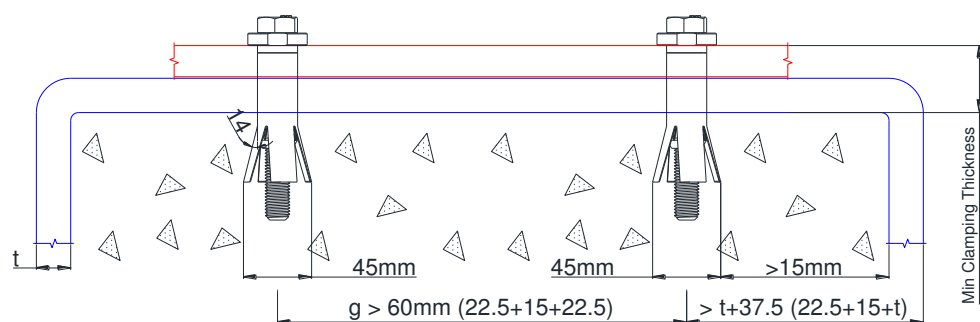
To define the experimental programme range, the geometry of the Hollo-Bolted connections needed to be carefully investigated. Referring to Figure 4.1, modification to Edge and minimum Gauge distances recommended by Lindapter in its catalogue was considered. Proposed modifications, and their justifications, are discussed in the following points:

1. Lindapter specifies minimum Edge distances for Hollo-Bolted connections in its manual. It does not, however, consider concrete-filled connections. To account for concrete in-fill, clear distance between the edge of opened Hollo-Bolt (i.e. edge of sleeves) and the internal edge of SHS is required. This distance is needed so the concrete can be placed and compacted satisfactorily for the development of adequate bond; hence, modification to these distances is needed.
2. According to section 8.2 of Eurocode 2, the clear distance between bars should not be less than the maximum of $k_1 \times$ bar diameter, $(d_g + k_2)$ or 20mm (CEN, 2004a). The recommended values for k_1 and k_2 for the UK are 1mm and 5mm respectively (CEN, 2004b). The condition ' $k_1 \times$ bar diameter' was not considered on the grounds that the complicated shape of Hollo-Bolt cannot be considered similar the reinforcement bar shape. Moreover, for the same reason, only the second condition ' $(d_g + k_2)$ ' was considered when calculating the Edge and minimum Gauge distances.
3. As a result of the previous point (Point No. 2), the calculation of Edge and minimum Gauge distances became directly related to max diameter of aggregate (d_g). Throughout this experimental programme, aggregate passed through 10mm sieve was used (max diameter of aggregate: $d_g=10\text{mm}$).
4. Hollo-Bolt HB16 sleeves open with an angle equal to the nut angle (14°). As a result, assuming minimum clamping thickness, the maximum theoretical width of an opened Hollo-Bolt is calculated to be $\approx 45\text{mm}$ (at end of sleeves level). This width has to be considered when calculating the minimum Edge and Gauge distances.

5. To tighten HB16, a recommended torque (190Nm) needs to be applied usually using a handheld torque wrench. The accuracy of this recommended torque cannot be guaranteed on-site which may lead to an increase/decrease in the maximum width of an opened Hollo-Bolt. Therefore, a small tolerance can be added to the calculated theoretical width. This tolerance is also to account for any possible variation that may occur during Hollo-Bolt nuts production. This tolerance has not been considered in this study.



(a) Minimum Bolt Diameter, Gauge and Edge distances recommended by Lindapter



(b) Minimum Gauge and Edge distances used in the experimental programme

Figure 4.1 Minimum Gauge and Edge distances

After careful consideration of the points mentioned above, minimum and maximum possible gauges can be calculated as shown in the following equations:

$$\begin{aligned} g_{min} &= \frac{45}{2} + (d_g + k_2) + \frac{45}{2} \\ &= \frac{45}{2} + (10 + 5) + \frac{45}{2} = 60mm \end{aligned} \tag{4-1}$$

$$\begin{aligned} g_{max} &= b - 2t - \left(\frac{45}{2} + \frac{45}{2} + 2 \times (d_g + k_2) \right) \\ &= b - 2t - \left(\frac{45}{2} + \frac{45}{2} + 2 \times (10 + 5) \right) \\ &= b - 2t - 75 \end{aligned} \tag{4-2}$$

Similarly, the geometry of SHS which can utilise Hollo-Bolted connections is considered. Referring to Table 4.1, the Hollo-Bolts Clamping thicknesses for HB16-1, HB16-2 and HB16-3 as specified by Lindapter are 12-29, 29-50 and 50-71 respectively. An 8mm thickness collar is used in all types of HB16. The bolt used for HB16-1 is M16x75. Likewise, M16x100 is used in HB16-2 and M16x120 is used in HB16-3. The maximum possible length of Hollo-Bolt shank which can be inside SHS was calculated as 63mm for HB16-1, 71mm for HB16-2 and 70mm for HB16-3 (including collar thickness). In this research, this length is called L_r .

The length L_r and the collar thickness (t_c) are used to calculate the minimum SHS width required so the SHS can utilise a joint where at least two adjacent walls of the SHS have Hollo-Bolted connections i.e. double-sided joint. This joint is the most commonly used in practice (i.e. two beams connected to a column).

As a result, the minimum SHS width can be calculated as:

$$\begin{aligned}
 b_{min} &= 2(L_r - t_c) + (d_g + k_2) \\
 &= 2(71 - 8) + 15 \\
 &= 141\text{mm}
 \end{aligned}
 \tag{4-3}$$

Again, as mentioned before, ' $(d_g + k_2)$ ' in Equation (4-3) represents the minimum clear distance specified in Eurocode 2. Illustration is shown in Figure 4.2 below. As a result, any SHS with width less than 141mm is not considered in this experimental programme.

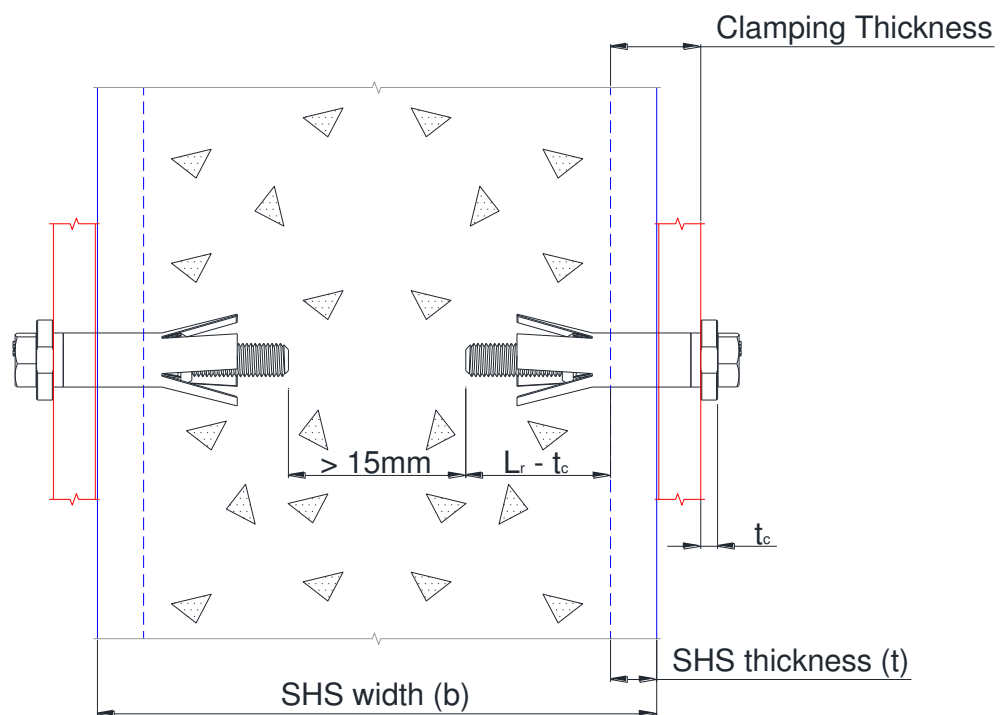


Figure 4.2 Illustration of minimum SHS width requirement

Referring to Table B.2 in BS EN 10210-2:2006, the SHS sections which satisfy the requirements highlighted earlier, range between SHS 150x150 and SHS 400x400 (BSI, 2006b).

In addition, SHS sections which have face bending yield load that significantly exceeds the Holo-Bolt M16 shank ultimate capacity (i.e. very rigid), were not considered in this experimental programme. This is due to the fact that, in practice, Holo-Bolts in Holo-Bolted connections to such sections will fail before SHS face bending occurs. Consequently, SHS which have slenderness ratio greater than 18.75 were not considered.

To investigate the effect of the concrete in-fill on the SHS face bending, the experimental programme also aimed to test various concrete grades. This was done by considering the use of low, medium and high strength concrete.

At the end, the parameter ranges which were considered are summarised as:

- i. The range for SHS slenderness ratio (μ) is between 18.75 and 40
- ii. The range of β is between β_{\min} and β_{\max} (calculated using g_{\min} and g_{\max} of each SHS)
- iii. Concrete grade ranges between C20 and C80

4.2.3 Test Matrix

Overall, the Test Matrix consists of 3 sets. Each set was designed to vary just one independent parameter (variable) and control all the others. Each test has a unique Test ID summarising its key information. How to read the Test ID is explained in Figure 4.3.

SHS 200x200 and SHS 300x300 sections were tested due to their availability in the lab during the period of testing. The full Test Matrix is shown in Table 4.2.



Figure 4.3 Test ID description

4.3 Description of the Samples

As anticipated by the analytical model described in Chapter 3, yield lines can form inside a restricted area of the SHS face. Referring to Figure 3.4, this area depends on the distance between bolt hole and SHS edge. This distance varies depending on SHS dimensions and bolt gauges. Within the range specified in the previous section, this distance is less than 70mm for SHS 200x200, and less than 120mm for SHS 300x300. Accordingly, SHS samples should be more than 240mm in length (to allow for yield lines at the top and the bottom of bolts to propagate). Any restraint to the SHS face within this length will affect the SHS face bending. In addition to that, more sample length is needed so it can be adequately placed in, and supported by the testing rig. Therefore, 600mm SHS samples were used in this experimental programme. The geometry of the testing rig also contributed in determining this length. Each sample has a row of two holes at the centre. This is to represent connections where only one row of Hollo-Bolts is in tension.

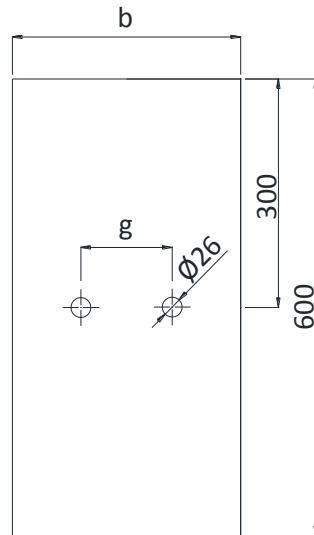
Table 4.2 Test Matrix

n.	Hollow Section	Width b (mm)	Thickness t (mm)	μ (b/t)	g_{min} (mm)	g_{max} (mm)	Selected β	Selected g (mm)	Concrete grade	Parameter varied	Test ID
1	SHS 200x200x8	200	8	25	60	109	0.4	80	C20	Concrete	b200t8g80c20-1
2	SHS 200x200x8	200	8	25	60	109	0.4	80	C20	Concrete	b200t8g80c20-2
3	SHS 200x200x8	200	8	25	60	109	0.4	80	C20	Concrete	b200t8g80c20-3
4	SHS 200x200x8	200	8	25	60	109	0.4	80	C50	Concrete	b200t8g80c50-1
5	SHS 200x200x8	200	8	25	60	109	0.4	80	C50	Concrete	b200t8g80c50-2
6	SHS 200x200x8	200	8	25	60	109	0.4	80	C50	Concrete	b200t8g80c50-3
7	SHS 200x200x8	200	8	25	60	109	0.4	80	C80	Concrete	b200t8g80c80-1
8	SHS 200x200x8	200	8	25	60	109	0.4	80	C80	Concrete	b200t8g80c80-2
9	SHS 200x200x8	200	8	25	60	109	0.3	60	C40	β	b200t8g60c40-1
10	SHS 200x200x8	200	8	25	60	109	0.3	60	C40	β	b200t8g60c40-2
11	SHS 200x200x8	200	8	25	60	109	0.3	60	C40	β	b200t8g60c40-3
12	SHS 200x200x8	200	8	25	60	109	0.4	80	C40	β and μ	b200t8g80c40-1
13	SHS 200x200x8	200	8	25	60	109	0.4	80	C40	β and μ	b200t8g80c40-2
14	SHS 200x200x8	200	8	25	60	109	0.4	80	C40	β and μ	b200t8g80c40-3
15	SHS 200x200x8	200	8	25	60	109	0.4	80	C40	β and μ	b200t8g80c40-4
16	SHS 200x200x8	200	8	25	60	109	0.5	100	C40	β	b200t8g100c40-1
17	SHS 200x200x8	200	8	25	60	109	0.5	100	C40	β	b200t8g100c40-2

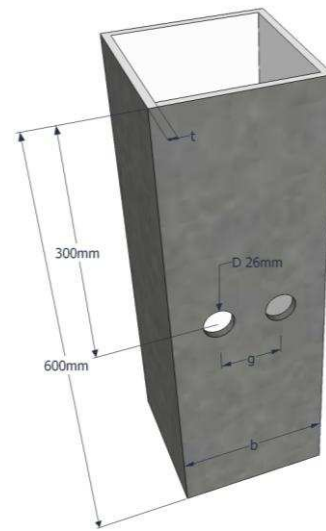
Table 4.2 **Test Matrix (continued)**

n.	Hollow Section	Width b (mm)	Thickness t (mm)	μ (b/t)	g_{\min} (mm)	g_{\max} (mm)	Selected β	Selected g (mm)	Concrete grade	Parameter varied	Test ID
18	SHS 200x200x10	200	10	20	60	105	0.4	80	C40	μ	b200t10g80c40-1
19	SHS 200x200x10	200	10	20	60	105	0.4	80	C40	μ	b200t10g80c40-2
20	SHS 200x200x6.3	200	6.3	31.75	60	112.4	0.4	80	C40	μ	b200t6.3g80c40-1
21	SHS 200x200x6.3	200	6.3	31.75	60	112.4	0.4	80	C40	μ	b200t6.3g80c40-2
22	SHS 200x200x8	200	5	40	60	115	0.4	80	C40	μ	b200t5g80c40-1
23	SHS 200x200x8	200	5	40	60	115	0.4	80	C40	μ	b200t5g80c40-2
24	SHS 200x200x8	200	8	25	60	109	0.4	80	C40	β and μ	b200t8g80c40-DIC
25	SHS 300x300x12.5	300	12.5	24	60	200	0.4	120	C40	μ	b300t12.5g120c40-1
26	SHS 300x300x12.5	300	12.5	24	60	200	0.4	120	C40	μ	b300t12.5g120c40-2
27	SHS 300x300x16	300	16	18.75	60	193	0.4	120	C40	μ	b300t16g120c40-1
28	SHS 300x300x16	300	16	18.75	60	193	0.4	120	C40	μ	b300t16g120c40-2

The compression part of connections was not considered for testing as it is negligible in concrete-filled SHS connections. The distance between the bolts (gauge) was varied as shown in the Test Matrix. A typical sample layout is shown in Figure 4.4.



(a) CAD plan



(b) 3D model (using Google SketchUp)

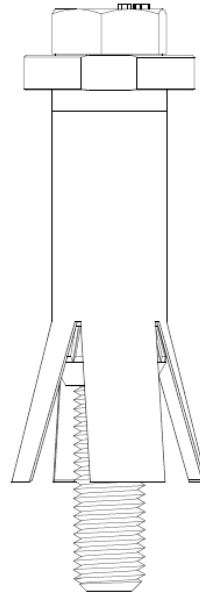
Figure 4.4 Typical SHS sample layout

4.4 Dummy Bolts

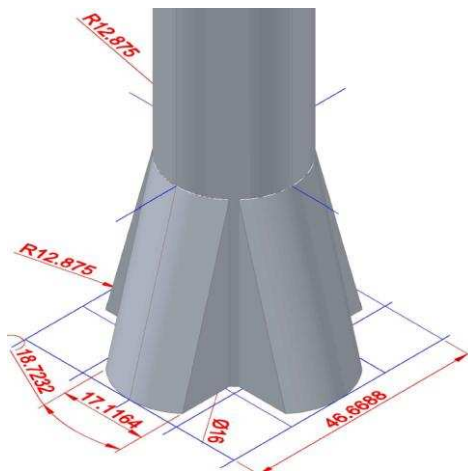
A dummy bolts were manufactured and used in this experimental programme to isolate any deformation or energy dissipation associated to the use of standard Holo-Bolts. Such deformations previously encountered in Elamin et al. (2010) experimental programme.

The dummy bolts were manufactured to the dimensions of opened Holo-Bolts HB16. A 3D CAD model of opened Holo-bolt HB16 was generated using Holo-Bolt CAD blocks. The CAD blocks can be downloaded from the Holo-Bolt manufacturer web page (Lindapter, 2013a). A snap-shot plot of the 3D model and one of the manufactured dummy bolts are shown in Figure 4.5. Future use of dummy bolts as

Extended Holo-Bolts which is currently being developed and tested in The University of Nottingham is also considered in the design. This is done by manufacturing a thread at the bottom of the dummy bolt to allow for the installation of an extension.



(a) Opened Holo-Bolt (HB16-3)



(b) 3D Model of dummy bolt



(c) Manufactured dummy bolt

Figure 4.5 Dummy Bolt

4.5 Test set-up

The experimental programme was designed to evaluate the SHS face bending. Both Pull-out and Push-out tests can be used in such

programmes. Initially 4 experiments were tested using Pull-out using the INSTRON Universal Testing Machine [reported in (Elamin, 2010)]. Problems related to monitoring the SHS face deformation were encountered. Connecting bolts to the testing machine while attaching traditional Potentiometers to SHS face proves to be very complicated. Push-out testing technique, where such problem does not exist, became favourable and was therefore elected. The layout of the test is described in the following sub-sections.

4.5.1 Testing Rig and Layout

A testing rig has to be designed and built for this programme. The rig is designed to safely withstand a force of 450kN which is the maximum capacity of the actuator. The load is planned to be applied to the samples horizontally and therefore the rig has to safely transfer the load to the lab strong floor. The rig has two main parts: a reaction frame to hold and push the sample against it and a frame to horizontally hold the actuator. The reaction frame was designed to hold SHS samples sides and provide enough un-restrained SHS face area. This area is needed to not obstruct yield lines formation (at least 240mm). A rectangular area which has a length of 350mm was un-restrained.

A mechanism to connect the sample to the actuator was needed. A thick plate was attached to the load cell front to apply push-out load to the dummy bolts. Two round bars were used to transfer loads from the plate to the bolts. Each bar has an M16 thread at the end where it is connected to the dummy bolt. M12 bolts were used to connect the plate and the bars and prevent any movement. CAD drawing of the test layout is shown in Figure 4.6 and Figure 4.7. Likewise, a photo of the whole testing rig and Zoom-in are shown in Figure 4.8 and Figure 4.9 respectively.

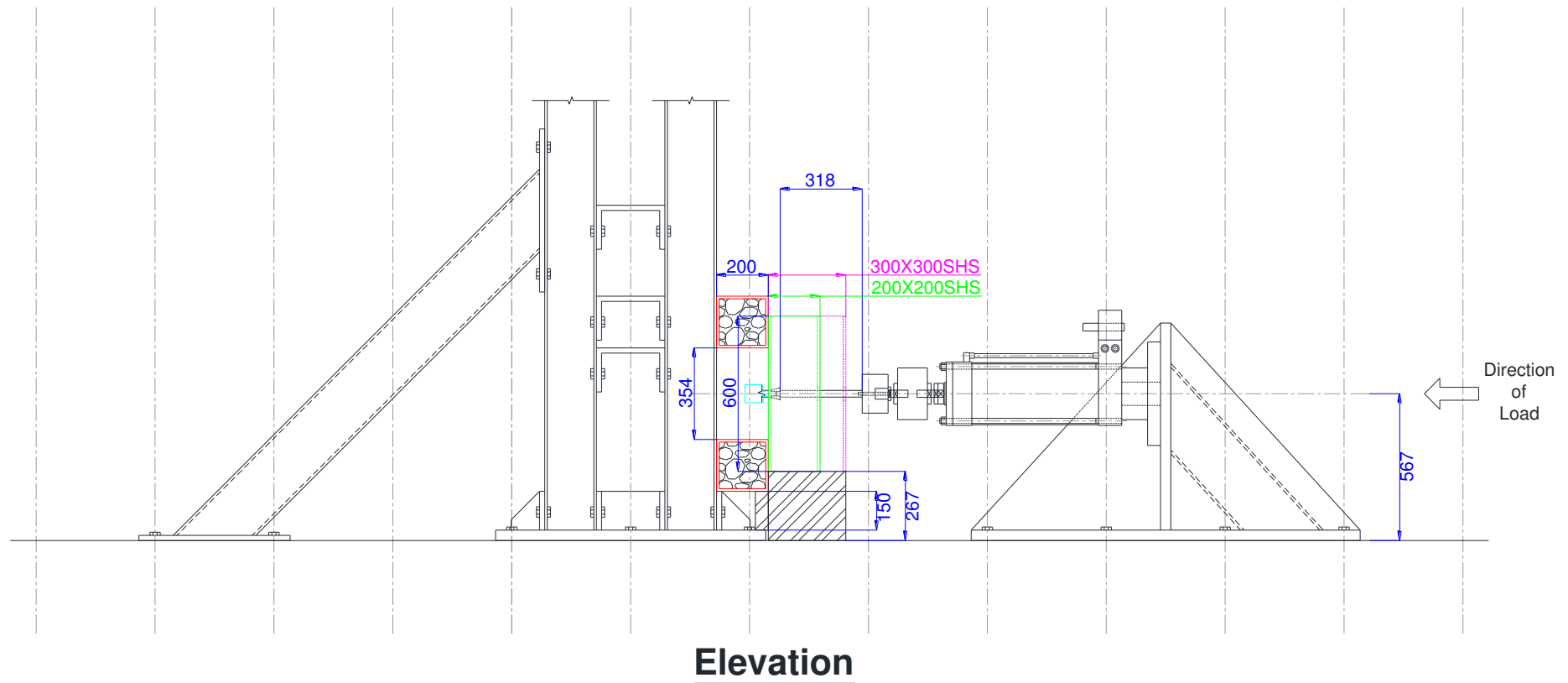


Figure 4.6 Test layout CAD drawing (Elevation)

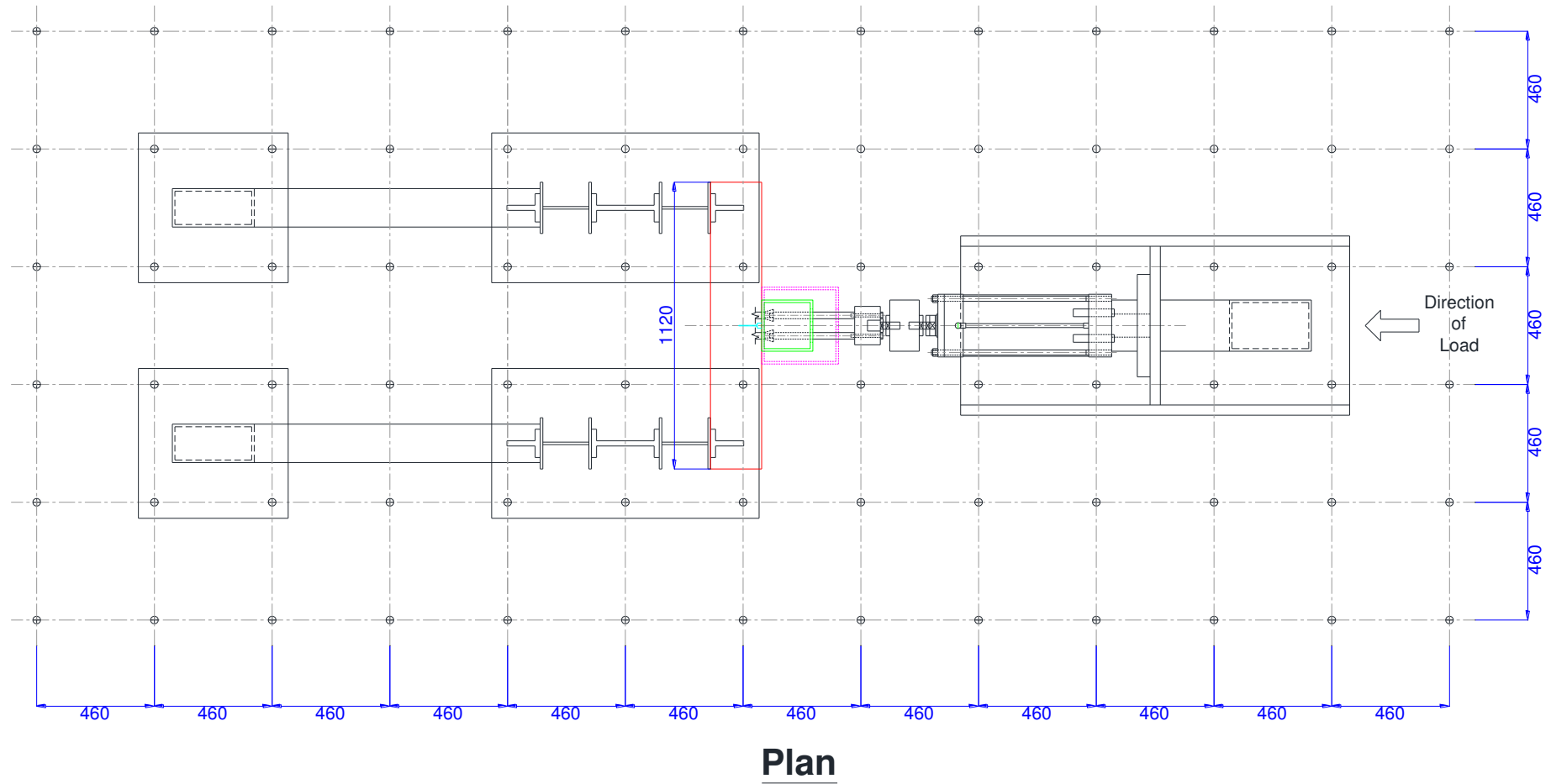


Figure 4.7 Test layout CAD drawing (Plan)

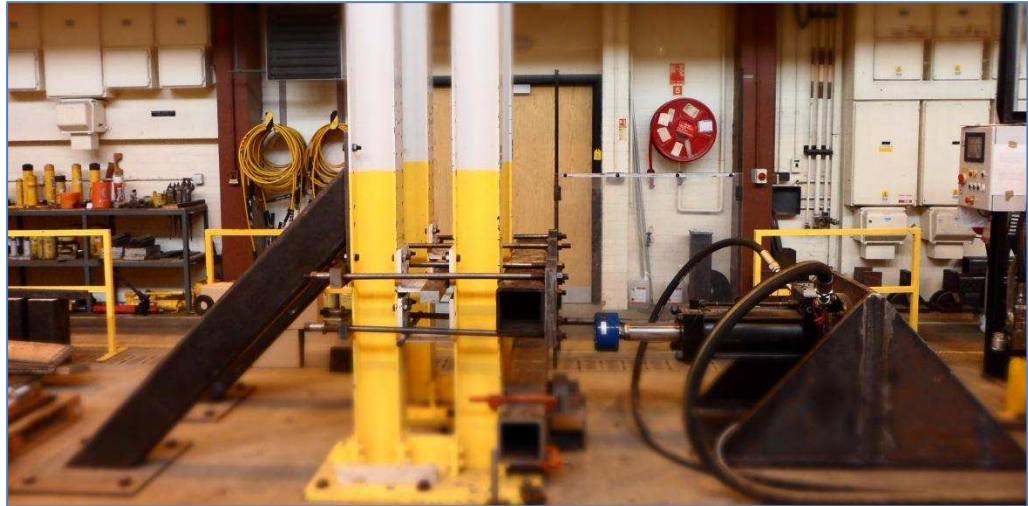
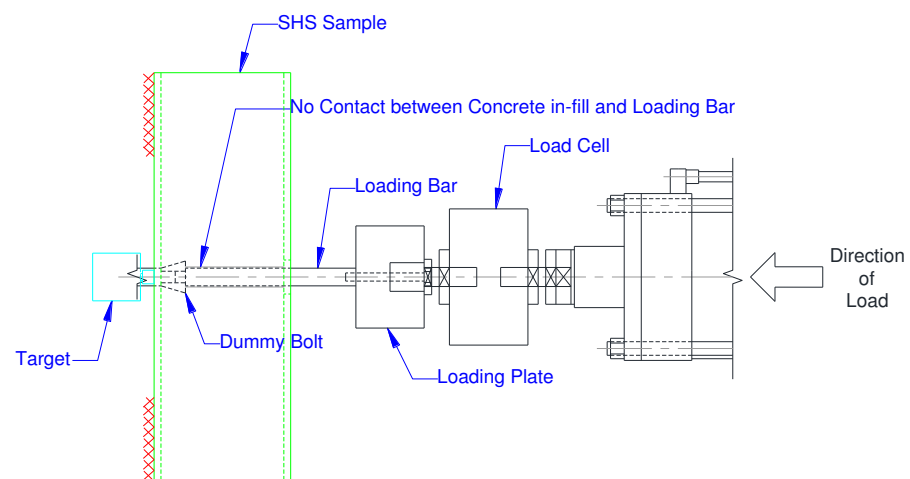
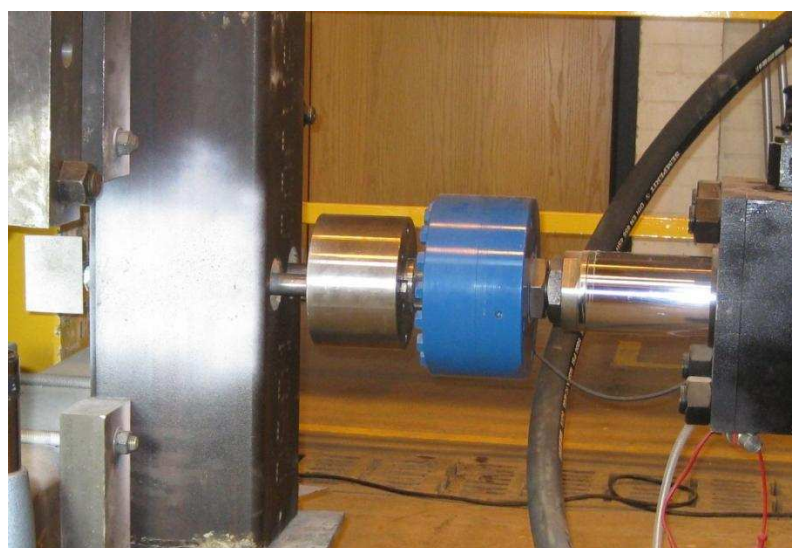


Figure 4.8 Testing rig



(a) CAD Zoom-in of testing layout (Elevation)



(b) Zoom-in of testing layout (Elevation)

Figure 4.9 Zoom-in of Test lay-out (Push-out)

4.5.2 Actuator and Control Program

An electro-hydraulic Servocon system is used in the testing. It comprises an actuator and calibrated 450kN load cell attached to it. The system has a control program called Servocon Digital Control supplied by its manufacturer.

The tests were performed and monitored using the control program. The program uses pre-defined profile for each test. The profile can have many load steps. The main data needed to create a load step are:

- Loading function: ramp or cyclic. *No cyclic tests were conducted during this experimental programme.*
- Mode of control: position or load. *All the tests were displacement controlled i.e. position mode of control.*
- Target position. *This was decided based on initial location of load cell and anticipated location at the end each test.*
- Rate per sec: load application rate. *0.003mm/sec was used throughout this experimental programme.*
- Hold Time: any position-hold after the each loading step. *No hold time was specified in this experimental programme.*

A snap-shot of the control program screen is shown in Figure 4.10.

The control program provide real-time test monitoring curve. During Ramp tests, load logged by load cell, position of load cell and test time can be monitored in real-time. The program can also plot two-axis figure of any two of the previously mentioned parameters in real-time. Example (screen snap-shot) of load cell load versus position during a test is shown in Figure 4.11. The program stores the test data in text file format at the end of the profile. The system can also output the voltage corresponded to the load and position of the load cell in real time.

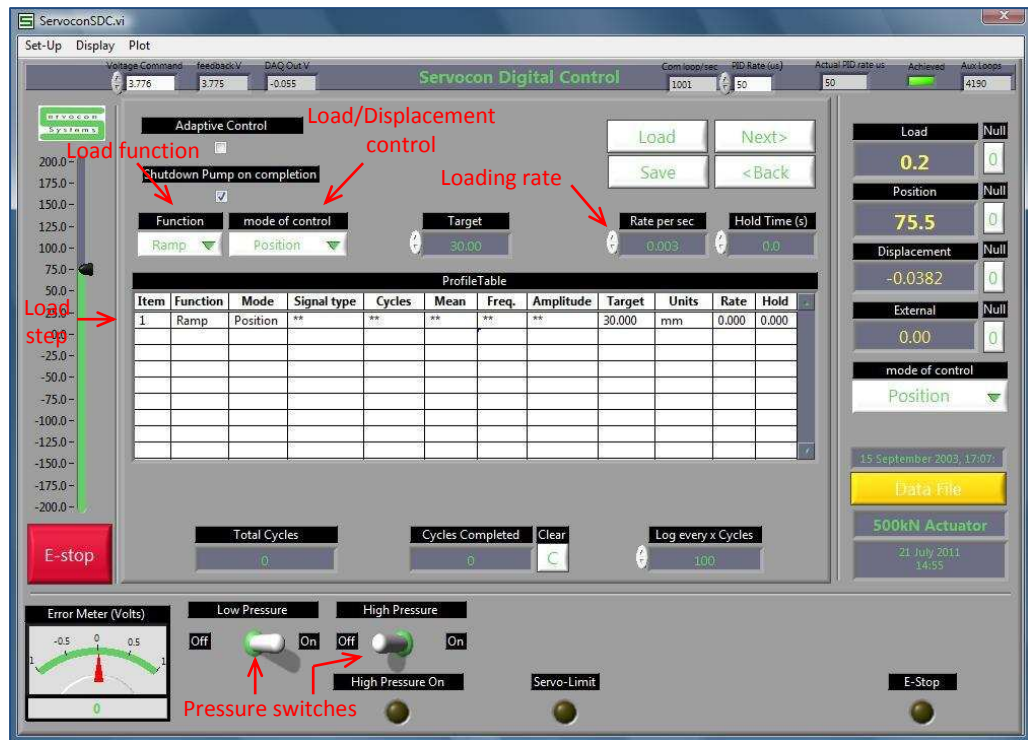


Figure 4.10 A screen snap-shot of actuator control program

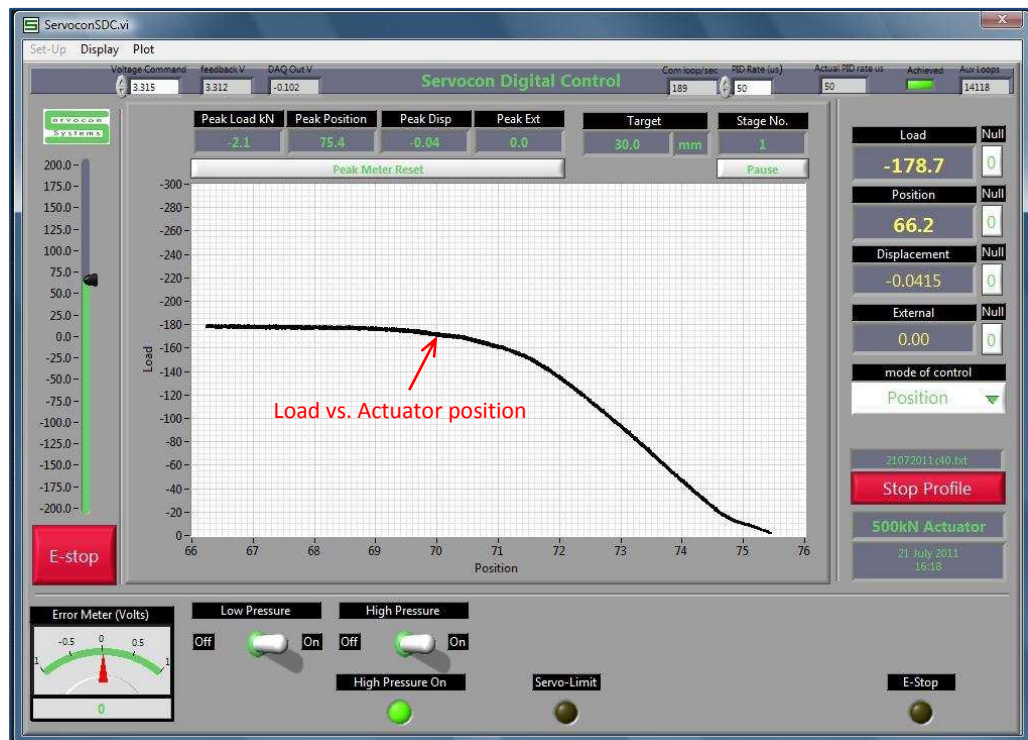


Figure 4.11 A screen snap-shot of actuator control program during test

4.6 Instrumentation A: The Video Gauge

4.6.1 Introduction

In this experimental programme Imetrum's Video Gauge was used to measure the deformation of SHS face. It is a non-contact, video based measurement instrument. It precisely measure 2D position of targets in real-time video camera frames.

Traditionally, the displacement is measured using Potentiometers or Linear variable differential transformers (LVDTs). However, problems related to keeping Potentiometers and LVDTs in desired location on SHS face were encountered in previous investigation (Elamin, 2009). It was reported that Potentiometers tend to slip from desired locations on SHS face when the face is largely deformed and report incorrect displacement. The Video Gauge has been adopted to solve and avoid these problems.

The Video Gauge system comprises the followings:

- Laptop, where is the Video Gauge software is installed
- High-resolution digital video camera
- Lenses
- Voltage input/output module
- Lighting
- Adjustable camera holder

Multiple cameras (such as the one shown in Figure 4.12a) can be used in the Video Gauge to allow simultaneous multiple area measurements. However one camera only has been used in this experimental programme. The camera is a high-resolution monochrome 1.3 Mega Pixels digital camera. It is connected to laptop using 1394a High Speed Serial Bus (Commercially known as FireWire).

A range of lenses is available to use with the Video Gauge system (Figure 4.12b). For each application, a suitable lens is chosen based on the lens's Field of View (FOV) and Working Distance (WD). The FOV is the visible size of area in the image. The WD is the distance between the lens and the object being measured.

The specification of the lens which found suitable for this experimental programme is highlighted in Table 4.3. It was selected based on the layout of testing rig and samples dimensions.

Table 4.3 Video Gauge lens specification (Imetrum¹)

Focal length (mm)	Min WD (mm)	Max WD (mm)	At min WD			At 1m WD		
			FOV (mm)	Displacement resolution (μm)	Strain resolution ($\mu\epsilon$)	FOV (mm)	Displacement resolution (μm)	Strain resolution ($\mu\epsilon$)
25	148.3	∞	35.3	0.35	20	238	2.4	20

The Voltage input/output module (Figure 4.12c) used in this experimental programme is National Instruments' NI USB-6211. It provides both analogue and digital inputs/outputs. It was used to input the load and the head movement from Actuator to the Video Gauge system (voltage signal from Actuator). This enables logging and recording Actuator load and camera measurement simultaneously.

A noise isolation module has been used few occasions when the lab was very busy during the test.

The lighting system (Figure 4.12d) used in this experimental programme is fitted with three low energy fluorescent lamps. It generates a cool diffuse light equivalent in brightness to a 250W tungsten lamp.

The Video Gauge normally comes with a tripod camera holder. Due to the nature of the tests and the layout of the testing rig an adjustable height camera holder is also utilised.



Figure 4.12 Video Gauge Components

4.6.2 Targets Identification

The Video Gauge manufacturer claims that it can measure the 2D position of any target. The target is identified in the system using the mouse to drag a bounding box around it. Up to 100 targets can be measured in real time at various rates (15Hz in this program).

As shown in test set-up, the SHS face deformation is out-of-plane and cannot be measured directly using the Video Gauge. Therefore for each test, a plate was magnetically attached to the SHS face at the position where the maximum SHS face deformation is expected. This arrangement allowed the measurement of the deformation of the SHS face, and the body motion of the sample using one camera (facing the side of the sample).

A speckle pattern is applied on the plate (magnetically attached to the SHS face), and on the desired side of each SHS sample. The pattern is

applied by spraying a thin layer of white matt paint. This is followed by sprinkling a thin layer of black paint on top of the white paint. The targets were then identified on these areas. Only three targets were identified in each experiment:

- Two targets to measure deformation of the SHS
- One target to measure the body motion of the entire sample

4.6.3 Calibration

The Video gauge measures 2D positions of targets in pixels. To get the measurement in mm, a calibration has to be done. Before conducting each test, and for each target, a calibration factor showing how many pixels in 1mm is measured using a steel line gauge (shown in Figure 4.13). The results produced by the Video Gauge are then converted from pixels to mm using these factors after the test is finished.

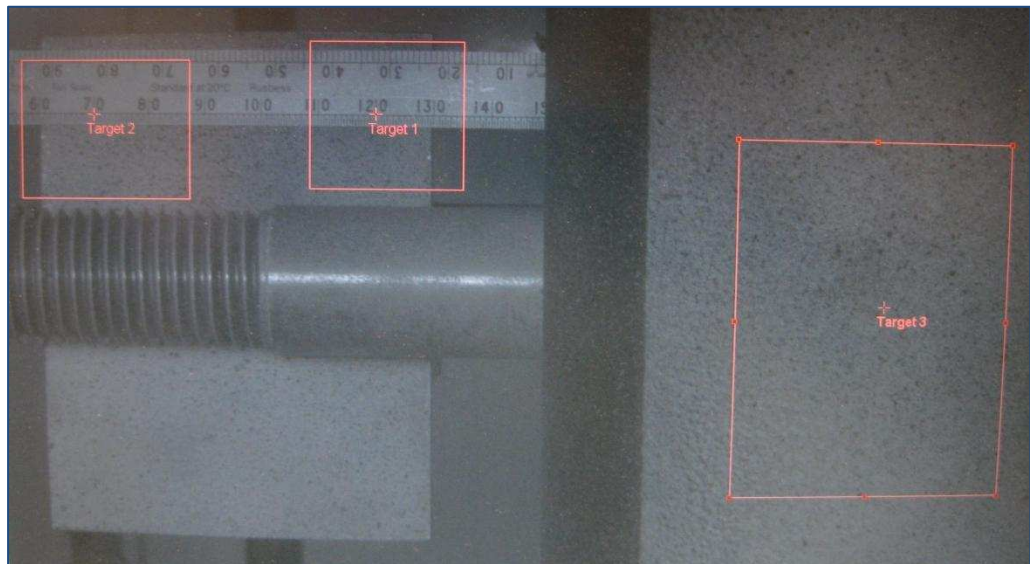


Figure 4.13 Video Gauge calibration

4.6.4 Accuracy

The accuracy of Video Gauge system has been compared to traditional displacement devices in several studies, and found acceptable.

Selected relevant studies are shown below:

- In (Pitrakkos, 2012) the results obtained using Video Gauge were compared against results obtained using standard linear potentiometers. Good agreement between both results was found as they fall within 95% confidence intervals.
- In independent experiment carried out by Airbus UK (Imetrum²), the Video Gauge results were compared against results obtained using calibrated Dial Test Indicator (DTI). The DTI and the Video Gauge outputs were found identical to within 0.1%.

4.7 Instrumentation B: The Digital Image Correlation

For one experiment, Digital Image Correlation (DIC) was used to study how the yield lines on the SHS face are occurring and the displacement profile on the SHS face. Dantec Dynamics Q-400 Digital 3D Correlation system was used. It is an optical measuring instrument for true full field, non-contact and three-dimensional analysis of displacements and strains on components and specimens. It can be used on any material without restrictions (Dantec).

In this system the surface of the test sample is observed using two cameras. A stochastic pattern has to be applied onto the surface. The system has to be calibrated first to determine cameras parameters using Calibration Plate. During the test the system captures images of the surface at desired rate. The data is then processed using a software called Astra 4D to determine the 3D position of the surface on each image using triangulation. The Q-400 Technical data are presented in Table 4.4.

The calibration process is done manually by simply holding the calibration plate on the sample surface and taking a required number of frames. Previous studies shown that calibration errors will introduce

systematic errors on resulting data, however these errors are limited to 0.05-0.2 mStrain depending on the focal length of cameras lenses (Becker et al., 2006, Siebert et al., 2007).

In this experimental programme, it was planned that the DIC results are to be used solely to study the development of yield lines pattern and the deformation profile of the SHS face i.e. no force-displacement curve is to be extracted from the DIC data.

Table 4.4 Digital Image Correlation Q-400 Technical Data (Dantec)

Measuring area:	Typical measurement areas are 20 x 15 mm ² up to 1000 x 750 mm ² , larger / smaller measurement areas on request e.g. some mm ² up to m ² , depending optical setup
Measuring results:	Full field surface contour, 3D displacements and strains
Measuring range:	up to 100% strain
Calibration plates:	Sizes: 105 x 148 mm ² up to 420 x 594 mm ² , other formats optional on request
Control electronic:	Portable Notebook Control Unit, Windows 7 or XP Professional Integrated analogue data acquisition and recording input and output: 8 independent free-selectable analogue Data Acquisition Channels, 16 Bit resolution, ± 0.05 V to ± 10 V synchronized to camera triggering, 2 Channels analogue output
Illumination:	Patented cold light system HILIS for very homogenous illumination of the specimen
Sensor chip:	Different Sensor types up to 16 Mpx are possible; Typical: CCD, 1/8", 1624 x 1234 pixel
Sensor details:	Shutter speed: 47 μ s – 67 s, Frame rate: up to 30 Hz, typical 5 Hz
Measuring sensitivity:	Up to 1/100.000 of the Field of View depending on measuring conditions, e.g. up to 1 μ m displacement sensitivity at a given Field of View of 100 mm
Applications:	Displacements and strain analysis for static and dynamic load tests on almost any material and surface

4.8 Material Properties

4.8.1 Structural Hollow Sections

The mechanical properties of SHS were determined by testing Mechanical test pieces. The pieces were designed and made in accordance to BS EN ISO 6892-1:2009 (BSI, 2009). Typical CAD drawing of the pieces is shown in Figure 4.14. At least three pieces were made from each SHS section.

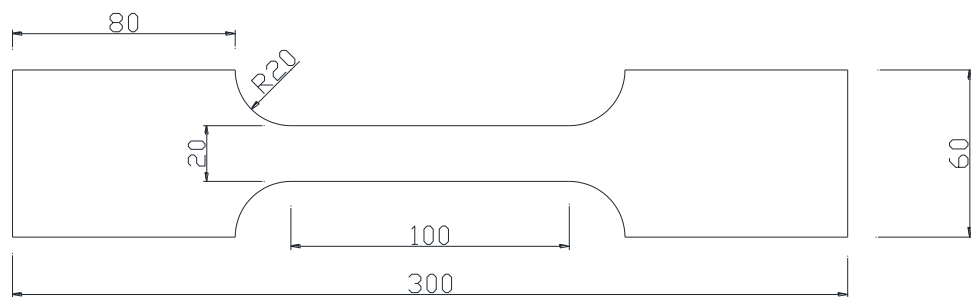


Figure 4.14 CAD drawing and testing process of mechanical pieces

Zwick/Roell ZMART.PRO 1484 computer controlled Universal Testing Machine was used to test the pieces. The tests were performed using Zwick/Roell PC version 5.50a software pre-defined tensile test program. The main mechanical properties obtained from pieces tests results (averaged) are summarised in Table 4.5.

The stresses presented in Table 4.5 found to fall within the stresses range recommended by relevant standards for S355 steel (BSI, 2006a). The recommended stresses range is presented in Table 4.6 (extracted from Table A.3 in EN 10210-1:2006).

Table 4.5 Structural Hollow Sections material properties

n	Specimen ID	SHS Section	Mechanical Properties		
			Yield stress	Ultimate stress	Young's modulus
			(N/mm ²)	(N/mm ²)	(N/mm ²)
1	b200t8g80c20-1	200x200x8	400.0	499.6	208553
	b200t8g80c20-2				
	b200t8g80c20-3				
	b200t8g80c50-1				
	b200t8g80c50-2				
	b200t8g80c50-3				
	b200t8g80c80-1				
	b200t8g80c80-2				
	b200t8g60c40-1				
	b200t8g60c40-2				
	b200t8g60c40-3				
	b200t8g80c40-1				
	b200t8g80c40-2				
	b200t8g80c40-3				
	b200t8g80c40-4				
	b200t8g100c40-1				
	b200t8g100c40-2				
2	b200t10g80c40-1	200x200x10	449.7	554.3	221789
	b200t10g80c40-2				
3	b200t6.3g80c40-1	200x200x6.3	428.7	501.5	208327
	b200t6.3g80c40-2				
4	b200t5g80c40-1	200x200x5	431.3	517.8	206043
	b200t5g80c40-2				
5	b200t8g80c40-DIC	200x200x8	400.0	499.6	208553
6	b300t12.5g120c40-1	300x300x12.5	399.7	521.1	201000
	b300t12.5g120c40-2				
7	b300t16g120c40-1	300x300x16	355.0	510.0	195310
	b300t16g120c40-2				

Table 4.6 Stresses range for Structural Hollow Sections grade S355

Steel Grade	Minimum yield stress (N/mm ²)	Tensile stress (N/mm ²)
	t ≤ 16mm	3mm < t ≤ 16mm
S355	355	470-630
(extracted from Table A.3 in EN 10210-1:2006)		

4.8.2 Dummy Bolts

The dummy bolts were manufactured from EN24 (also known as BS 970 817M40). It is a high quality, high tensile alloy steel. Due to the cost and time needed to manufacture these dummy bolts, they have to be re-usable for as many tests as possible. The use of EN24 steel assures that all stresses applied to the dummy bolt lie within its elastic range i.e. negligible and ensures bolts re-usability. The main mechanical properties of EN24 are shown in Table 4.7 (as reported by its supplier to this study West Yorkshire Steel).

Table 4.7 Mechanical Properties of EN24U

Type	Tensile Strength (N/mm ²)	Yield Stress (N/mm ²)	Impact Izod J	Impact KCV J	Proof Stress (N/mm ²)	Hardness HB
EN24 (U)	925/1075	755	47	54	740	269/331

4.8.3 Concrete in-fill

Four concrete mixes were used to fill the SHS sections in this programme: C20, C40, C50 and C80 which respectively denote concrete that have 20, 40, 50 and 80N/mm² cube compressive strength on the day of testing. The nominal aggregate size specified for all mixes is 10mm. For C20, C50 and C80 mixes, the cement, aggregate and sand were used from the same delivery patch to minimize any variation on the material properties. Admixtures were only used in C80 mix to speed the curing time. The mix design for all the mixes are shown in Table 4.8.

Table 4.8 Concrete in-infill Mix Design

Mix Grade	Cement (kg/m ³)	Water (kg/m ³)	Fine Agg. (kg/m ³)	Coarse Agg. (kg/m ³)	Admixtures (kg/m ³)	
C40	CEM I 52.5N	235	183	941	941	
C20	CEM II AL32.5R	440	210	735	1020	
C50	CEM I 52.5N	359	194	719	1128	
C80	CEM I 52.5N	642	194	625	834	9.6 Silica Hydrate 64 Silica Fume

The Properties of the concrete were determined using cube compressive tests. 100mm cubes were tested. Concrete cubes from each mix were cured in water and in air (in lab room condition not-submerged in water). The compressive tests were conducted on the day of test. An average of at least three cubes compressive strengths of each specimen is shown in Table 4.9.

Table 4.9 Cube Compressive Strength of Concrete-infill

n	Specimen ID	Targeted Mix	Concrete Compressive Strength (N/mm ²)	
			Cubes cured in Water	Cubes cured in Air
1	b200t8g80c20-1	C20	22.5	22.8
2	b200t8g80c20-2	C20	23.2	23.7
3	b200t8g80c20-3	C20	22.1	23.2
4	b200t8g80c50-1	C50	49.2	42.1
5	b200t8g80c50-2	C50	50.4	45.4
6	b200t8g80c50-3	C50	54.4	47.7
7	b200t8g80c80-1	C80	82.5	87.5
8	b200t8g80c80-2	C80	83.2	90.8
9	b200t8g60c40-1	C40	41.2	40.8
10	b200t8g60c40-2	C40	40.7	41.1
11	b200t8g60c40-3	C40	40.7	41.1
12	b200t8g80c40-1	C40	38.1	36.9
13	b200t8g80c40-2	C40	38.1	36.9
14	b200t8g80c40-3	C40	39.1	38.1
15	b200t8g80c40-4	C40	39.1	38.1
16	b200t8g100c40-1	C40	40.8	39.3
17	b200t8g100c40-2	C40	40.8	39.3
18	b200t10g80c40-1	C40	41.7	38.5
19	b200t10g80c40-2	C40	41.7	38.5
20	b200t6.3g80c40-1	C40	44.1	43.9
21	b200t6.3g80c40-2	C40	44.1	43.9
22	b200t5g80c40-1	C40	40.6	40.0
23	b200t5g80c40-2	C40	40.6	40.0
24	b200t8g80c40-DIC	C40	39.5	38.7
25	b300t12.5g120c40-1	C40	35.7	36.8
26	b300t12.5g120c40-2	C40	35.7	36.8
27	b300t16g120c40-1	C40	36.9	34.9
28	b300t16g120c40-2	C40	36.9	34.9

4.9 Test Procedure

The tests were carried out using the following procedure:

1. Cut and prepare the SHS sample and attached dummy bolts to it.
2. Connect two loading bars to the back of dummy bolts and level the bolts and the loading bars.
3. Fill sample with concrete ensuring that there is no contact between concrete in-fill and loading bars. *In this experimental programme, loading bars were encased in plastic tubes which were removed before testing commence.*
4. Turn on the actuator system (both power and hydraulic) and run its control program.
5. Using the control program, move the actuator head towards its head to ensure enough space to attach the sample to testing rig.
6. Place the sample into the testing rig. *In this experimental programme, electric lifter was used to lift up SHS 200x200 samples from the ground to desired level, then the sample and was moved and placed in the testing rig manually. A crane was used to do the same for SHS 300x300 samples. An eye lit connecter has to be casted in the concrete to enable the crane to hold the sample as shown in Figure 4.15.*
7. Move the actuator head towards sample and connect the actuator to the dummy bolts.
8. Use actuator to fix the sample to testing rig without applying load on it. *Load was monitored on actuator control program.*

9. Set-up the Video Gauge system and place target in desired location.
10. Connect load and movement logged from the actuator to the Video Gauge system via the voltage module.
11. Load Video Gauge program, set its preferences and calibrate targets.
12. Load the loading profile in the actuator control program and choose the destination of test data file where the test data will be saved.
13. Start the test. (The Video Gauge system should start recording at the same time when the actuator start applying load or before).
14. When the test finishes, collect test data from both the Video Gauge System and actuator control program. *Data collected from actuator control program was used for reference only.*
15. Remove the sample from testing rig and shut down actuator and Video Gauge systems.
16. Recover dummy bolts for future tests by cutting and removing the sample face.



(a) Eye-lit connector used with SHS 300x300



(b) Using Crane to attach SHS 300x300 to rig

Figure 4.15 **Handling SHS 300x300 samples**

4.10 Summary

This chapter details the experimental programme carried out during this research. The programme scope and how parameters and ranges were decided were described herein. A summary of the ranges and limitations are listed in Table 4.10 below. This chapter also describes the instrumentations utilised to collect results and summarises their key technical specifications. The test procedure is also explained in this chapter.

Table 4.10 **Experimental programme ranges and limitations**

Item	Limitation/Range
Hollow Sections	Square Hollow Sections (SHS)
Blind Bolts	Hollo-Bolts 16 (HB16)
Slenderness ratio of Hollow Section ($\mu = b/t$)	$18.75 \leq \mu \leq 40$
Ratio of bolts gauge to Hollow Section width ($\beta = g/b$)	$0.3 \leq \beta \leq 0.5$
Concrete in-fill grade	C20 ~ C80

The results of this experimental programme are presented in the next chapter.

Chapter 5

Experimental Results

5.1 Introduction

Results obtained from the experimental programme developed and conducted during the course of this study are presented in this chapter. Two different sets of results are presented namely: force-displacement curves of the hollow section face bending and displacement and strain distributions of the face of the hollow section. The chapter commences by detailing the errors encountered during experiments which used to get the force-displacement curves, and how they were corrected. It also describes the failure criteria of experiments. This is followed by presentation of the raw force-displacement results. Results normalization and effect of varying parameters namely concrete strength, SHS face slenderness and bolt gauge to SHS width ratio are also presented in this chapter. Lastly, SHS face strain and deformation results are presented.

5.2 Errors & Corrections

Any quantity in any experiment is measured to the best possible accuracy and precision. The accuracy of any measurement represents how close it is to the actual/true value of the quantity, while the precision of the measurements represent how a repeated number of measurements under un-changed condition are close to each other's. A basic representation of this is shown in Figure 5.1.

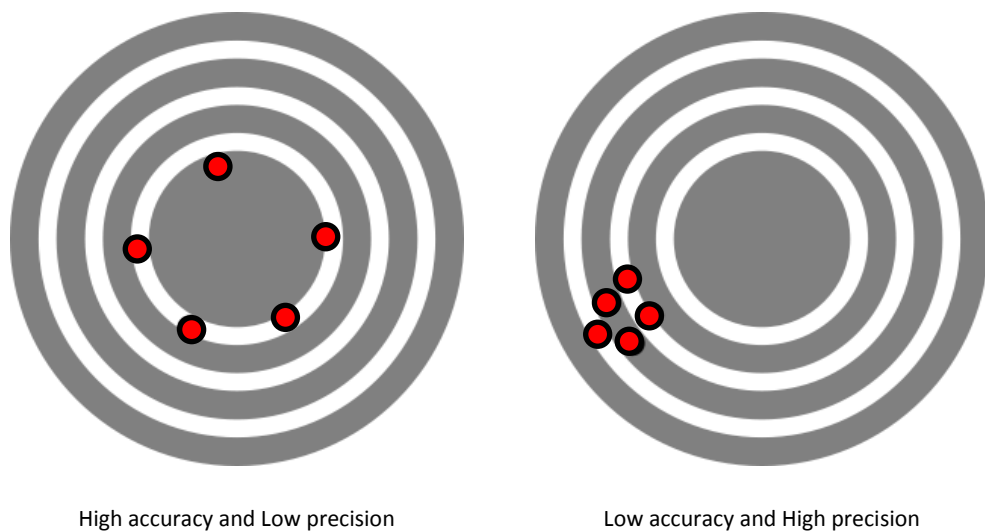


Figure 5.1 Accuracy and Precision

Errors can be introduced into an experiment by the experiment setup, the observer or external conditions (Wood and Martin, 1974). Errors affect the accuracy and precision of the results and are widely classed as:

- Systematic Errors
- Random Errors

Systematic errors affect the accuracy of the measurement. They can occur due to many reasons such as faults in instruments calibration and poor equipment maintenance. The systematic errors cannot be enhanced by repeating experiments. However, sharp and critical eye

with help of experience while properly maintaining and calibrating equipments could help to avoid and cure such errors.

Random Errors occur due to various numbers of reasons. The effect of such errors can be reduced by repeating as many as possible experiments under un-changed condition.

During the course of the experimental programme, all the equipment was calibrated and maintained to a high standard. A systematic error was noticed when reading the applied force value from the actuator load cell by the Video Gauge system. An error of 2.71kN was noticed in all experiments i.e. the applied force was reading 2.71kN on the Video Gauge system while it was reading 0kN in the actuator before the start of the test. This error was monitored closely and found to be constant during all the stages of each experiment. It was attributed to different voltage sensitivity between the Video Gauge system and the actuator load cell. This error was corrected while post-processing the experimental results by zeroing the force at the start of the tests.

5.3 Failure Criteria

Experiment failure criteria are defined to mark the end of each experiment. In real joints, the failure of a connection could occur in many ways and connection component e.g. bolt reach its ultimate tension capacity. In many design guides such as CIDECT 3 (Packer et al., 2009), the ultimate capacity of a joint is defined by the lower of:

- Ultimate strength of the joint
- Load corresponding to ultimate deformation limit

In this study it was observed that the failure of the experiment does not occur due to materials reaching their ultimate strength. Instead, failure of the experiment occurs due to large deformation of SHS holes/face.

During the tests the dummy-bolts try to push out of the SHS. This leads to large stretch of bolt holes in the SHS face. It was observed that at a late stage of the tests, the SHS holes stretch to an extent where they can no longer transfer the applied load to the SHS face effectively. At this stage, the dummy bolts push out of the SHS holes as shown in Figure 5.2. This leads to significant loss in force as shown in Figure 5.3 (more than 40% in this particular experiment).

The geometrical failure observed during this experimental programme take place at SHS face deformation greater than the ultimate deformation limit for unfilled Hollow Section. This limit is 3% of the connecting face width i.e. 6mm in the experiment shown in Figure 5.3, and often reduced to 1% due to serviceability requirements. It was initially proposed by (Lu et al., 1994) and is adopted in many hollow section design guides. In fact, in all experiments, SHS face deformation greater than 3% of the connecting SHS face width was achieved.



Figure 5.2 **Dummy-bolt push-out of SHS hole**

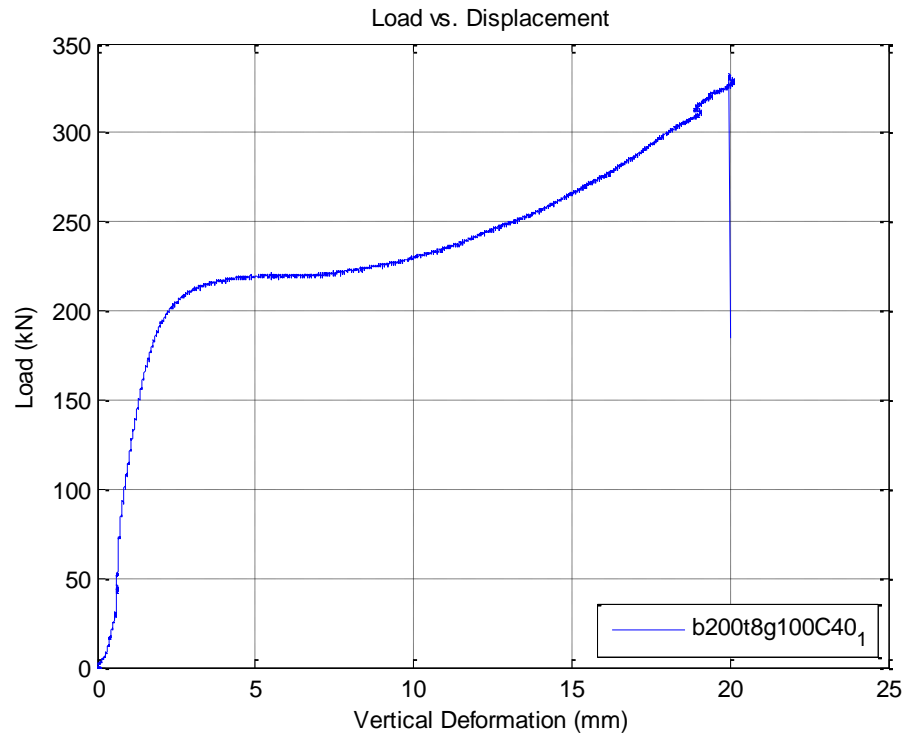


Figure 5.3 Experiment b200t8g100C40-1 failure

5.4 Visual Observations

The followings were observed during the experimental programme:

- The SHS face bending behaviour was generally as expected, deforming in a shape similar to a volcano positioned at each bolt hole. The face behaved as a plate which has two point loads in bending. The SHS wall held the plate at its ends. The concrete-infill was the main reason behind this as it prevented the SHS walls from deforming. This disposes very well with the literature.
- Significant face deformation was observed around the bolt holes compared to the rest of the face. In fact, the maximum deformation on the SHS face was recorded at the bolt holes.
- Various face bending behaviours were visually observed in the part of the SHS face between the bolt holes. Minimal face bending deformation was observed in this part in thick SHS and/or SHS with

small bolt gauge. Further face bending deformation was observed with the decrease of SHS thickness and/or the increase of bolt gauge. A simple example of this is shown in Figure 5.4. This variation in SHS face bending deformation can be related to the SHS face bending mechanism. In SHS that has high face slenderness ratio, the two bolt holes are more likely to behave separately where the opposite is more expected to occur in thick SHS.

- No difference in the bending behaviour was visually observed in the part of SHS face between the bolt holes and SHS walls/edges.



a. Sample b200t8g80C50-2



b. Sample b200t8g100C40-1

Figure 5.4 Different SHS face bending behaviour

- During the course of the testing programme it was attempted to explore the behaviour of the concrete-infill. Although it proved to be

difficult to cut the SHS face to expose the concrete-infill without disturbing it, successful attempt is shown in Figure 5.5. In this figure, two patterns concrete cracks are shown: one at a parameter around the two bolts (re-drawn in black) and the second at outer perimeter restrained by SHS walls (re-drawn in white). The outer cracks resemble the SHS face bending deformation.

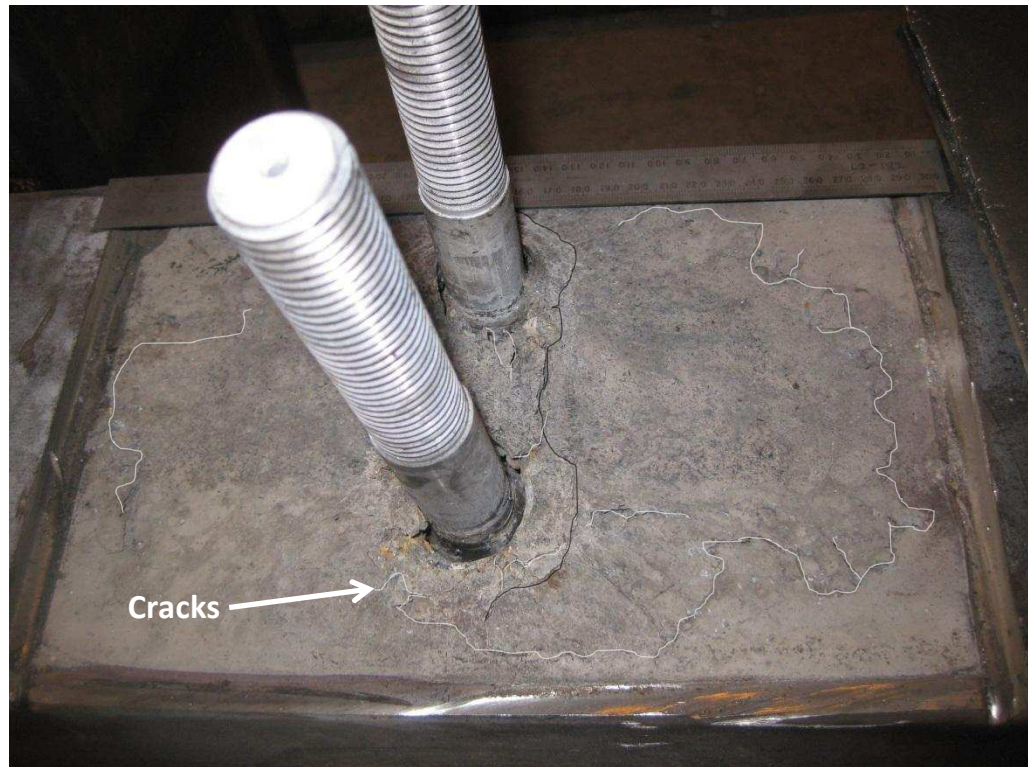


Figure 5.5 Sample b200t8g80C40-2 after the concrete-infill was exposed

- In another experiment i.e. b200t8g60C40-3, the concrete attached to dummy bolts was successfully recovered after the test without disturbing the concrete in-fill. This is shown in Figure 5.6 and it is similar to the crack pattern around the bolts shown in Figure 5.5. In this figure, it can be clearly seen that the bolts slipped from the concrete without crushing it as the concrete was initially at level of the start-of-sleeves and was held by the SHS. Also, it can be noticed that the concrete was shaped in the same way as the deformed SHS

face where more deformation occurs towards the SHS wall and less deformation between the two bolts. It is very difficult to reach any conclusion based on this, however, it does hint to the existence of theoretical concrete-cone assumed in Chapter 3.



a. Side-Elevation



b. Plan

Figure 5.6 Concrete attachment to dummy-bolts in sample b200t8g60C40-3

- Lastly, a close look at the yield lines developed on the SHS face show that some yield lines extended to the SHS edge and developed on the SHS side walls (An example is shown in Figure 5.7). This observation contradicts with the literature which assumes that the lines develop and extend until half of the side wall thickness only.

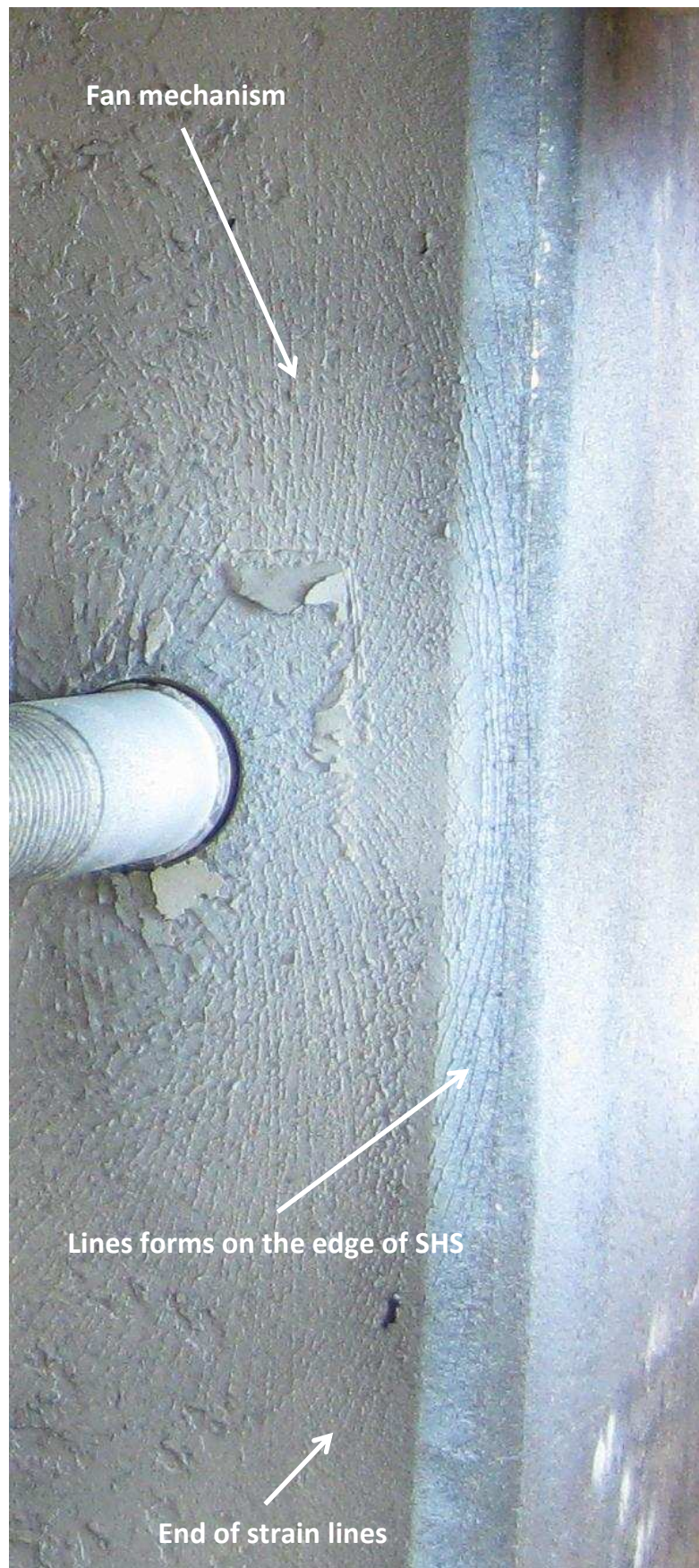


Figure 5.7 **Strain distribution on SHS face**

5.5 Force-Displacement Results

5.5.1 Raw Force-Displacement Results

In this section the raw data of force-displacement curves are presented. The displacement of the SHS face was recorded using a Video Gauge system as pixels. The force was measured simultaneously (with displacement) using loading cell attached to the actuator which was then fed to the Video Gauge system. This is done through a data logger which also acted as noise filtration unit. After each test, the displacement is converted from pixels to millimetres using a pre-defined calibration factor. Full description of test set-up and instrumentation is presented in the previous chapter. The results obtained from the Video Gauge are post-processed using MATLAB to graph the force-displacement curves. The force-displacement curves of the identical samples of test b200t8g80C20 are plotted in Figure 5.8. Similarly, the force-displacement curves of the identical samples of tests b200t8g80C50, b200t8g80C80, b200t8g60C40, b200t8g80C40, b200t8g100C40, b200t10g80C40, b200t10g80C40, b200t5g80C40, b300t12.5g120C40 and b300t16g120C40 are shown in Figure 5.9 to Figure 5.18 respectively.

The outlines of the force-displacement curves follow the same pattern in all tests. The force initially increases linearly with the SHS face displacement until it reaches a magnitude where no or minimal increase occurs with the displacement increase. In the majority of test, the force climbs again with the increase of displacement at lower rate until the failure is reached or the test stopped. However, in samples where the SHS was filled with stronger concrete, the force drops with the increase of displacement before it climbs again as shown in Figure 5.9 and 5.10; the stronger the concrete the greater the drop magnitude.

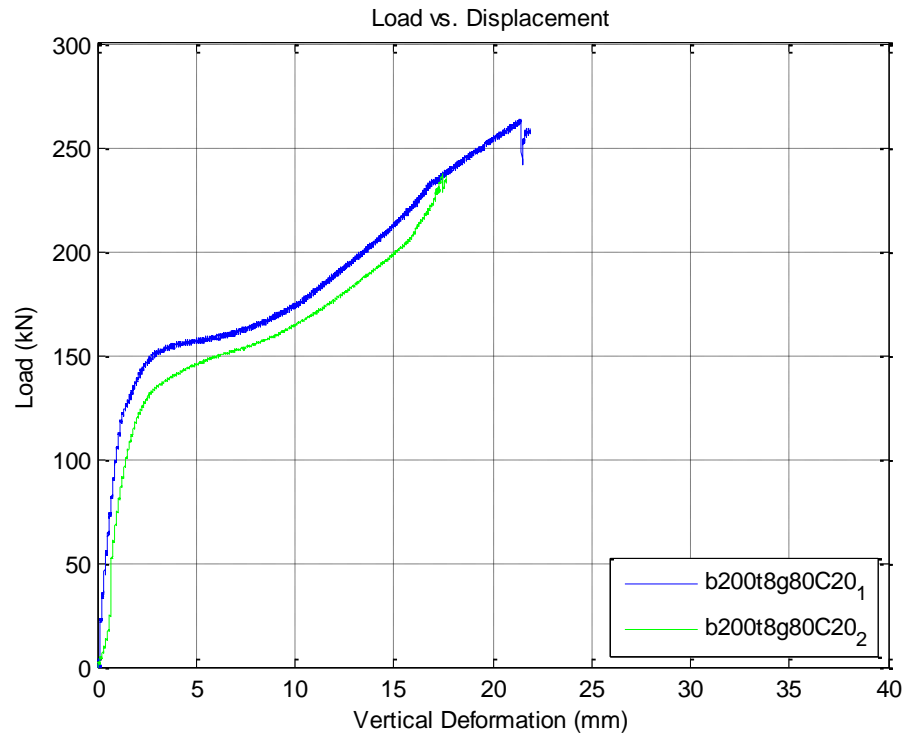


Figure 5.8 Force-Displacement relationship of b200t8g80C20-1&2 (raw)

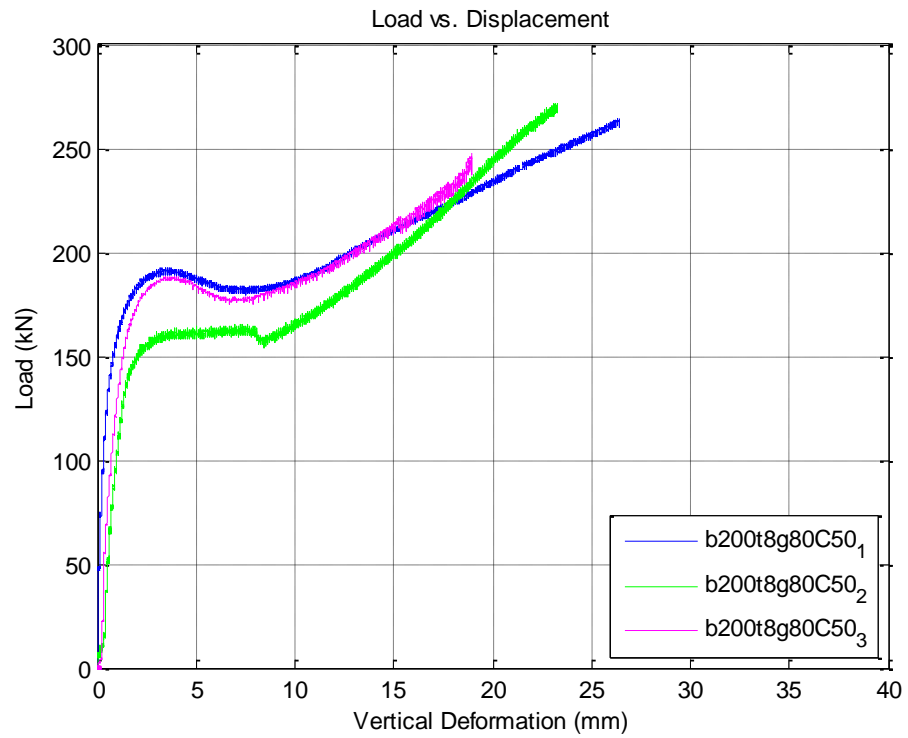


Figure 5.9 Force-Displacement relationship of b200t8g80C50-1,2&3 (raw)

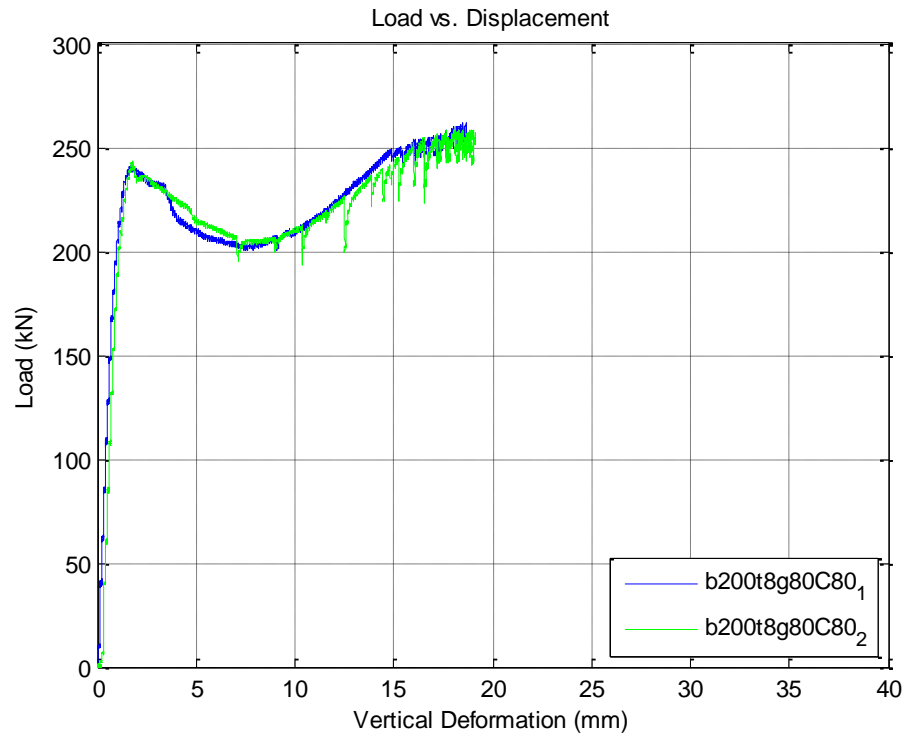


Figure 5.10 Force-Displacement relationship of b200t8g80C80-1&2 (raw)

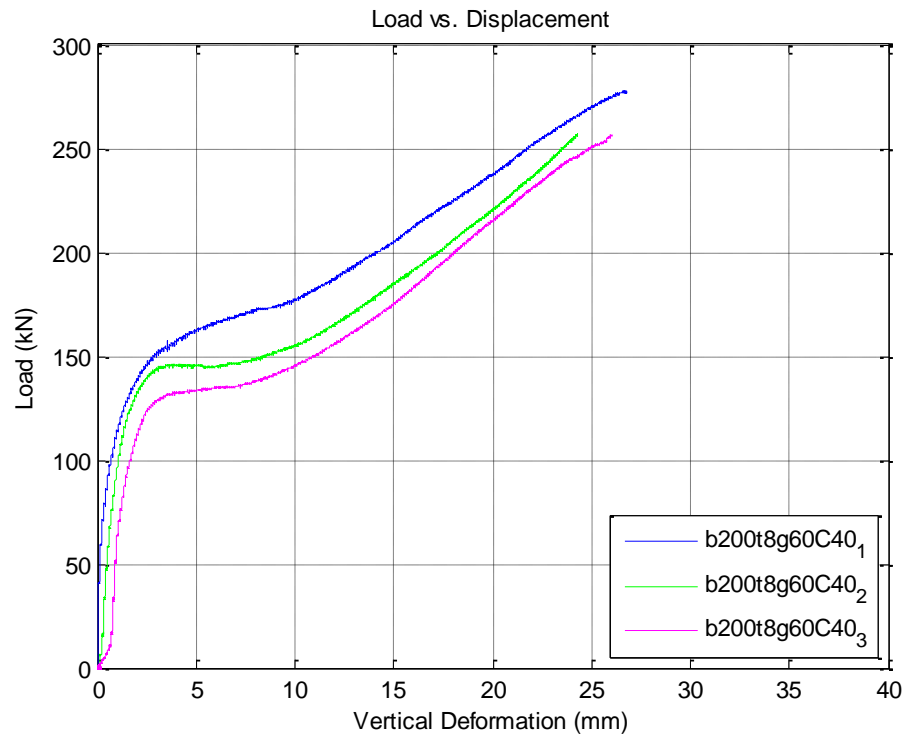


Figure 5.11 Force-Displacement relationship of b200t8g60C40-1,2&3 (raw)

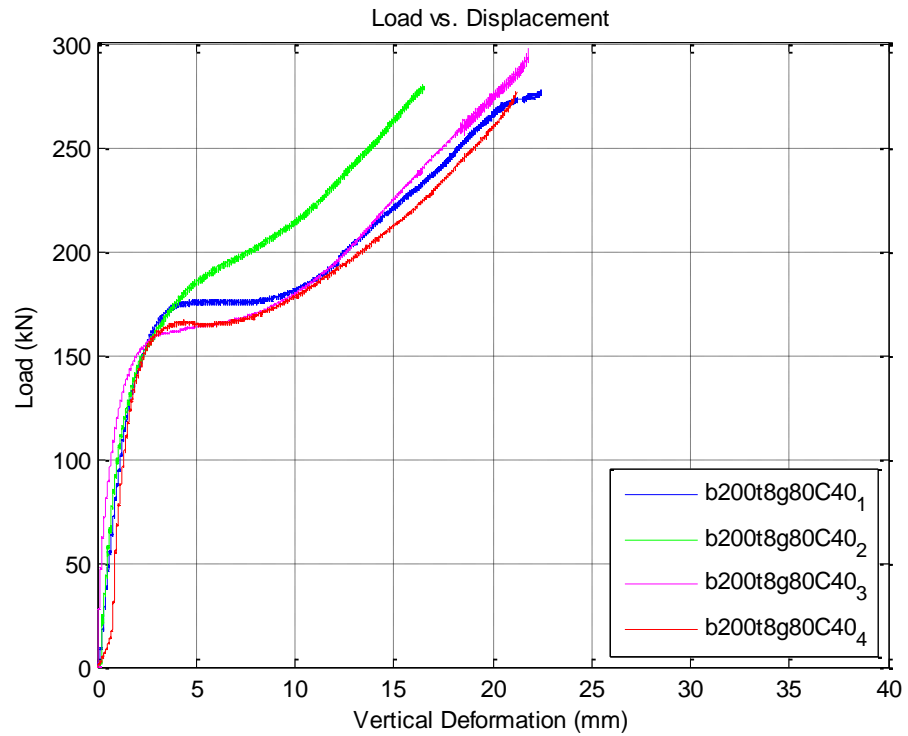


Figure 5.12 Force-Displacement relationship of b200t8g80C40-1,2,3&4 (raw)

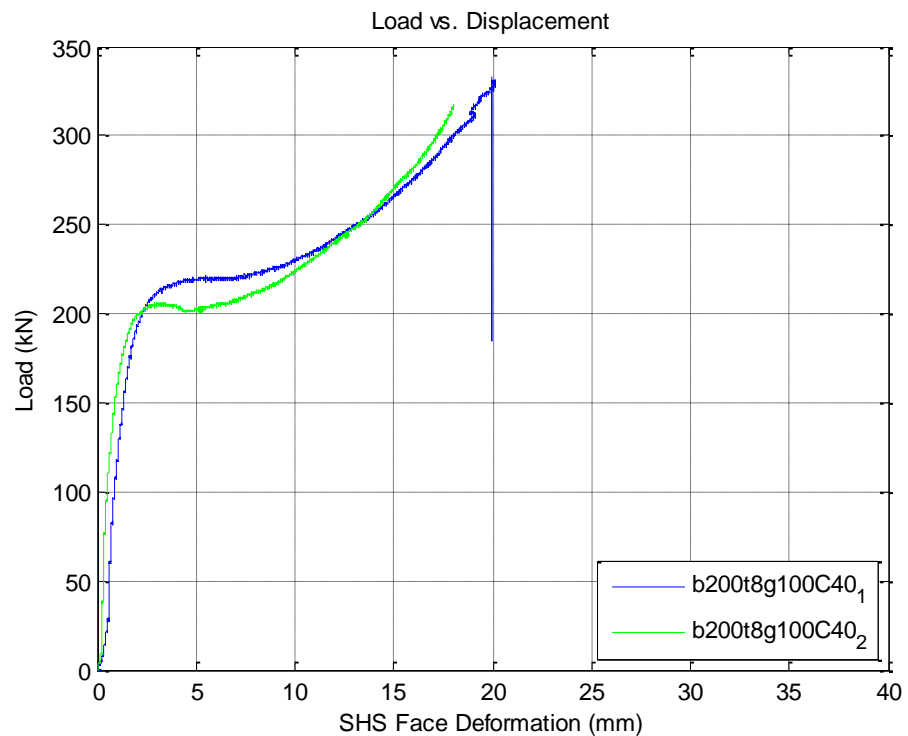


Figure 5.13 Force-Displacement relationship of b200t8g100C40-1&2 (raw)

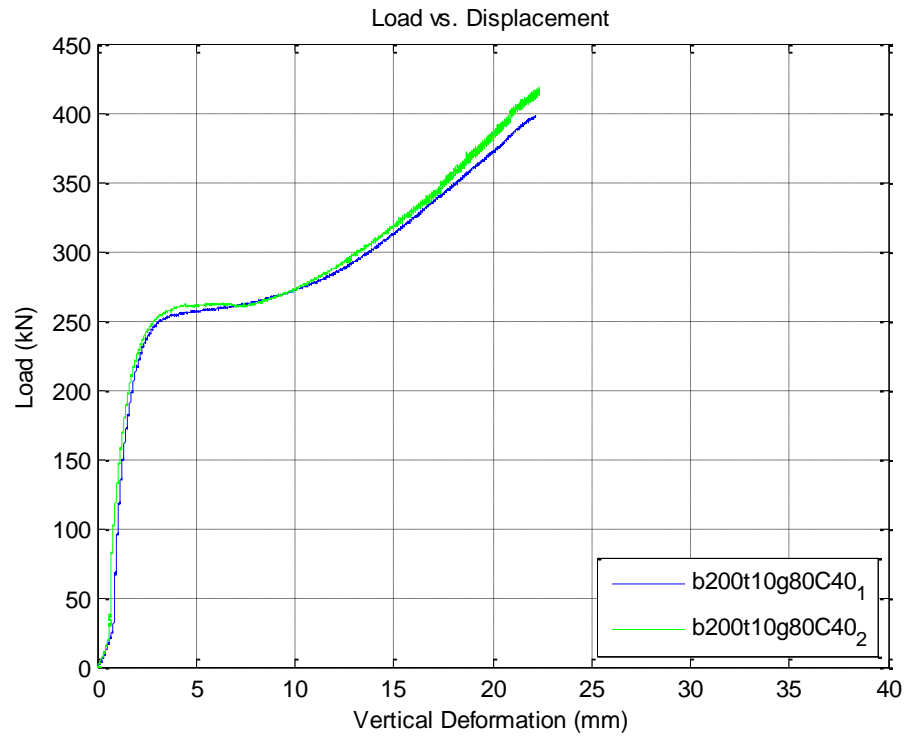


Figure 5.14 Force-Displacement relationship of b200t10g80C40-1&2 (raw)

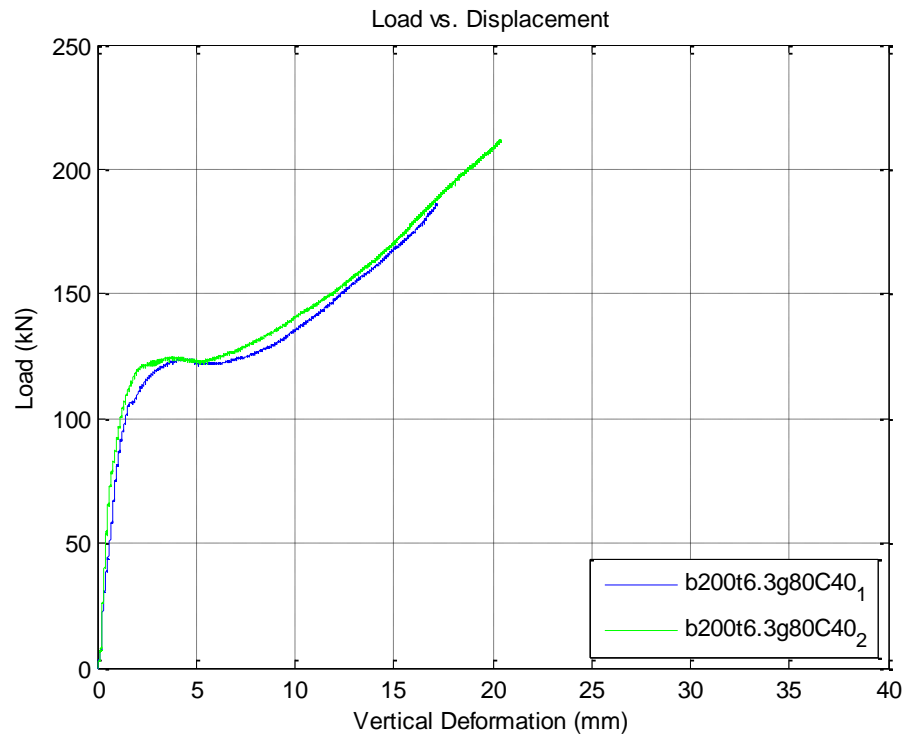


Figure 5.15 Force-Displacement relationship of b200t6.3g80C40-1&2 (raw)

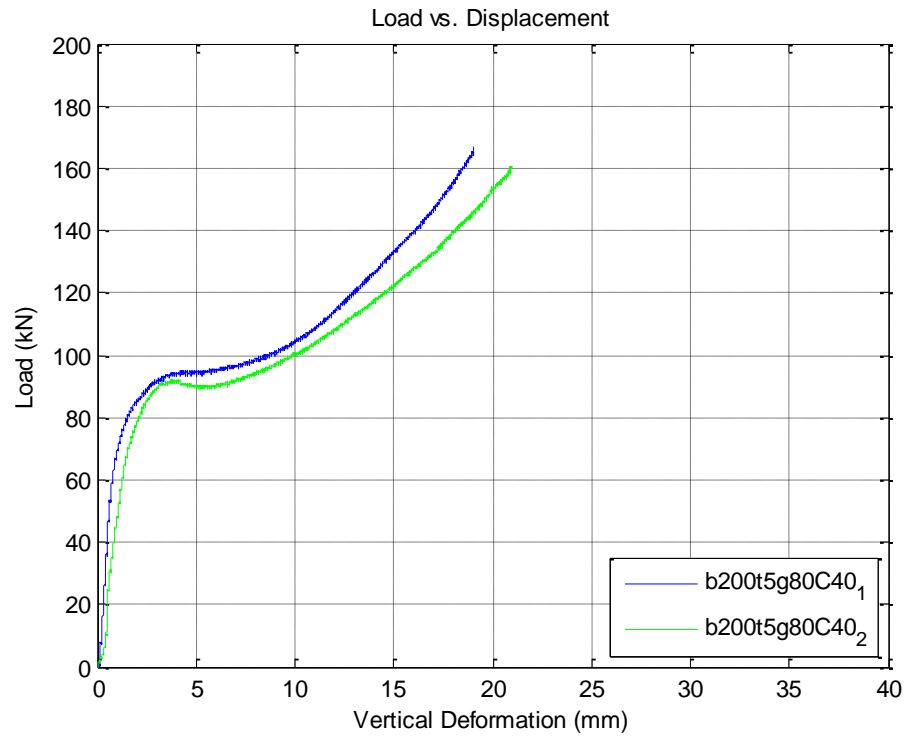


Figure 5.16 Force-Displacement relationship of b200t5g80C40-1&2 (raw)

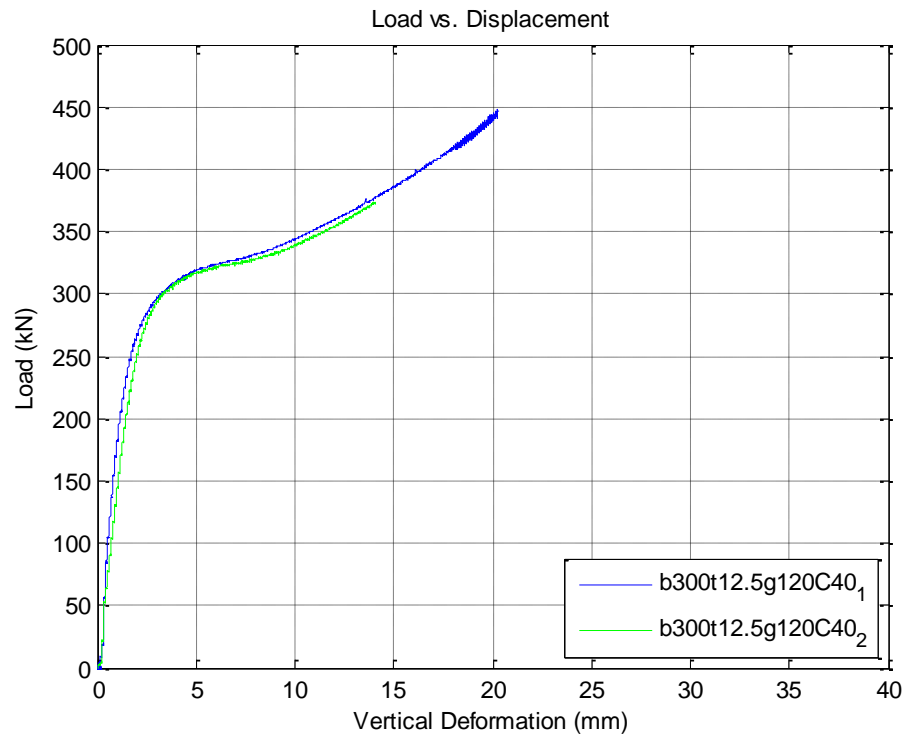


Figure 5.17 Force-Displacement relationship of b300t12.5g120C40-1&2 (raw)

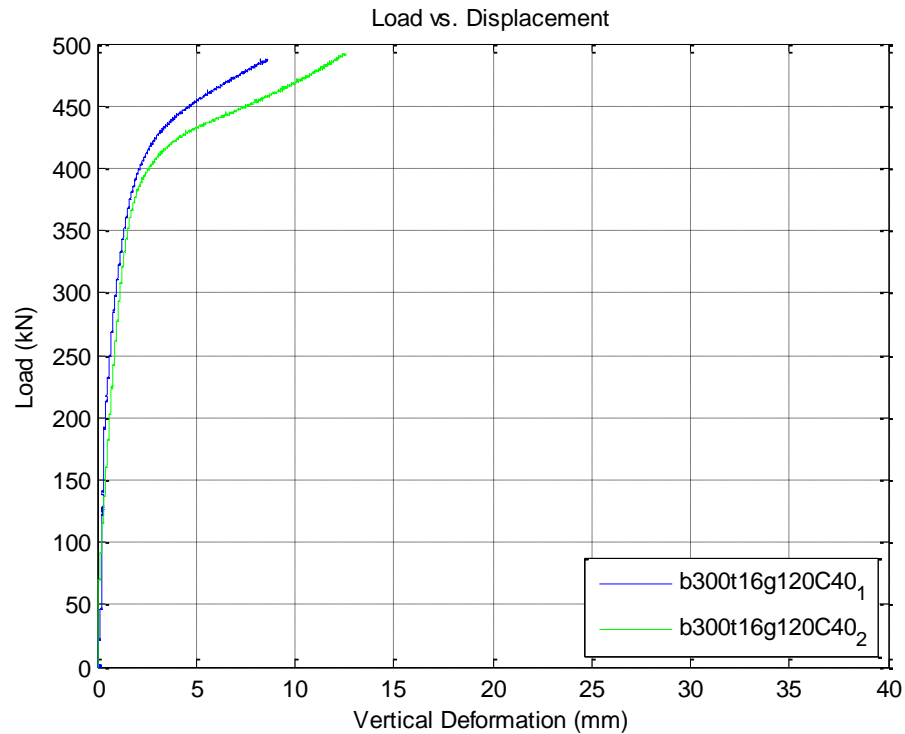


Figure 5.18 Force-Displacement relationship of b300t16g120C40-1&2 (raw)

It can be seen from Figure 5.8 to Figure 5.18 that the force-displacement relationship could be bi-linearly represented. The force increase-and-drop in the relationships presented in Figure 5.9 and Figure 5.10 is not considered. This is because the suitability of such behaviour, i.e. safety, for design purposes can be argued. Commonly, this bilinear representation could be defined by evaluating the initial stiffness, the yield force, and the post-yield stiffness. Going back to the experimental results, for each test, the first linear part of the relationship defines the initial stiffness. The stage which saw no or minimal increase of force could be used to define the yield. Finally, the final part of the relationship defines the post yield stiffness. This observation could provide further support to the assumption made in Chapter 3 that the concrete-filled SHS face bending can be represented by bi-linear model. The work done to verify this is presented in Chapter 7 of this thesis.

5.5.2 Possible Sources of Variation in Repeated Tests

In general, similar force-displacement relationships have resulted from repeated tests. However, some variation in these relationships was found in repeated identical samples.

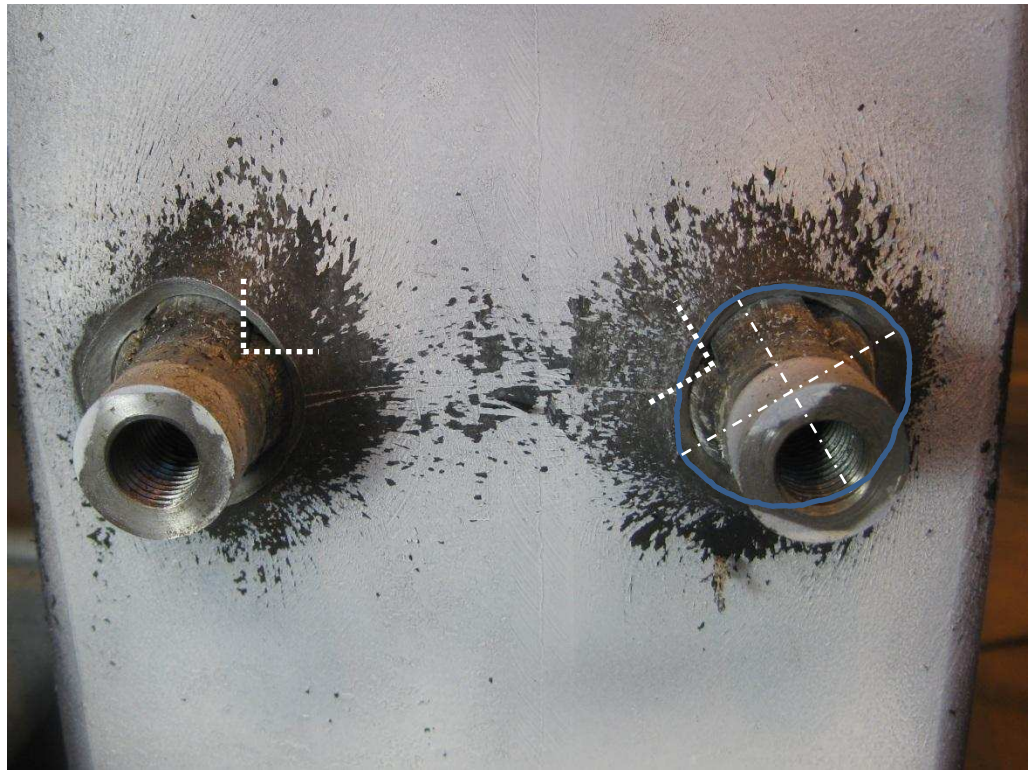
A clear example of this can be seen in b200t8g80C50-1&2 and b200t8g60C40-1,2&3 (shown in Figure 5.9 and Figure 5.11 respectively). Additionally, some variation was reported in just part of the force-displacement relationship. Samples b300t16g120C40-1 and b300t16g120C40-2 which are shown in Figure 5.18 demonstrate a good example of this variation (in the post-yield part of the relationship).

The same testing condition was maintained where possible through-out the testing programme, however, several possible sources of variation are presented and discussed in the following sections.

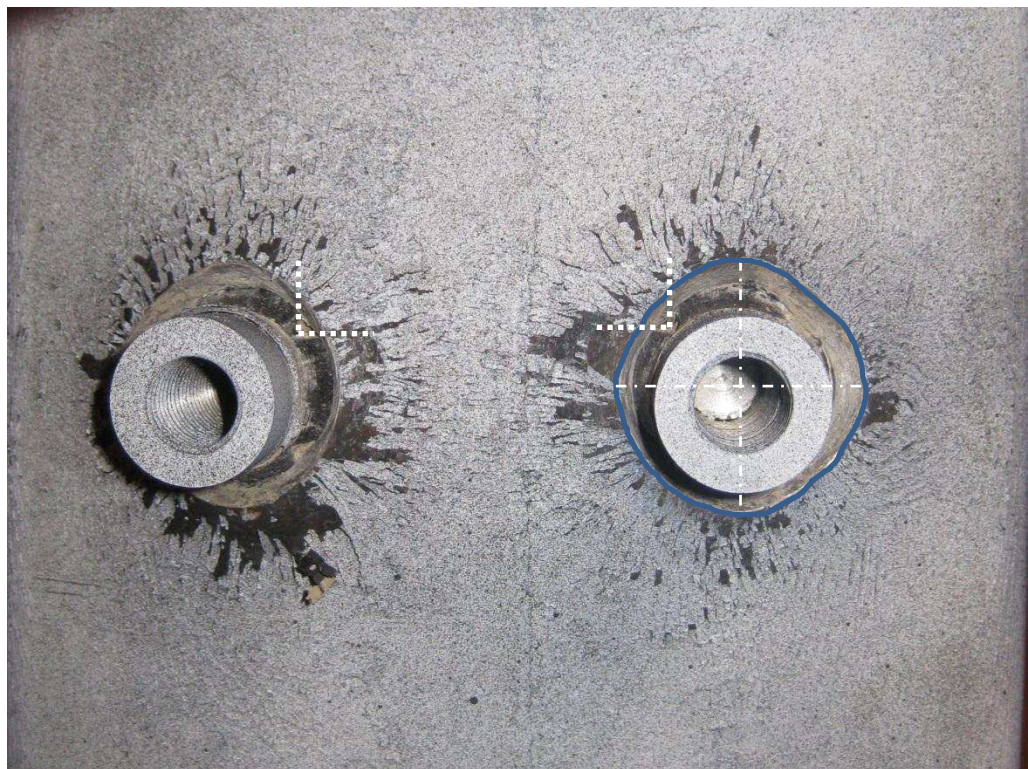
Test Set-up

As mentioned before, the same set-up procedure was followed in preparing all the samples. However, in some samples the dummy bolts were not properly aligned as shown in Figure 5.19. This means that the sleeves location differs in repeated samples, which affects the location of the maximum deformation in the parameter of bolt's holes in the SHS face.

An example of this was clearly noticed at late stage of the tests as shown in Figure 5.19 where the deformed bolt's holes parameter is drawn in blue. The difference in bolt alignment theoretically could have affected the force transfer mechanism from the bolt to the SHS face through the concrete in-fill. No evidence of this was found, however, more investigation is needed to reach a firm conclusion on this. This was recommended for further future work.



a. Improper dummy bolt alignment (Sample b200t8g100C40-2)



b. Proper dummy bolt alignment (Sample b200t8g80C40-4)

Figure 5.19 Proper and improper dummy bolts alignment

SHS Tested Face

The hot-rolled SHS are originally made from a flat steel sheet. This sheet is bent during the manufacturing to form the shape of SHS. The edges of the sheets are then welded together.

In most tests, the welded SHS face was not tested, however, it was tested in few tests in error like in Sample b200t8g100C40-2. The weld-seam of the tested SHS face on this sample is shown in Figure 5.20.

As welding changes the steel microstructure (Boumerzoug et al., 2010), this can change the stress distribution on the SHS face. The effects of this on the SHS face bending behaviour was not investigated in this study and was recommended for further future work.



Figure 5.20 The weld-seam in tested face of Sample b200t8g100C40-2

Concrete-infill Compressive Strength

Repeated versions of identical samples are often tested in separate days. This means that either tests were conducted at different concrete maturity or different casts were used to make the concrete-infill. Therefore the concrete-infill properties are investigated.

Commonly, the compressive strength of concrete is defined using compression tests. In this study, this was done by testing 100mm concrete cubes. Although the same mix design and material properties were used to produce the concrete-infill, variations were still found in the cube compressive strengths as shown in Table 5.1.

Table 5.1 Variation in Concrete-infill Compressive Strength

n	Specimen ID	Targeted Strength (N/mm ²)	Actual Cube Strength (N/mm ²)	Error % $1 - (\frac{\text{target}}{\text{actual}})$	Error % $1 - (\frac{\text{mean}}{\text{actual}})$
1	b200t8g80c20-1	20	22.5	11.1	-0.4
2	b200t8g80c20-2	20	23.2	13.8	2.6
3	b200t8g80c20-3	20	22.1	9.5	-2.3
4	b200t8g80c50-1	50	49.2	-1.6	-4.3
5	b200t8g80c50-2	50	50.4	0.8	-1.9
6	b200t8g80c50-3	50	54.4	8.1	5.6
7	b200t8g80c80-1	80	82.5	3.0	-0.4
8	b200t8g80c80-2	80	83.2	3.8	0.4
9	b200t8g60c40-1	40	41.2	2.9	0.8
10	b200t8g60c40-2	40	40.7	1.7	-0.4
11	b200t8g60c40-3	40	40.7	1.7	-0.4
12	b200t8g80c40-1	40	38.1	-5.0	-1.3
13	b200t8g80c40-2	40	38.1	-5.0	-1.3
14	b200t8g80c40-3	40	39.1	-2.3	1.3
15	b200t8g80c40-4	40	39.1	-2.3	1.3
16	b200t8g100c40-1	40	40.8	2.0	0.0
17	b200t8g100c40-2	40	40.8	2.0	0.0
18	b200t10g80c40-1	40	41.7	4.1	0.0
19	b200t10g80c40-2	40	41.7	4.1	0.0
20	b200t6.3g80c40-1	40	44.1	9.3	0.0
21	b200t6.3g80c40-2	40	44.1	9.3	0.0
22	b200t5g80c40-1	40	40.6	1.5	0.0
23	b200t5g80c40-2	40	40.6	1.5	0.0
24	b200t8g80c40-DIC	40	39.5	-1.3	0.0
25	b300t12.5g120c40-1	40	35.7	-12.0	0.0
26	b300t12.5g120c40-2	40	35.7	-12.0	0.0
27	b300t16g120c40-1	40	36.9	-8.4	0.0
28	b300t16g120c40-2	40	36.9	-8.4	0.0

The variation in cube compressive strengths can be categorized into two types:

1. Variation between actual concrete compressive strength of repeated identical samples. In this case an error is calculated using:

$$\text{Error} = \left(1 - \frac{\text{Cube compressive strength}_{\text{sample mean}}}{\text{Cube compressive strength}_{\text{sample actual}}} \right) \% \quad (5-1)$$

A maximum error of 5.6% error was reported in this case. This was reported in sample b200t8g80c50-3 as shown in Table 5.1. This variation occurs in only few experiments. It is thought to have no significant effect on the reliability of the results if samples which have odd compressive strengths are not considered for further analysis. For example, if sample b200t8g80c50-3 is not considered, this will reduce the error in sample b200t8g80c50-1 from -4.3% to 1.2% as the mean compressive strength will become 49.8N/mm².

2. Variation between target and actual concrete compressive strength. An error of this variation is calculated using:

$$\text{Error} = \left(1 - \frac{\text{Cube compressive strength}_{\text{target}}}{\text{Cube compressive strength}_{\text{actual}}} \right) \% \quad (5-2)$$

A maximum error of 13.8% was reported in this case. This was reported in sample b200t8g80c20-2 as shown in Table 5.1. This variation was noticed at early stage of the testing programme. It directly affects the results on repeated identical samples level. The reason for this is the force-displacement curves of samples that have various concrete-infill compressive strengths cannot be compared with each other. Result normalisation was proposed to account for this variation which is details in the following section.

5.5.3 Normalised Force-Displacement Results

Normalisation of the force displacement results was done primarily to account for the variation of concrete-infill compressive strength. To distinguish between the raw results from the normalised ones, the letter N is added to the end of normalised Test ID as shown in Figure 5.21.



Figure 5.21 Updated Test ID description

The normalisation was done to the force-displacement curve by editing the actual load values using the following expression:

$$Load_{normalised} = Load_{actual} \times \frac{f_{cu_{target}}}{f_{cu_{actual}}} \quad (5-3)$$

The normalised force-displacement curves of the experiments are shown in Figure 5.22 to Figure 5.32.

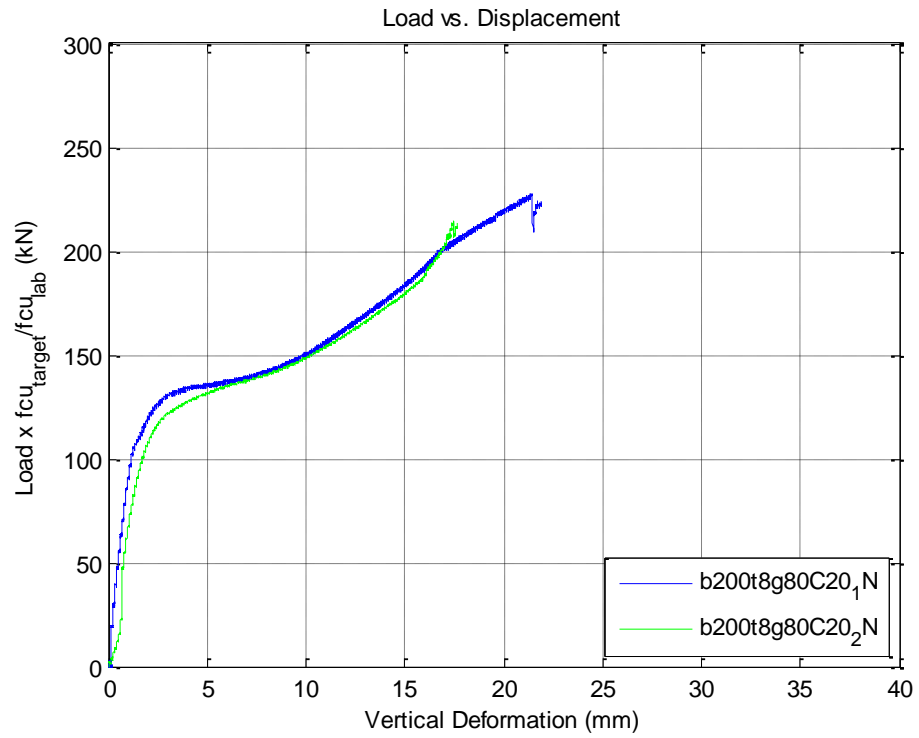


Figure 5.22 b200t8g80C20-1&2 Normalised Force-Displacement relationships (compared with Figure 5.8)

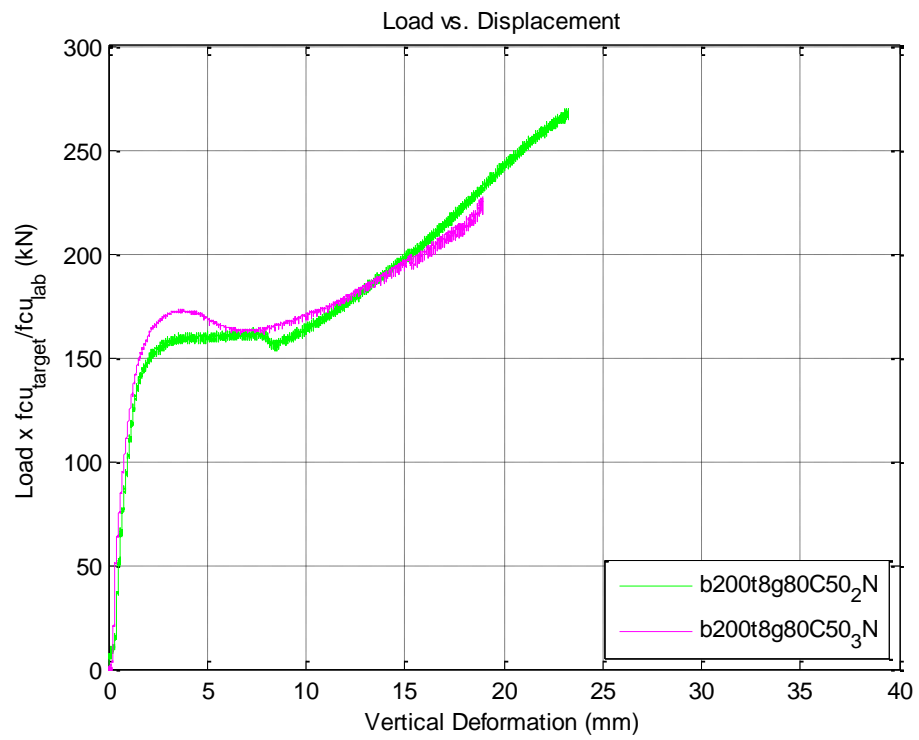


Figure 5.23 b200t8g80C50-2&3 Normalised Force-Displacement relationships (compared with Figure 5.9)

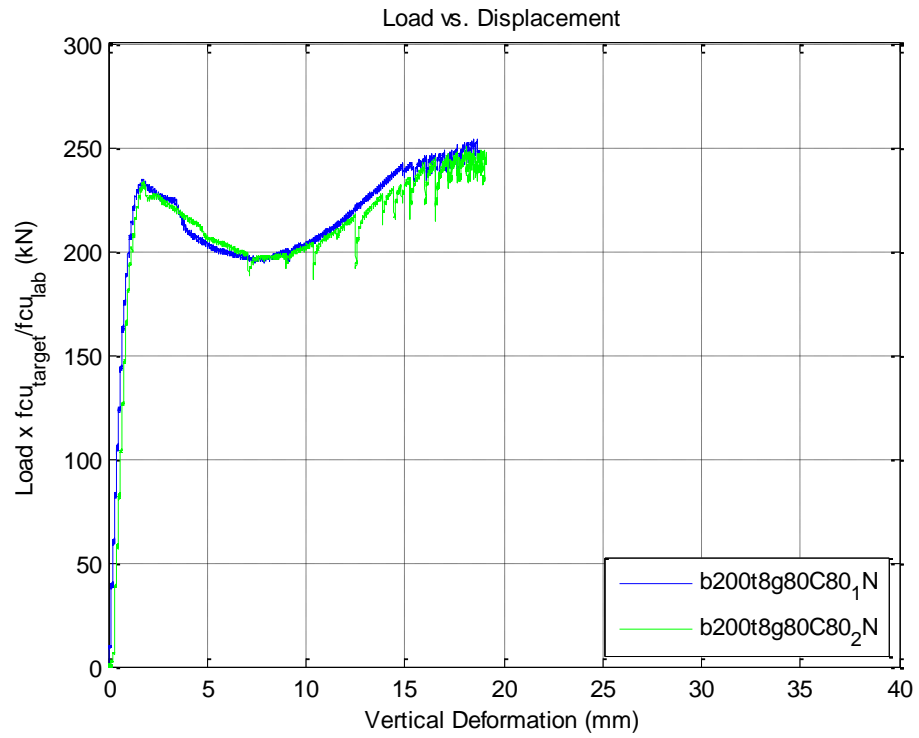


Figure 5.24 b200t8g80C80-1&2 Normalised Force-Displacement relationships (compared with Figure 5.10)

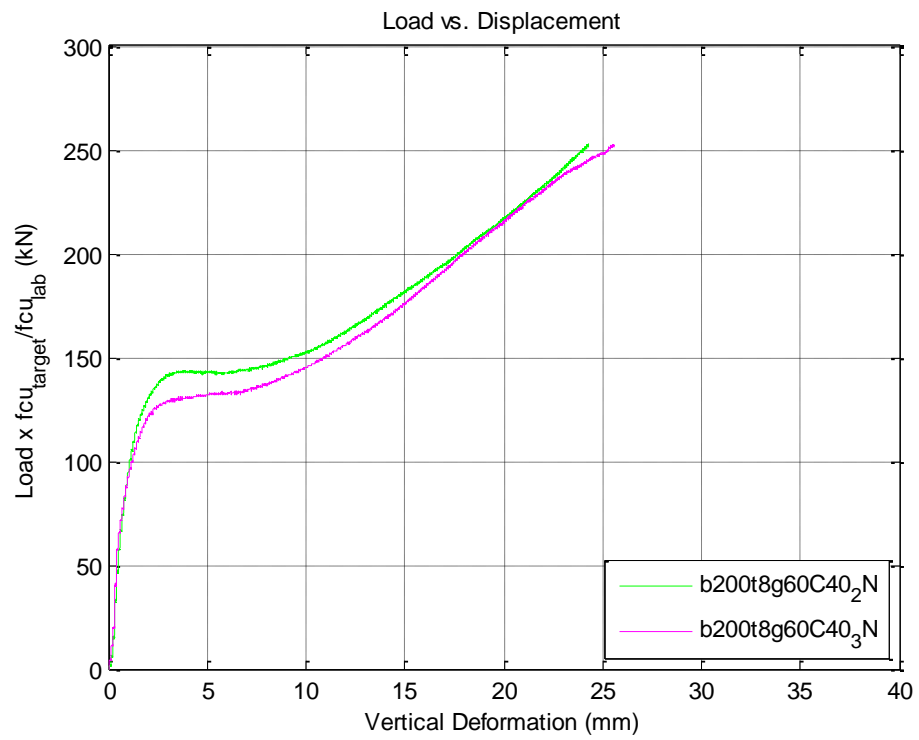


Figure 5.25 b200t8g60C40-2&3 Normalised Force-Displacement relationships (compared with Figure 5.11)

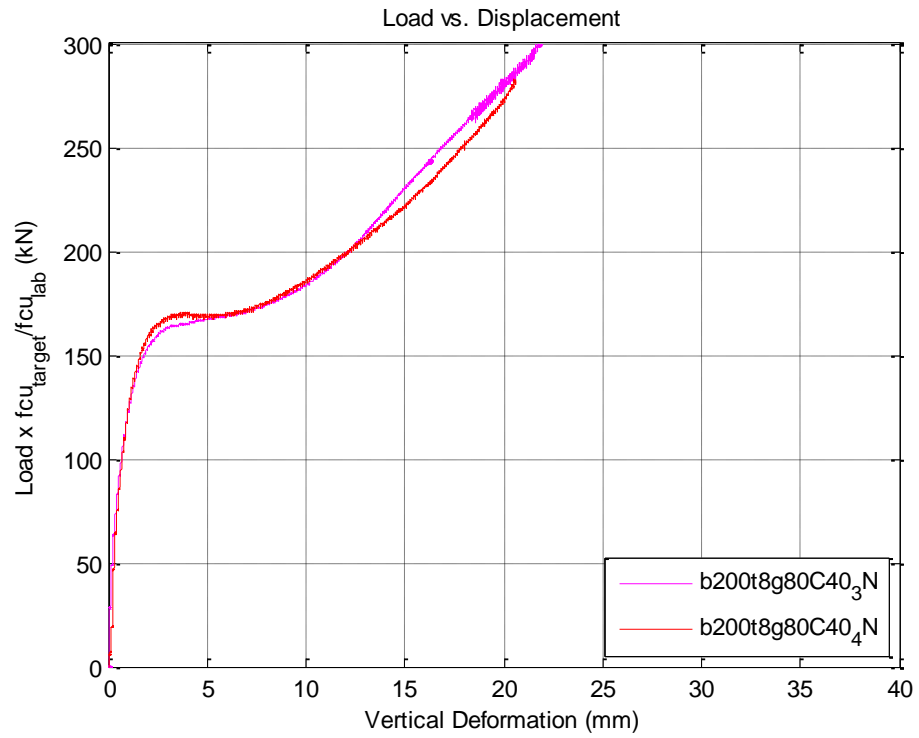


Figure 5.26 b200t8g80C40-3&4 Normalised Force-Displacement relationships (compared with Figure 5.12)

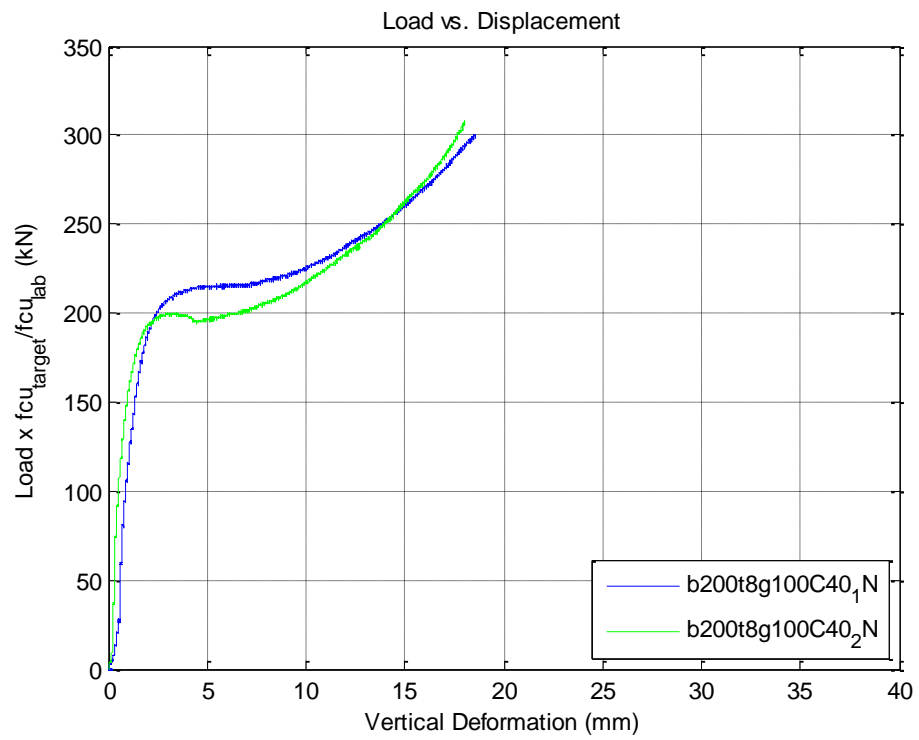


Figure 5.27 b200t8g100C40-1&2 Normalised Force-Displacement relationships (compared with Figure 5.13)

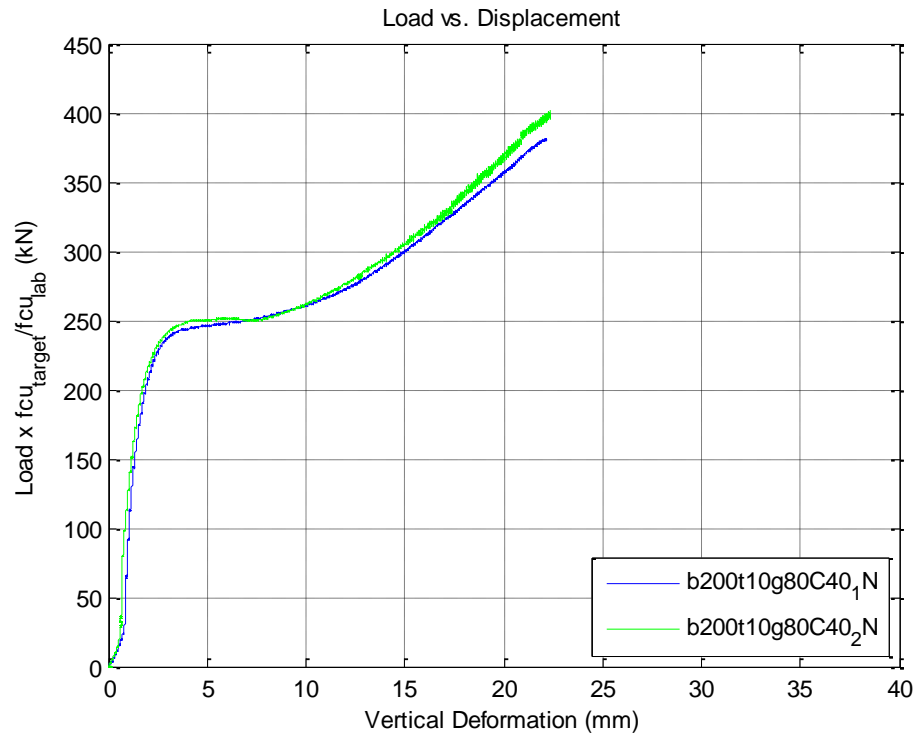


Figure 5.28 b200t10g80C40-1&2 Normalised Force-Displacement relationships (compared with Figure 5.14)

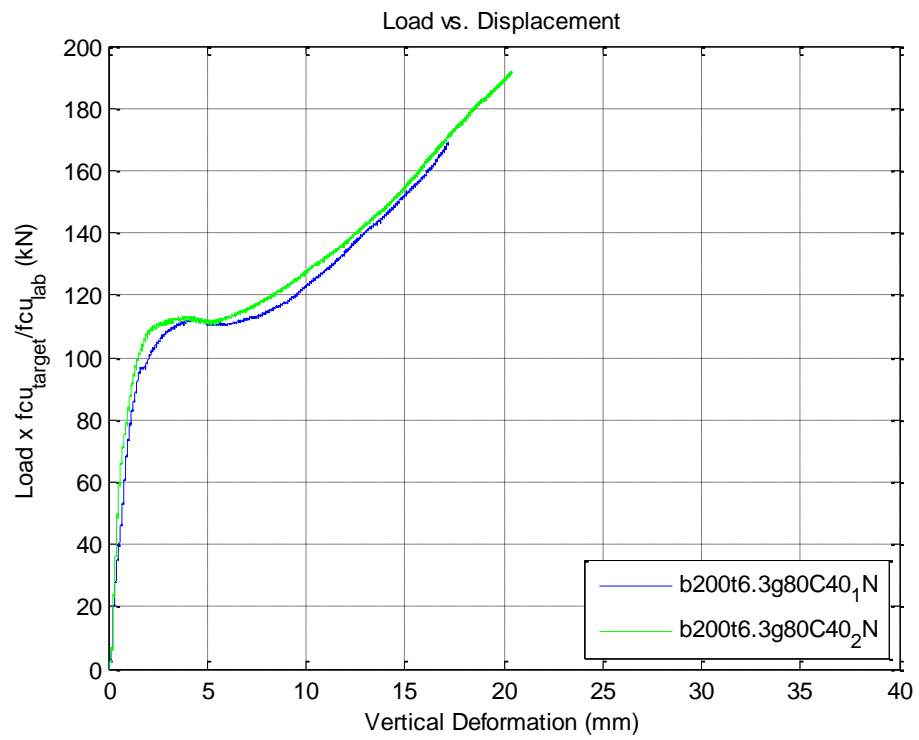


Figure 5.29 b200t6.3g80C40-1&2 Normalised Force-Displacement relationships (compared with Figure 5.15)

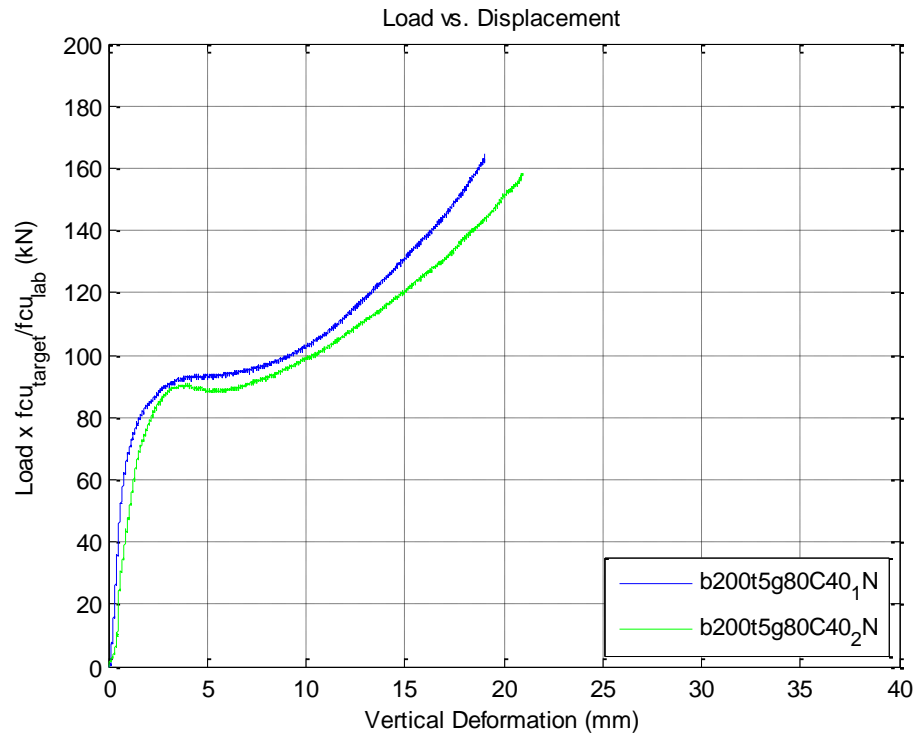


Figure 5.30 b200t5g80C40-1&2 Normalised Force-Displacement relationships (compared with Figure 5.16)

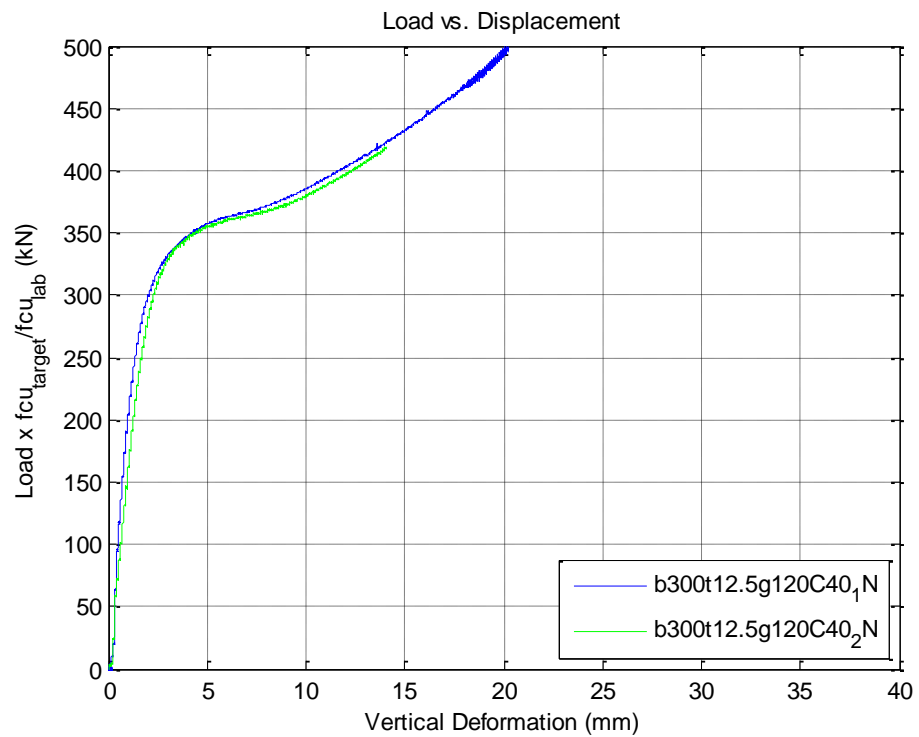


Figure 5.31 b300t12.5g120C40-1&2 Normalised Force-Displacement relationships (compared with Figure 5.17)

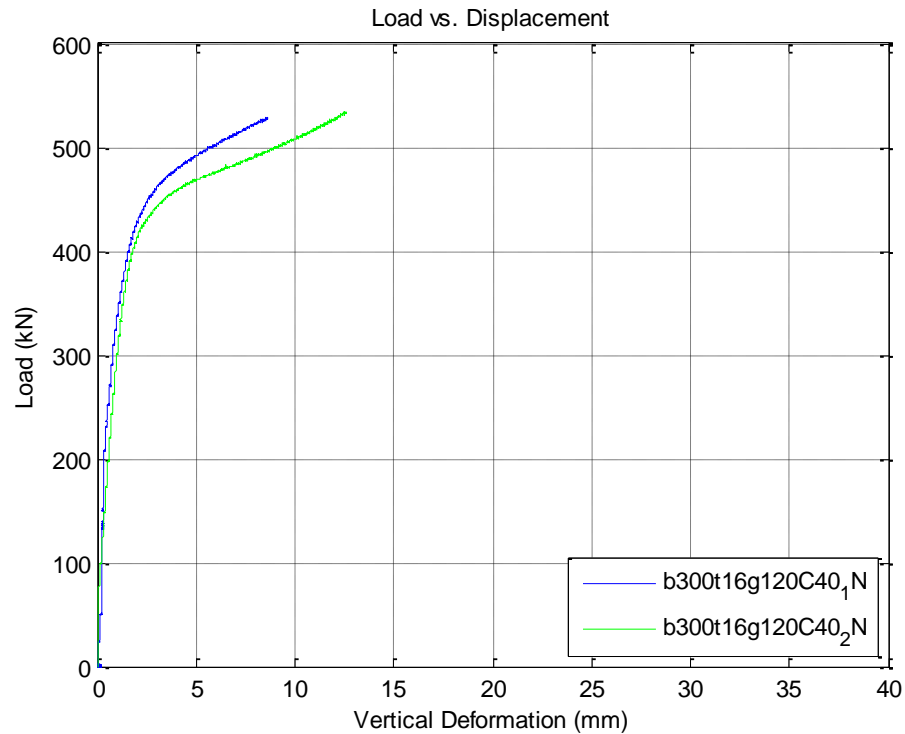


Figure 5.32 b300t16g120C40-1&2 Normalised Force-Displacement relationships (compared with Figure 5.18)

The normalisation done to the force-displacement curves has reduced the variation in similar/identical tests. This can be seen in most of the figures above especially in the case of samples b200t8g80C50-2&3 in Figure 5.23 and in samples b200t8g80C40-3&4 in Figure 5.26 where the variation in the raw force-displacement curves has been significantly reduced. On the other hand, in some tests, variation in force-displacement curves of similar/identical tests still exists. It was noticed that after normalisation the variation exists mostly in the post-yield part of force-displacement curves such as between samples b200t5g80C40-1&2 in Figure 5.30, and between samples b300t16g120C40-1&2 in Figure 5.32. The SHS face is thought to be the main factor of the face bending behaviour at this stage as the stresses in concrete-infill would have been greater than its compression capacity. Therefore, this variation could be attributed to errors in the test set-up and dummy bolt sleeves alignment.

5.5.4 Parametric Analysis

In this section, the experimental results of selected tests are used to study the effect of relevant parameters on the SHS face bending behaviour. These parameters are:

- Bolt gauge to SHS width ratio known as β
- SHS face slenderness ratio which is the ratio between SHS width to SHS thickness
- The compressive strength of concrete-infill

Bolt gauge to SHS width ratio

In the experimental program, for SHS 200x200x8, three different bolts gauges were tested: 60mm, 80mm and 100mm. This created three values of β which are 0.3, 0.4 and 0.5. The normalised force-displacement curves of selected samples representing these values i.e. b200t8g60C40-2, b200t8g80C40-4 and b200t8g100C40-1 are plotted in Figure 5.33. Zoom-in showing the initial part of the force-displacement curves of the same samples is plotted in Figure 5.34.

The figures show that the bolts gauge does not have any effect on the general behaviour as the same pattern was observed in the three experiments. The behaviour could be classed into three parts: the initial stiffness part where the force increases sharply with displacement, the yield force part where there is no increase in the force magnitude with the increase of the displacement and the lastly the post-yield part where the force undergoes a softer increase with the displacement. Figure 5.33 show that the bolts gauge has a significant effect on the magnitude of the yield force. An increase of about 15% of the yield force was observed when the bolt gauge increased from 60mm to 80mm (from $\beta=0.3$ to $\beta=0.4$). Moreover, when the bolt gauge increased from 80mm to 100mm, the yield force increased by more than 25%.

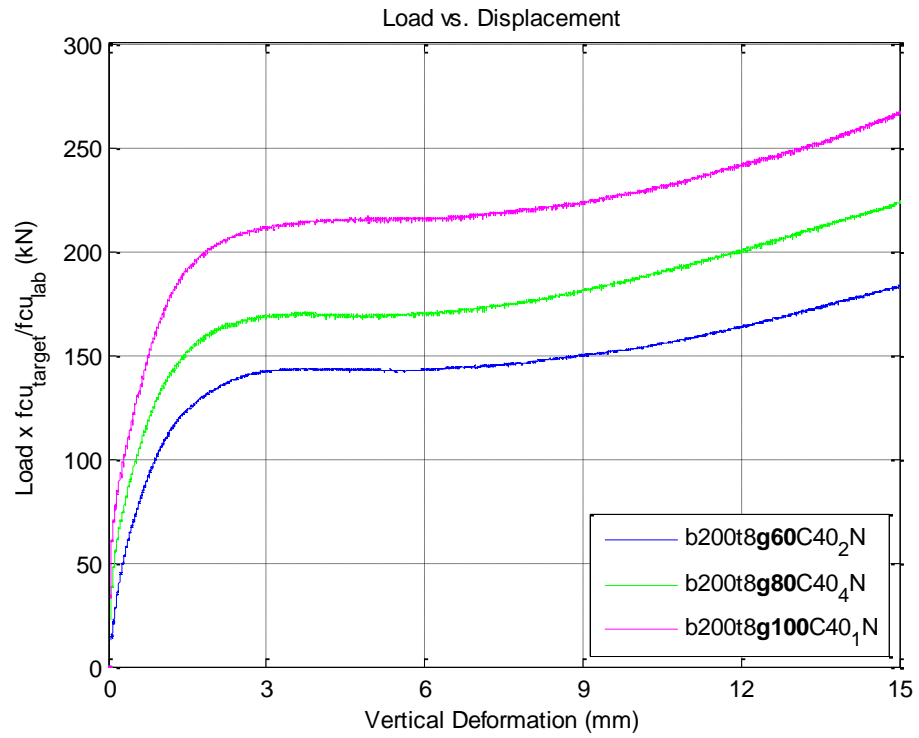


Figure 5.33 The effect of bolt gauge on SHS face bending

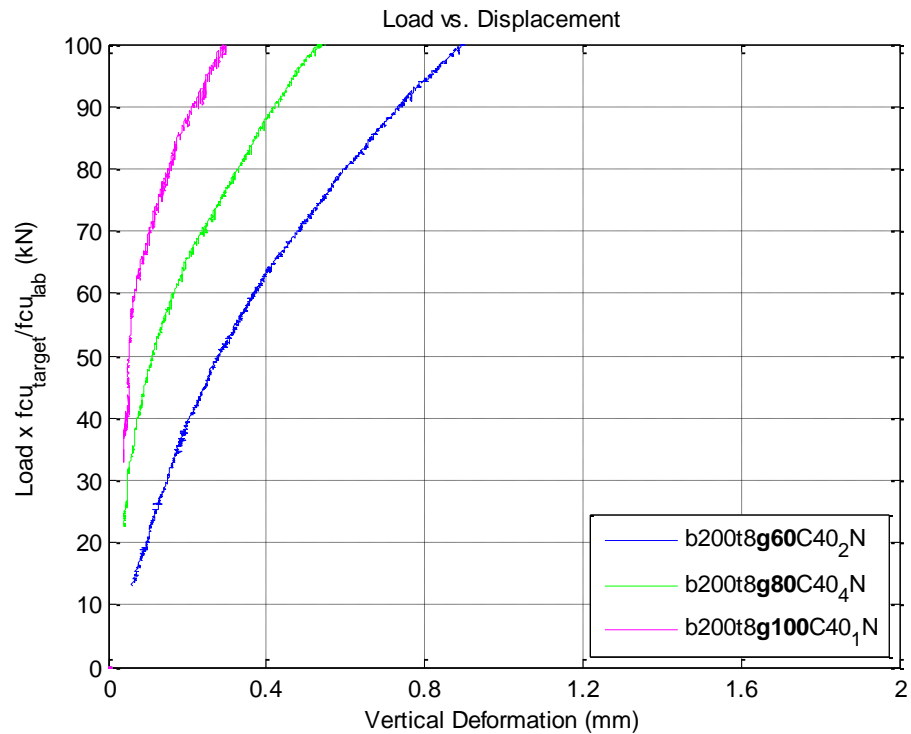


Figure 5.34 The effect of bolt gauge on SHS face bending (zoom-in)

The increase of the yield force lay well with the yield line analysis done in the course of this study to develop the analytical model. This is because SHS with wider bolts gauge require more work to bend the SHS face i.e. it provide more resistance hence higher yield force.

Furthermore, it can be seen in Figure 5.34 that the initial stiffness force-displacement curve representing the SHS face bending behaviour increases with the increase of the bolt gauge. The post yield part of the curve was almost not affected by the change of bolt gauge in the three tests.

It is important to note that the above mentioned findings are only valid across the range of parameters considered in this programme.

Slenderness ratio of SHS face

The slenderness ratio of SHS face (i.e. width/thickness) was also varied in the experimental program. This was done for SHS 200x200 with a bolt gauge equal to 80mm. Common ratios were tested: 20, 25, 31.75, and 40. This represents SHS 200x200 with thicknesses 10mm, 8mm, 6.3mm and 5mm respectively. The normalised force-displacement curves of selected samples representing these values i.e. b200t10g80C40-1, b200t8g80C40-4, b200t6.3g80C40-2 and b200t5g80C40-1 are plotted in Figure 5.35. Zoom-in showing the initial part of the force-displacement curves of the same samples is plotted in Figure 5.36.

Generally, the same SHS face bending behavioural pattern was observed for the tested face slenderness ratios. Figure 5.36 and 5.37 show that both yield force magnitude and the initial stiffness of the bending behaviour had a noticeable increase with the increase of the SHS thickness (i.e. decrease of SHS face slenderness ratio). The post yield part of the curve was almost not affected by the change of slenderness in the four tests.

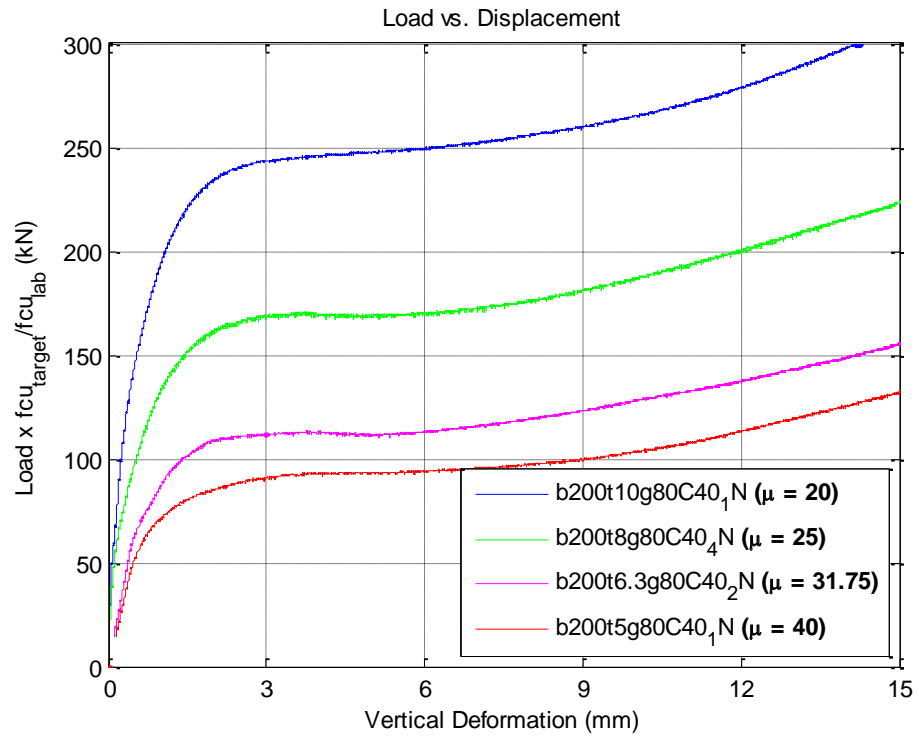


Figure 5.35 The effect of SHS face slenderness on SHS face bending

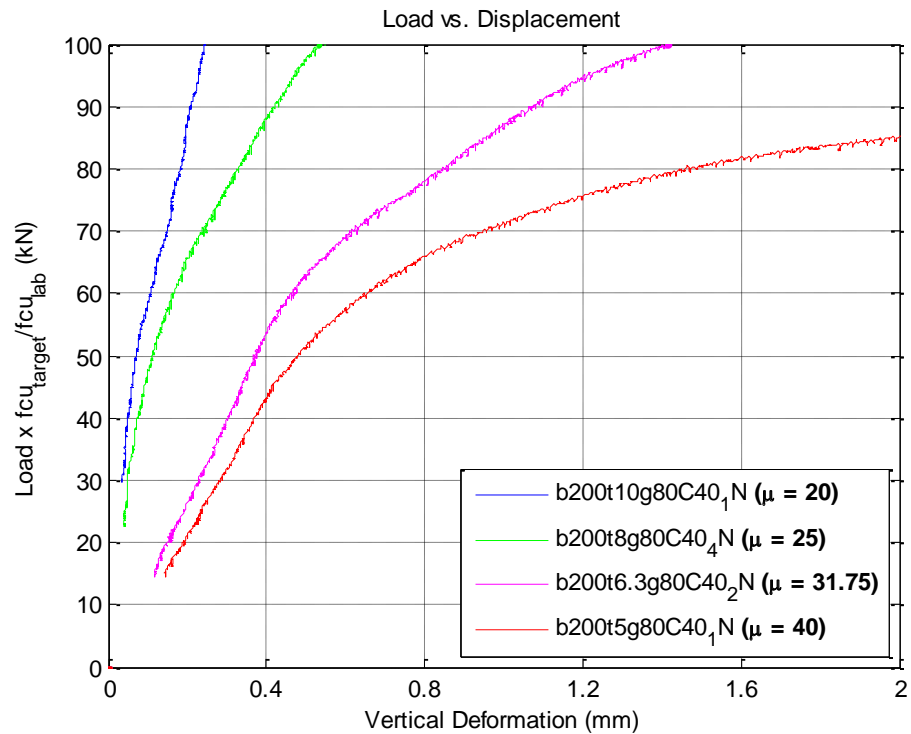


Figure 5.36 The effect of SHS face slenderness on SHS face bending (zoom-in)

The increase of the yield force magnitude of the force-displacement relationships observed in Figure 5.35 could be attributed to the increase of SHS face resistance. Theoretically, if a unit length of a yield line is considered, the thicker the SHS face the higher the yield moment of the unit length of yield line.

Concrete-infill compressive strength

The effect of the concrete-infill compressive strength was also investigated in the experimental program. This was done for SHS 200x200x8 with a bolt gauge equal to 80mm. The concrete mixes which are designed to produce compressive strength of 20N/mm^2 , 50N/mm^2 and 80N/mm^2 were used. These mixes represent concrete that have low, medium and high strength. The normalised force-displacement curves of selected samples representing these mixes i.e. b200t8g80C20-2, b200t8g80C50-3, and b200t8g80C80-1 are plotted in Figure 5.37.

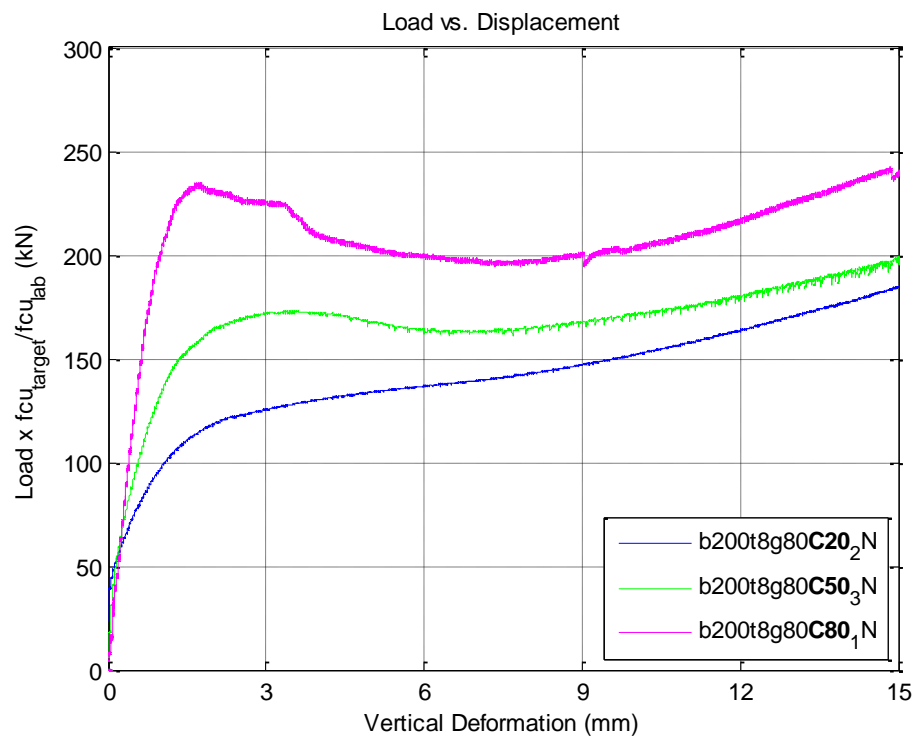


Figure 5.37 The effect concrete compressive strength on SHS face bending

As shown in Figure 5.37, the compressive strength of Concrete-infill is found to affect the general behaviour of SHS face bending. Improvement in the force-displacement curves of SHS face bending with the increase of concrete-infill compressive strength occurred. The initial part and the post-yield part of the force-displacement curves were not significantly affected by the change in the concrete-infill compressive strength. However, as seen in Figure 5.37, this was not the case for the part of the curve which represents the yielding of the SHS face. In fact, the force-displacement curve for the tests where concrete-infill is used is no longer Bi-Linear.

An increase in the magnitude of yield force was observed with the increase of the compressive strength of the concrete in-fill. Despite this, as shown in Figure 5.37 in tests b200t8g80C50 where 50N/mm^2 concrete-infill was used, a small drop of about 5% in force magnitude preceded the increase of force magnitude. This drop occurred after the yielding stage before it climbed again in the post-yield part of the curve. Similarly, in tests b200t8g80C80, where 80N/mm^2 concrete-infill was used, a sharper drop (about 20%) preceded the increase of force magnitude at the yielding stage. No drop in the force magnitude was observed in tests b200t8g80C20 where 20N/mm^2 concrete-infill was used.

The effect of concrete-infill strength on the SHS face bending behaviour can be described in three stages. The initial stage in which both the SHS face and concrete-infill work together to take loads transferred from the bolt. This stage ends when some deformation occurs on the SHS face i.e. the bolts have to move. This movement cannot take place unless the part of concrete-infill in front of the bolts' sleeves is crushed or separated from the rest of restrained concrete. In theory, a concrete cone forms in front of bolts' sleeves at this stage and moves with the

bolts as no crushing was observed during the tests (observed cracks were shown in Figure 5.5). The compressive strength of the concrete-infill has a direct effect on this stage (i.e. initial stage of the test) as it can be seen from the tests that the use of higher strength concrete-infill results in higher yielding force. The contribution of the concrete-infill becomes minimal after this stages hence the similarity in the post-yield part of the force displacement-curves which represent the final stage. However, as the contribution of the concrete-infill becomes minimal, the force drops, from the yield force magnitude, to a level of which the SHS face becomes the main source of resistance i.e. intermediate stage. This drop which preceded the increase in the force magnitude in the force-displacement curve following the yield stage is found to be directly related to the concrete-infill compressive strength: the higher the compressive strength, the sharper the drop.

5.6 Digital Image Correlation Results (DIC)

Digital Image correlation (DIC) was utilised in the experimental programme to study the face Strain distribution and deformation occurs due the SHS face bending.

The DIC is a very powerful tool which can be used to record 3D strain and displacement of a components and specimens i.e. the SHS face in this experimental programme. A speckle pattern was applied on the SHS face using black and white matt paint. During the test, this pattern was disturbed in the area closed to the bolts due to its large deformation. This is shown in Figure 5.38. This has affected the results obtained from the DIC as its cameras track this pattern to produce the results. Nevertheless, DIC results have provided sufficient information on how the strain and displacement were developed and distributed on the SHS face. Such information was not available experimentally.

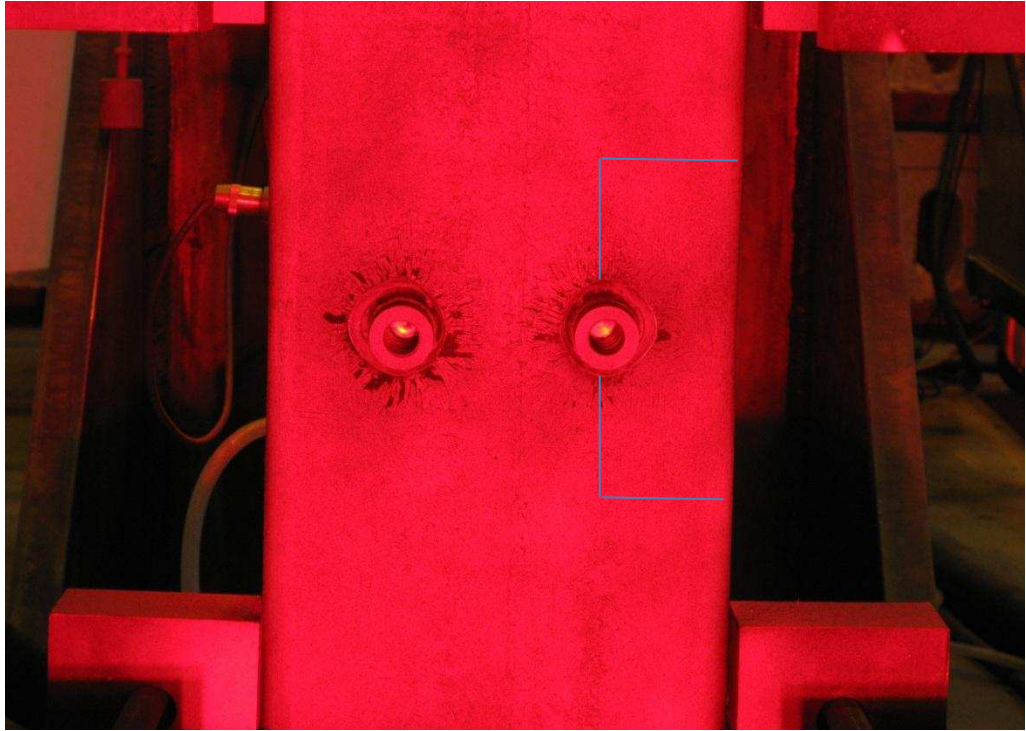


Figure 5.38 Speckle pattern disturbed in b200t8g80C40-DIC

The development of strain distribution across SHS face is shown in Figure 5.39 (for the SHS part highlighted in the figure above). It can be seen from this figure that the strain distribution is similar to the yield line pattern theoretically assumed using yield line analysis in Chapter 3. This is clear when comparing Figure 5.39 (b) and (c) with Mechanism 3 in Figure 3.4. Likewise, the DIC results were used to plot experimental displacement profile of section-lines across the SHS face. This was done to show the deformation of the SHS face for different loading stages during the test. The SHS face displacement profiles of section-line which passes across the two bolts are shown in Figure 5.40. Similarly, the SHS face displacement profiles of section-line which passes across just one bolt are shown in Figure 5.41. In both figures, the bolt hole is represented by a straight line at earlier stage and with no line at later stage when the speckle pattern was disturbed. The figures show that the DIC results exhibit expected displacement behaviour.

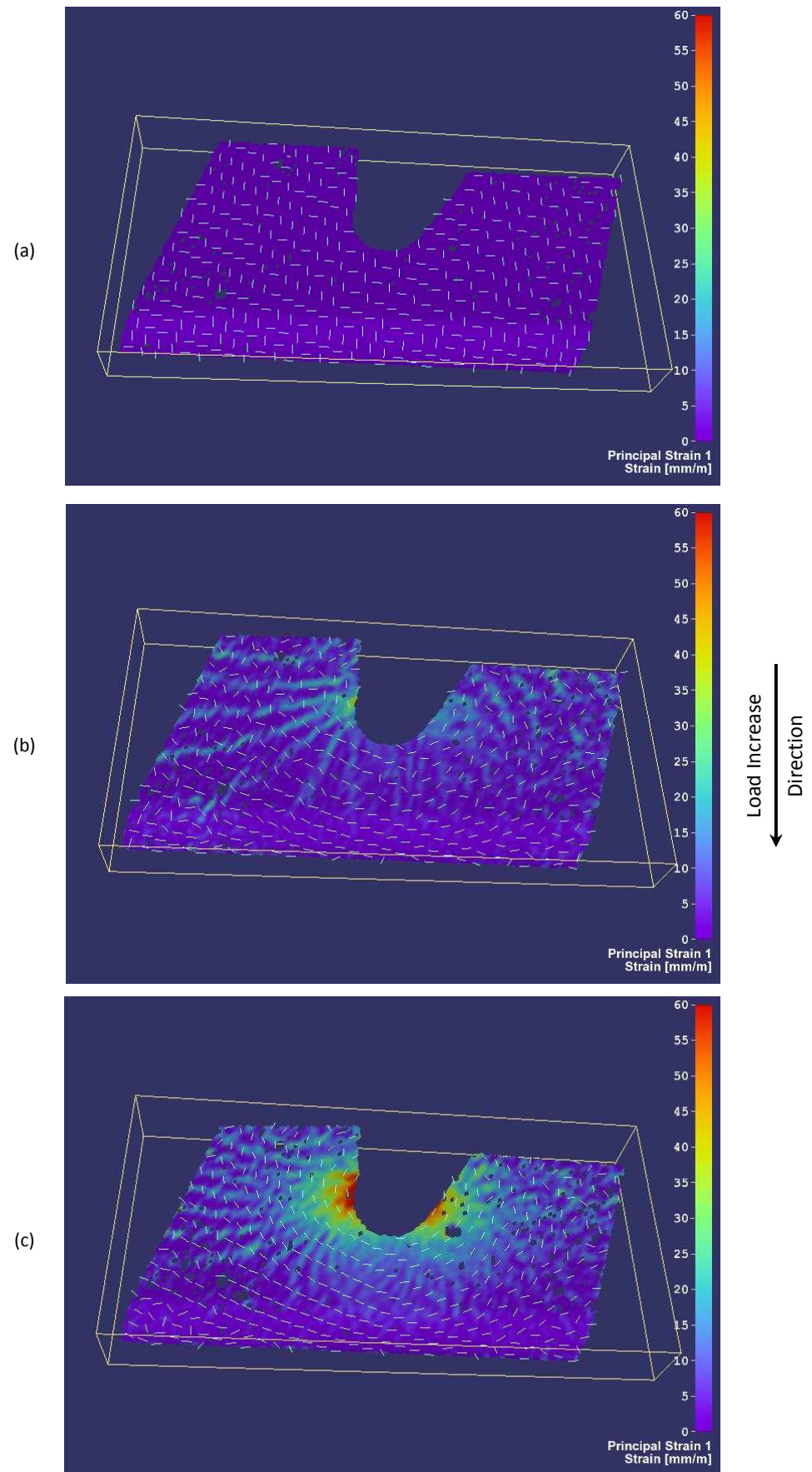


Figure 5.39 Strain development on SHS face captured using DIC

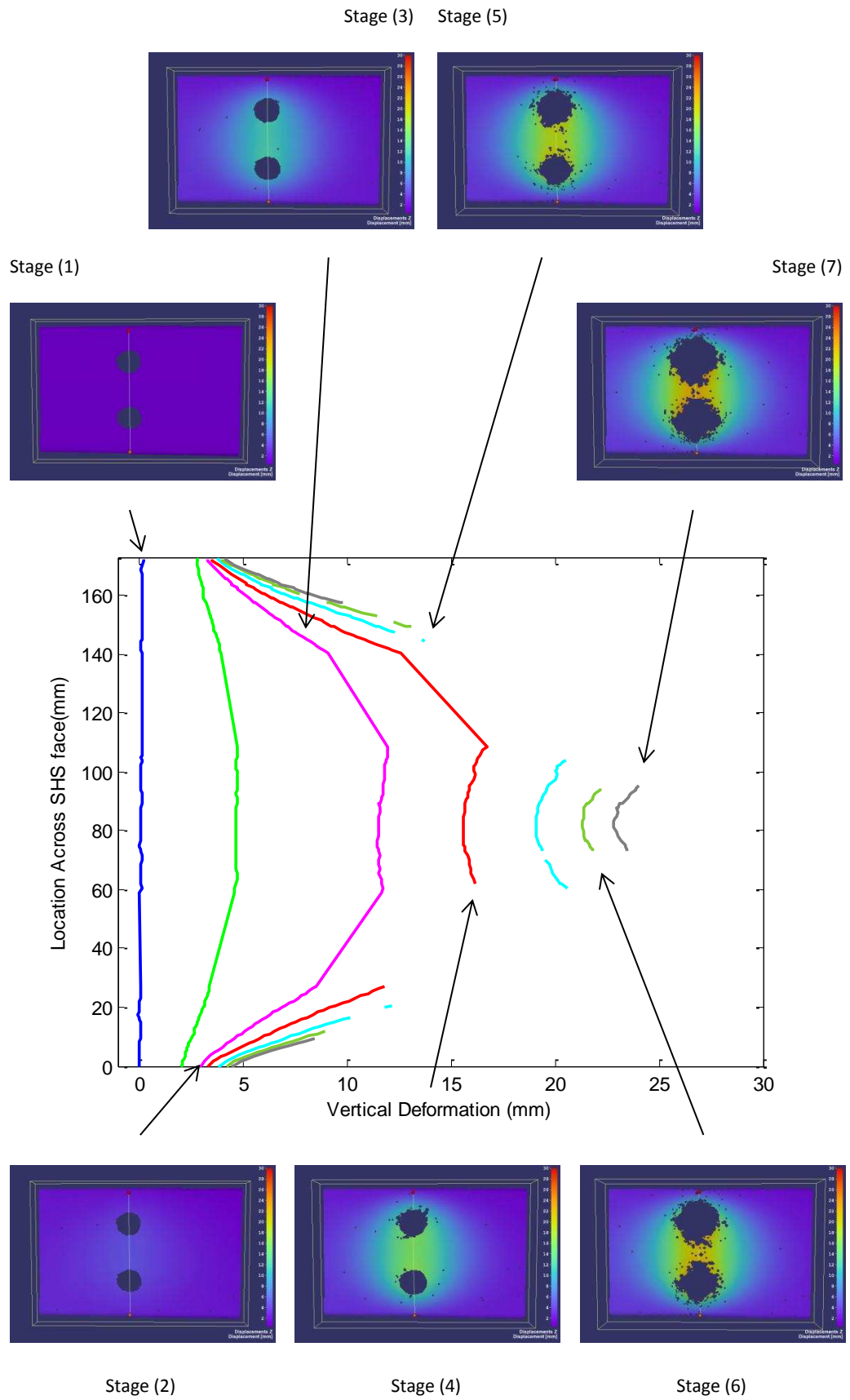


Figure 5.40 SHS face deformation across a section-line passing over the bolts

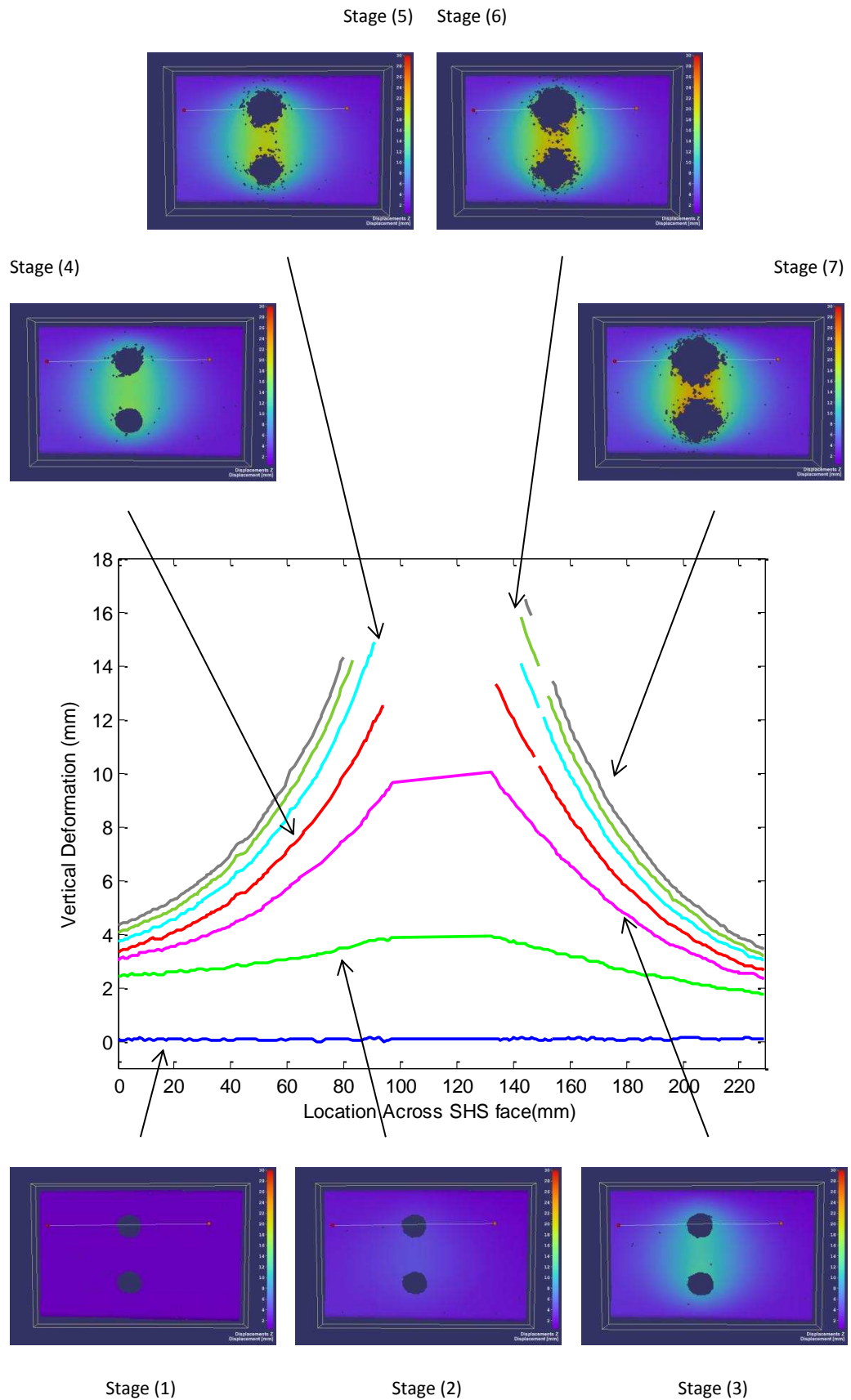


Figure 5.41 SHS face deformation across a section-line passing over one bolt

5.7 Summary

This chapter presented the experimental results. Raw force-displacement curves obtained during the experimental programme was presented first. Sources of variation between the outcomes of identical repeated experiments were discussed. This was followed by presenting normalised force-displacement curves in which the normalisation was done based on concrete-infill compressive strength. Selected experiments were used to investigate the effect of bolt gauge, SHS face slenderness and concrete in-fill compressive strength on the SHS face bending behaviour. Finally, DIC result which were used to study the face Strain distribution and deformation occurred due the SHS face bending were presented.

The next chapter details the finite element model developed in the course of this study and presents its results. Demonstration of how the experimental results were used to calibrate the Bi-Linear analytical model developed in the course of this study is shown in Chapter 7.

Chapter 6

Finite Element Modelling

6.1 Introduction

Parallel to the Experimental Programme conducted in the course of this research, finite element modelling was used to study the face bending behaviour of concrete filled Square Hollow Sections. Experimental outcomes provide appropriate description of the behaviour, but they are limited in many aspects. The ranges of geometry and material properties in experiments are governed by what is available in the market. Physically possible and available instruments limit the data which can be measured in each experiment. The cost and timeline associated with experimental work might not allow many repetitive experiments, which improve results reliability, neither extensive parametric study. The development of Finite modelling technology in recent time provided a solution for all these limitations. Complex engineering problems are often now simulated using finite element

modelling with great success. A finite element model with acceptable accuracy can complement the experimental work. It can also be very efficient tool when conducting parametric study.

Many finite element modelling packages are now available in the market for both research and commercial use. In this research, ANSYS Release 13 software was used to carry out the finite element modelling. ANSYS is widely known for its powerful capabilities in simulating complex problems in multi physics, mechanical and fluid mechanics fields. It has a wide range of materials and elements, and the capable of performing different types of analysis. The software is widely used by both academia and industry, and had produced high quality and reliable simulations.

In ANSYS, a finite element model can be developed through two ways:

- Graphical User Interface (GUI)
- ANSYS Parametric Design Language (APDL)

The GUI gives users easy, interactive access to program functions, commands, documentation and reference material (ANSYS, 2010d). GUI menu system helps users navigate through the program. Data can be entered using a mouse, a keyboard or a combination of both. However it can be very difficult to pick specific nodes from the screen especially for problems which have complicated geometry.

The APDL is a scripting language that can be used to build models in term of parameters (variables). The APDL commands are true scripting commands and encompass a wide range of features such as do-loops, if-then-else branching and vector/matrix operations. This enables APDL to be is the foundation for sophisticated features such as design optimization and adaptive meshing (ANSYS, 2010e). The APDL has a superior effectiveness for parametric studies.

Description of the finite element model developed in the course of this research is presented in the next section, followed by model observations, results and validation. Parametric variation analysis performed using the finite element model is also presented herein.

6.2 Description of the Model

A full-scale 3D finite element model was developed using APDL. It was favoured as a parametric investigation was required to understand the concrete-filled SHS face bending behaviour. A typical model takes more than 1500 line of scripting to be built and analysed. Self-explanatory APDL script for a SHS 200X200x5 with bolt gauge of 80mm (similar to experiment *b200t5g80c40-1*) is presented in the Elamin (2012) Appendix. The APDL script creates the model geometry depending on the following parameters/variables (noted as writing in the script):

- SHS associated:
 - Thickness of section (*t*)
 - Width of section (*w*)
 - Depth of section (*ds*)
 - Internal radius of section corners (*r1*)
 - External radius of corner of section (*r2*)
 - Bolts gauge (*g*)
 - Bolt hole diameter (*bhd*)
 - Length of section (*L*)
 - Distance from edge to end of support (*sup*)
- Hollo-Bolt associated
 - Hollo-bolt/dummy bolt diameter (*hbd*)
 - Length of sleeve (*los*)
 - Sleeves opening angle in degrees (*sa*)
 - Extension of bolt from Hollow Section (*Bext*)

The script follows typical process to build the model. The process is commonly divided into three phases in ANSYS: pre-processing phase, solution phase and post-processing phase. Typical flow chart of the model illustrating the three phases is shown in Figure 6.1.

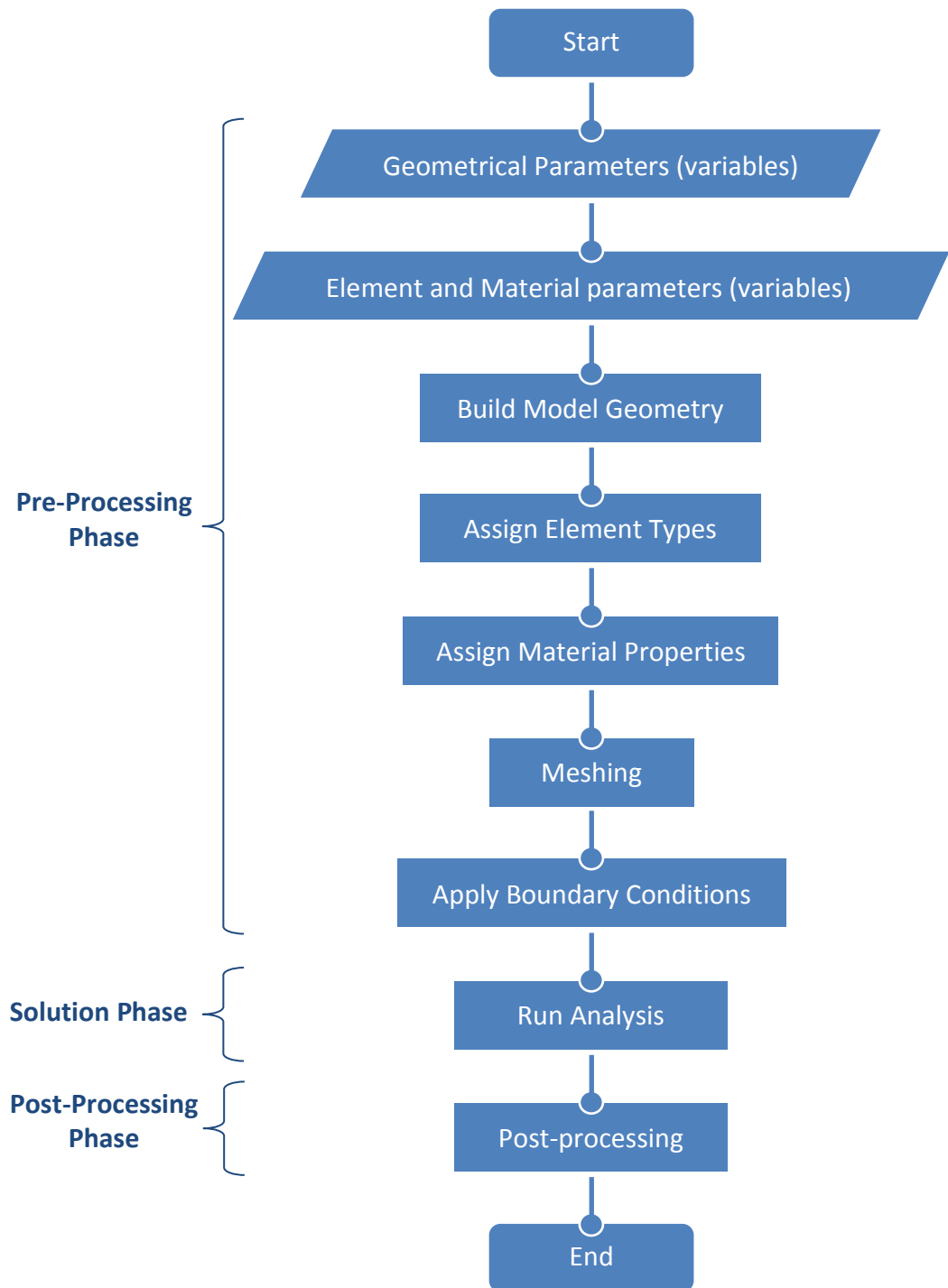


Figure 6.1 Numerical model Flowchart

6.2.1 Element Types

The first stage of creating a finite element model is to shape its geometry. In ANSYS, this process begins by defining key points using a coordinate system. Volumes are then built using these key points. When the geometry of the model is created, ANSYS elements are associated to relevant volumes. Each element has a set of items which characterise its behaviour during analysis. This set typically includes the following items (ANSYS, 2010c):

- Element Name
- Nodes
- Degrees of Freedom
- Real Constants
- Material Properties
- Surface Loads
- Body Loads
- Special Features
- Key Options (KEYOPTs)

A wide range of elements is available in ANSYS element library such as Solid elements which are 3D elements, Shell/Plane element which are 2D elements and Contact elements.

Solid and Shell elements are normally used when modelling structural problems. Shell elements are preferred when the thickness of structural element can be neglected. Many cases of plates or slabs modelling are an example of when Shell elements are used. Solid elements on the other hand are used when modelling an actual physical structural system. It can provide an identical look to the system. Generally, Solid elements require more computational power as they introduce more nodes and degrees of freedom compared to Shell elements.

Solid elements were used to model the Square Hollow Section, bolt and concrete in-fill in this model. Relevant Contact and Target elements were used to simulate the contact between Square Hollow Section, bolt and concrete. This section presents an outlined description of these elements.

Square Hollow Section and Bolts

In this model, SOLID185 was used to model the SHS and the Bolts. It is a 3D 8-Node Structural Solid which means that this element is defined by eight nodes. Each node has three degrees of freedom: translation in the nodal x, y and z directions. Two forms of SOLID185 are available:

- Homogeneous Structural Solid
- Layered Structural Solid

The Homogeneous Structural Solid is used in this model. It is suitable for modelling general 3D solid structures. It allows for prism and tetrahedral options degeneration when used in irregular regions (ANSYS, 2010c). However, the tetrahedral is not recommended as shown in Figure 6.2.

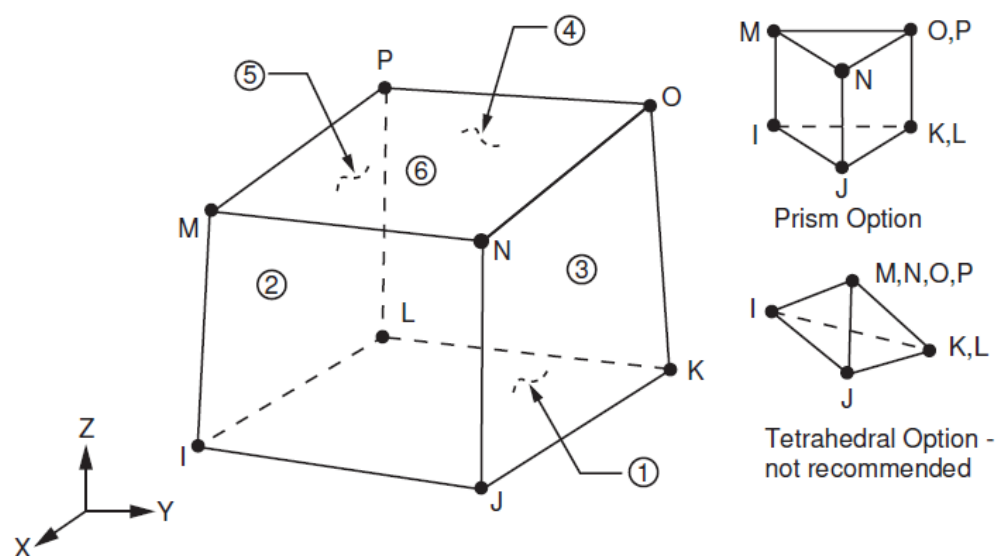


Figure 6.2 SOLID185 Geometry (ANSYS, 2010c)

The default coordinate system of this element is along global directions, yet an element coordinate system can be redefined if required.

In similar models, metallic materials were modelled using SOLID45 and SOLID95 with success (Al-Mughairi, 2010). Both Solids became obsolete in ANSYS Release 13.

A higher order version of SOLID185 is available i.e. SOLID186. However using this element, which is a 20-Node Structural Solid, will impose more computational cost and slower analysis for identical problems.

Details on how the Real Constants and Key Options (KEYOPTs) have been configured for this element type can be found in the APDL script.

Concrete in-fill

SOLID65 was used to model the concrete which fill the Hollow Section in this model (shown in Figure 6.3). It is a 3D 8-Node Structural Solid used to model solids, such as reinforced concrete and composites, with or without reinforcing bars. It has the capability of crushing in compression and cracking in tension.

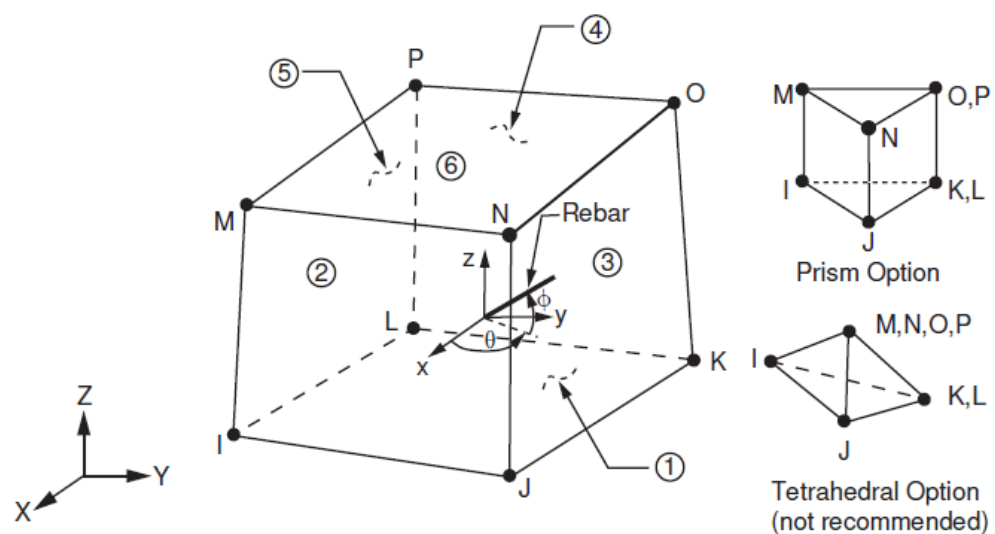


Figure 6.3 SOLID65 Geometry (ANSYS, 2010c)

Similar to SOLID185, it is defined by eight nodes. Each node has three degrees of freedom: translation in the nodal x, y and z directions. The default coordinate system of this element is along global directions, yet an element coordinate system can be redefined if required.

The concrete element is similar to a 3D structural solid with the addition of special cracking and curing capabilities. The concrete, when modelled using this element, is capable of cracking in three orthogonal directions, crushing, plastic deformation and creep (ANSYS, 2010c).

Details on how the Real Constants and Key Options (KEYOPTs) have been configured for SOLID65 can be found in the APDL script.

Contact Surfaces

Contact surfaces had to be used in the model to ensure proper force transfer between the interacting surfaces. There are five contact models available in ANSYS:

- Node-to-Node
- Node-to-Surface
- Surface-to-Surface
- Line-to-Surface
- Line-to-Line

Each model uses different set of contact elements and is appropriate for specific types of problems (ANSYS, 2010b). Surface-to-Surface contact model was used in this study. It consists of a Contact surface and a Target Surface.

For Surface-to-Surface contact in 3D problems, two elements can be used as a Contact surface: CONTA173 and CONTA174. The latter is used when a higher order Solids are considered, i.e. solids with midside nodes, and was not used in this study. TARGE170 can be used as a

Target surface with both of CONTA173 and CONTA174 and was used in this finite element model.

CONTA173 is used to represent contact and sliding between 3D target surfaces and a deformable surface defined by this element. This element is applicable to 3D structural analysis and located on the surface of 3D solid elements (SOLID65 and SOLID185 in this study). Contact occurs when this element penetrates the Target elements on a specified target surface (ANSYS, 2010c). In addition to Coulomb friction model (also known as shear stress model), user defined friction model can be used with this element.

Different behaviours of the contact surface can be selected using Key Option (12). These behaviours are: Standard, Rough, No separation (sliding permitted), Bonded, No separation (always), Bonded (always) and Bonded (initial contact).

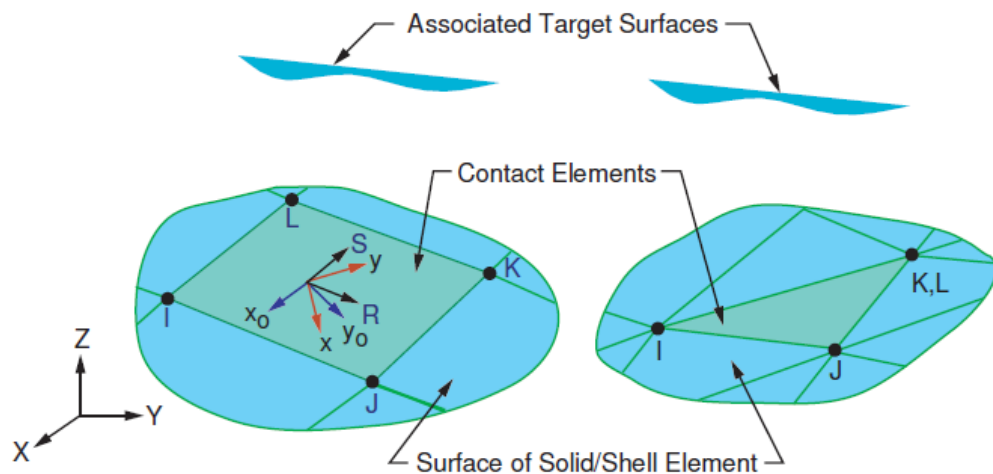


Figure 6.4 CONTA173 Geometry ((ANSYS, 2010c)

TARGE170 is used to represent 3D target surfaces for the associated contact element (CONTA173 in this model). While the Contact elements overlay the Solid elements describing the boundary of deformable body and, in most cases, in contact with the target surface, the Target surface

is modelled by set of target segment. The Target surface is paired with its associated Contact surface via a shared Real Constant set (ANSYS, 2010c). Each contact surface can be associated with only one target surface to form a pair of contact element, but several pairs of contact element could use the same target/contact surface.

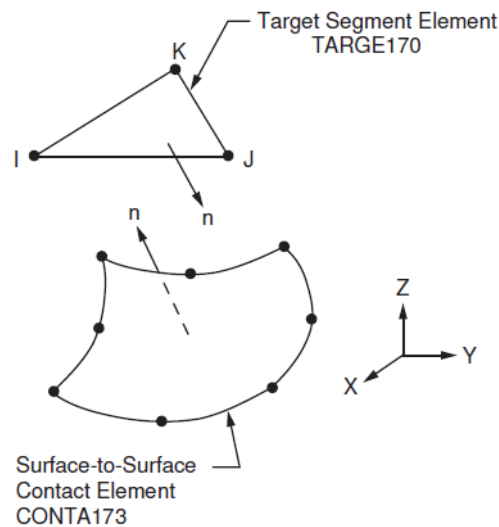


Figure 6.5 TARGE170 Geometry (ANSYS, 2010c)

Due to the complex nature of force transfer between Bolt to Concrete in-fill and Concrete in-fill and SHS, four different contact behaviours were defined:

- Between *SHS* and *Concrete in-fill* (Bonded initially)
- Between *Bolt sleeves (front)* and *Concrete in-fill* (Bonded always)
- Between *Bolt sleeves (sides)* and *Concrete in-fill* (No separation but sliding)
- Between *back of Bolt* and *Concrete in-fill* (Standard)

Four different pairs of contact surfaces (CONTA173 and TARGE170) were used to model these contact behaviours. Each pair shares different real constant set.

Details on how the Real Constants and Key Options (KEYOPTs) have been configured for each contact surfaces pair can be found in the APDL script.

6.2.2 Concrete Failure Criteria in ANSYS

The failure criteria of Concrete in ANSYS is based on Willam and Wranke failure criteria (ANSYS, 2010a). It account for cracking as well as crushing failure modes. Failure due to multi-axial stress state in this criterion as described in Willam and Warnke (1975) can be expressed as:

$$\frac{F}{f_c} - S \geq 0 \quad (6-1)$$

where F in the above equation represents a function of the principal stress state (σ_{xp} , σ_{yp} , σ_{zp}). σ_{xp} , σ_{yp} and σ_{zp} are the principal stresses in the three principal directions. S represents the failure surface. This failure surface is expressed in terms of the following parameters:

- Principal stresses (σ_{xp} , σ_{yp} , σ_{zp})
- Ultimate uni-axial tensile strength (f_t)
- Ultimate uni-axial compressive strength (f_c)
- Ultimate bi-axial compressive strength (f_{cb})
- Ultimate compressive strength for state of bi-axial compression superimposed on hydrostatic stress state (f_1)
- Ultimate compressive strength for state of uni-axial compression superimposed on hydrostatic stress state (f_2)

The failure surface S can be defined by the Ultimate uni-axial tensile strength (f_t) and the Ultimate uni-axial compressive strength (f_c) only. In this case the other three parameters will be set to default values specified by Willam and Wranke (Willam and Warnke, 1975, ANSYS,

2010a). However, ANSYS documentation also notes that if a large hydrostatic stress is expected, using Willam and Wranke default values may incorrectly evaluate the strength of the concrete, and therefore recommends specifying all the parameters in such cases (ANSYS, 2010a).

The failure of concrete categorized into four domains. These domains are:

1. *Compression - Compression - Compression* ($0 \geq \sigma_1 \geq \sigma_2 \geq \sigma_3$)
2. *Tensile - Compression - Compression* ($\sigma_1 \geq 0 \geq \sigma_2 \geq \sigma_3$)
3. *Tensile - Tensile - Compression* ($\sigma_1 \geq \sigma_2 \geq 0 \geq \sigma_3$)
4. *Tensile - Tensile - Tensile* ($\sigma_1 \geq \sigma_2 \geq \sigma_3 \geq 0$)

Where:

$$\sigma_1 = \max(\sigma_{xp}, \sigma_{yp}, \sigma_{zp}) \quad (6-2)$$

$$\sigma_3 = \min(\sigma_{xp}, \sigma_{yp}, \sigma_{zp}) \quad (6-3)$$

Independent functions are used to describe F and the failure surface S in each domain and are described in ANSYS documentation (ANSYS, 2010a).

6.2.3 Material Models

The behaviour of a material in a finite element model is governed by its material model. ANSYS uses Young's modulus and Poisson's ratio to define the materials linear behaviour. If a non-linear behaviour of a material is desired in ANSYS finite element model, a stress-strain relationship has to be defined. Many ways are available to define such relationships in ANSYS. This section describes how the material behaviour was defined in this finite element model.

Square Hollow Sections

The linear material properties of were obtained by conducting a series of coupon tensile tests. The coupons were cut from Square Hollow Sections and were tested during the course of this research (details can be found in section 4.7.1 of this thesis).

The non-linear behaviour of Square Hollow Sections was modelled in the model by defining stress-strain relationship. The relationship was obtained from the coupon tests performed in the course of this study and from former investigations where Square Hollow Sections from the same patch were tested (Abd Rahman, 2012, Al-Mughairi, 2010).

The true stress-strain relationship of the Square Hollow Section has to be defined in ANSYS. The true stress-strain relationship was calculated from the Engineering stress-strain relationship using the following equations:

$$\sigma_t = \sigma_{en}(1 + \varepsilon_{en}) \quad (6-4)$$

$$\varepsilon_t = \ln(1 + \varepsilon_{en}) \quad (6-5)$$

The non-linear true stress-strain relationship was inputted into ANSYS code using multi-linear kinematic hardening command KINH. This command is used to model metal plasticity behaviour.

The Square Hollow Sections assumed to have a Young's modulus of 200kN/mm², which can be altered according to the non-linear true stress-strain relationship to avoid warnings, and a Poisson's ratio of 0.3. The code also uses IF routine to enable users to select the desired Square Hollow Section material behaviour for each numerical experiment.

Dummy Bolts

The bolts in this study are assumed to be very strong as explained in section 4.7.2 of this thesis. This has been demonstrated in the finite element model by using a strong material that has a Young's modulus of 390kN/mm^2 , and a Poisson's ratio of 0.3, as the bolt material.

Concrete in-fill

Many ways to estimate Young's modulus of concrete are available in literature. Traditionally, equation suggested by Hughes (1976) was used to calculate Young's modulus (Equation 2.1.2 in page 49 of the text book). The withdrawn British Standard code of practice BS 8110 used another equation to calculate Young's modulus described in Figure 2.1 of BSI (1997). The current Eurocode 2 for concrete has different representation of Young's modulus. Although all these methods can be used in this model, and due to the current status of the Eurocode 2, it was decided to utilise the Eurocode 2 equation shown below:

$$E_{cm} = 22000 \left(\frac{f_{cm}}{10} \right)^{0.3} \quad (6-6)$$

The above equation is extracted from Table 3.1 of Eurocode 2 (CEN, 2004), and it is a function of mean value of concrete cylinder compressive strength (f_{cm}). According to Eurocode 2, f_{cm} can be directly estimated from the characteristic compressive cylinder strength of concrete (f_{ck}) as shown in the following equation:

$$f_{cm} = f_{ck} + 8 \quad (6-7)$$

As the non-linear behaviour of concrete was desired in this model, the stress-strain relationship was obtained using re-arranged version of

Equation 3.14 of Eurocode 2 (CEN, 2004), which predicts concrete stress-strain relationship for non-linear structural analysis:

$$\sigma_c = \frac{k\eta - \eta^2}{1 + (k - 2)\eta} (f_{cm}) \quad (6-8)$$

Where:

$$\eta = \frac{\varepsilon_c}{\varepsilon_{c1}} \quad (6-9)$$

$$\varepsilon_{c1} = 0.0007 (f_{cm})^{0.31} \leq 0.0028 \quad (6-10)$$

$$k = 1.05 E_{cm} \frac{|\varepsilon_{c1}|}{f_{cm}} \quad (6-11)$$

To avoid any finite element modelling difficulties and non-convergence issues, the stress is considered constant from the stage when it reaches its peak until the ultimate compressive strain is reached. Following Eurocode 2, the Ultimate compressive strain (ε_{cu1}) is assumed as shown in the following equation:

$$\varepsilon_{cu1} = \begin{cases} 0.0035, & f_{ck} \leq 50 \\ 0.0028 + 0.027 \left(\frac{98 - f_{cm}}{100} \right)^4, & f_{ck} > 50 \end{cases} \quad (6-12)$$

Equation 6-12 above was extracted and re-arranged from Table 3.1 of the Eurocode 2 (CEN, 2004).

The non-linear stress-strain relationship obtained from the above equations was inputted into ANSYS code using multi-linear elasticity command MELAS. This command uses set of lines starting from origin to represent the non-linear material behaviour. In this command, the slope

of the first line corresponds to Young's modulus of the material. The slope of the successive lines can be greater than the preceding lines but no slope can be greater than Young's modulus of the material (ANSYS, 2010c).

The code uses IF routine to enable users to choose the desired concrete model by selecting the concrete grade for each numerical experiment. Poisson's ratio of 0.2 was used for all concrete strengths in this model.

To compare the outcomes of this finite element model to the experiments outcomes, like-with-like concrete properties has to be considered. Only cube compressive strength of concrete was estimated in the experimental program (as described in section 4.7.3).

Initially, four mixes was considered: C20, C40, C50 and C80 which respectively denote concrete that have 20, 40, 50 and 80N/mm² cube compressive strength at the day of testing. Due to time constrains only C40 concrete were tested. The concrete non-linear behaviour described above is based on compressive cylinder strength of concrete (f_{ck}). Many methods are available in the literature to estimate the compressive cylinder strength of concrete from compressive cube strength and vice versa. Interpolation of the values given in Table 3.1 of Eurocode 2 was used in this study. The values adopted are shown in Table 6.1.

Table 6.1 Concrete mixes theoretical Cube and Cylinder compressive strength

Mix	Compressive Strength (N/mm ²)	
	Cube	Cylinder
C20	20	16
C40	40	31.875
C50	50	40
C80	80	65

The stress-strain relationships which are used in the APDL code for concrete grades C20, C40, C50 and C80 are plotted in Figure 6.6.

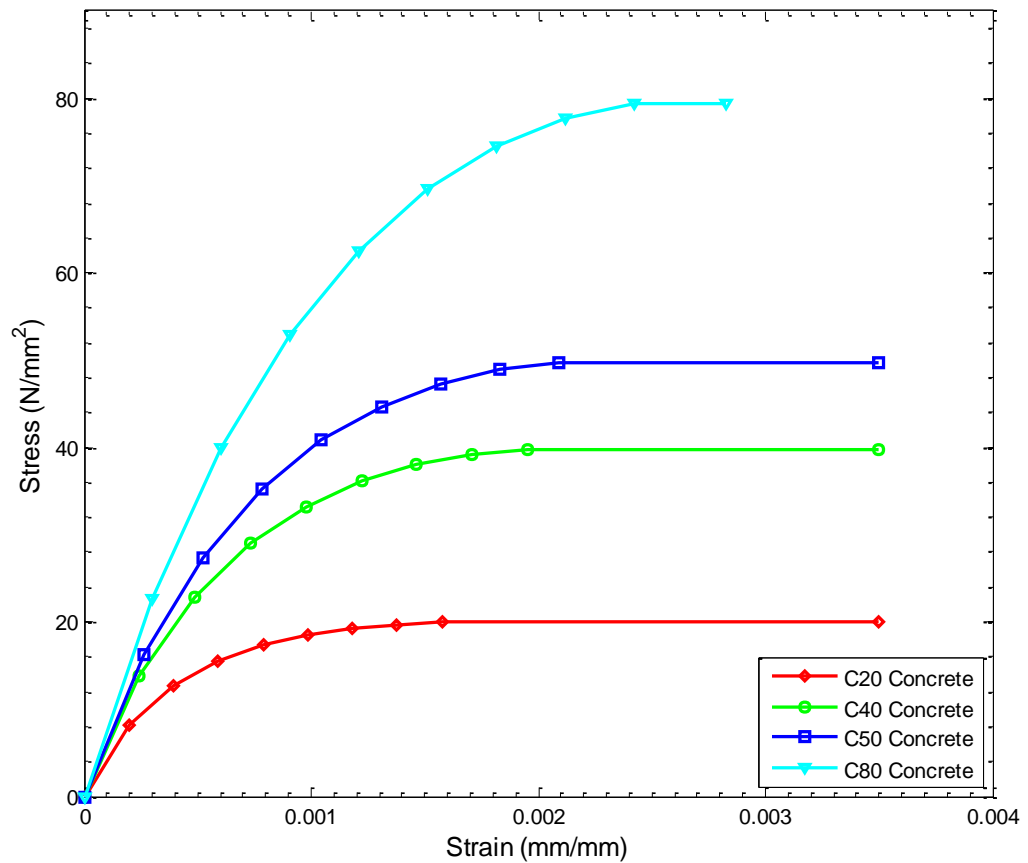


Figure 6.6 Stress-Strain relationship for different concrete grades

6.2.4 Boundary Conditions

Boundary conditions of the finite element model needed to be set so the model represents the experimental tests. The boundary condition which exists in experiments is the support in the load direction. This is due to the fact that the reaction frame restrained the samples from moving in the load direction. Furthermore, since each sample in the experimental program was sat on the raiser plates on the lab strong floor, it was restrained from moving in the direction off the strong floor plane. This restraint is also a boundary condition. These boundary conditions were resembled in the finite element model by restraining the translation in all directions of part of the Square Hollow Section front face ($U_x = U_y = U_z = 0$).

In the experiments, the reaction frame was in contact with Square Hollow Section sample at two areas: in the top and bottom of the front face of sample. The restrained areas in the finite element model are equal to these areas (shown in Figure 6.7 below).

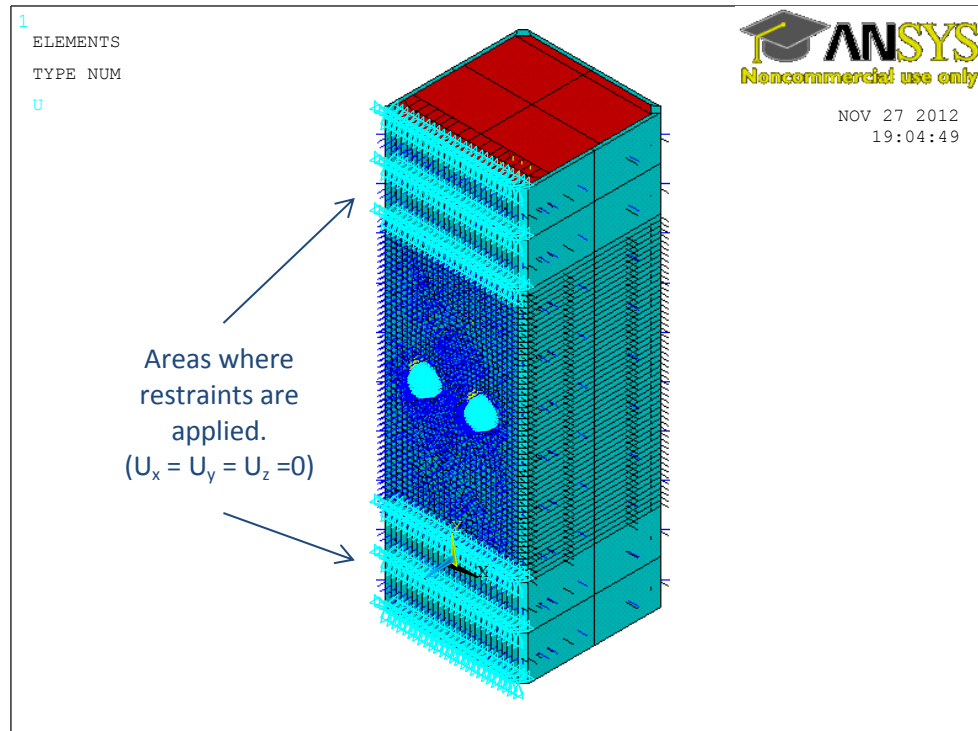


Figure 6.7 Finite element model Boundary Conditions

The restraints were applied in ANSYS model using DA command. This command defines degrees of freedom of pre-selected areas.

6.2.5 Loading and Solution

The load in the finite element model was applied as displacement on both bolts. The displacement was applied in the direction out of the Square Hollow Section (shown in Figure 6.8; Z direction in the model).

The displacement was applied this way to represent the load application process in the experiments where the actuator was pulling the bolts from the Square Hollow Section.

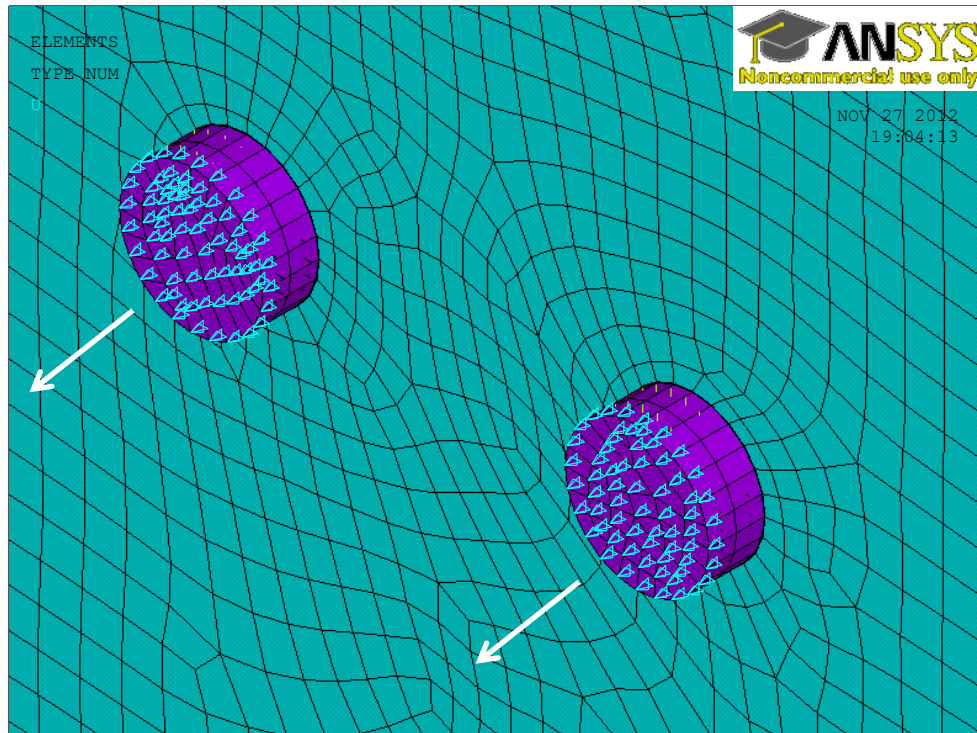


Figure 6.8 The direction of applied displacement in the finite element model

The Static solution option was selected in the finite element model. The load was applied in one load step which has many sub steps. The appropriate number of sub steps was decided automatically by ANSYS. Nevertheless, the maximum number of sub steps was limited in the model to insure that it will converge in a practical timeframe (using the command NSUBST).

6.2.6 Model Mesh

The mesh adopted for the dummy bolts is shown in Figure 6.9. Automatic (Smart) meshing was used to mesh the dummy bolts.

In the case of SHS and concrete in-fill, the mesh was done by deciding the number of divisions in lines. More divisions were decided in the front/face of the SHS and concrete in-fill, hence finer mesh. The appropriate lines' number of divisions was determined using mesh sensitivity analysis.

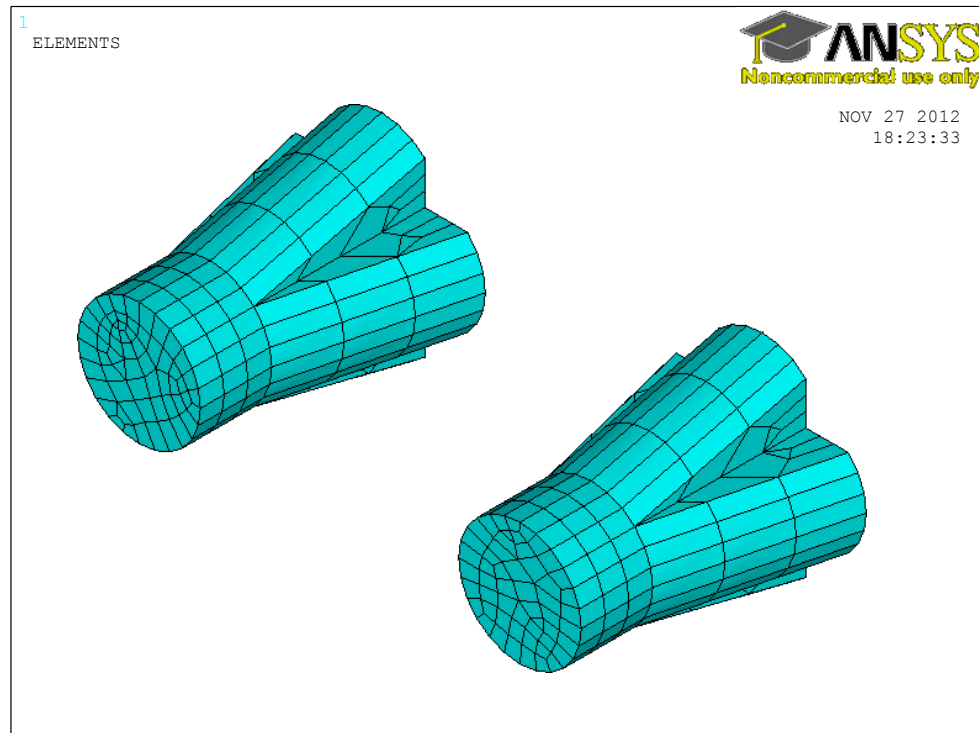


Figure 6.9 **Meshed dummy bolts**

In the mesh sensitivity analysis, the lines' number of divisions was increased leading to a finer mesh each time while investigating the effect of the increase on the outcomes of the model. This is done to achieve the best possible outcomes from the model with the minimum time and computational cost.

Figure 6.10 shows the outcome of the sensitivity analysis for SHS 200x200x5 with a bolt gauge of 80mm. It also highlights the mesh adopted in the reminder of this work. Details about the adopted mesh can be found in the APDL script.

The mesh adopted for the SHS and concrete in-fill is shown in Figure 6.11.

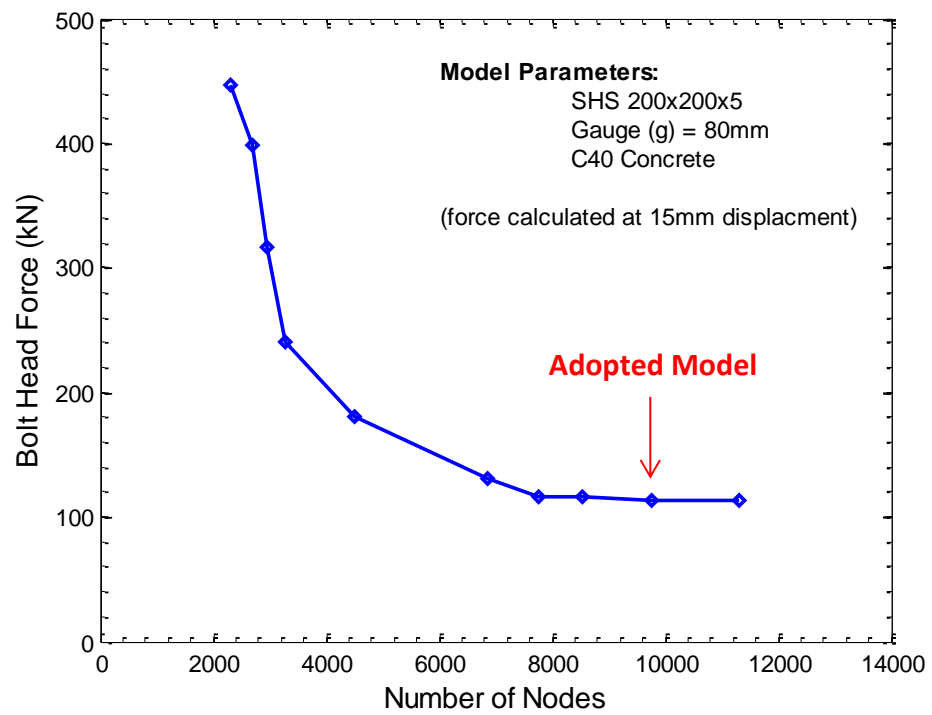


Figure 6.10 Mesh sensitivity analysis

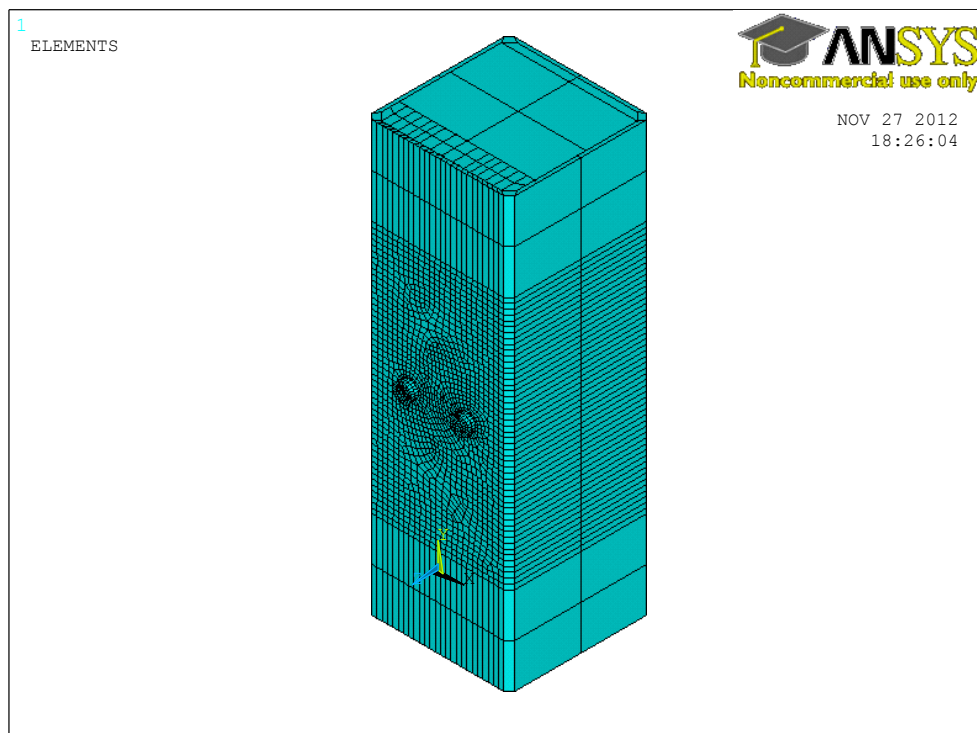


Figure 6.11 The finite element model fully meshed

6.2.7 Model Illustration

Illustration of the 3D finite element model components is shown in this section. Figure 6.12 shows how a typical SHS geometry is modelled. SHS dimensions, including external and internal corner radii, are calculated following BS EN 10210-2:2006 (BSI, 2006).

Illustration of the dummy bolts is shown in Figure 6.13 while Illustration of the concrete-infill is shown in Figure 6.14.

Illustration of the four different contact surfaces used in the model is shown in: Figure 6.15 which shows the contact surfaces between SHS and concrete-infill, Figure 6.16 which shows the contact surfaces between bolt sleeves and concrete-infill, Figure 6.17 which shows the contact surfaces between bolt sleeves and concrete-infill and Figure 6.18 which shows the contact surfaces between bolt sides and concrete-infill.

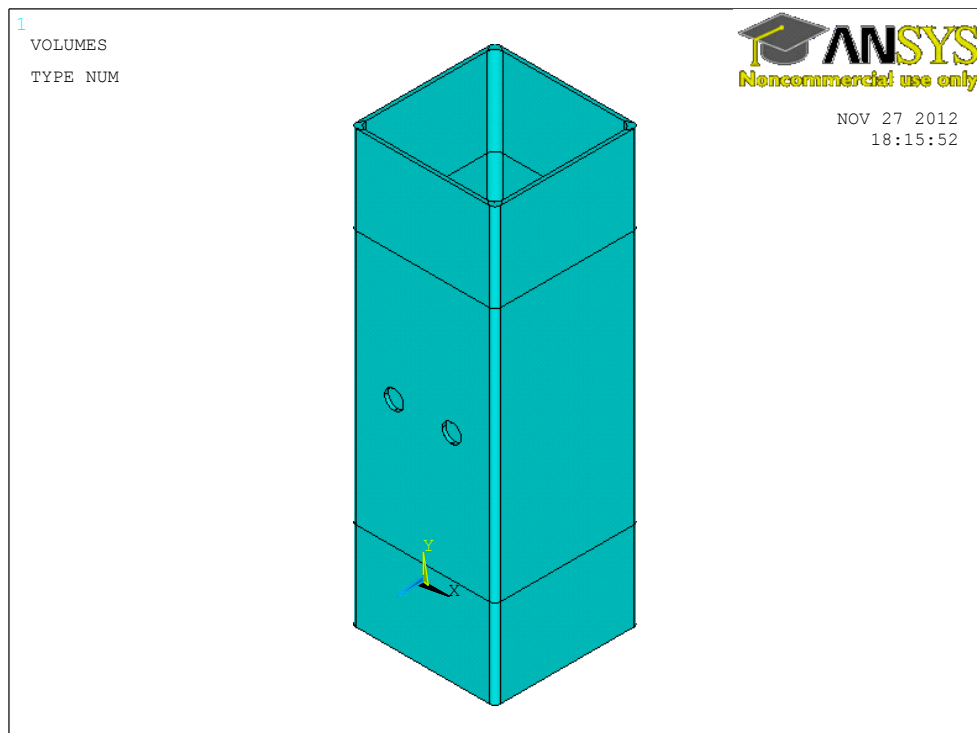


Figure 6.12 Typical SHS in the finite element model

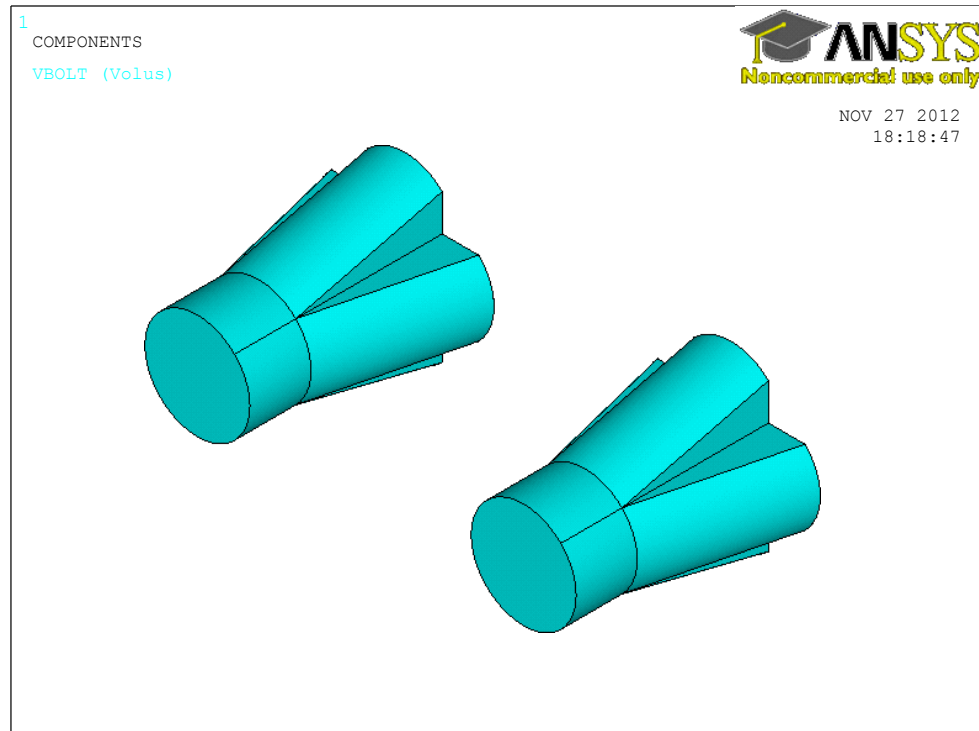


Figure 6.13 Typical Dummy Bolts in the finite element model

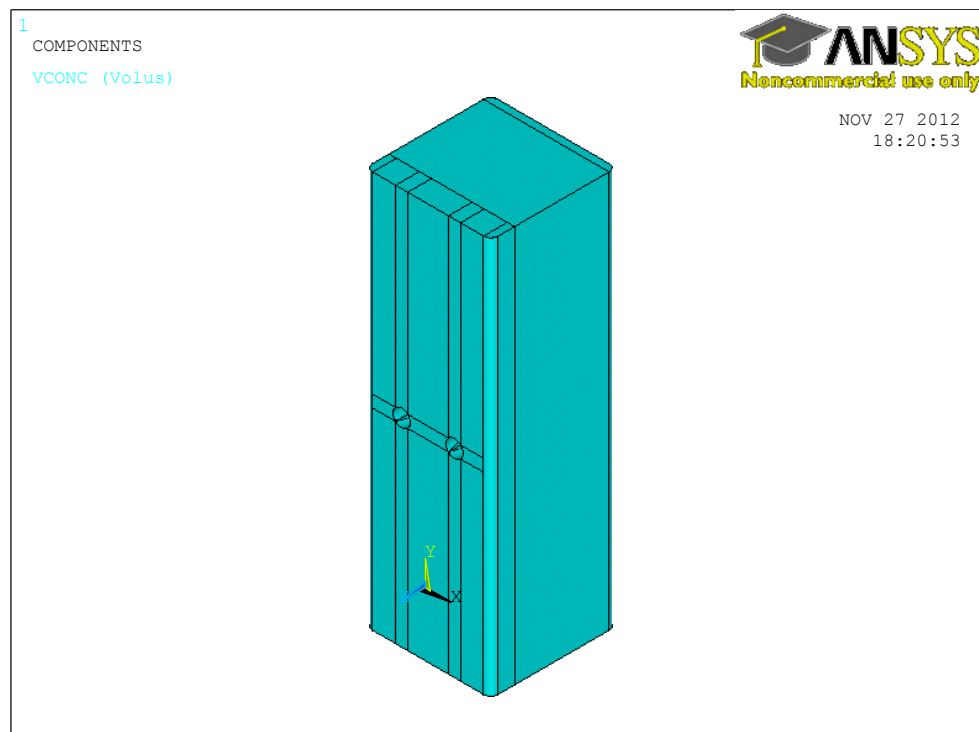


Figure 6.14 Typical concrete-infill in the finite element model

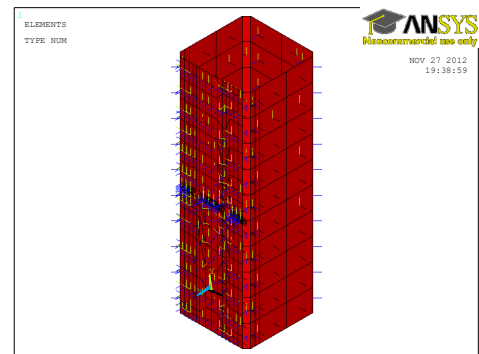
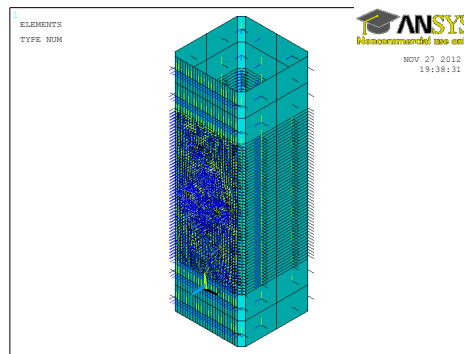


Figure 6.15 Contact surfaces between SHS and concrete-infill

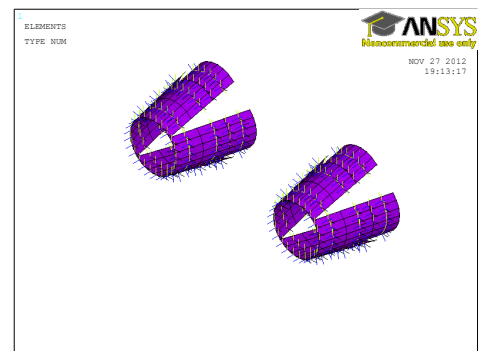
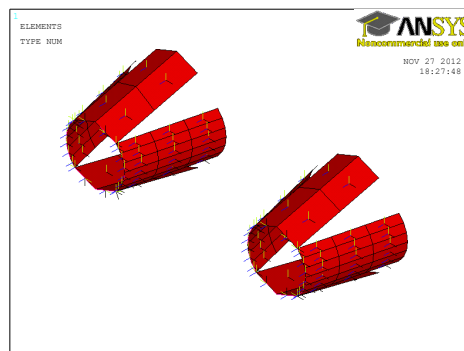


Figure 6.16 Contact surfaces between bolt sleeves and concrete-infill

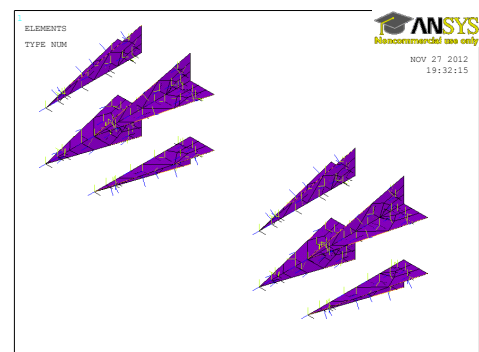
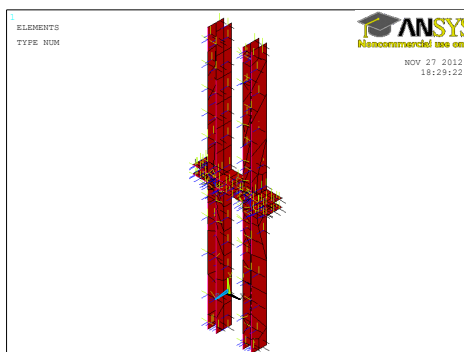


Figure 6.17 Contact surfaces between bolt sides and concrete-infill

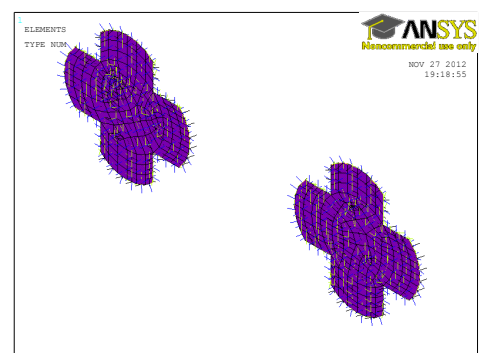
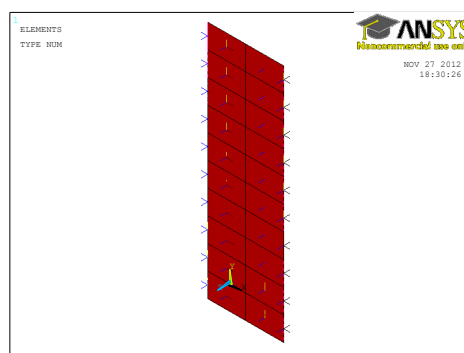


Figure 6.18 Contact surfaces between back of bolts and concrete-infill

6.3 General Behaviour of the Finite Element Model

6.3.1 SHS Face Bending

Typical SHS face bending behaviour captured using the finite element model is shown in Figure 6.19. This behaviour was found to resemble the SHS face bending behaviour observed experimentally as expected.

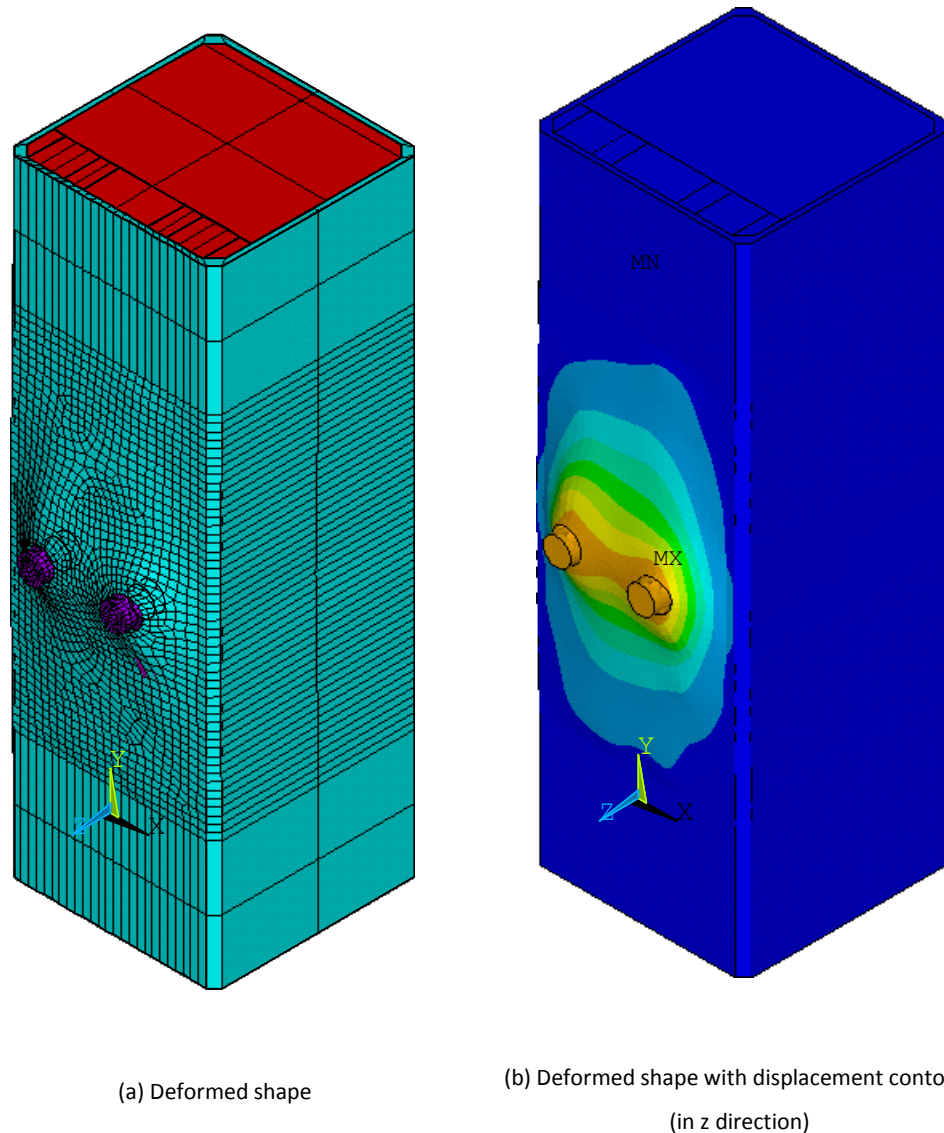
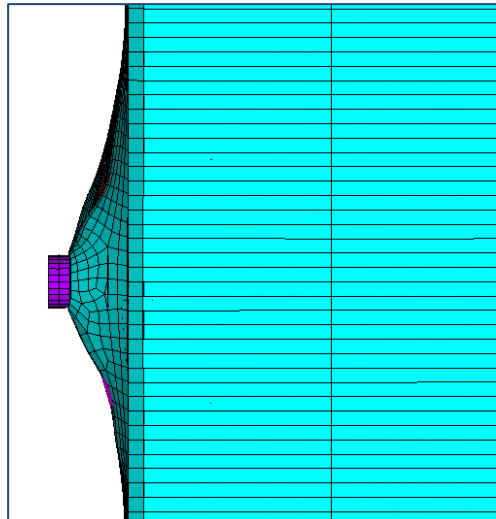


Figure 6.19 Typical SHS face bending

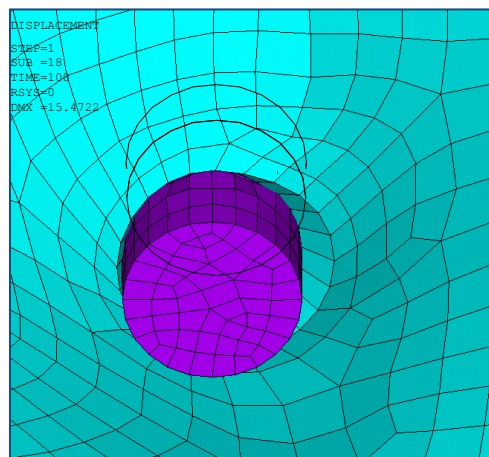
Cross checks also demonstrated that deformations observed in the experiments were similar to the observed in the finite element model. Two examples of these checks are shown in Figure 6.20.



(a-1) Finite element model



(a-2) Experiment



(b-1) Finite element model



(b-2) Experiment

Figure 6.20 General behaviour cross-checks

6.3.2 Observations

It was observed that the bolt sleeves have direct effect on the SHS face bending as expected. The evidence of this observation is obvious when plotting the SHS plastic strain (von Mises) as shown in Figure 6.21, and stress (von Mises) as shown in Figure 6.22.

The variation in plotted contours in the locations of left and right bolts is important to consider in these figures as symmetry is expected. This variation is attributed to the non-symmetry of SHS face and bolts mesh.

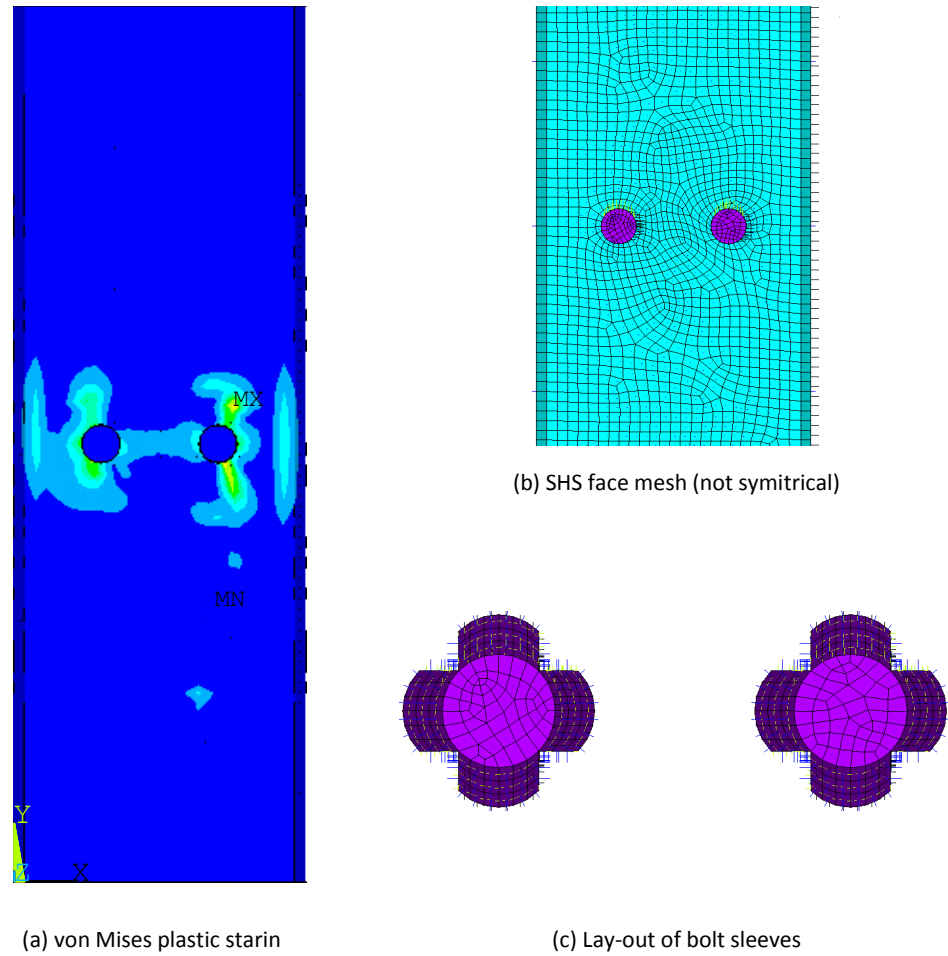


Figure 6.21 von Mises plastic strain of SHS face

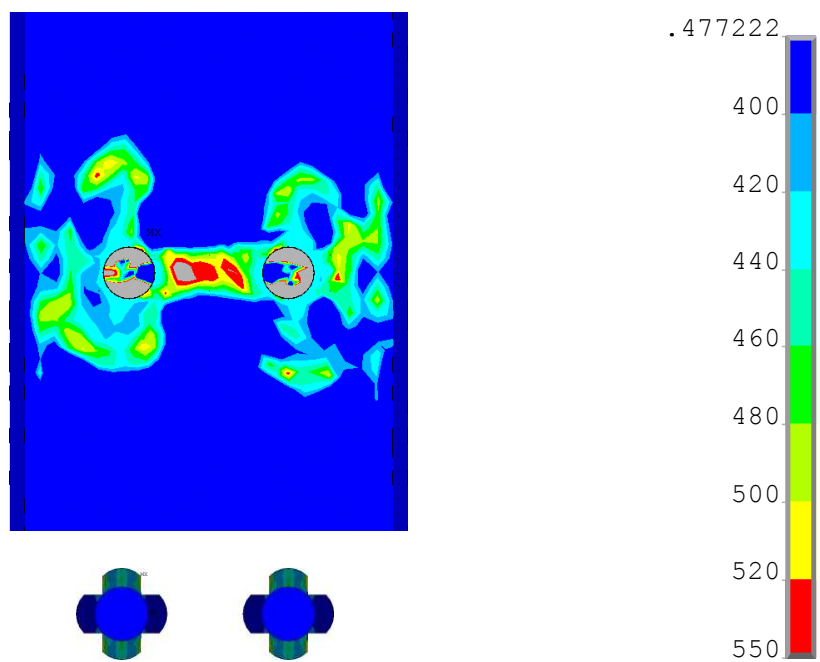


Figure 6.22 von Mises stresses of SHS face and Bolt sleeves

6.3.3 Strain Distribution on SHS Face

One of the advantages of finite element modelling is that it makes it possible to measure and investigate data that is very difficult or not possible to measure experimentally, data like the strain distribution on the SHS face. Figure 6.23 shows the development of strain on the SHS face in the finite element model.

The strain distribution on the SHS face can support the theory presented in Chapter 3 to calculate resistance in the analytical model. To investigate this, referring to the same chapter, the yield line pattern of Mechanism 3 was positioning on top of SHS face strain observed from the finite element analysis as shown in Figure 6.24. The figure shows that Mechanism 3 yield line pattern is in good match with the strain distribution from the finite element analysis.

As mentioned before, as symmetry is expected, the variation in plotted contours vector lines in the locations of left and right bolts is attributed to the un-symmetry of SHS face and bolts mesh.

6.4 Results and Validation (force-displacement curves)

The outcomes of the finite element model analysis are compared with the experimental results mainly in the form of force-displacement curves.

To calculate the force from the finite element model, the stresses on dummy bolt head are averaged, and then multiplied by the area of bolt head. Conversely, the displacement is defined from the average displacement of SHS nodes in a position similar to the position where the displacement was measured in the experimental programme. The locations where the force and displacement are calculated are illustrated in Figure 6.25.

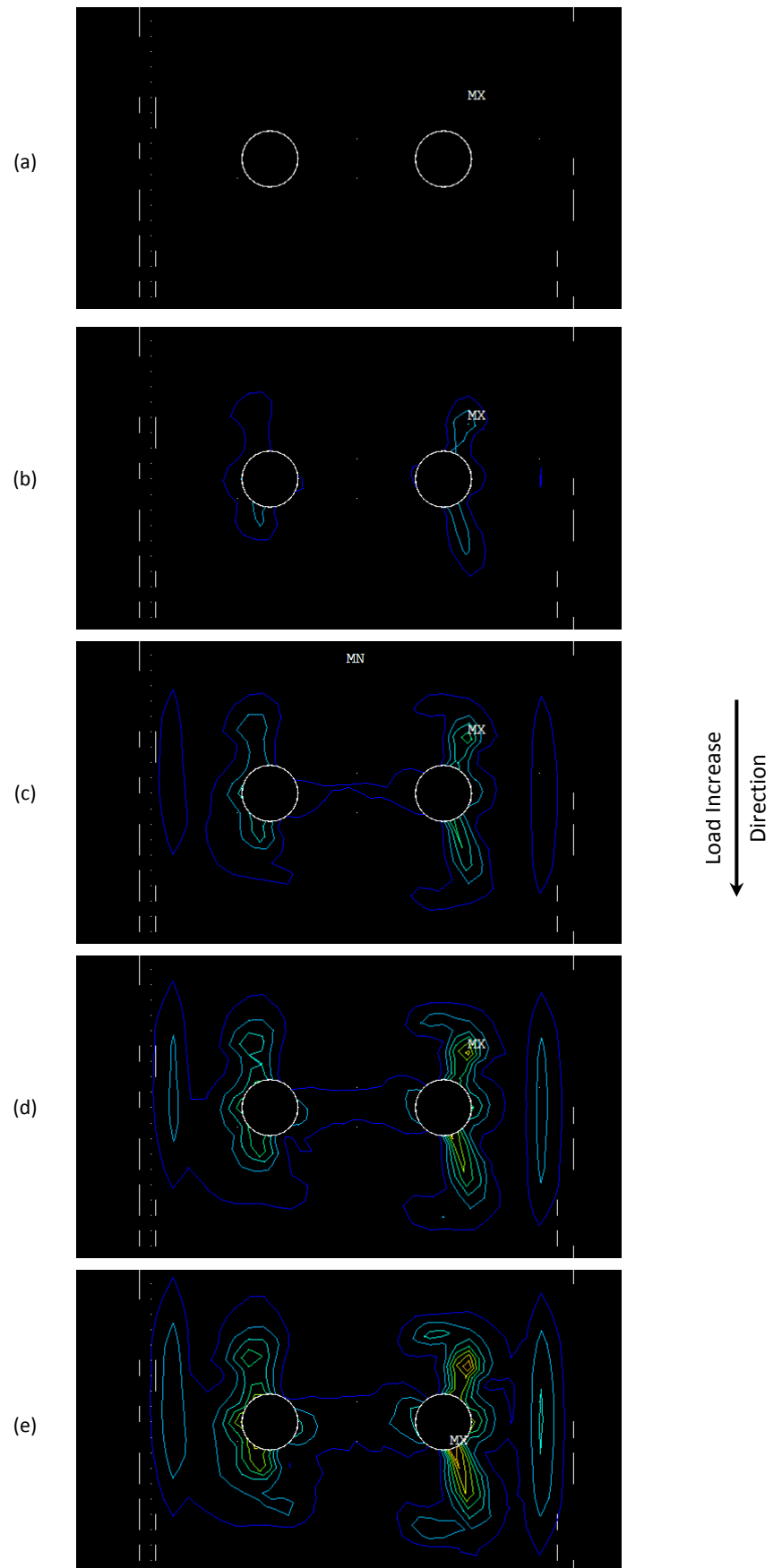


Figure 6.23 Strain development on SHS face

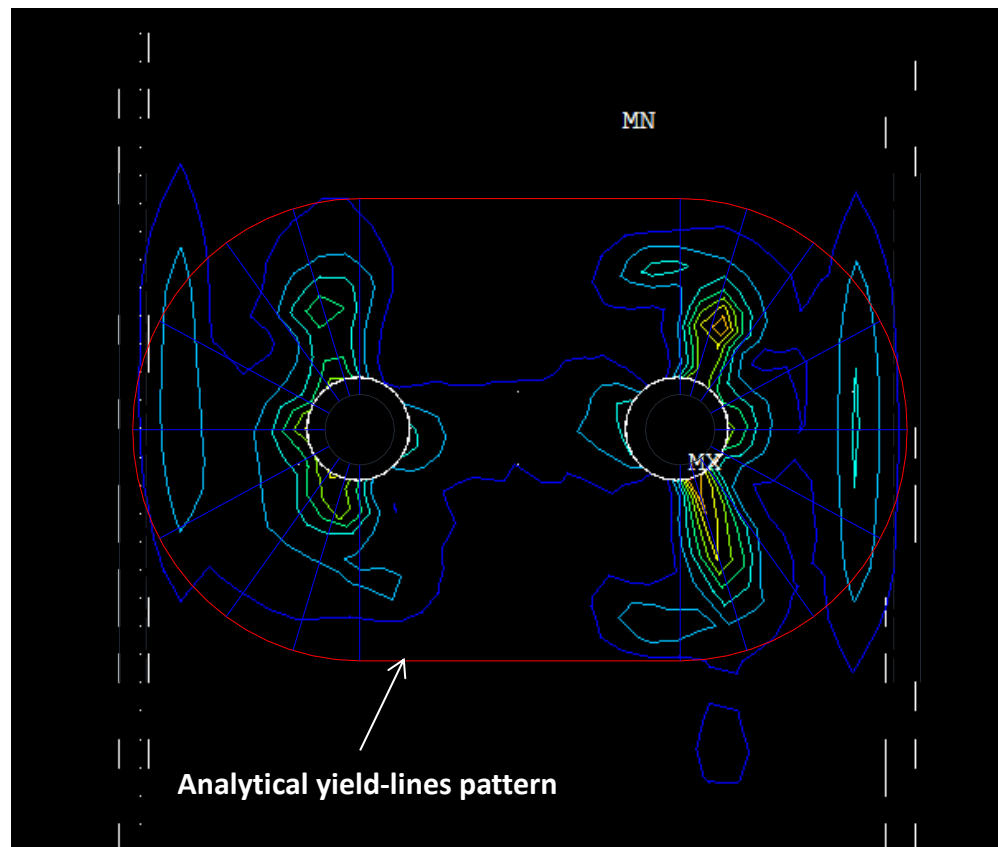


Figure 6.24 Analytical yield-lines pattern and Finite Element strains

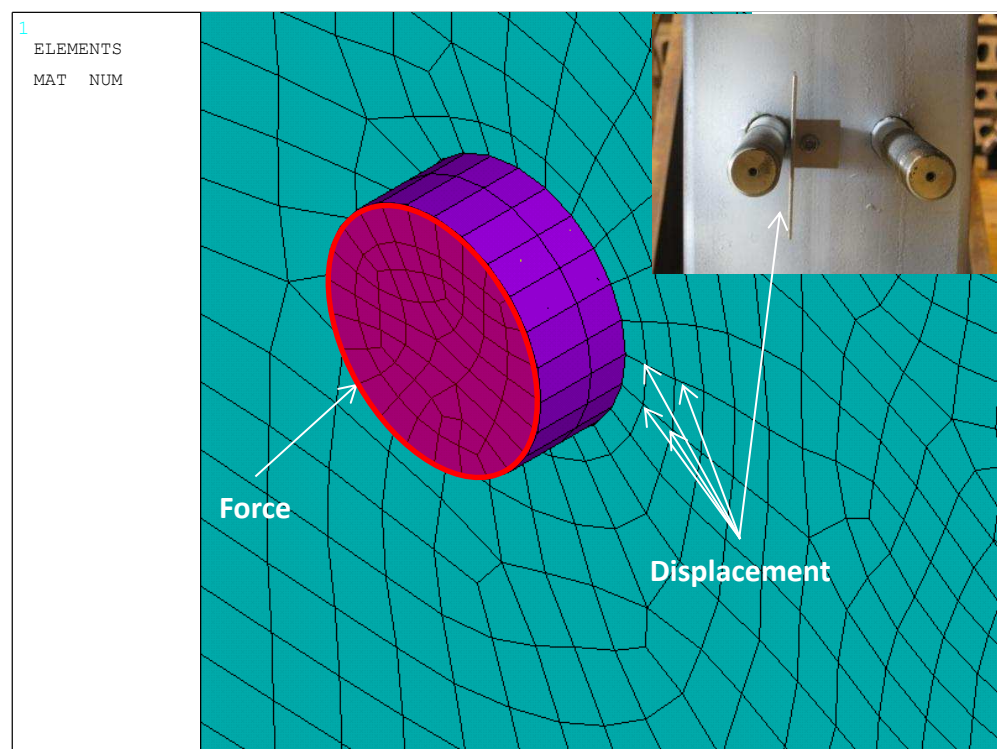


Figure 6.25 Positions where force and displacement are numerically calculated

This process is done through separate ANSYS APDL code due to a limitation in ANSYS post-processing capabilities which allows only for the stresses in three nodes to be added together in a single command. The data is then stored in the form of spread-sheets to be plotted and compared with experimental data using MATLAB powerful data-processing capabilities.

The force-displacement curves obtained from the finite element model are compared to their counterpart from the experimental programme. Figure 6.26 shows the force-displacement curves from finite element model and the experiments of b200t6.3g80C40 (i.e. SHS 200x200x6.3, bolt gauge of 80mm and concrete in-fill which have compressive cube strength of 40N/mm^2). Similarly, Figure 6.27 - Figure 6.30 show similar curves for b200t8g60C40, b200t8g80C40, b200t8g100C40 and b200t10g80C40 respectively. Error bands of $\pm 10\%$ from the finite element model's curves were also generated in these figures.

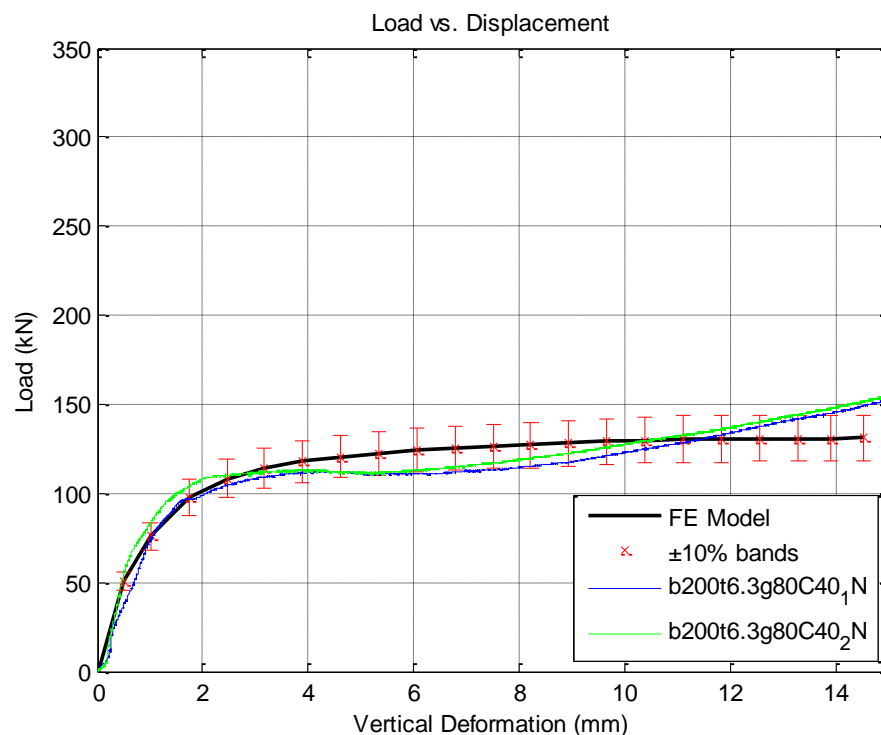
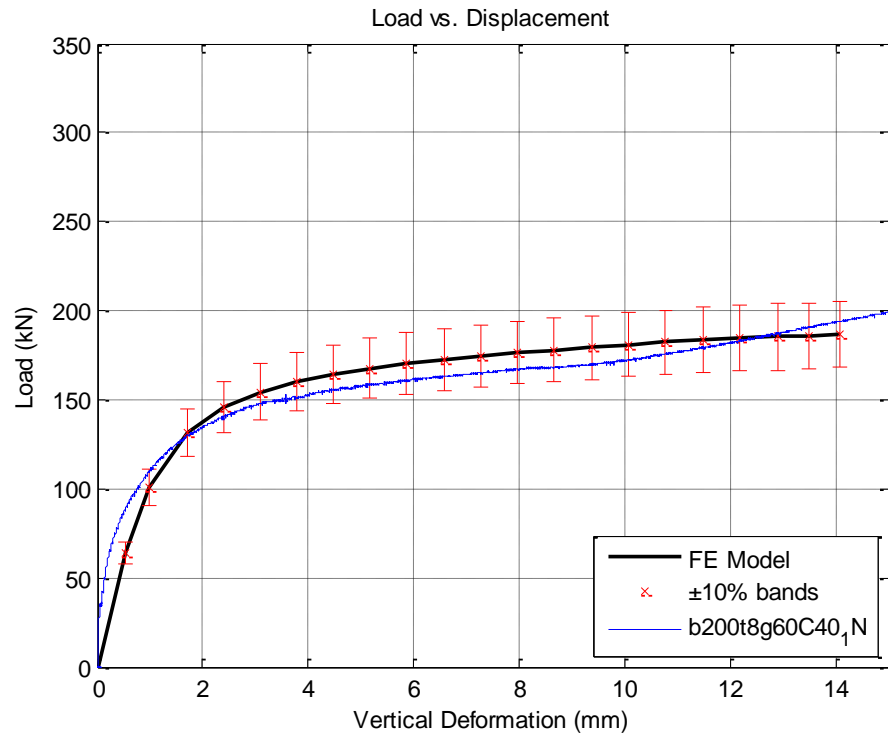
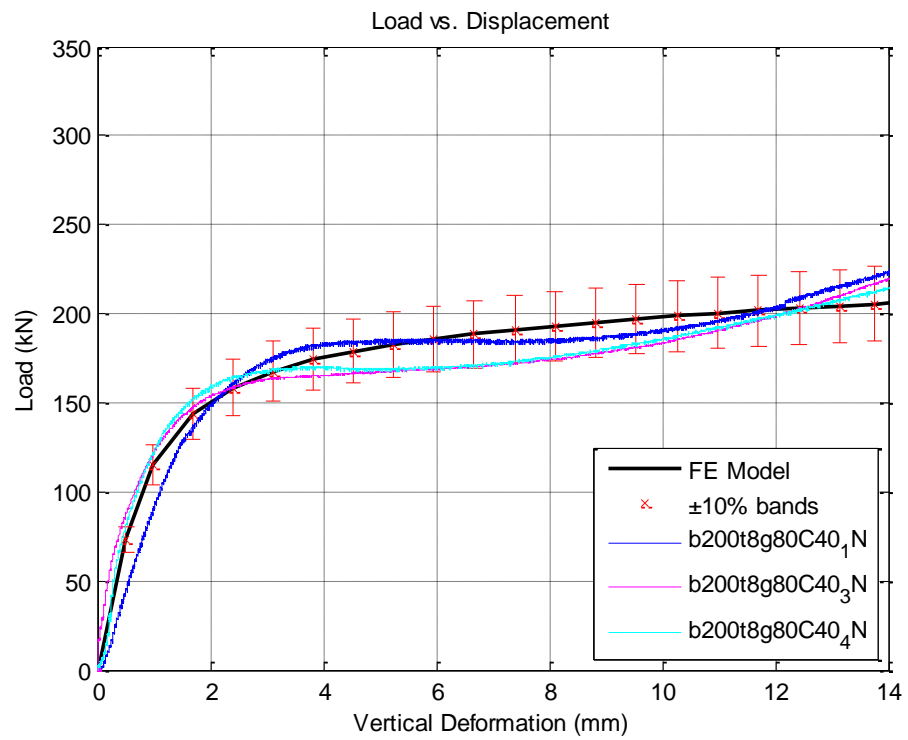


Figure 6.26 FE vs. Experiment of b200t6.3g80C40

**Figure 6.27** FE vs. Experiment of b200t8g60C40**Figure 6.28** FE vs. Experiment of b200t8g80C40

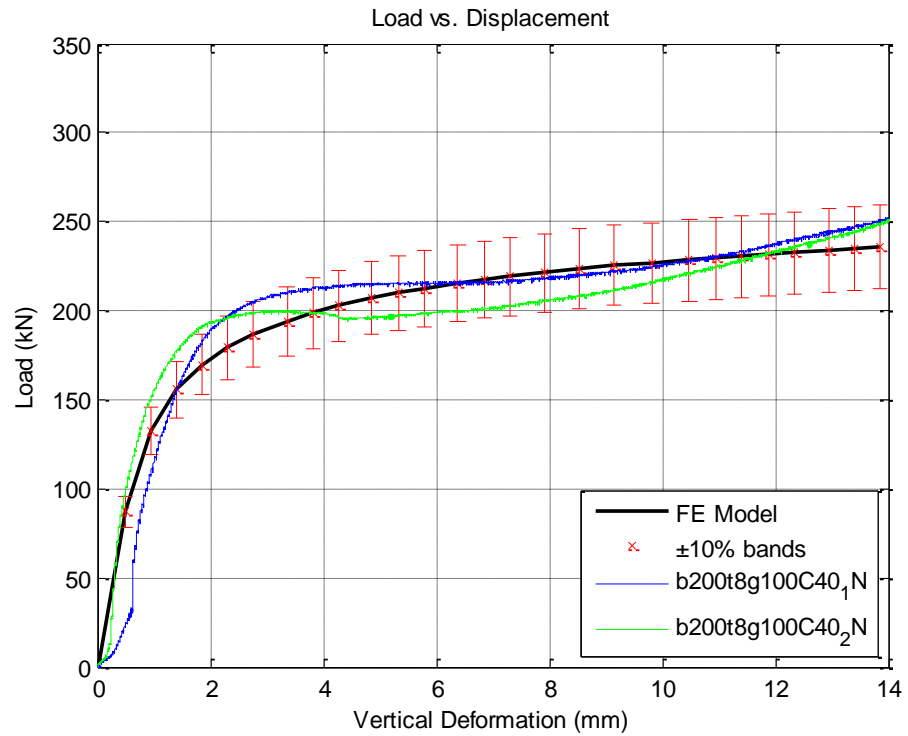


Figure 6.29 FE vs. Experiment of b200t8g100C40

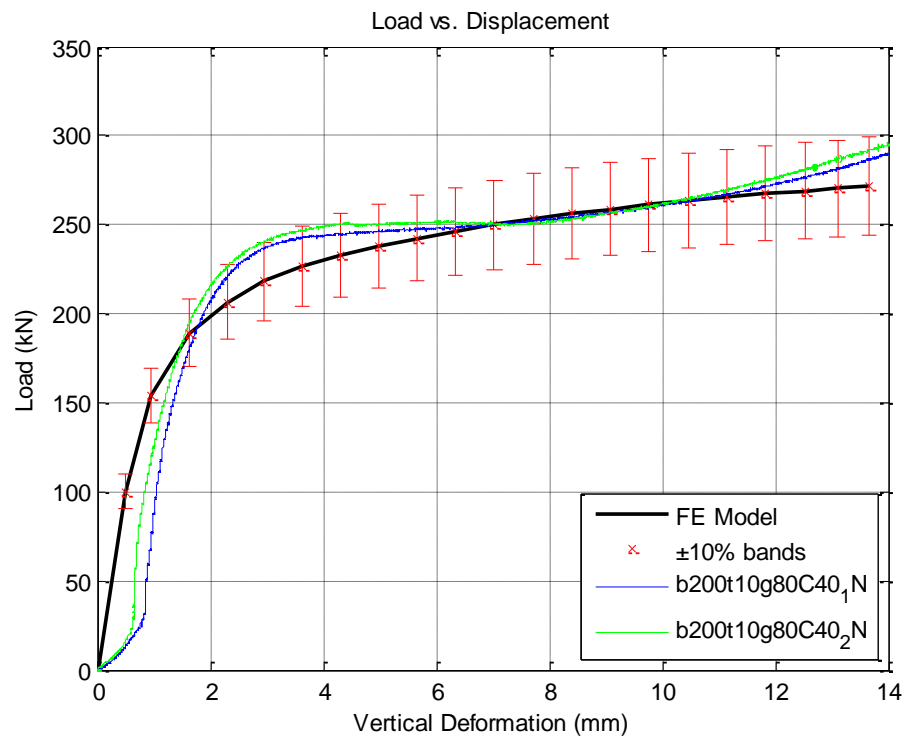


Figure 6.30 FE vs. Experiment of b200t10g80C40

It can be seen in the figures that the experimental force-displacement curves are in close agreement with the finite element model curves i.e. lay within $\pm 10\%$ of the finite element model curves.

A comparison of the initial stiffness and the yield force calculated from the finite element model for b200t8g80C40, b200t8g100C40 and b200t10g80C40 are shown in Table 6.2 below. In this table, the Initial stiffness was calculated from the initial linear part of the force-displacement curve of each experiment/FE test. In contrast, the yield force was assumed to be at the intersection between the lines which represent the Initial stiffness and the post-yield stiffness (tangent line in the case of post-yield stiffness).

Table 6.2 Comparison between FE and experimental outcomes

FE test ID	Initial Stiffness (kN/mm)			Yield Force (kN)		
	FE	Experiment (Average)	Error	FE	Experiment (Average)	Error
b200t8g80C40	142.61	157.15	-9.3%	176.20	150.18	+17.3%
b200t8g100C40	175.29	171.36	+2.3%	197.66	173.78	+13.7%
b200t10g80C40	200.15	178.07	+12.4%	229.10	198.77	+15.3%

6.5 Parameters Variation Analysis

A parametric variation analysis has been conducted to study the effect of varying parameters using the finite element model. SHS 200x200 were considered in this analysis. The SHS are assumed to be filled with concrete that have compressive cube strength of 40N/mm^2 . SHS thickness and bolt gauge were varied within the practical range described in section 4.2 of this thesis to cover all possible arrangement of SHS 200x200. The tests conducted for the parametric variation analysis are described in Table 6.3.

Table 6.3 Test Matrix for the finite element modelling

n.	Hollow Section	Width b (mm)	Thickness t (mm)	μ (b/t)	g (mm)	β (g/b)	Concrete grade	Finite Element Test ID	Experimental Test ID (if applicable)
1	SHS 200x200x5	200	5	40	60	0.3	C40	b200t5g60c40-FE	
2	SHS 200x200x5	200	5	40	80	0.4	C40	b200t5g80c40-FE	b200t5g80c40-1 and 2
3	SHS 200x200x5	200	5	40	100	0.5	C40	b200t5g100c40-FE	
4	SHS 200x200x6.3	200	6.3	31.75	60	0.3	C40	b200t6g60c40-FE	
5	SHS 200x200x6.3	200	6.3	31.75	80	0.4	C40	b200t6g80c40-FE	b200t6.3g80c40-1 and 2
6	SHS 200x200x6.3	200	6.3	31.75	100	0.5	C40	b200t6g100c40-FE	
7	SHS 200x200x8	200	8	25	60	0.3	C40	b200t8g60c40-FE	b200t8g60c40-1,2 and 3
8	SHS 200x200x8	200	8	25	80	0.4	C40	b200t8g80c40-FE	b200t8g80c40-1,2,3 and 4
9	SHS 200x200x8	200	8	25	100	0.5	C40	b200t8g100c40-FE	b200t8g100c40-1 and 2
10	SHS 200x200x10	200	10	20	60	0.3	C40	b200t10g60c40-FE	
11	SHS 200x200x10	200	10	20	80	0.4	C40	b200t10g80c40-FE	b200t10g80c40-1 and 2
12	SHS 200x200x10	200	10	20	100	0.5	C40	b200t10g100c40-FE	
13	SHS 200x200x12.5	200	12.5	16	60	0.3	C40	b200t12g60c40-FE	
14	SHS 200x200x12.5	200	12.5	16	80	0.4	C40	b200t12g80c40-FE	
15	SHS 200x200x12.5	200	12.5	16	100	0.5	C40	b200t12g100c40-FE	
16	SHS 200x200x16	200	16	12.5	60	0.3	C40	b200t16g60c40-FE	
17	SHS 200x200x16	200	16	12.5	80	0.4	C40	b200t16g80c40-FE	
18	SHS 200x200x16	200	16	12.5	100	0.5	C40	b200t16g100c40-FE	

6.5.1 The effect of SHS slenderness

To study the effect of the slenderness ratio on the face bending behaviour of concrete filled SHS all the other parameters were fixed for all SHS 200x200 sections. These parameters are the SHS behaviour, concrete-infill behaviour and bolts geometrical arrangement. The SHS thickness was varied between 12.5 and 40 for three different groups: $\beta = 0.3$ where $g = 60\text{mm}$, $\beta = 0.4$ where $g = 80\text{mm}$ and $\beta = 0.5$ where $g = 100\text{mm}$. The outcomes of the finite element model for each of these groups are shown in Figure 6.31, Figure 6.32 and Figure 6.33.

Overall, the SHS face bending behaviour was as expected. Initial stiffness and yield force were increased with the reduction of the slenderness ratio across the considered bolt gauge range i.e. increase of SHS thickness. Both the initial stiffness and the yield force of each test were determined using the approach described in section 6.4. The ratio between post-yield stiffness and initial stiffness varied between: 0.8% to 1.6% for $\beta = 0.3$, 0.9% to 2% for $\beta = 0.4$ and 1.5% to 2.5% for $\beta = 0.5$.

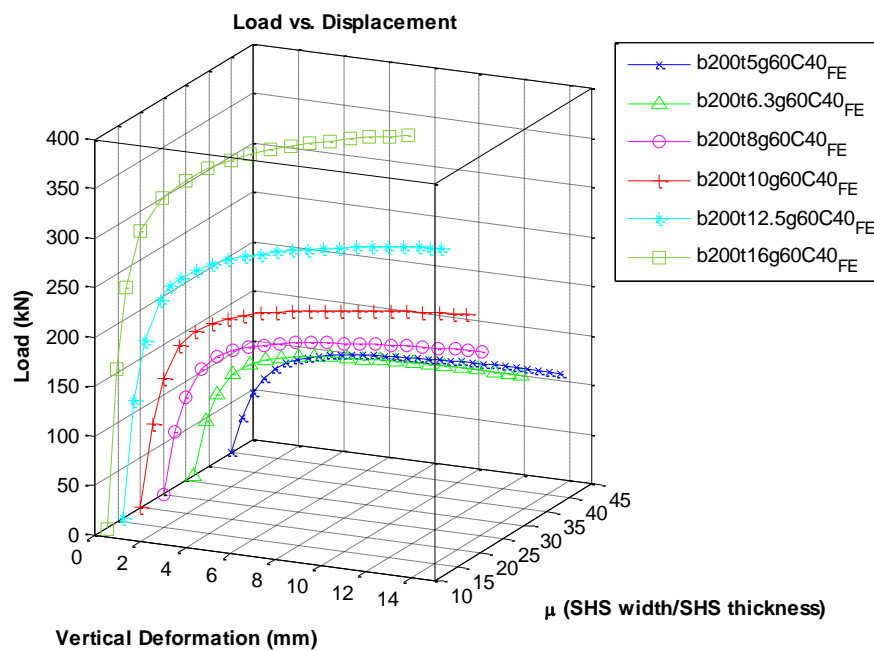


Figure 6.31 The face bending of concrete-filled SHS 200x200 when $\beta = 0.3$ (compiled using FE results)

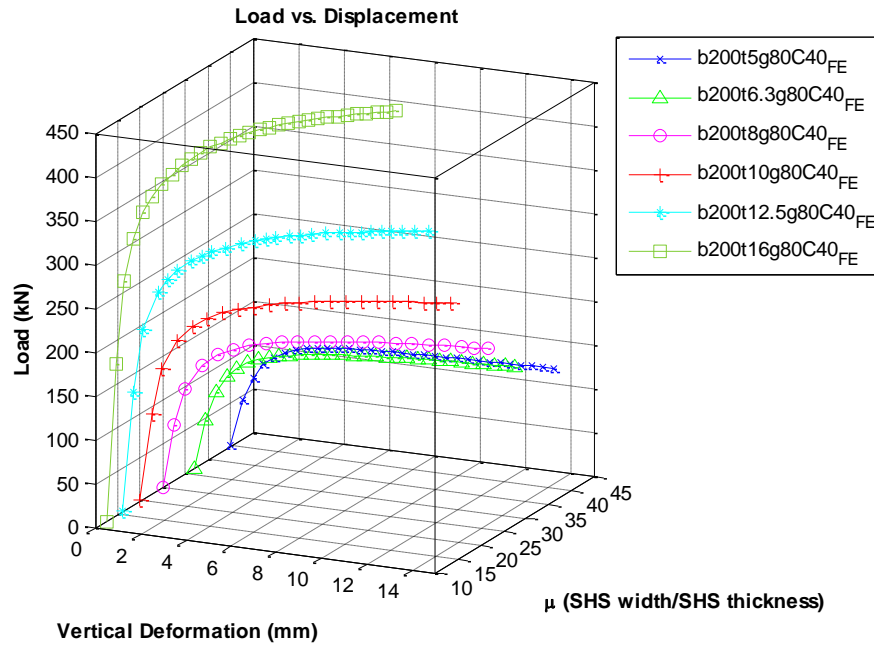


Figure 6.32 The face bending of concrete-filled SHS 200x200 when $\beta = 0.4$ (compiled using FE results)

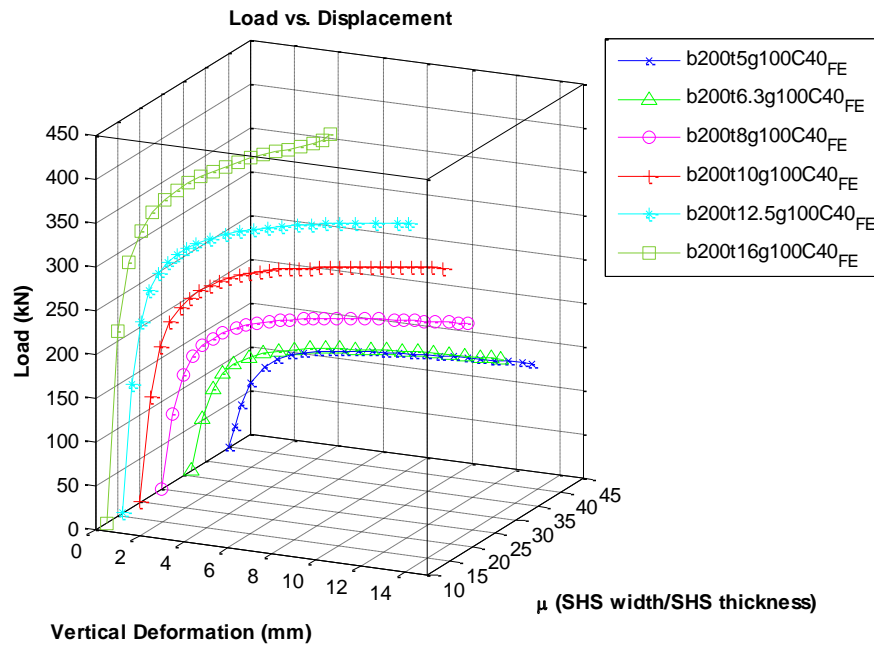


Figure 6.33 The face bending of concrete-filled SHS 200x200 when $\beta = 0.5$ (compiled using FE results)

6.5.2 The effect of bolt gauge

In turn, to study the effect of the bolt gauge on the face bending behaviour of concrete filled SHS all the other parameters were fixed for all SHS 200x200 sections. These parameters are the SHS material behaviour, concrete-infill behaviour and SHS thickness.

Three different values of bolts gauge were numerically modelled for each SHS 200x200 thickness namely $t = 5\text{mm}$, 6.3mm , 8mm , 10mm , 12.5mm and 16mm . The outcomes of the finite element model for each of the corresponded slenderness ratios are shown in Figure 6.34 - Figure 6.39.

Similar to what was observed from the finite element results when the SHS slenderness ratio was varied, the SHS face bending behaviour was as expected when varying the bolt gauge. Initial stiffness and yield force were increased with the increase of the bolt gauge. This was the case across the entire SHS slenderness ratio range considered except for $\mu = 12.5$ (as shown in Figure 6.34) and $\mu = 40$ (as shown in Figure 6.39). In these two ratios, higher initial stiffness and yield force were observed for the bolt gauge 80 (i.e. $\beta = 0.4$). This can be attributed to the fact that these ratios represent the ends of the range considered where it is possible to have mixed yielding behaviour/mechanism as was observed in theoretical observation noted in Chapter 3.

Once again, both the initial stiffness and the yield force of each test were determined using the same approach described in section 6.4.

The ratio between post-yield stiffness and initial stiffness varied between: 1.5% to 2.5% for $\mu = 12.5$, 1.5% to 1.8% for $\mu = 16$, 1.6% to 1.8% for $\mu = 20$, 1.6% to 1.8% for $\mu = 25$, 0.8% to 1.7% for $\mu = 31.75$ and 0.9% to 2.1% for $\mu = 40$.

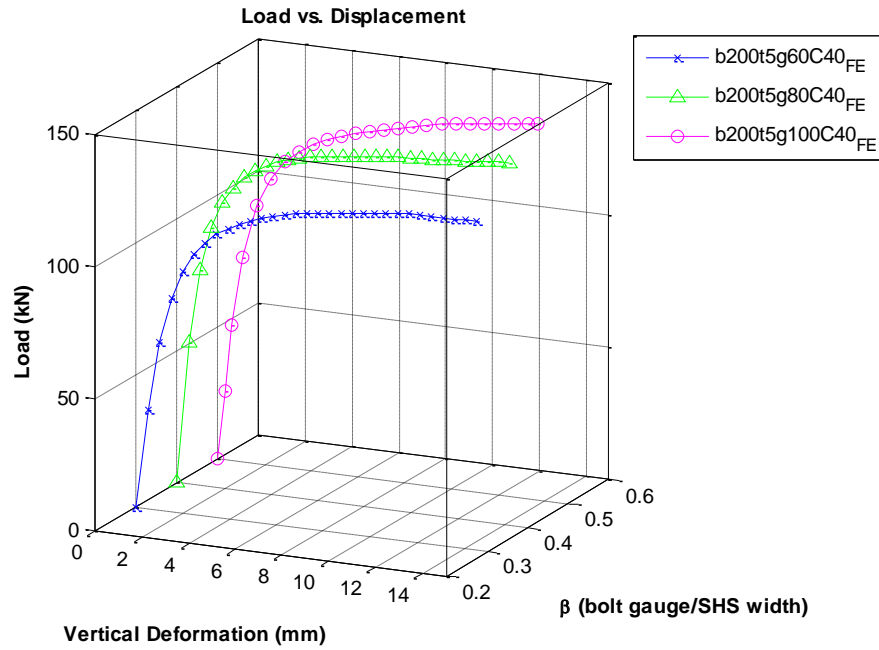


Figure 6.34 The face bending of concrete-filled SHS 200x200 when $\mu = 40$ (compiled using FE results)

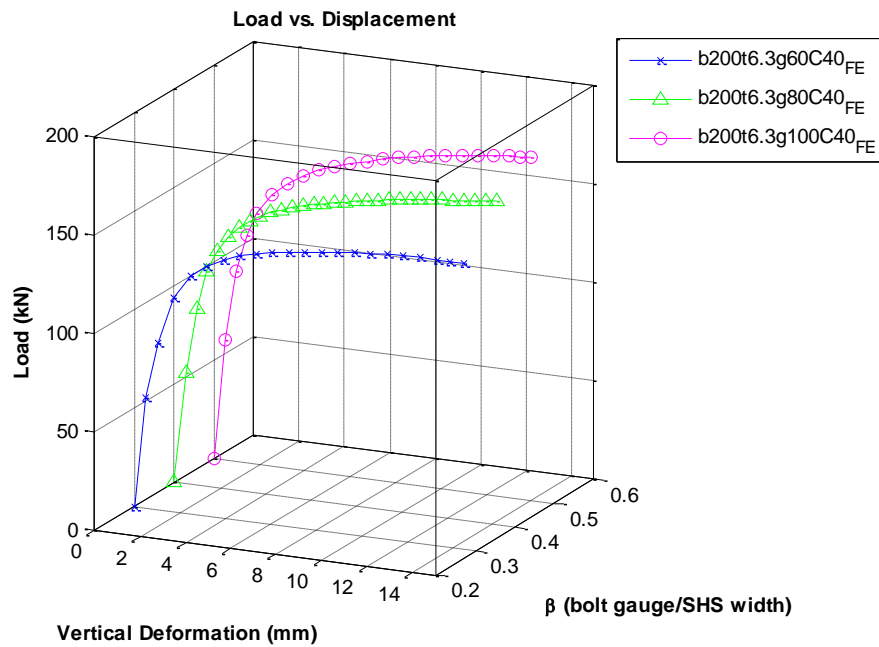


Figure 6.35 The face bending of concrete-filled SHS 200x200 when $\mu = 31.75$ (compiled using FE results)

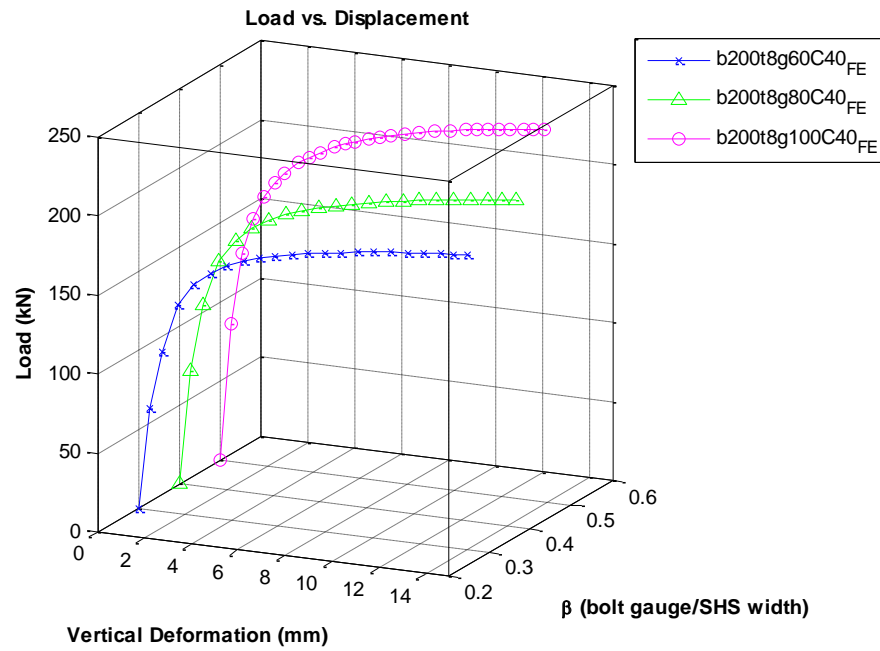


Figure 6.36 The face bending of concrete-filled SHS 200x200 when $\mu = 25$ (compiled using FE results)

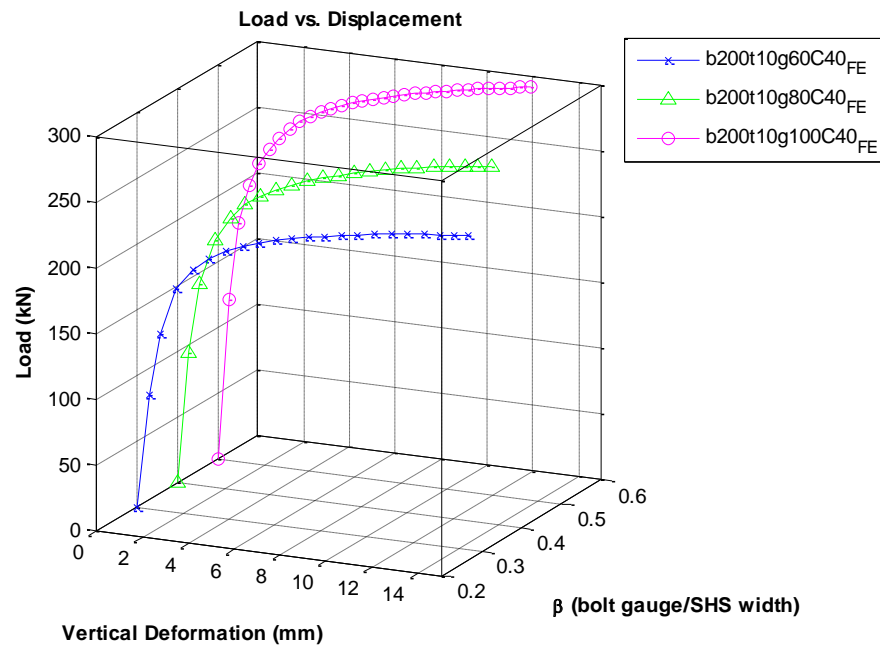


Figure 6.37 The face bending of concrete-filled SHS 200x200 when $\mu = 20$ (compiled using FE results)

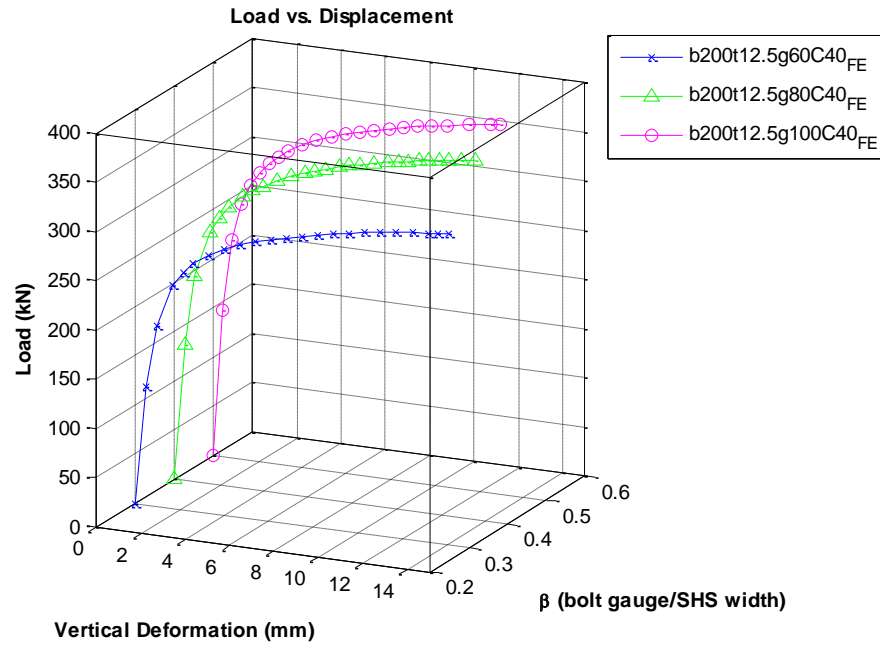


Figure 6.38 The face bending of concrete-filled SHS 200x200 when $\mu = 16$ (compiled using FE results)

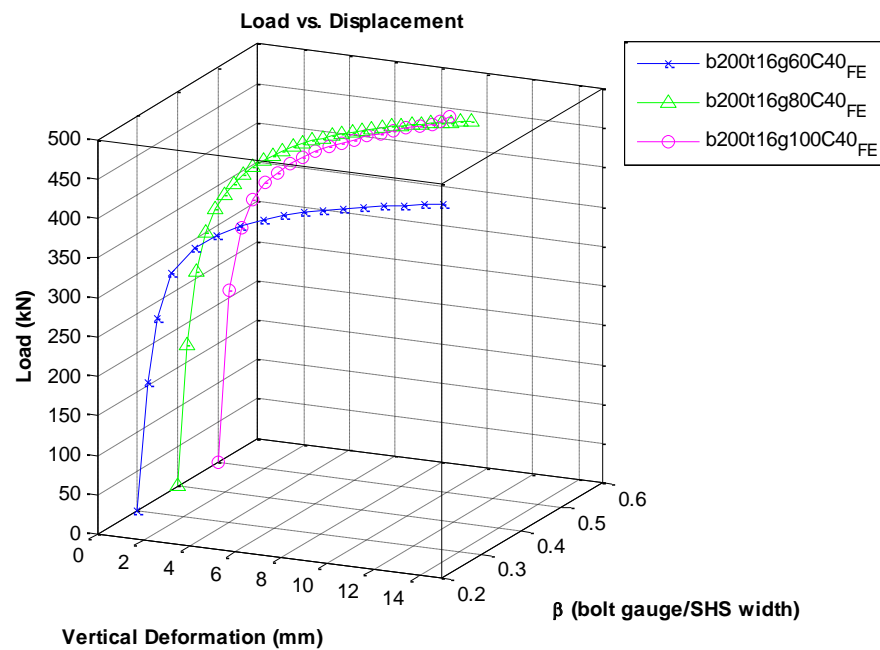


Figure 6.39 The face bending of concrete-filled SHS 200x200 when $\mu = 12.5$ (compiled using FE results)

6.6 Proposed Charts for SHS 200x200

The outcomes of the finite element modelling are also used to compile charts of the face bending of concrete-filled SHS component. These charts could be used in connection design after applying appropriate safety factors. These charts are shown hereafter.

The charts were produced for all the thickness of SHS 200x200 and for three bolt gauges: 60mm, 80mm and 100mm, filled with concrete that have 40N/mm^2 compressive strength.

The charts for SHS 200x200 with a bolts gauge of 60mm are plotted in Figure 6.40. Similarly, the charts for SHS 200x200 with a bolts gauge of 60mm and 80mm are plotted in Figure 6.41 and Figure 6.42 respectively.

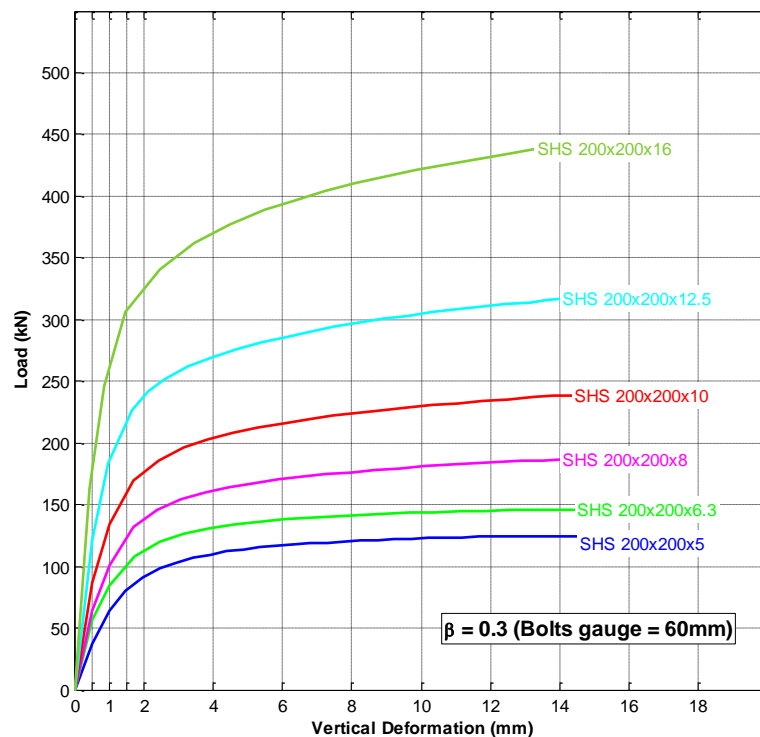


Figure 6.40 The face bending of concrete-filled SHS 200x200 ($\beta=0.3$)

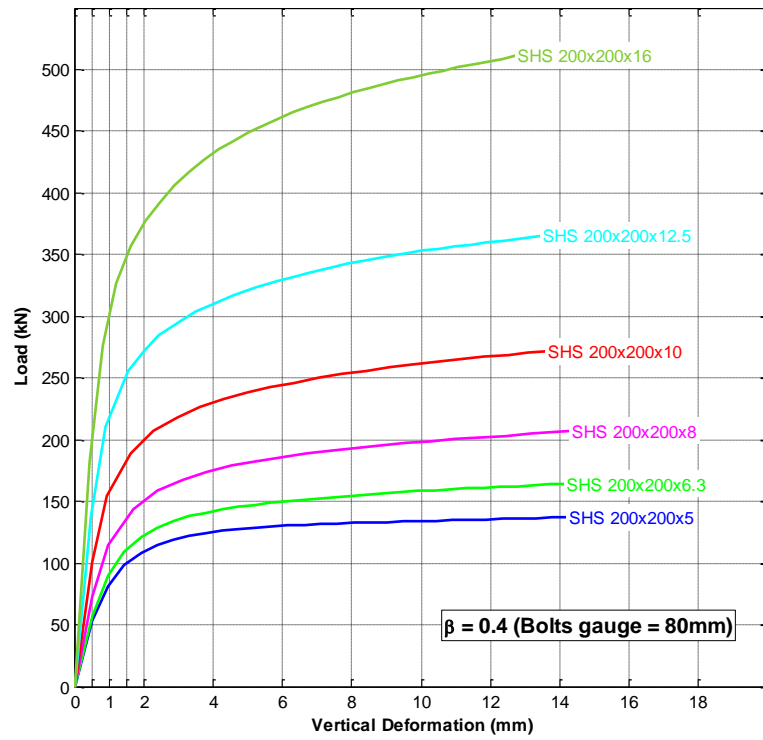


Figure 6.41 The face bending of concrete-filled SHS 200x200 ($\beta=0.4$)

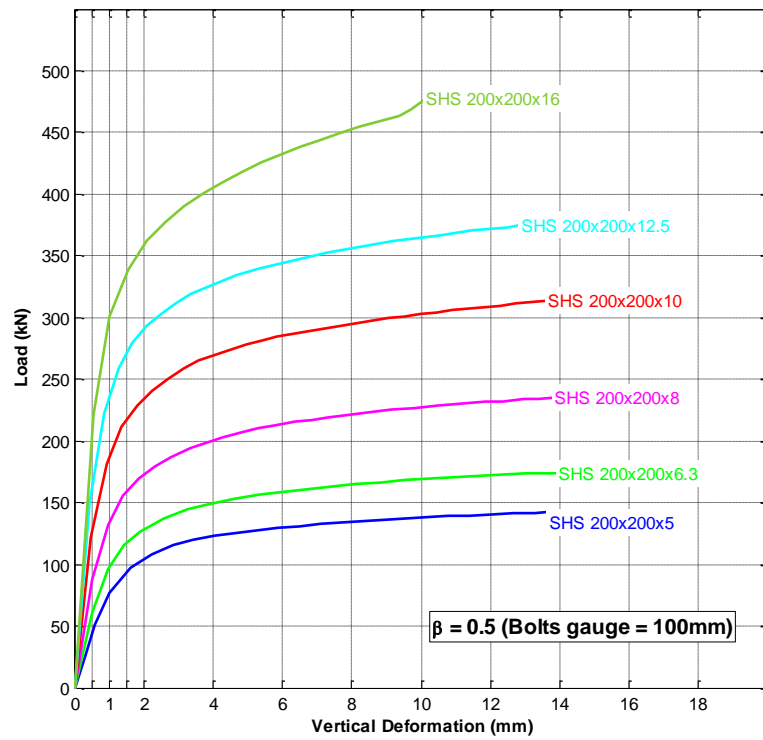


Figure 6.42 The face bending of concrete-filled SHS 200x200 ($\beta=0.5$)

6.7 Summary

This chapter detailed the finite element modelling carried out during this research using ANSYS 13 APDL. It described the material models used in the finite element modelling. The parameters which were varied in this work and their ranges are highlighted in Table 6.4 below.

Table 6.4 Finite element modelling ranges and limitations

Item	Limitation/Range
Hollow Sections	Square Hollow Sections (SHS 200x200)
Blind Bolts	Hollo-Bolts 16 (HB16)
Slenderness ratio of Hollow Section ($\mu = b/t$)	$12.5 \leq \mu \leq 40$
Ratio of bolts gauge to Hollow Section width ($\beta = g/b$)	$0.3 \leq \beta \leq 0.5$
Concrete in-fill grade	C40

Furthermore, this chapter compared the outcomes of the finite element modelling and experimental results. This included both behaviour observation and force-displacement curves for relevant experiments. It also discussed the effect of both the bolt gauge and SHS slenderness on the SHS face bending behaviour.

Finally, the outcomes of the finite element modelling were used to compile charts of the face bending of concrete-filled SHS components which could be used in design.

The next chapter demonstrates how the experimental and finite element analysis results were used to calibrate the Bi-Linear analytical model developed during this study.

Chapter 7

Semi-Analytical Model

7.1 Introduction

The results obtained in the course of this investigation are analysed in this chapter. The chapter commences by detailing how the Initial Stiffness and Post-Yield Stiffness were determined from the experimental results using data best-fitting. It also shows how the Yield Force of each experiment is calculated using these stiffness's. The calculated Initial Stiffness and Yield Force are then used to estimate the analytical model calibration factor k which was proposed in Chapter 3 as well as the post-yield stiffness ratio.

This chapter also examines how the calibration factor k and the post-yield stiffness ratio are affected by SHS face slenderness, bolts gauge and concrete-infill compressive strength. Finally, it presents the final state of the Analytical Model and highlights its limitations.

7.2 Experimental Linear Data-Fit

As assumed in previous chapters, the force-displacement relationship of the face bending behaviour of concrete-filled SHS could be represented Bi-Linearly. The majority of experimental force-displacement curves obtained during this study and presented in the previous chapter support this assumption. The Bi-Linear representation has three parts: Initial Stiffness, Yield Force and Post-Yield Stiffness. Data-fit of experimental force-displacement curves was used to estimate the values which represent these three parts using the Least Square method.

The Least Square method is commonly used to determine the best-fit line for data points. If a line is compared to a set of data points, a deviation between the line and each point befalls as shown in Figure 7.1.

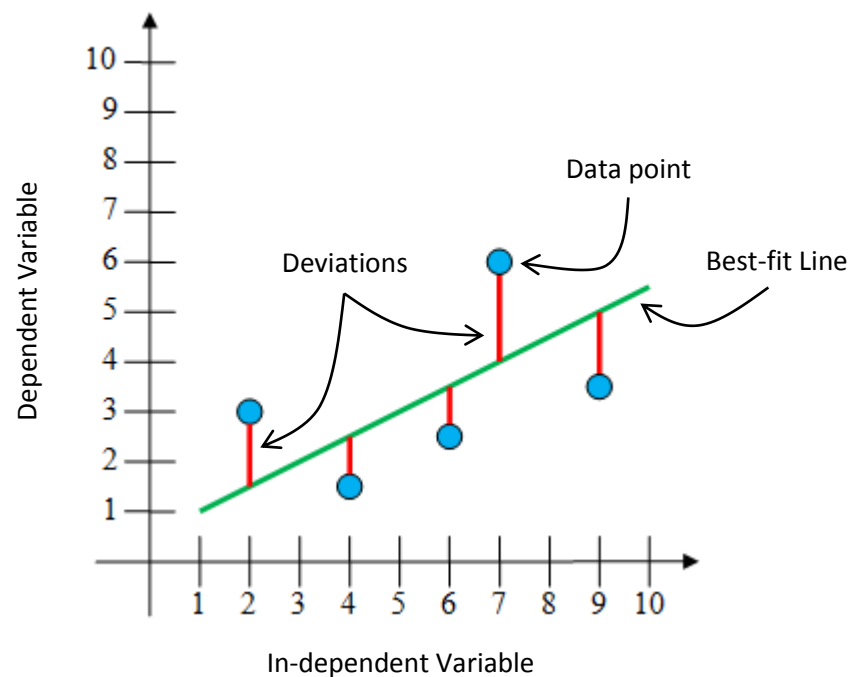


Figure 7.1 Vertical deviation from data point to best-fit line

The sum of the squared deviation between the line and each point is then used to assess the fit goodness of the line to the considered data points. According to the principles of Least Square method, the line that gives the best fit to the data is the one that minimises this sum (Devore and Farnum, 2005). This line could also be called the Least Square line.

For each experiment's force-displacement curve, linear data-fit was done for the initial and the final part of the curve as shown in Figure 7.2 and Figure 7.3. No less than 1000 data points were used to calculate the linear data-fit of each part of the force-displacement curve. The quality of the linear data-fit was evaluated by calculating the error between the actual data and the fitted data i.e. residuals using:

$$\text{Error} = Load_{actual} - Load_{from\ fit} \quad (7-1)$$

The mean of the errors was calculated and found to be very small (less than 0.0001 in most cases). This is attributed to the fact that the number of data points used to estimate the linear data-fit is very high. The Initial Stiffness was then calculated from the slope of the initial part linear-fit. Similarly, the Post-Yield Stiffness was calculated from the slope of the final part linear data-fit.

The Yield Force was calculated from the intersection between the initial part linear data-fit and final part linear data-fit. The Initial Stiffness and Post-Yield Stiffness estimated using the linear data-fit for each experiment are shown in Table 7.1. Errors mean and calculated Yield Force are also shown in same table. The estimated Initial Stiffness and Post-Yield Stiffness as well as the calculated Yield Force are used to calibrate the Analytical Model which was introduced in Chapter 3. This is detailed in the following sections.

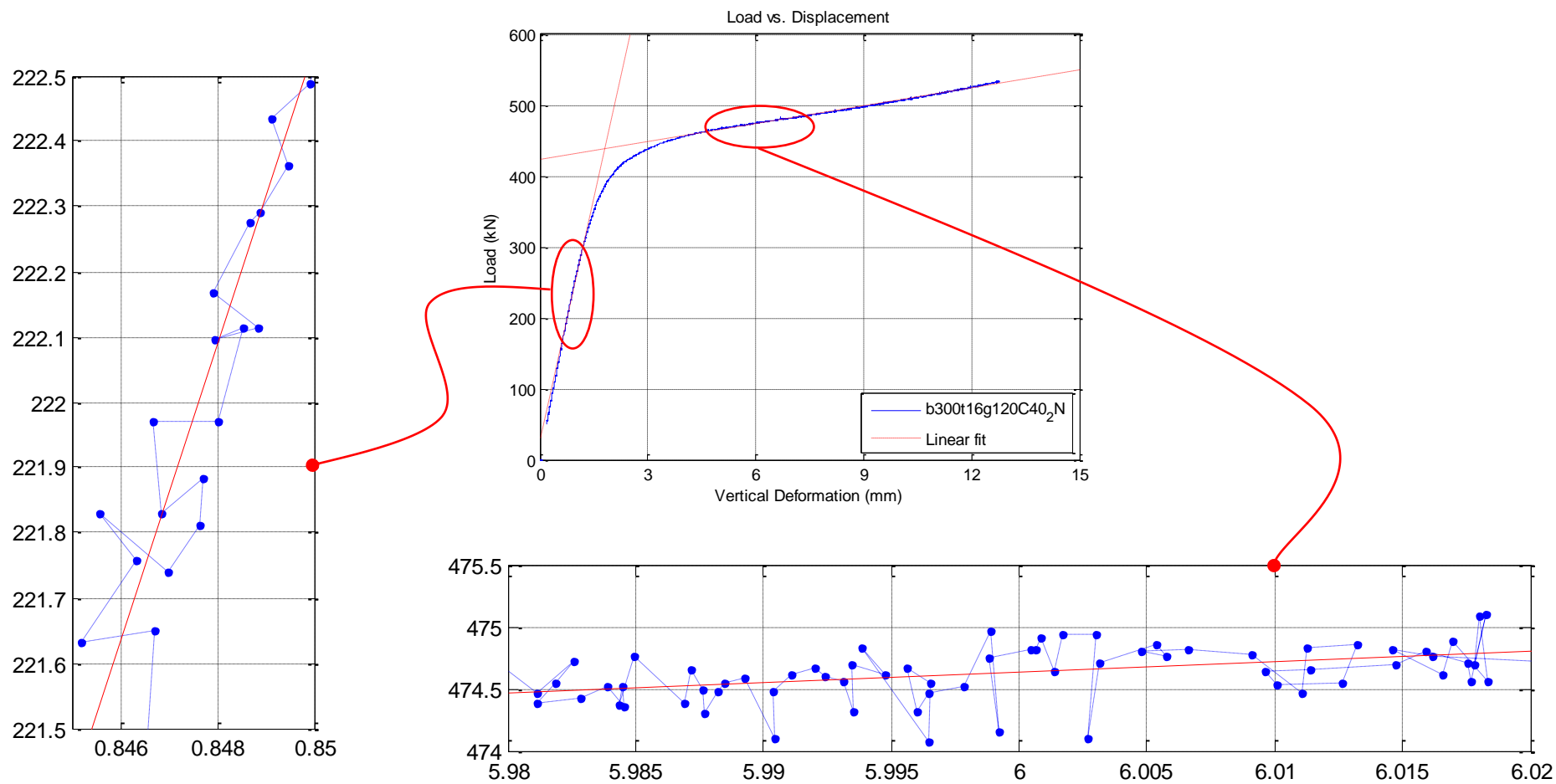


Figure 7.2 Example of linear fit: test b300t16g120C40-2N

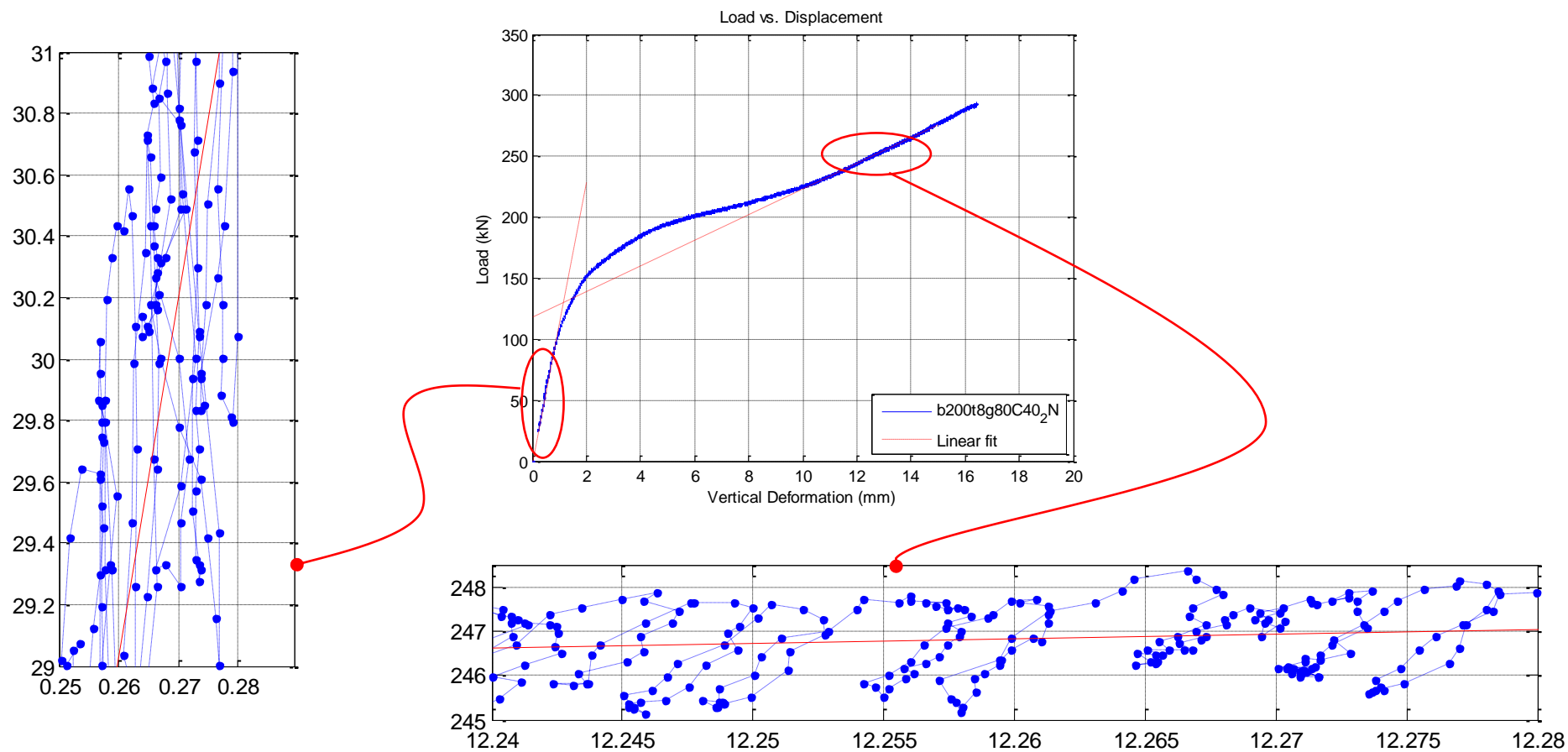


Figure 7.3 Example of linear fit: test b200t8g80C40-2

Table 7.1 Linear data-fit estimations

n	Specimen ID	Initial Stiffness		Post-Yield Stiffness		Yield Force
		Estimate kN/mm	Error Mean ($\times 10^{-14}$)	Estimate kN/mm	Error Mean ($\times 10^{-13}$)	kN
1	b200t8g80c20-1	98.5584	-0.15	5.0500	9.88	106.1563
2	b200t8g80c20-2	73.0686	0.43	4.5002	1.01	111.7854
3	b200t8g80c50-1	295.3483	1.08	4.7047	2.84	145.8194
4	b200t8g80c50-2	179.5600	0.29	7.5098	-2.19	90.7473
5	b200t8g80c50-3	341.9262	0.32	3.8098	-0.75	134.5329
6	b200t8g80c80-1	278.3613	0.13	7.7893	9.50	127.1548
7	b200t8g80c80-2	253.6608	-0.12	7.0731	2.29	133.6615
8	b200t8g60c40-1	112.5523	-0.26	6.2529	-6.01	111.2728
9	b200t8g60c40-2	128.0402	0.45	7.0259	-2.85	81.8110
10	b200t8g60c40-3	188.8559	1.45	7.9534	5.35	60.8597
11	b200t8g80c40-1	102.5893	0.51	9.2108	2.91	104.4282
12	b200t8g80c40-2	113.8471	0.68	10.4705	6.44	130.4467
13	b200t8g80c40-3	176.2633	0.51	10.7245	-3.83	73.1285
14	b200t8g80c40-4	191.9669	0.19	8.0282	2.51	107.8981
15	b200t8g100c40-1	198.0463	-3.11	7.3535	1.37	159.2184
16	b200t8g100c40-2	236.5783	-0.17	7.9901	1.33	143.5833
17	b200t10g80c40-1	298.1506	0.11	9.8453	-5.95	165.4420
18	b200t10g80c40-2	269.9153	-0.68	9.6422	-1.22	171.9068
19	b200t6.3g80c40-1	90.8451	1.12	5.9618	2.01	68.0899
20	b200t6.3g80c40-2	122.7768	-0.83	5.4163	-3.60	76.1883
21	b200t5g80c40-1	82.1101	0.18	5.9217	-2.46	44.9389
22	b200t5g80c40-2	82.0722	0.05	4.5845	-3.52	56.8867
23	b300t12.5g120c40-1	267.5020	0.93	8.9302	-0.70	308.3315
24	b300t12.5g120c40-2	180.0556	-0.30	8.7537	-1.23	308.6816
25	b300t16g120c40-1	239.1260	2.57	11.3011	-1.38	451.2584
26	b300t16g120c40-2	242.9313	1.74	8.3470	2.13	439.6573

7.3 Calibration Factor k

In Chapter 3, a calibration factor denoted k was introduced to account for the complex geometry of Hollo-Bolts and how it will transfer the load to the SHS face. The Initial Stiffness and Yield Force estimated from the experimental results are used to determine this factor. This is done

by calculating the value of c in Equations (3-2) and (3-23), reproduced below as Equations (7-2) and (7-3), which correspond to the estimated Initial Stiffness and Yield Force of each experiment. The calibration factor is then calculated by dividing c by the Hollo-Bolt diameter.

$$S = \frac{16Et^3}{(b-t)^2} \frac{\frac{c}{(b-t)} + \left(1 - \frac{g+c}{b-t}\right) \tan \theta}{\left(1 - \frac{g+c}{b-t}\right)^3 + \frac{10.4 \left[1.5 - 1.6 \left(\frac{g+c}{b-t}\right)\right]}{\left(\frac{b-t}{t}\right)^2}} \quad (7-2)$$

$$F_{Mec. 3} = 2 \pi M \left(1 + \frac{r}{r - \frac{c}{2}}\right) + 2 M \frac{g}{r} \quad (7-3)$$

Two versions of the calibration factor k are considered:

- k_{is} which is to be determined using the experimentally estimated Initial Stiffness data and Equation (7-2)
- k_{yf} which is to be determined using the experimentally estimated Yield Force data and (7-3).

Statistical analysis is subsequently used to develop charts for the calibration factor k , and investigate how it is affected by SHS face slenderness, bolts gauge and concrete-infill compressive strength.

7.3.1 Background

A statistical relation between pairs of independent and dependant variables, e.g. x and y , in a sample could be often observed. This relation is statistically called Correlation and commonly measured by determining sample Correlation Coefficient. The principle of Correlation and how to calculate Correlation Coefficient are available in many statistics text books.

Additionally, a line/curve fit could be determined for the sample pairs. The Least Squared method is commonly used to determine the line/curve fit as explained in the previous section. Regression describes the relationship between the least squares line/curve and the sample Correlation Coefficient (Devore and Farnum, 2005). This relation is widely measured with a coefficient called the Coefficient of Determination and denoted r^2 . This coefficient is between 0 and 1, the higher the value the better the relationship. For example if r^2 for an approximated linear fit of a data (set of x_i, y_i) is calculated to be 0.80, this mean that 80% of the observed y_i is attributed to (can be explained by) the approximated linear fit relationship. According to Devore and Farnum (2005), r^2 is calculated using the following equation:

$$r^2 = 1 - \frac{SSResiduals}{SSTotal} \quad (7-4)$$

in which *SSResiduals* is the residuals sum of squares and *SSTotal* is the total sum of squares.

The relation between the calculated k for each experiment and the parameters which could affect the SHS face bending is examined in the following sections. The Coefficient of Determination (r^2) is used to measure this relation. The criterion used to examine the relation can be summarised in the following steps:

1. Substitute the calculated Initial Stiffness and Yield Force values for each experiment in Equations (7-2) and (7-3) respectively.
2. Solve Equations (7-2) and (7-3) for c for each experiment.
3. Calculate k_{is} and k_{yf} from c which are determined in the previous step: k_{is} from c which calculated using Equation (7-2) and k_{yf} from c which calculated using Equation (7-3). This is done by dividing each c by the Hollo-bolt diameter.

4. Average k_{is} and k_{yf} with respect of each set of experiments which was designed to examine the effect of SHS face slenderness, bolts gauge and concrete-infill compressive strength on the SHS face bending.
5. Approximate and examine the relation between each of the averaged k_{is} and k_{yf} with respect to SHS face slenderness, bolts gauge and concrete-infill compressive strength.

7.3.2 Initial Stiffness calibration factor (k_{is})

Effect of SHS face slenderness ratio (μ)

The relation between k_{is} and SHS face slenderness ratio (μ) is examined in this section. Table 7.2 shows the calculated k_{is} for the experiments in which the SHS slenderness ratio only was varied. The average of calculated k_{is} for identical experiments is presented in this table.

Table 7.2 k_{is} for experiments which vary SHS face slenderness

n	Specimen ID	μ	β	Concrete Strength N/mm ²	k_{is}	
		b/t	g/b		c/d _h (d _h =26)	Average
1	b200t5g80c40-1	40	0.4	40	3.11	3.11
	b200t5g80c40-2	40	0.4	40	3.11	
2	b200t6.3g80c40-1	31.75	0.4	40	2.81	2.89
	b200t6.3g80c40-2	31.75	0.4	40	2.97	
3	b200t8g80c40-3	25	0.4	40	2.80	2.82
	b200t8g80c40-4	25	0.4	40	2.84	
4	b200t10g80c40-1	20	0.4	40	2.71	2.68
	b200t10g80c40-2	20	0.4	40	2.65	

Strong relation between the averaged k_{is} and the SHS face slenderness ratio was observed. The factor k_{is} is found to increase with the increase of the SHS face slenderness ratio. This relation could be represented linearly as shown in Figure 7.4.

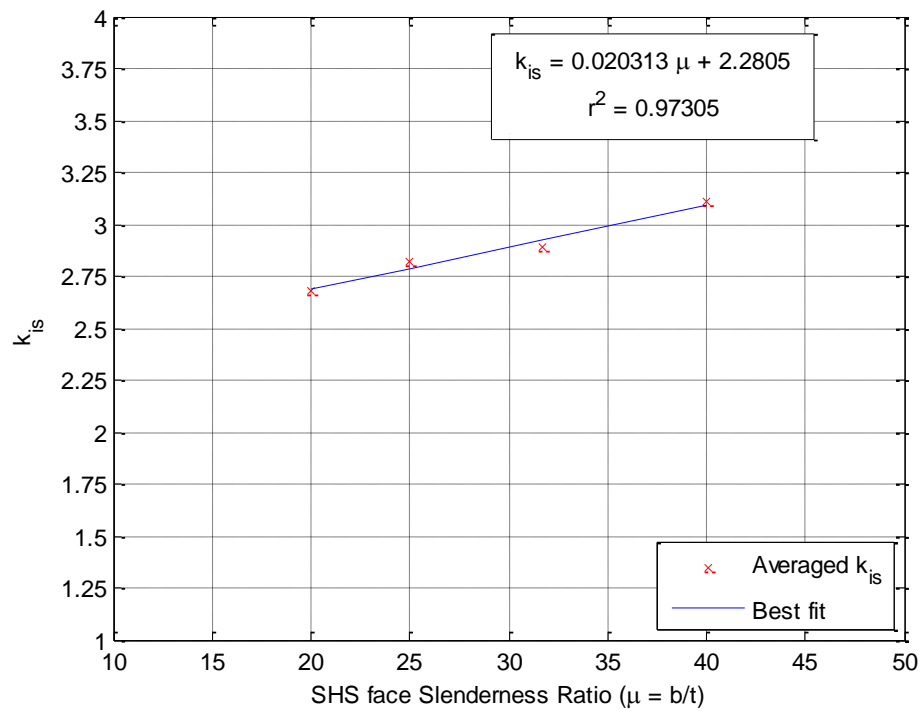


Figure 7.4 k_{is} for experiments which vary SHS face slenderness

Effect of bolt gauge to SHS width ratio (β)

The relation between k_{is} and bolt gauge to SHS width ratio (β) is examined in this section. Table 7.3 shows the calculated k_{is} for the experiments which only varied the ratio (β). The average of calculated k_{is} for identical experiments is presented in this table.

Table 7.3 k_{is} for experiments which vary Bolt gauge to SHS width ratio

n	Specimen ID	μ	β	Concrete Strength N/mm ²	k_{is}	
		b/t	g/b		k=c/d _h (d _h =26)	Average
1	b200t8g60c40-1	25	0.3	40	3.16	3.30
	b200t8g60c40-2	25	0.3	40	3.25	
	b200t8g60c40-3	25	0.3	40	3.49	
2	b200t8g80c40-3	25	0.4	40	2.80	2.82
	b200t8g80c40-4	25	0.4	40	2.84	
3	b200t8g100c40-1	25	0.5	40	2.21	2.26
	b200t8g100c40-2	25	0.5	40	2.30	

Strong relation between the averaged k_{is} and the ratio (β) was observed. Any increase in the ratio (β) is found to reduce the factor k_{is} . This relation could be represented linearly as shown in Figure 7.5.

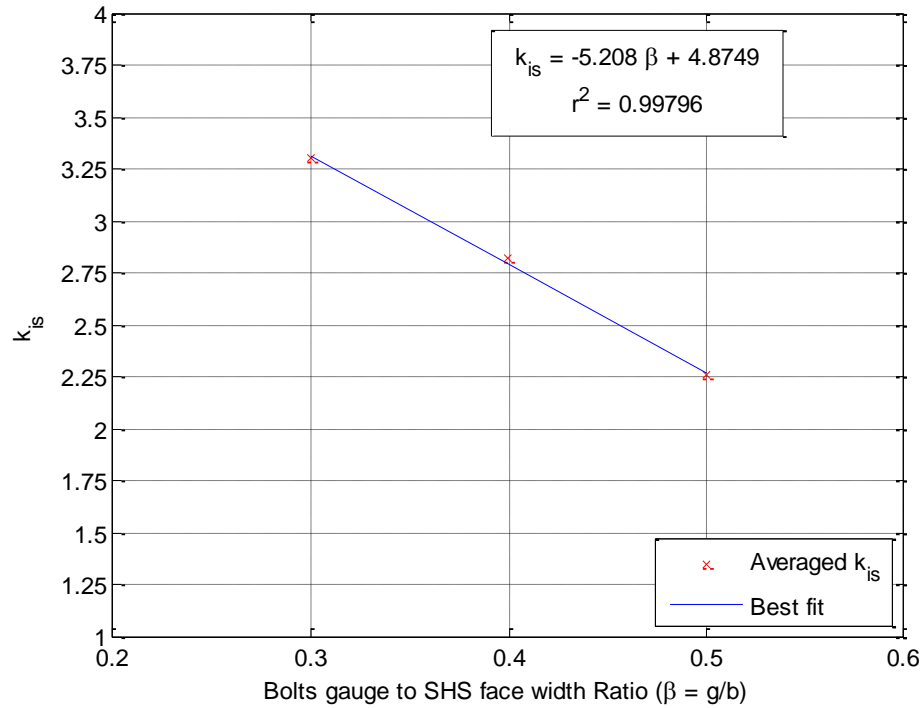


Figure 7.5 k_{is} for experiments which vary Bolt gauge to SHS width ratio

Effect of concrete in-fill compressive strength

The relation between k_{is} and concrete in-fill compressive strength is examined in this section. Table 7.4 shows the calculated k_{is} for the experiments in which the concrete in-fill compressive strength only was varied. The average of calculated k_{is} for identical experiments is also presented in this table.

A linear relation between the averaged k_{is} and the concrete in-fill compressive strength was observed. Nevertheless, a relatively low r^2 was calculated for this relation if compared with other similar relations between k_{is} and μ or β . However, strong 2nd degree polynomial relation between the averaged k_{is} and the concrete in-fill compressive strength

was observed. This relation is shown in Figure 7.6. The calculated r^2 for this relation is 0.99866 as shown in the figure. This is the only non-linear relation observed between both k_{is} and k_{yf} and any parameter investigated in the course of this study.

Table 7.4 k_{is} for experiments which vary Concrete in-fill compressive strength

n	Specimen ID	μ	β	Concrete Strength N/mm ²	k_{is}	
		b/t	g/b		$k=c/d_h$ ($d_h=26$)	Average
1	b200t8g80c20-1	25	0.4	20	2.44	2.33
	b200t8g80c20-2	25	0.4	20	2.23	
2	b200t8g80c40-3	25	0.4	40	2.80	2.82
	b200t8g80c40-4	25	0.4	40	2.84	
3	b200t8g80c50-1	25	0.4	50	3.06	2.93
	b200t8g80c50-2	25	0.4	50	2.81	
4	b200t8g80c80-1	25	0.4	80	3.04	3.01
	b200t8g80c80-2	25	0.4	80	2.99	

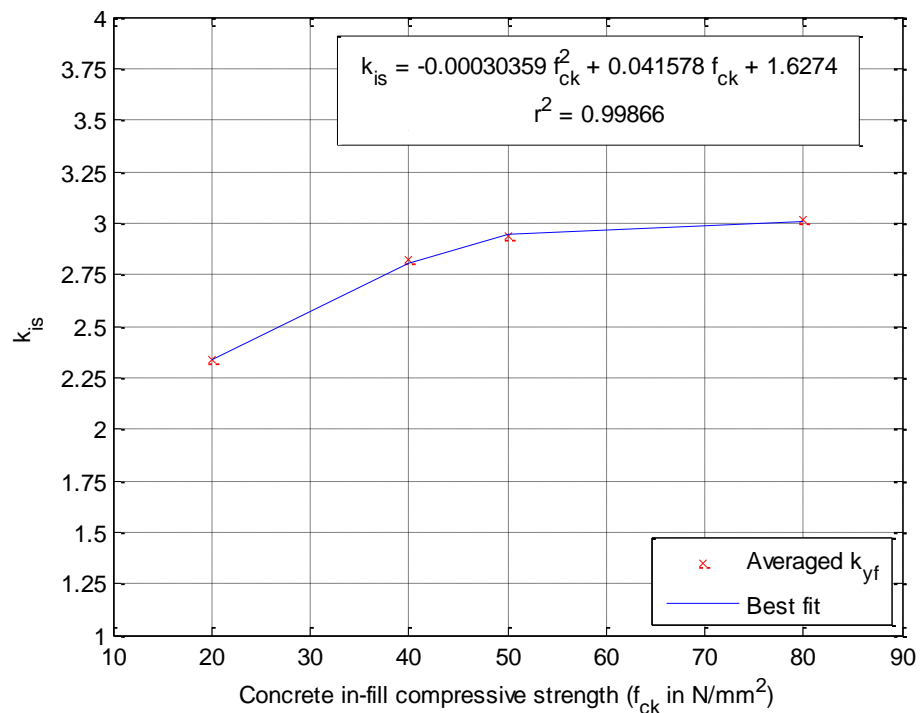


Figure 7.6 k_{is} for experiments which vary Concrete in-fill compressive strength

7.3.3 Yield Force calibration factor (k_{yf})

The same steps presented at the end of section 7.3.1 are followed here to determine the Yield Force calibration factor (k_{yf}).

Effect of SHS face slenderness ratio (μ)

The relation between k_{yf} and SHS face slenderness ratio (μ) is examined in this section. Table 7.5 shows the calculated k_{yf} for the experiments which varied the SHS slenderness ratio only.

The average of calculated k_{yf} for identical experiments is presented in this table.

Table 7.5 k_{yf} for experiments which vary SHS face slenderness

n	Specimen ID	μ b/t	β g/b	Concrete Strength N/mm ²	k_{yf}	
					k=c/d _h (d _h =26)	Average
1	b200t5g80c40-1	40	0.4	40	1.21	1.33
	b200t5g80c40-2	40	0.4	40	1.45	
2	b200t6.3g80c40-1	31.75	0.4	40	1.14	1.21
	b200t6.3g80c40-2	31.75	0.4	40	1.28	
3	b200t8g80c40-1	25	0.4	40	1.15	1.07
	b200t8g80c40-2	25	0.4	40	1.38	
	b200t8g80c40-3	25	0.4	40	0.57	
	b200t8g80c40-4	25	0.4	40	1.19	
4	b200t10g80c40-1	20	0.4	40	0.99	1.02
	b200t10g80c40-2	20	0.4	40	1.04	

Strong relation between the averaged k_{yf} and the SHS face slenderness ratio was observed. The factor k_{yf} is found to increase with the increase of the SHS face slenderness ratio. This relation could be represented linearly as shown in Figure 7.7. The calculated r^2 for this relation is 0.9923 as shown in the figure.

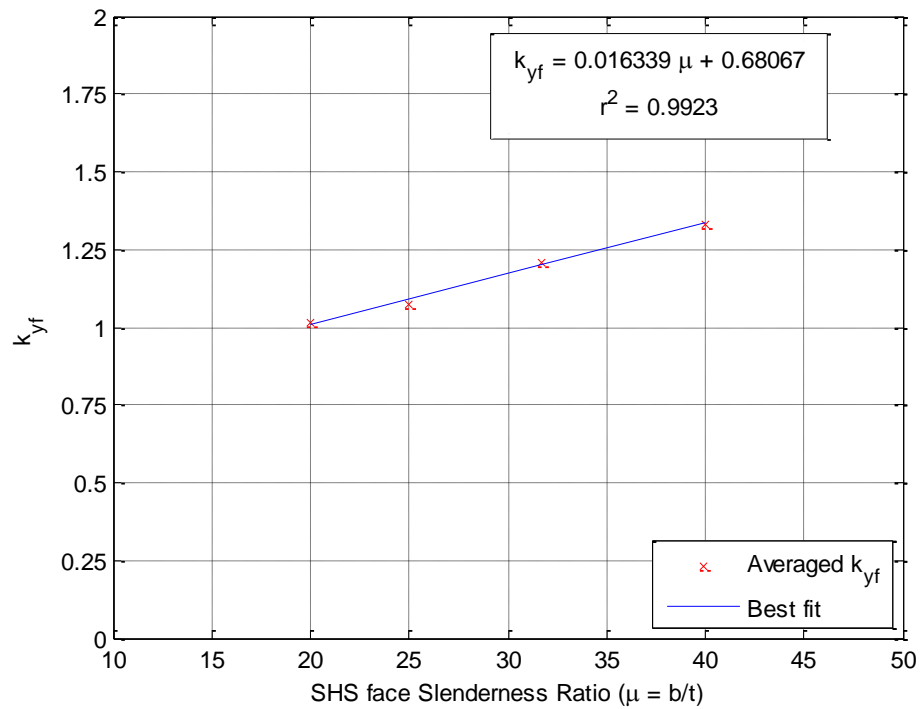


Figure 7.7 k_{yf} for experiments which vary SHS face slenderness

Effect of bolt gauge to SHS width ratio (β)

This section examines the relation between k_{yf} and bolt gauge to SHS width ratio (β). Table 7.6 shows the calculated k_{yf} for the experiments in which the ratio (β) only was varied. The average of calculated k_{yf} for identical experiments is presented in this table.

Table 7.6 k_{yf} for experiments which vary Bolt gauge to SHS width ratio

n	Specimen ID	μ b/t	β g/b	Concrete Strength N/mm ²	k_{yf}	
					k=c/d _h (d _h =26)	Average
1	b200t8g60c40-1	25	0.3	40	1.51	1.02
	b200t8g60c40-2	25	0.3	40	1.08	
	b200t8g60c40-3	25	0.3	40	0.46	
2	b200t8g80c40-1	25	0.4	40	1.15	1.07
	b200t8g80c40-2	25	0.4	40	1.38	
	b200t8g80c40-3	25	0.4	40	0.57	
	b200t8g80c40-4	25	0.4	40	1.19	
3	b200t8g100c40-1	25	0.5	40	1.23	1.21
	b200t8g100c40-2	25	0.5	40	1.19	

Strong relation between the averaged k_{yf} and the ratio (β) was observed. Contradicting to relation between the averaged k_{is} and the ratio (β), any increase in the ratio (β) is found to increase the factor k_{yf} . This relation could be represented linearly as shown in Figure 7.8.

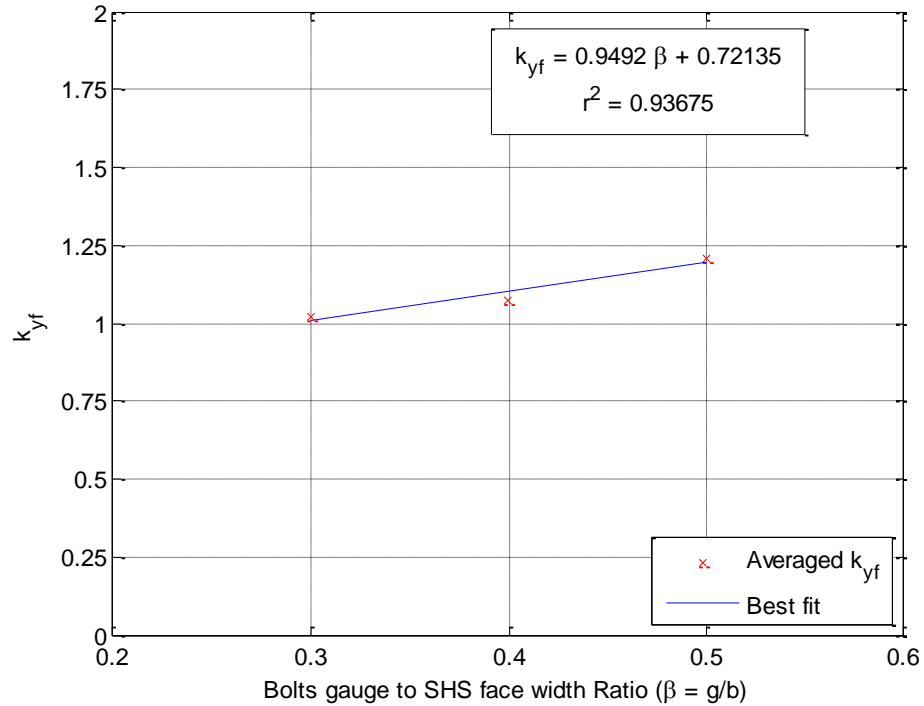


Figure 7.8 k_{yf} for experiments which vary Bolt gauge to SHS width ratio

Effect of concrete in-fill compressive strength

The relation between k_{yf} and concrete in-fill compressive strength is examined in this section. Table 7.7 shows the calculated k_{yf} for the experiments which varied the concrete in-fill compressive strength only. The average of calculated k_{yf} for identical experiments is also presented in Table 7.7.

Unlike the relation between k_{is} and concrete in-fill compressive strength, a strong linear relation between the averaged k_{yf} and the concrete in-fill compressive strength was observed. The increase of concrete in-fill compressive strength found to linearly increase the

factor k_{yf} . This relation is shown in Figure 7.9. The calculated r^2 for this relation is 0.98629 as shown in the figure.

Table 7.7 k_{yf} for experiments which vary Concrete in-fill compressive strength

n	Specimen ID	μ	β	Concrete Strength N/mm ²	k_{yf}	
		b/t	g/b		k=c/d _h (d _h =26)	Average
1	b200t8g80c20-1	25	0.4	20	1.17	1.20
	b200t8g80c20-2	25	0.4	20	1.23	
2	b200t8g80c40-1	25	0.4	40	1.15	1.24
	b200t8g80c40-2	25	0.4	40	1.38	
	b200t8g80c40-4	25	0.4	40	1.19	
3	b200t8g80c50-1	25	0.4	50	1.47	1.28
	b200t8g80c50-2	25	0.4	50	0.96	
	b200t8g80c50-3	25	0.4	50	1.41	
4	b200t8g80c80-1	25	0.4	80	1.36	1.38
	b200t8g80c80-2	25	0.4	80	1.40	

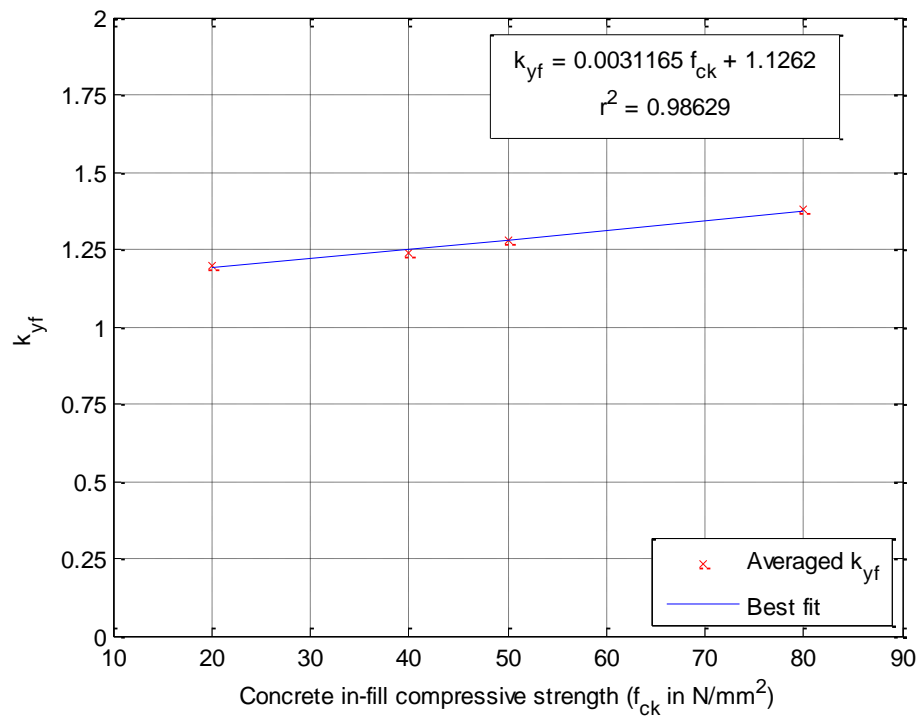


Figure 7.9 k_{yf} for experiments which vary Concrete in-fill compressive strength

7.3.4 Discussion

As seen in the previous two sub-sections, the calculated k_{yf} is significantly lower than its counterpart k_{is} (at least 50% less). This hints that the concrete in-fill behave differently at each stage of the tests as discussed hereafter.

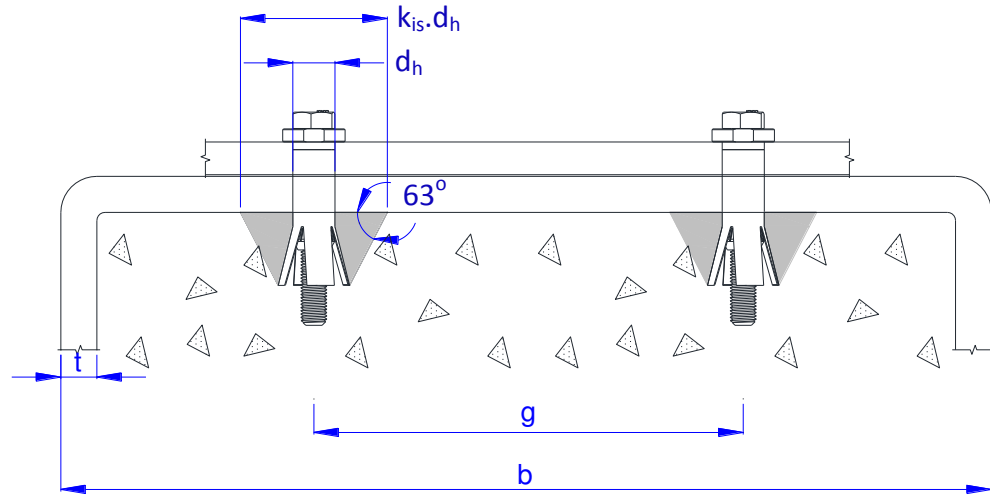
At the initial stage, more concrete in-fill are involved in the loading mechanism hence the reported higher value of k_{is} . This could be attributed to the fact that the applied load low magnitude at the initial stage of the test causes low level of stresses in the concrete-infill around the bolts.

At the later stage of the tests, the low calculated k_{yf} indicate that less concrete in-fill around the bolt is involved in the loading mechanism. This could be also attributed to the stresses on the concrete in-fill. The magnitude of the applied force at the later stage of the tests indicates that the stresses at part of the concrete-infill must have exceeded its ultimate capacity.

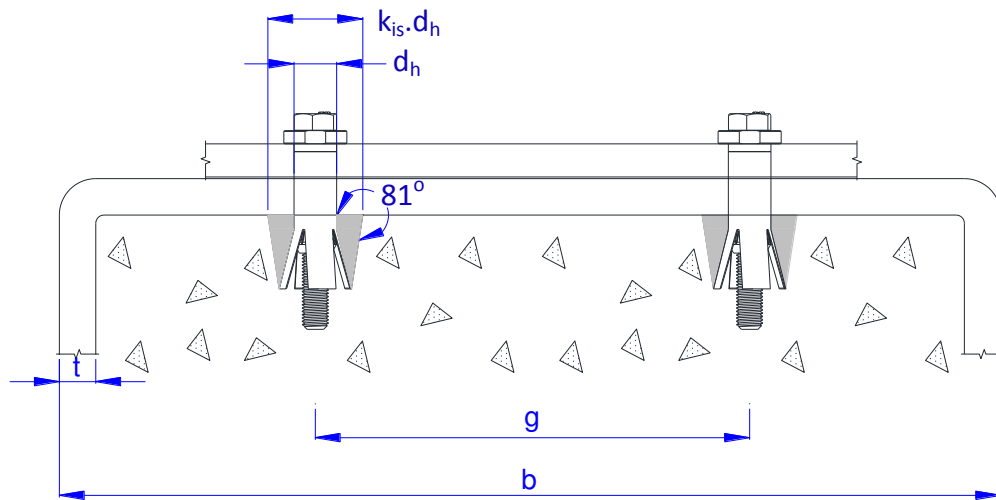
Also, the reported high deformation in the SHS face at the later stage of the tests could not have happened unless part of the concrete in-fill around the bolt breaks from the rest of concrete in-fill. This conclusion could not be fully verified however, there was no significant concrete in-fill crushing reported in each of the tests.

Furthermore, going back to the load transfer mechanism discussed in Chapter 3, it was assumed that the bolt's opened sleeves apply the load on the SHS column face through the concrete-infill. A concrete cone was expected to develop. The calculated k_{is} could be used to determine the shape of the assumed cone at the initial stage of the tests. The angle of the concrete cone which shown in Figure 7.10 is found to vary between

63° calculated for test b200t8g60c40-3 and 81° calculated for test b200t8g100c40-1.



a) Minimum assumed cone angle (calculated for test b200t8g60c40-3)



b) Maximum assumed cone angle (calculated for test b200t8g100c40-1)

Figure 7.10 Minimum & Maximum calculated angles of assumed concrete cone

Conversely, the calculated k_{yf} cannot be used to determine the shape of the assumed concrete cone at the stage of the test which Yield Force is calculated (and k_{yf}). This is down to the deformation of the SHS bolt holes observed during this stage. This deformation is caused by the

applied force pushing the bolts through the holes as reported in Chapter 5 of this thesis. The deformation of the bolt holes dismisses the possibility of estimating the shape of the assumed concrete cone using this calibration factor. A way of doing this is needed to experimentally understand the behaviour of concrete in-fill at that stage of the tests as well as the following stages.

The best-fit functions for k_{is} and k_{yf} are used to develop charts that can be used to estimate both factors. These charts are to be used to calibrate the proposed Analytical Model as presented in the following sections.

7.4 Post-Yield Stiffness

This section examines the Post-Yield Stiffness to Initial Stiffness ratio in respect to SHS face slenderness, bolts gauge and concrete-infill compressive strength. Ultimately, this ratio is to be used to determine the Post-Yield Stiffness from the analytically calculated Initial Stiffness. The ratio for each experiment is calculated using the linear experimental data-fit presented in Table 7.1. The same procedure which was stated in Section 7.3 is used to determine the effect of SHS face slenderness, bolts gauge and concrete-infill compressive strength on the Post-Yield Stiffness ratio.

7.4.1 Effect of SHS face slenderness ratio (μ)

The relation between Post-Yield Stiffness ratio and SHS face slenderness ratio (μ) is examined in this section. Table 7.2 shows the calculated Post-Yield Stiffness ratio for the experiments in which the SHS slenderness ratio only was varied. The average of calculated Post-Yield Stiffness ratios for identical experiments is also presented in this table.

Strong correlation between the averaged Post-Yield Stiffness ratios and the SHS face slenderness ratio was observed. The Post-Yield Stiffness ratio is found to increase with the increase of the SHS face slenderness ratio. This relation could be represented with a 2nd degree polynomial as shown in Figure 7.11.

Table 7.8 Post-Yield Stiffness ratio when varying SHS face slenderness

n	Specimen ID	μ	β	Concrete Strength N/mm ²	Post-Yield Stiffness ratio	
		b/t	g/b		S_i/S_{py}	Average
1	b200t5g80c40-1	40	0.4	40	0.07	0.064
	b200t5g80c40-2	40	0.4	40	0.06	
2	b200t6.3g80c40-1	31.75	0.4	40	0.07	0.055
	b200t6.3g80c40-2	31.75	0.4	40	0.04	
3	b200t8g80c40-3	25	0.4	40	0.06	0.051
	b200t8g80c40-4	25	0.4	40	0.04	
4	b200t10g80c40-1	20	0.4	40	0.03	0.034
	b200t10g80c40-2	20	0.4	40	0.04	

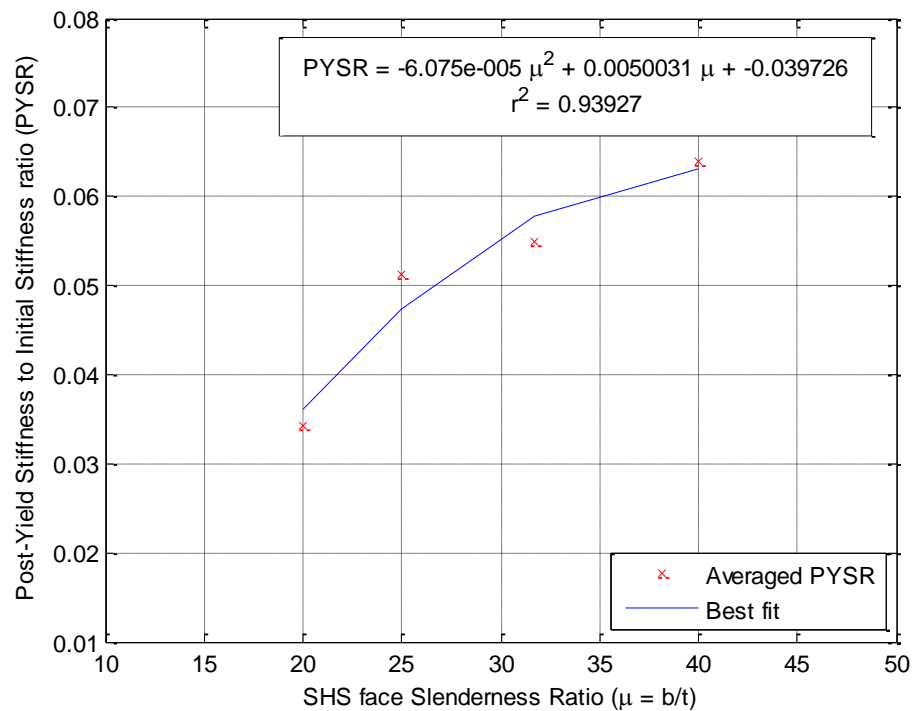


Figure 7.11 Post-Yield Stiffness ratio when varying SHS face slenderness

7.4.2 Effect of bolt gauge to SHS width ratio (β)

The relation between Post-Yield Stiffness ratio and bolt gauge to SHS width ratio (β) is examined in this section. Table 7.9 shows the calculated Post-Yield Stiffness ratio for the experiments which varied the ratio (β) only. The average of calculated Post-Yield Stiffness ratios for identical experiments is also presented in Table 7.9.

Table 7.9 Post-Yield Stiffness ratio when varying Bolt gauge

n	Specimen ID	μ	β	Concrete Strength N/mm ²	Post-Yield Stiffness ratio	
		b/t	g/b		S_i/S_{py}	Average
1	b200t8g60c40-1	25	0.3	40	0.06	0.052
	b200t8g60c40-2	25	0.3	40	0.06	
	b200t8g60c40-3	25	0.3	40	0.04	
2	b200t8g80c40-3	25	0.4	40	0.06	0.051
	b200t8g80c40-4	25	0.4	40	0.04	
3	b200t8g100c40-1	25	0.5	40	0.04	0.035
	b200t8g100c40-2	25	0.5	40	0.03	

A relation between the averaged Post-Yield Stiffness ratios and the ratio (β) was observed. This relation could be represented linearly as shown in Figure 7.12. Any increase in the ratio (β) is found to reduce the Post-Yield Stiffness ratio.

The Coefficient of Determination (r^2) of the relation observed herein is relatively low compared to previously reported coefficients ($r^2 = 0.7759$). Although it is still acceptable, it would benefit from more experiments.

Results obtained from the finite element model are used in an attempt to increase the Coefficient of Determination (r^2) and subsequently improve the quality of the relation between the averaged Post-Yield Stiffness ratios and the ratio (β).

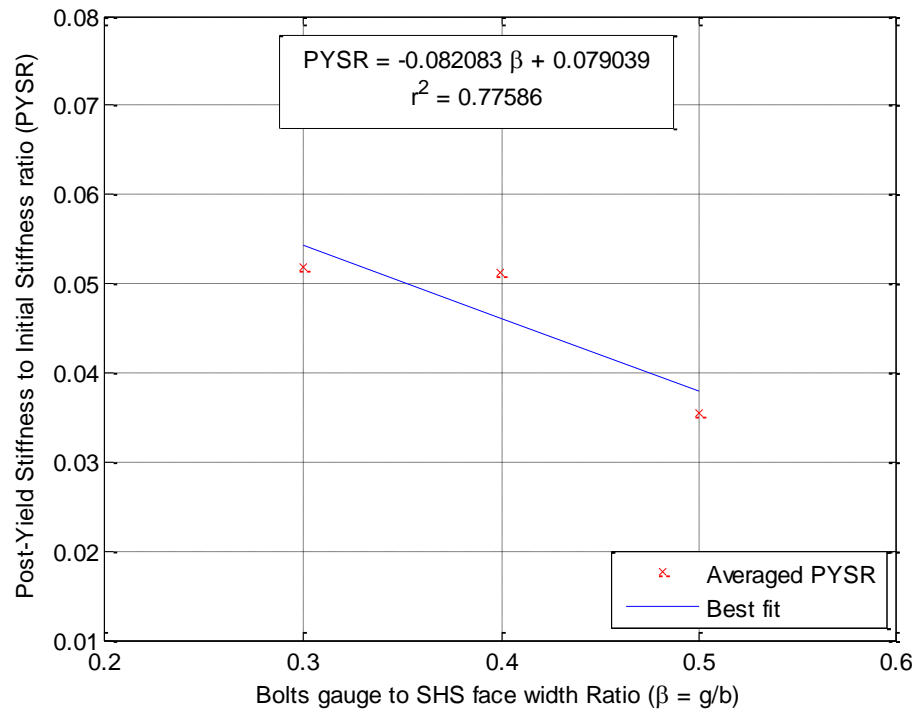


Figure 7.12 Post-Yield Stiffness ratio when varying Bolt gauge

Post-Yield Stiffness ratios of the force-displacement curves obtained from finite element model results are calculated following the same procedure used for the experimental results.

The relation between the averaged Post-Yield Stiffness ratios of experimental and finite element results and the ratio (β) are shown in Figure 7.13. This relation is also represented linearly.

The Coefficient of Determination (r^2) of the relation observed when the finite element results are used has increased considerably. The Coefficient of Determination (r^2) increased from $r^2 = 0.7759$ as shown in Figure 7.12 to $r^2 = 0.9581$ as shown in Figure 7.13.

The quality of the relation between the averaged Post-Yield Stiffness ratios and the ratio (β) has improved after using the outcomes of the finite element model.

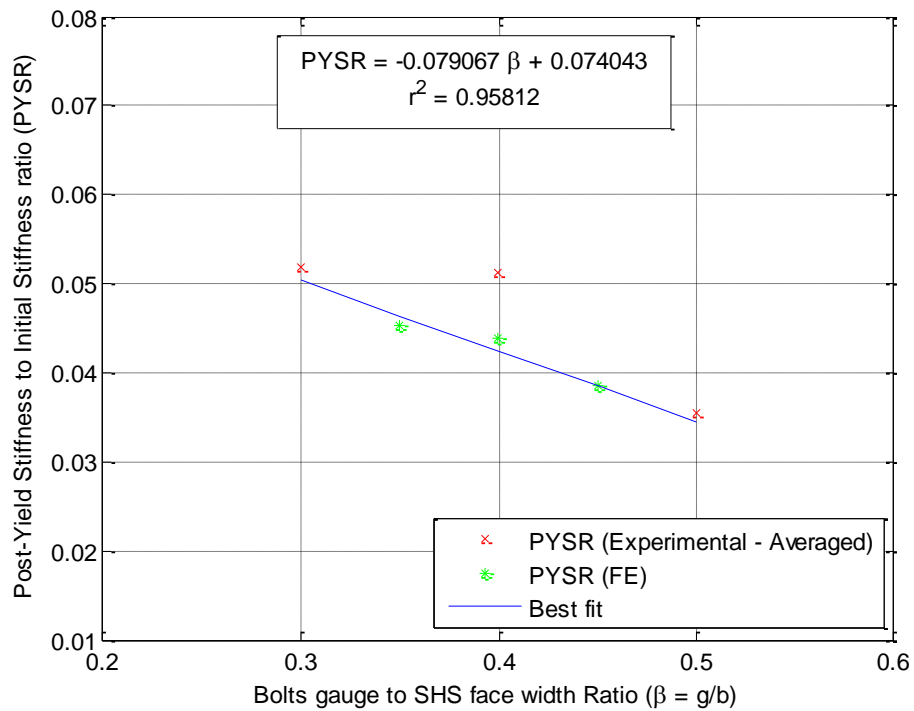


Figure 7.13 Post-Yield Stiffness ratio when varying Bolt gauge (FE + Experiments)

7.4.3 Effect of concrete in-fill compressive strength

The relation between Post-Yield Stiffness ratio and concrete in-fill compressive strength is examined in this section. Table 7.10 shows the calculated Post-Yield Stiffness ratio for the experiments which varied the concrete in-fill compressive strength only. The average of calculated Post-Yield Stiffness ratios for identical experiments is also presented in this table.

A relation between the averaged Post-Yield Stiffness ratios and concrete in-fill compressive strength was observed. This relation could be represented with a 2nd degree polynomial as shown in Figure 7.14. Any increase in the concrete in-fill compressive strength is found to reduce the Post-Yield Stiffness ratio.

Similar to the relation between the averaged Post-Yield Stiffness ratios and the ratio (β), the Coefficient of Determination (r^2) of the relation observed herein is relatively low compared to previously reported coefficients ($r^2 = 0.7849$). Although it is still acceptable, it would benefit from more experiments.

Table 7.10 Post-Yield Stiffness ratio when varying concrete in-fill strength

n	Specimen ID	μ b/t	β g/b	Concrete Strength N/mm ²	Post-Yield Stiffness ratio	
					S_i/S_{py}	Average
1	b200t8g80c20-1	25	0.4	20	0.05	0.056
	b200t8g80c20-2	25	0.4	20	0.06	
2	b200t8g80c40-3	25	0.4	40	0.06	0.051
	b200t8g80c40-4	25	0.4	40	0.04	
3	b200t8g80c50-1	25	0.4	50	0.02	0.029
	b200t8g80c50-2	25	0.4	50	0.04	
4	b200t8g80c80-1	25	0.4	80	0.03	0.028
	b200t8g80c80-2	25	0.4	80	0.03	

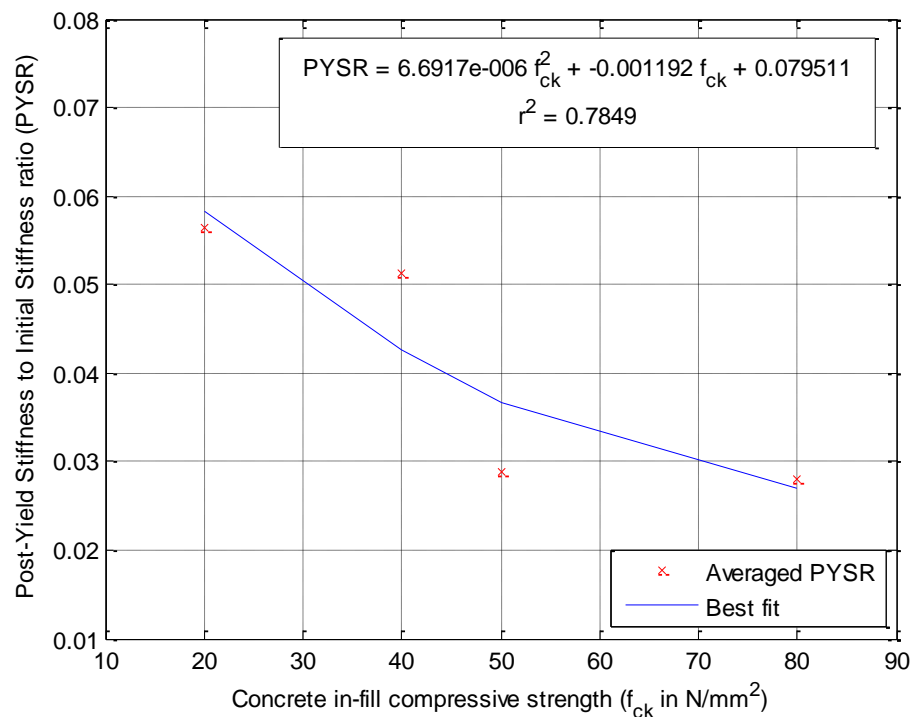


Figure 7.14 Post-Yield Stiffness ratio when varying concrete in-fill strength

Results obtained from the finite element model are used in attempt to increase the Coefficient of Determination (r^2) and subsequently improve the quality of the relation between the averaged Post-Yield Stiffness ratios and the concrete in-fill compressive strength. Post-Yield Stiffness ratios of the force-displacement curves obtained from finite element model results are calculated following the same procedure used for the experimental results.

The relation between the averaged Post-Yield Stiffness ratios of experimental and finite element results and the concrete in-fill compressive strength are shown in Figure 7.15. This relation is also represented with a 2nd degree polynomial.

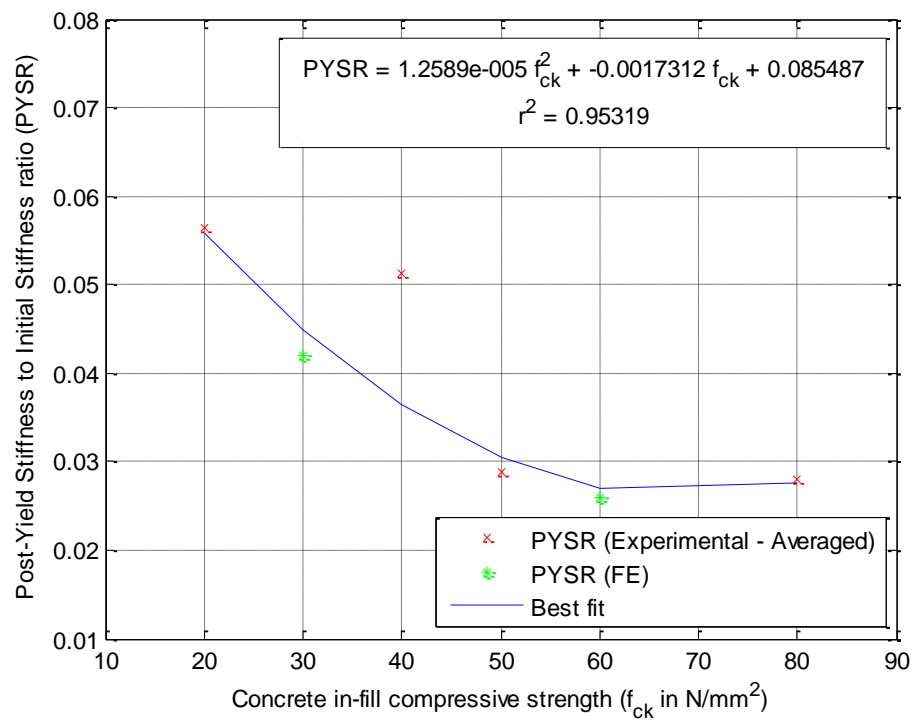


Figure 7.15 Post-Yield Stiffness ratio when varying concrete in-fill strength (FE + Experiments)

The Coefficient of Determination (r^2) of the relation observed when the finite element results are used has improved significantly. The

Coefficient of Determination (r^2) increased from $r^2 = 0.7849$ as shown in Figure 7.14 to $r^2 = 0.95319$ as shown in Figure 7.15. The quality of the relation between the averaged Post-Yield Stiffness ratios and the ratio the concrete in-fill compressive strength has improved after using the outcomes of the finite element model.

The best-fit functions for Post-Yield Stiffness ratio are used to develop charts that can be used to estimate this ratio. These charts, in addition to k_{is} and k_{yf} charts, are to be used calibrate the Analytical Model proposed in Chapter 3 as presented in the following section.

7.5 Proposed Semi-Analytical Model

This section details the final version of the Analytical Model proposed in Chapter 3 to predict the face bending behaviour of concrete-filled SHS. The approximated values for k_{is} , k_{yf} and Post-Yield Stiffness ratio are used in the calibration resulting in a Semi-Analytical Model shown in Figure 7.20. This model has three parts:

7.5.1 Part 1: Initial Stiffness

The Initial Stiffness of the model is to be calculated using:

$$S = \frac{16Et^3}{(b-t)^2} \frac{\frac{c_{is}}{(b-t)} + \left(1 - \frac{g+c_{is}}{b-t}\right) \tan \theta}{\left(1 - \frac{g+c_{is}}{b-t}\right)^3 + \frac{10.4 \left[1.5 - 1.6 \left(\frac{g+c_{is}}{b-t}\right)\right]}{\left(\frac{b-t}{t}\right)^2}} \quad (7-5)$$

in which E is the steel young's modulus, b is the SHS width, t is the SHS thickness and g is the bolts gauge. θ is an angle calculated as:

$$\theta = 35 - 10 \left(\frac{g+c_{is}}{b-t}\right) \quad (7-6)$$

The dimension c_{is} is calculated using:

$$c_{is} = k_{is} \times d_h \quad (7-7)$$

in which d_h is the bolt diameter and k_{is} is a calibration factor determined using the charts shown in Figure 7.17. These charts are developed using the best-fit functions for k_{is} determined in Section 7.3 of this thesis.

7.5.2 Part 2: Yield Force

The yield force of the model is to be calculated using:

$$F = 2 \pi M \left(1 + \frac{r}{r - \frac{c_{yf}}{2}} \right) + 2 M \frac{g}{r} \quad (7-8)$$

in which g is the bolt gauge. The dimension r is calculated using:

$$r = \frac{b - g - t}{2} \quad (7-9)$$

in which b is the SHS width, t is the SHS thickness. The yield moment of a unit length of the SHS face M is calculated using:

$$M = \frac{f_y t^2}{4} \quad (7-10)$$

where f_y and t are the yield stress of the SHS steel and the thickness of the SHS respectively. The dimension c_{yf} is calculated using:

$$c_{yf} = k_{yf} \times d_h \quad (7-11)$$

in which d_h is the bolt diameter and k_{yf} is a calibration factor determined using the charts shown in Figure 7.18. These charts are developed using the best-fit functions for k_{yf} determined in Section 7.3 of this thesis.

7.5.3 Part 3: Post-Yield Stiffness ratio

In the model, the Post-Yield Stiffness to Initial Stiffness ratio is to be determined from the charts shown in Figure 7.19. These charts are developed using the best-fit functions for Post-Yield Stiffness ratio determined in Section 7.4 of this thesis.

7.5.4 How to use the proposed charts

The following steps are used to determine each of k_{is} , k_{yf} or Post-Yield Stiffness ratio from the charts presented in Figure 7.17 to Figure 7.19:

1. Find the chart which corresponds to the desired concrete in-fill compressive strength.
2. In this chart, find the desired SHS face slenderness ratio in x-axis and draw a line upwards parallel to y-axis.
3. Find the line which corresponds to the desired β (bolt gauge to SHS face width ratio).
4. Draw a line from the intersection points between the two lines to the left (parallel to x-axis) until it crosses y axis to find k_{is} , k_{yf} or Post-Yield Stiffness ratio.

These steps are illustrated graphically in Figure 7.16. An example of how to determine k_{is} for SHS that have face slenderness ratio of 30, bolt gauge to SHS width ratio of 0.4 and 40N/mm² concrete infill is shown in the same figure (the number inside the circle is the step number).

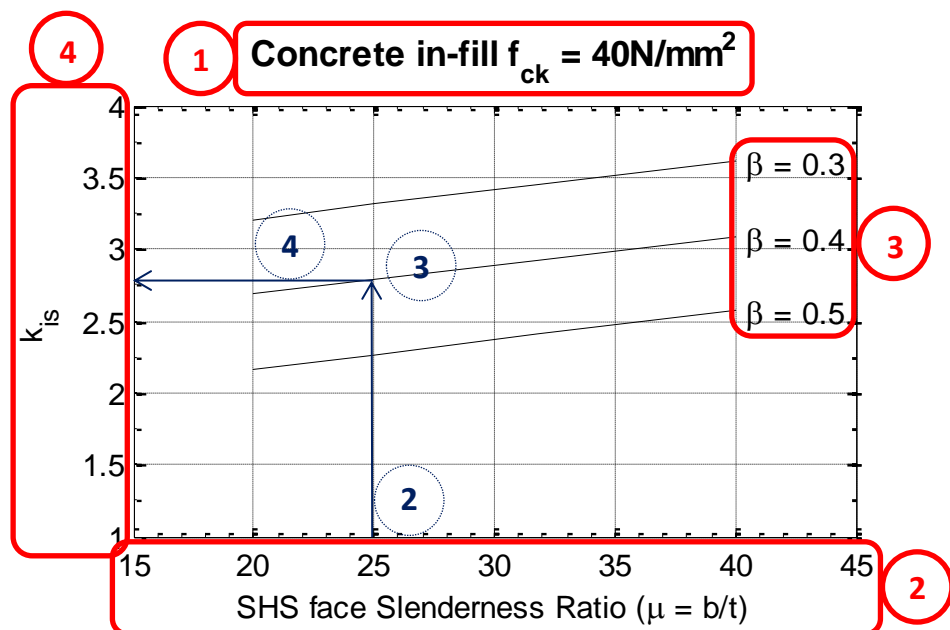
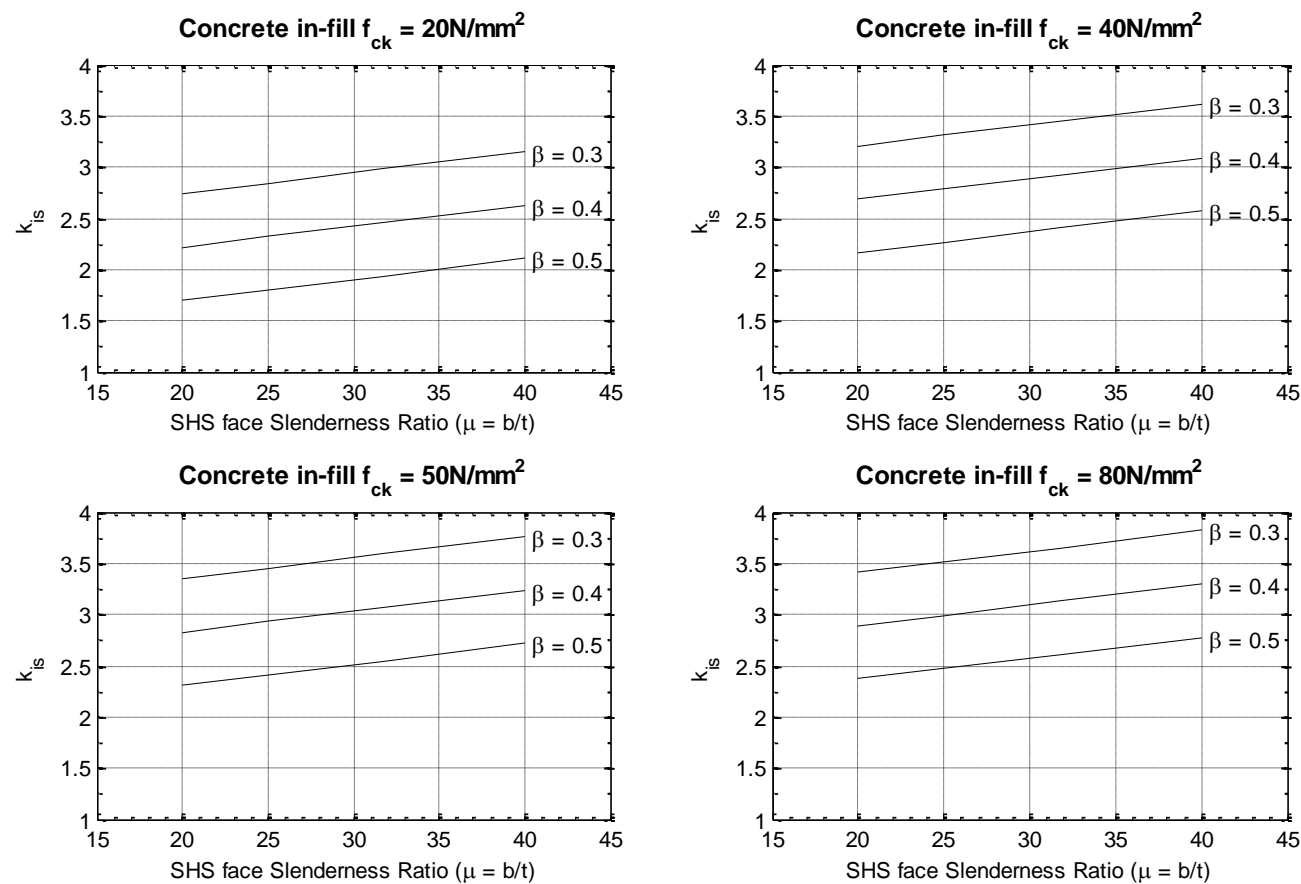
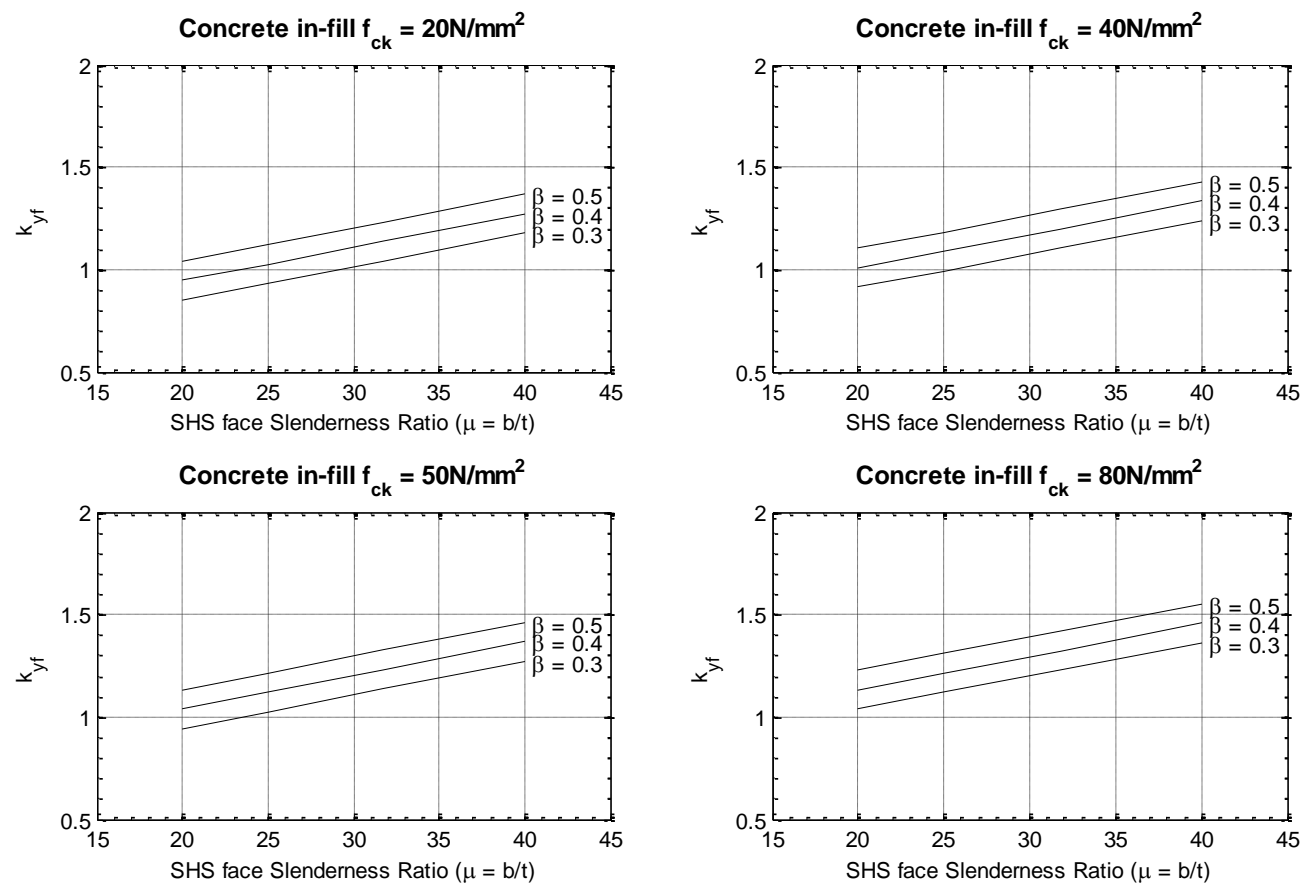


Figure 7.16 Illustration of how to use k_{is} , k_{yf} or Post-Yield Stiffness ratio proposed charts

Figure 7.17 Calibration factor k_{is} charts

Figure 7.18 Calibration factor k_{yf} charts

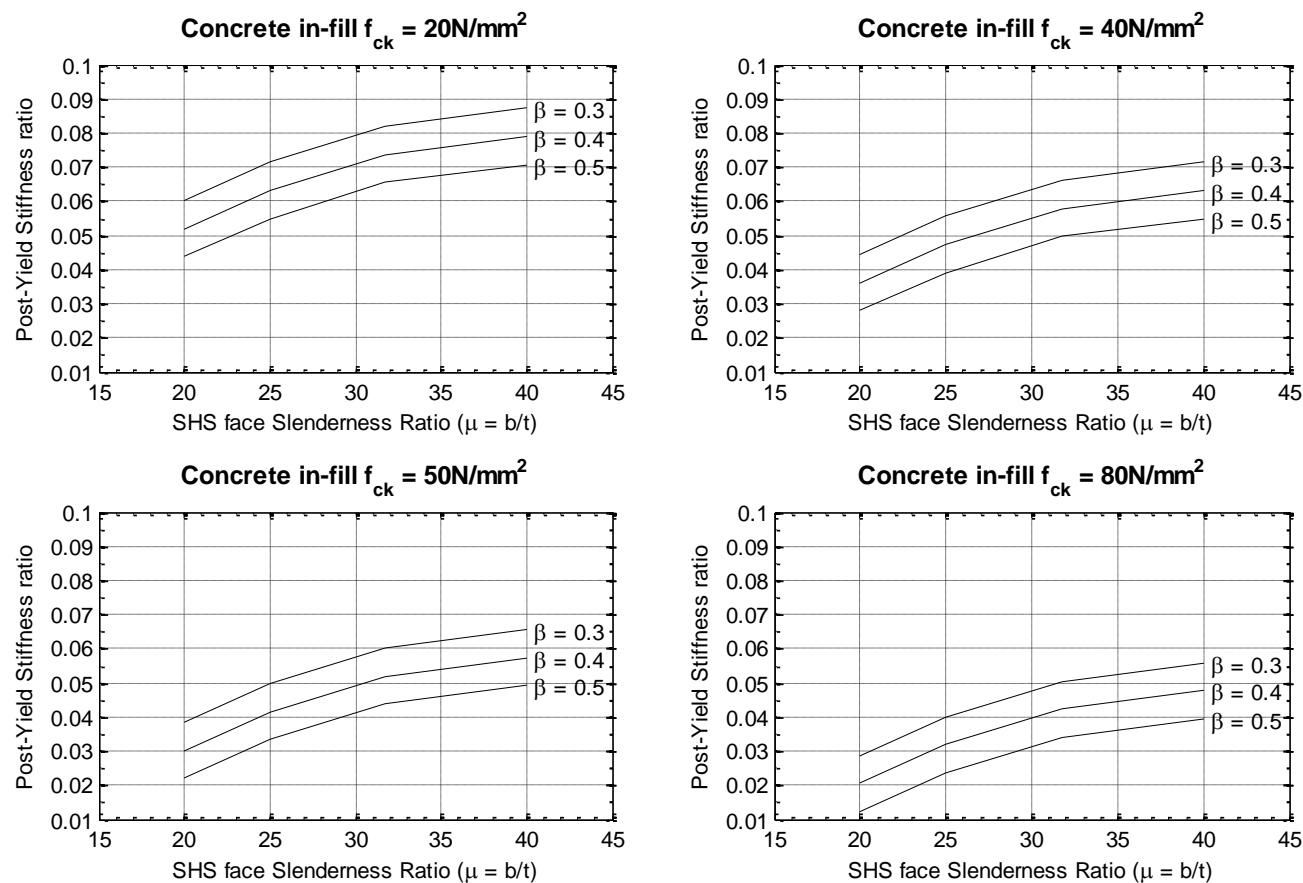


Figure 7.19 Post-Yield Stiffness ratio charts

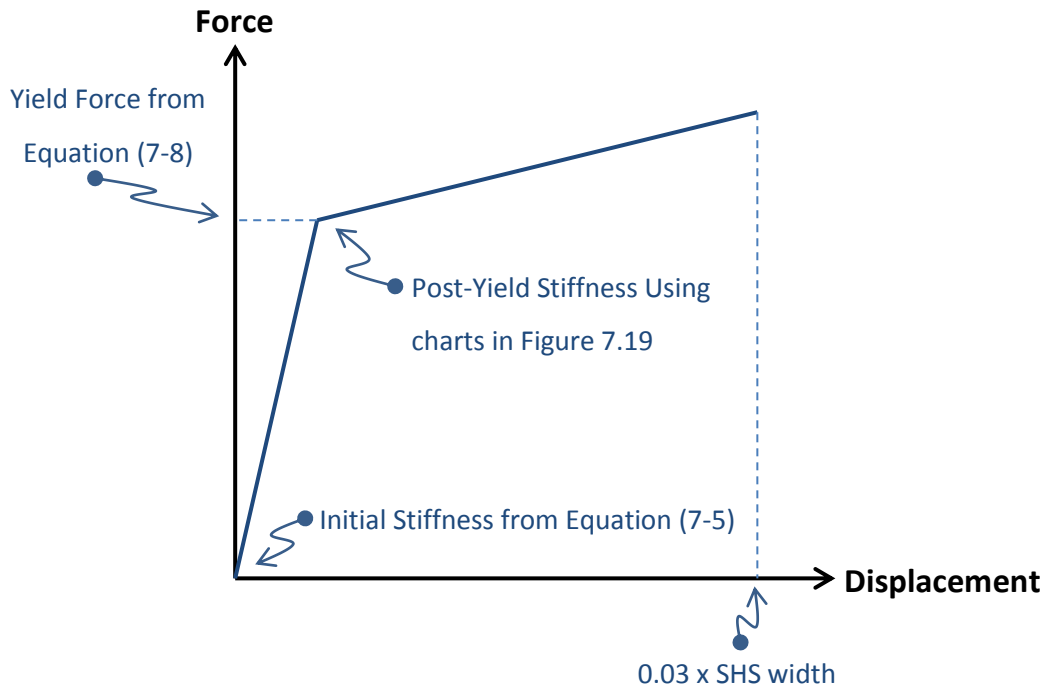


Figure 7.20 Proposed Model for the concrete-filled SHS face in bending

The maximum displacement of the SHS face is limited to 3% of the SHS width which is adopted in hollow sections design guides.

7.6 Statistical Analysis

The proposed Semi-Analytical Model is compared to the experimental results in this section. The Semi-Analytical Model is calculated using k_{is} , k_{yf} and Post-Yield Stiffness ratio determined from the charts shown in Figure 7.17, Figure 7.18 and Figure 7.19 respectively.

As the true concrete-filled SHS face bending behaviour cannot be determined, 90% prediction intervals are used to statistically predict the range in which 90% of future experiments will lay between. These intervals are compared with the proposed model. The prediction intervals are calculated using the experimental results obtained in this study assuming that they belong to a normal distribution. The prediction intervals are commonly calculated using:

$$\text{Intervals} = \bar{x} \pm t_{critical\ value} \cdot s \sqrt{1 + \frac{1}{n}} \quad (7-12)$$

in which n is the size of sample, \bar{x} is sample average, s is the sample standard deviation and t is determined from statistical tables (Devore and Farnum, 2005).

The best-fit of Initial Stiffness, Yield Force and Post Yield Stiffness are used to calculate \bar{x} and s of each set of identical samples. The calculated intervals are then plotted with the experimental results to define the ranges which statistically contain 90% of future identical samples. Similarly, the proposed model for each set of identical experiments is also plotted as shown in Figure 7.21 - Figure 7.29. It is clear from the figures that the proposed model is within the calculated 90% prediction intervals of experiments in all the considered experiments. The model predicted the concrete-filled SHS face bending behaviour with acceptable accuracy.

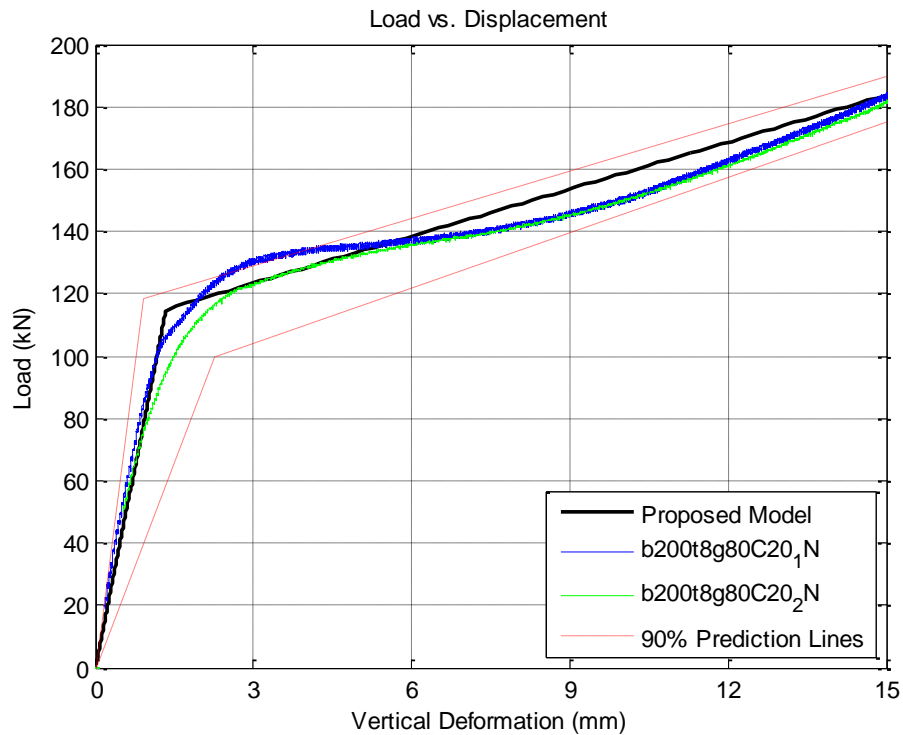


Figure 7.21 Proposed Semi-Analytical Model and b200t8g80C20-1&2

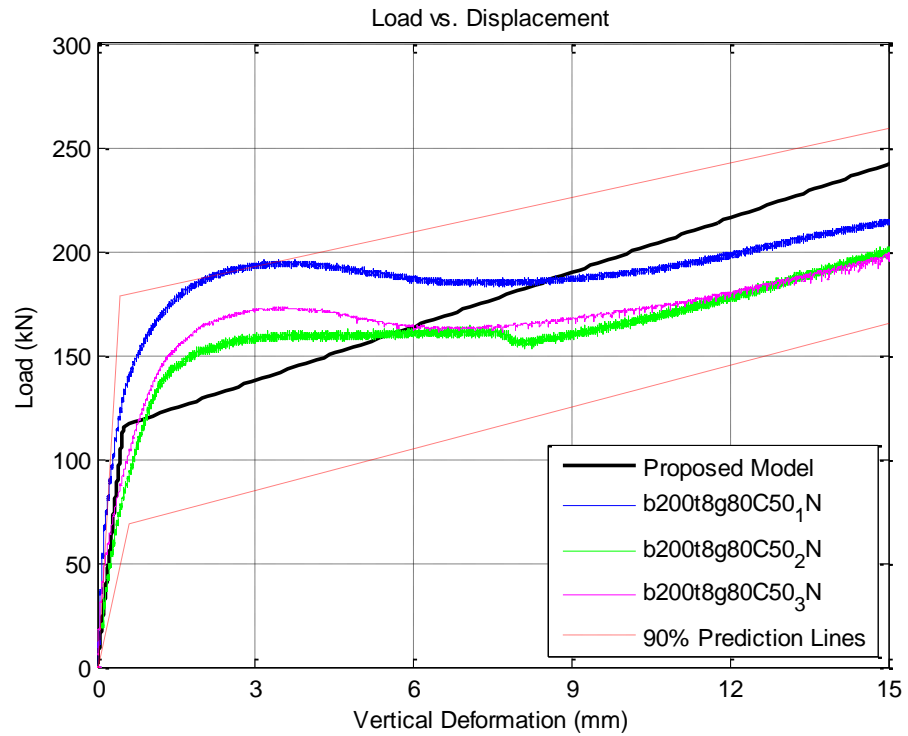


Figure 7.22 Proposed Semi-Analytical Model and b200t8g80C50-1,2&3

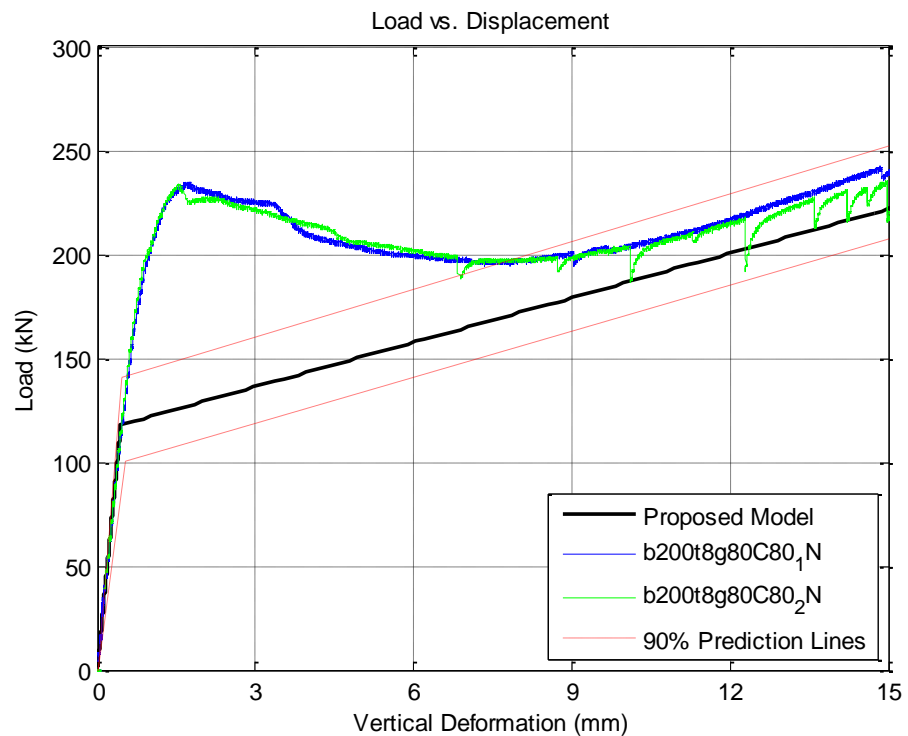


Figure 7.23 Proposed Semi-Analytical Model and b200t8g80C80-1&2

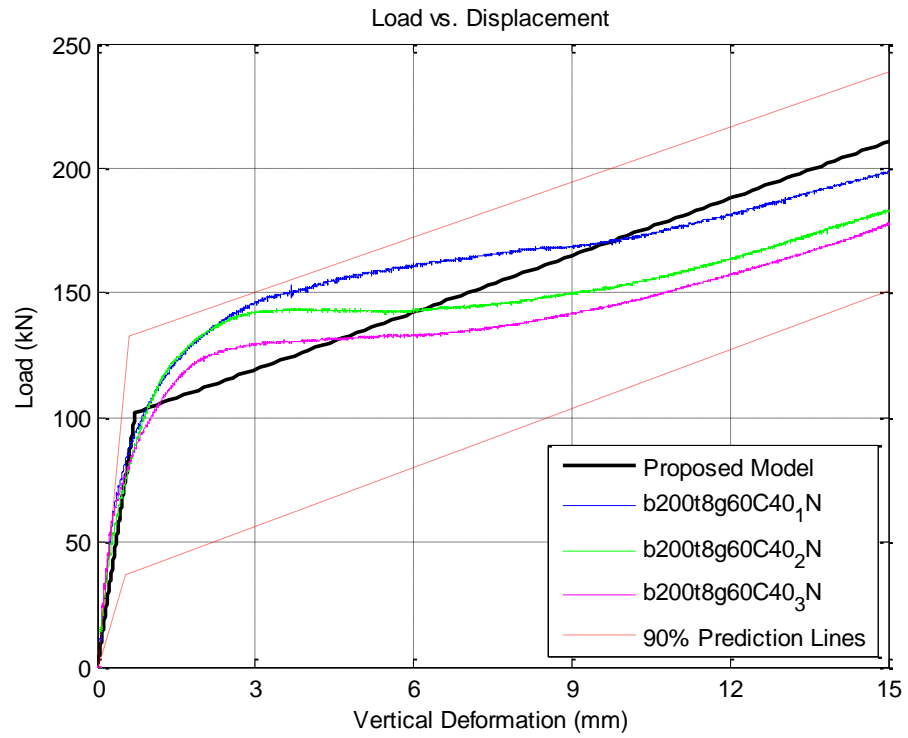


Figure 7.24 Proposed Semi-Analytical Model and b200t8g60C40-1,2&3

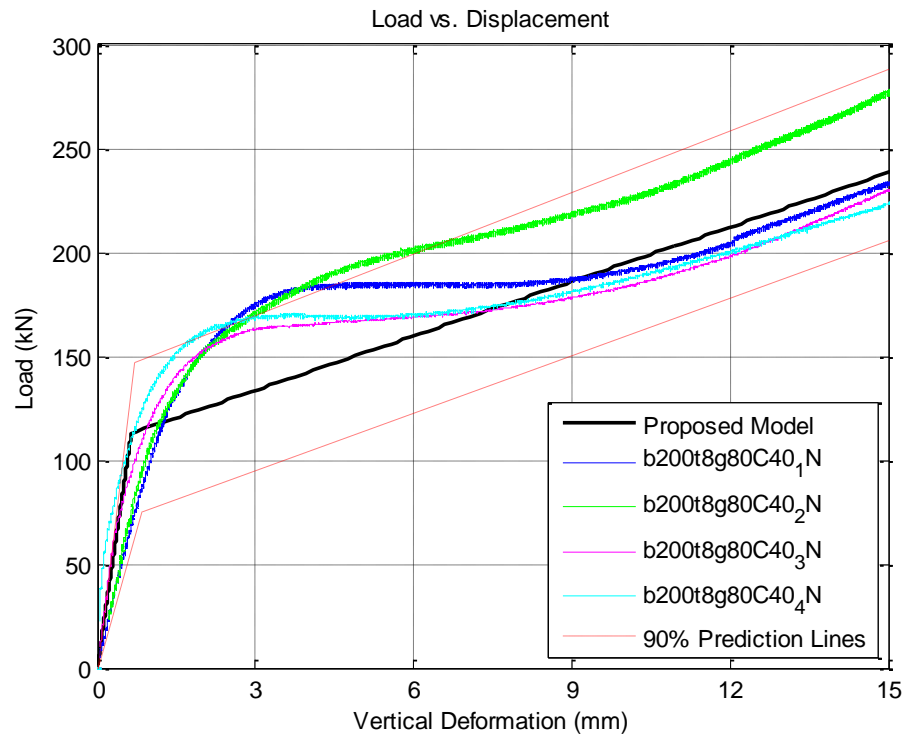


Figure 7.25 Proposed Semi-Analytical Model and b200t8g80C40-1,2,3&4

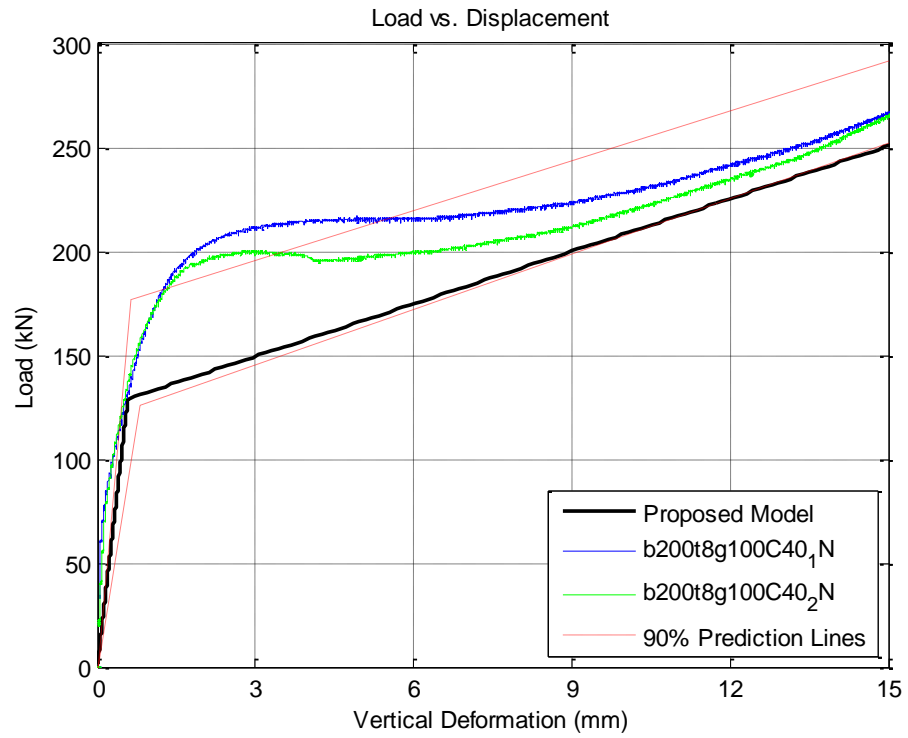


Figure 7.26 Proposed Semi-Analytical Model and b200t8g100C40-1&2

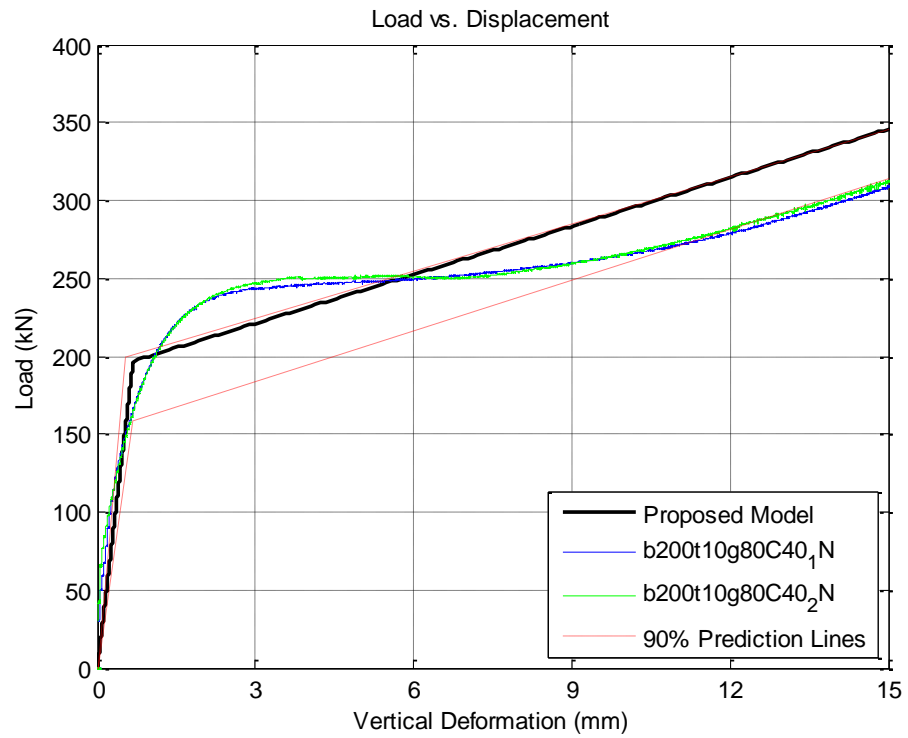


Figure 7.27 Proposed Semi-Analytical Model and b200t10g80C40-1&2

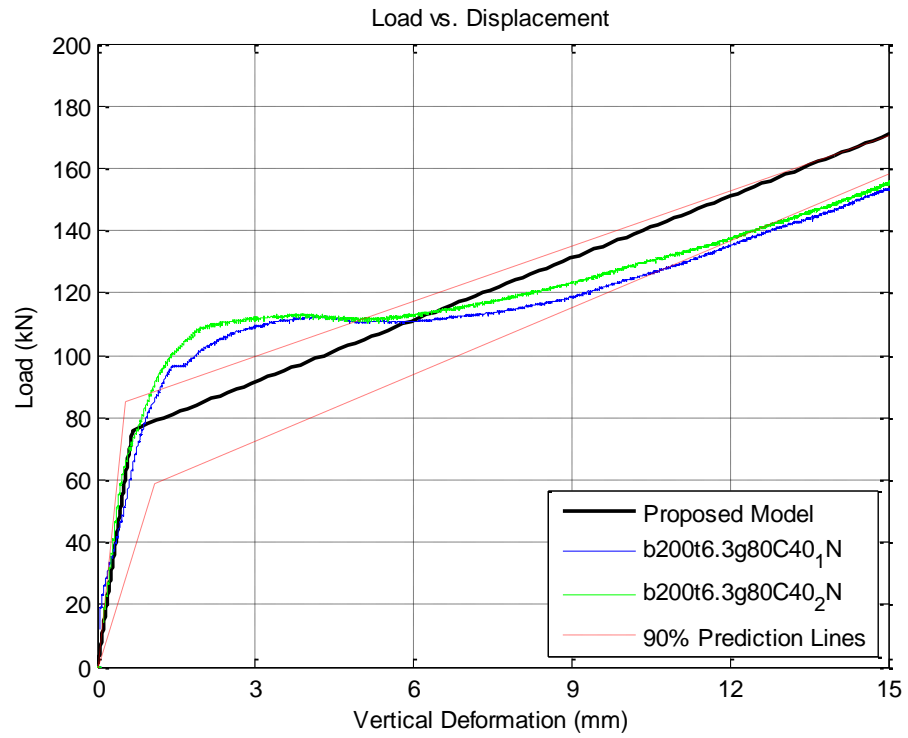


Figure 7.28 Proposed Semi-Analytical Model and b200t6.3g80C40-1&2

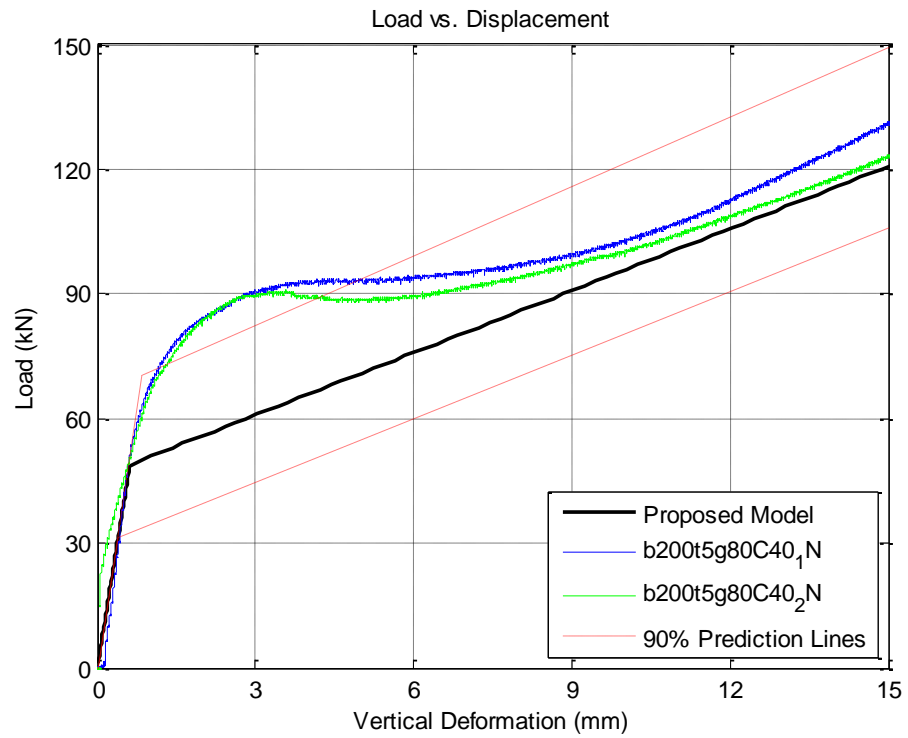


Figure 7.29 Proposed Semi-Analytical Model and b200t5g80C40-1&2

The model curve fluctuates between the 90% prediction lines: close to the lower prediction line such as in the case of samples b200t8g100C40-1&2 which are shown Figure 7.26, and close to the upper prediction line such as in the case of samples b200t10g80C40-1&2 which are shown Figure 7.26.

The proposed semi analytical model predicts a Yield Force less than the reported experimentally in some cases such as in Figure 7.23 when C80 concrete infill was utilised. From the shape of the experimental force-displacement curves of these cases, a Tri-Linear or Multi-Linear model would be more appropriate to predict such curves. The proposed model does not cater for the gain in yield force resulted by the use of high strength concrete in these cases. Yet, this would not have significant effect if the model is used for connection design not for predicting the actual yield force for these cases as it provide a conservative representation of the force-displacement relation.

The proposed model is also compared with Samples b300t12.5g120C40-1&2 as shown in Figure 7.30. These samples have slenderness ratio and bolt gauge to SHS width ratio that lay between the testing programme ranges. The only difference is that the samples are cut from SHS 300x300 rather than SHS 200x200.

90% prediction intervals are calculated for this comparison and are also shown in Figure 7.30.

As it can be seen from this figure, the model successfully predicted the Yield Force of the concrete-filled SHS face bending behaviour. However, the model failed to capture the Initial Stiffness of the behaviour neither the post-yield stiffness. The change in concrete-infill confinement state introduced when wider SHS is utilised could be the main reason behind this.

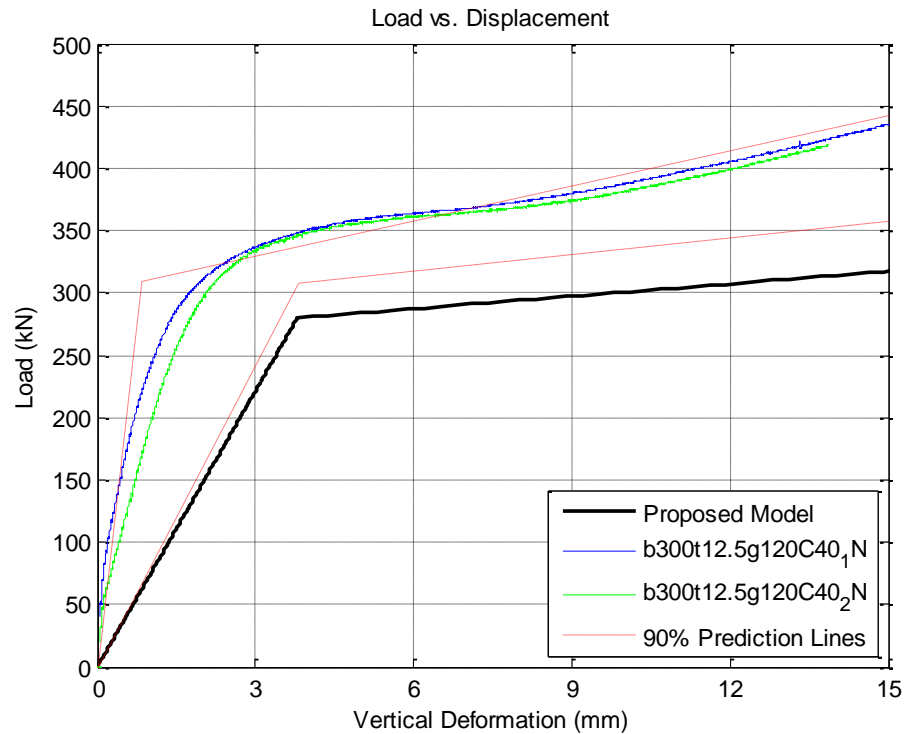


Figure 7.30 Proposed Semi-Analytical Model and b300t12.5g120C40-1&2

The same conclusion is found when the model was compared with samples b300t16g120C40-1&2 which is shown in Figure 7.31.

These were pilot experiments to test the model ability to predict the concrete-filled SHS face bending behaviour when the SHS has parameters outside the experimental programme range as the slenderness ratio of these samples is not within the range specified in Chapter 4.

In consequence, the proposed model should not be used if the considered SHS connection have SHS slenderness ratio and bolt gauge to SHS width ratio not within the testing programme range.

The limitations of the Semi Analytical Model proposed herein are listed in the following section.

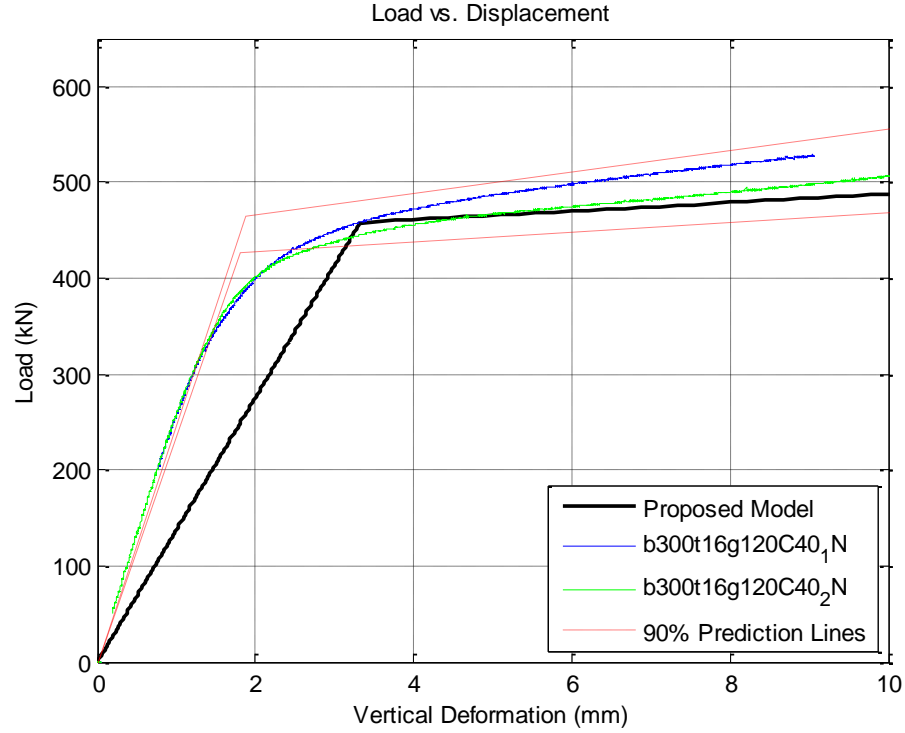


Figure 7.31 Proposed Semi-Analytical Model and b300t16g120C40-1&2

7.7 Prediction of Yield Force in the proposed model

As it can be seen from Figure 7.21 - Figure 7.29, the proposed model predicts a relatively low yield force when compared to the experimental load-deflection response when a high-strength concrete-infill is used (concrete compressive strength of 50N/mm^2 and 80N/mm^2). For these cases, a tri-linear or a multi-linear model would be more suitable to predict the higher yield point controlled by the concrete-infill. Investigation of such model is recommended for further research to account for the yield force controlled by the concrete-infill compressive strength. To use the proposed model in these cases, the yield force could be calculated using Equation (7-8) where the parameter c_{yf} is calculated using the following equation:

$$c_{yf} = 2 \times k_{yf} \times d_h \quad (7-13)$$

in which d_h is the bolt diameter and k_{yf} is a calibration factor determined using the charts previously shown in Figure 7.18. This calibration factor is influenced by the concrete strength. However, it is still underestimating the yield from very strong concrete (e.g. C80). It is therefore recommended that further research is done on the calibration of the k_{yf} factor.

The yield force calculated using Equations (7-8) and (7-13) for each experiment is shown in Figure 7.32 - Figure 7.40. As it can be seen from These figures, using Equation (7-13) to calculate the yield force lead to more accurate prediction of the yield point especially when high strength concrete-infill was used. However, the predicted post-yield stiffness accuracy has been affected.

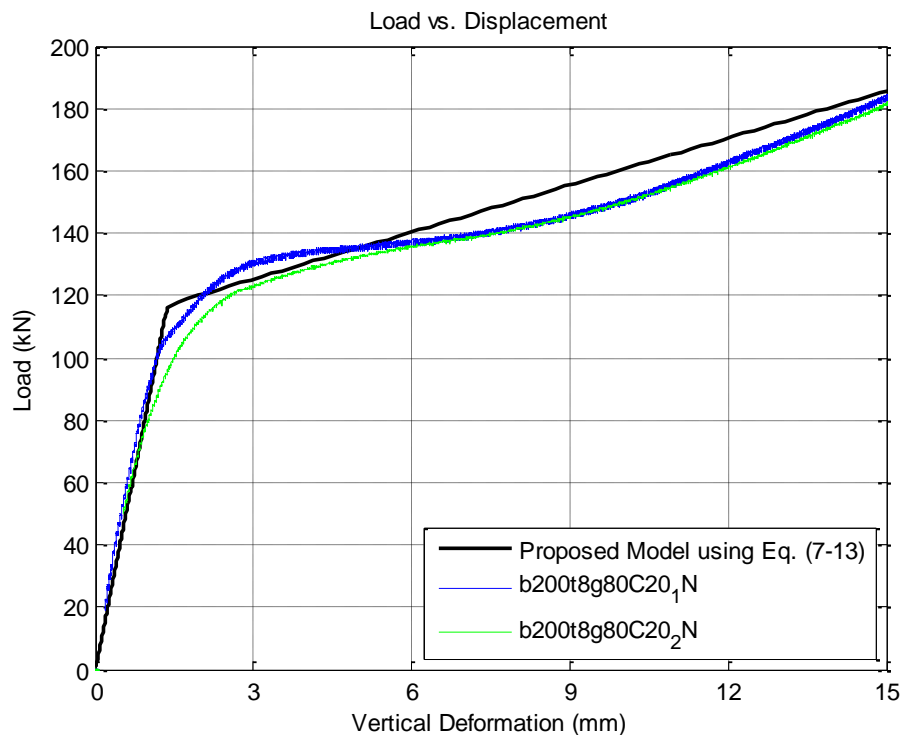


Figure 7.32 Proposed Model using Eq. (7-13) for b200t8g80C20-1&2

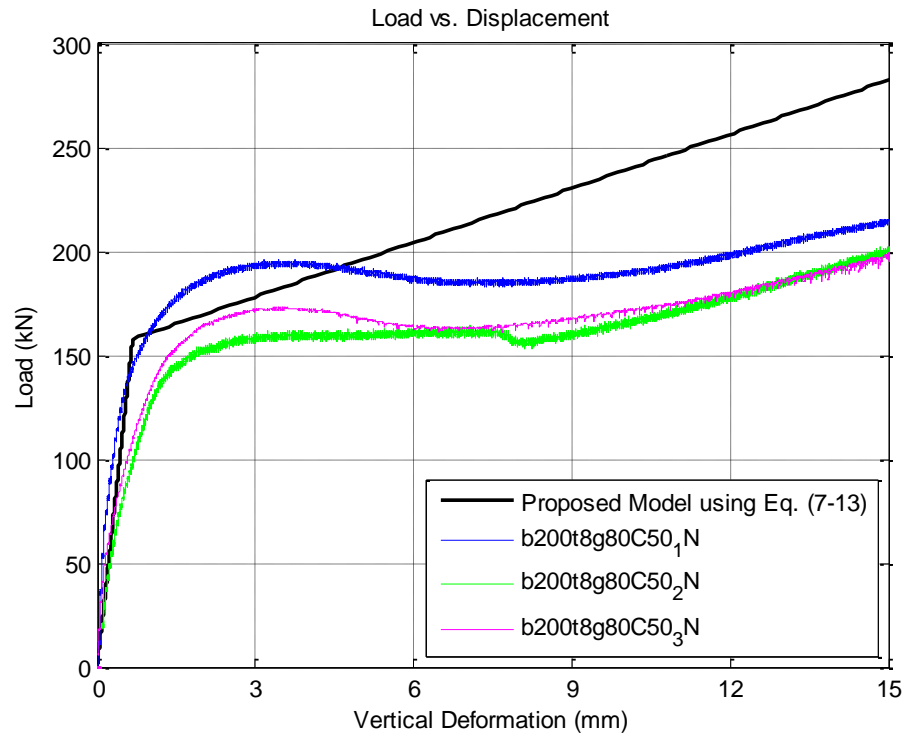


Figure 7.33 Proposed Model using Eq. (7-13) for b200t8g80C50-1,2&3

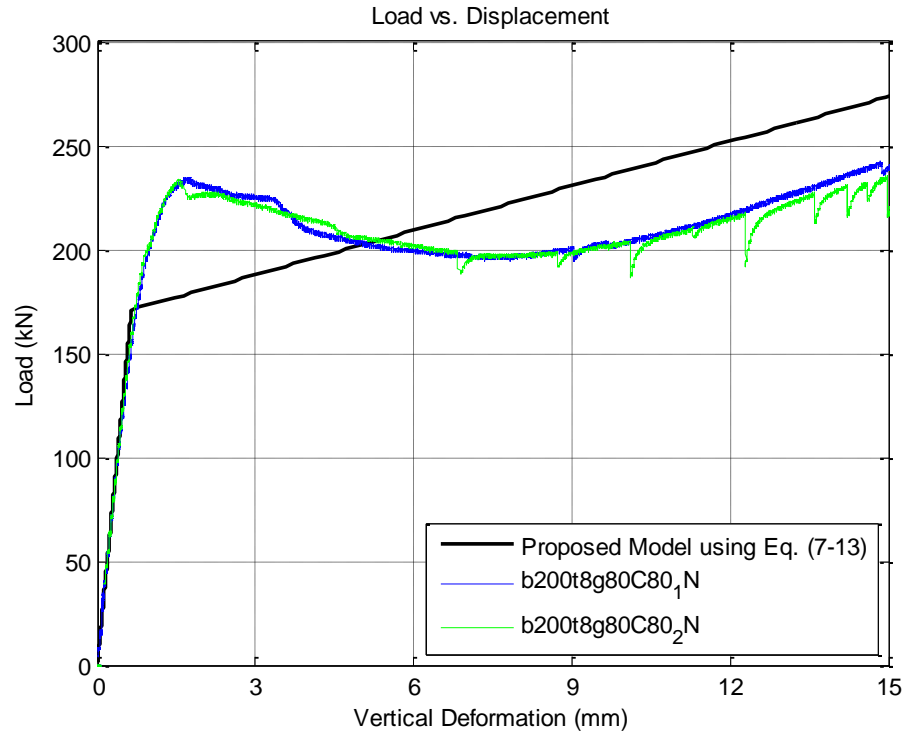


Figure 7.34 Proposed Model using Eq. (7-13) for b200t8g80C80-1&2

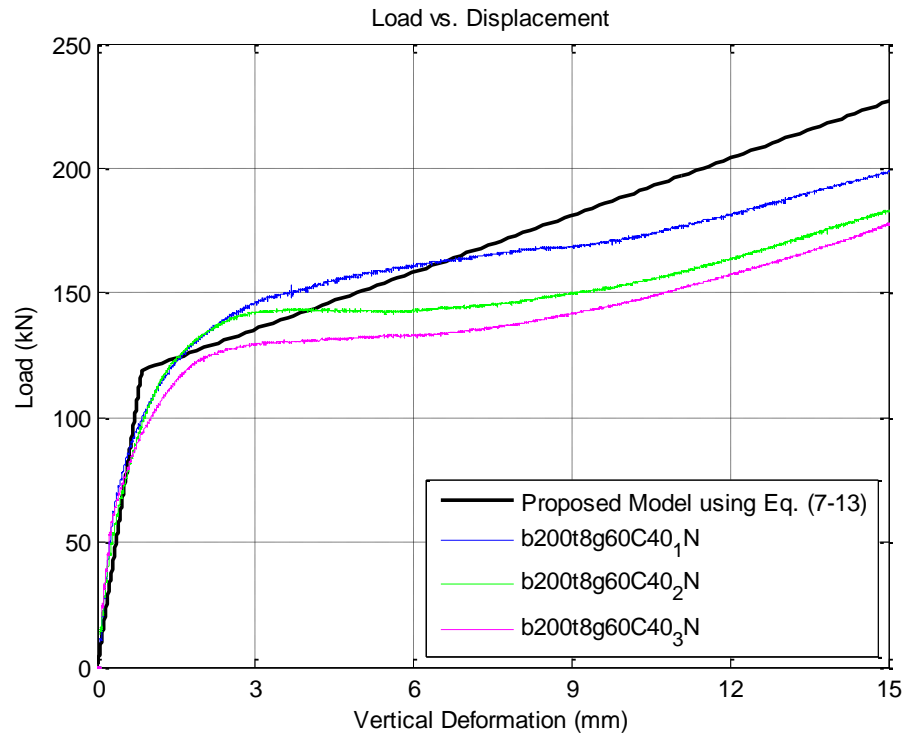


Figure 7.35 Proposed Model using Eq. (7-13) for b200t8g60C40-1,2&3

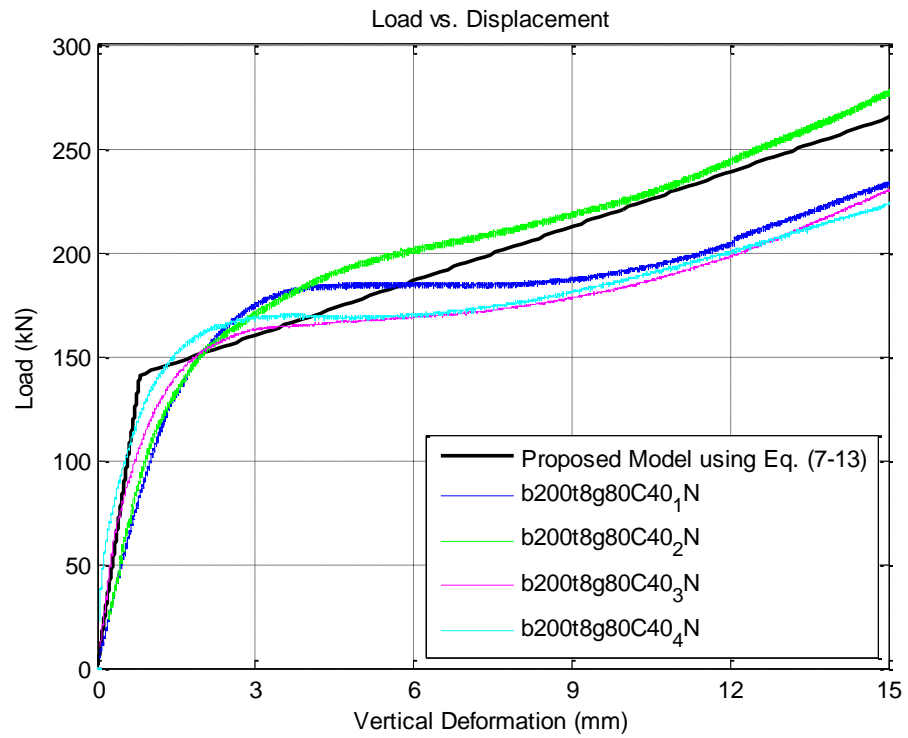


Figure 7.36 Proposed Model using Eq. (7-13) for b200t8g80C40-1,2,3&4

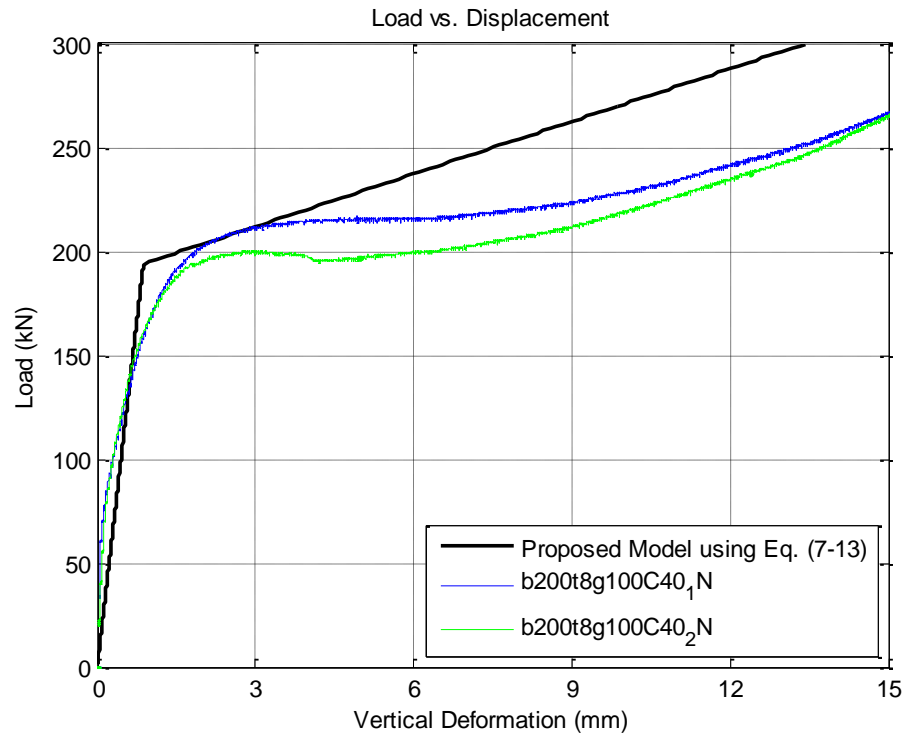


Figure 7.37 Proposed Model using Eq. (7-13) for b200t8g100C40-1&2

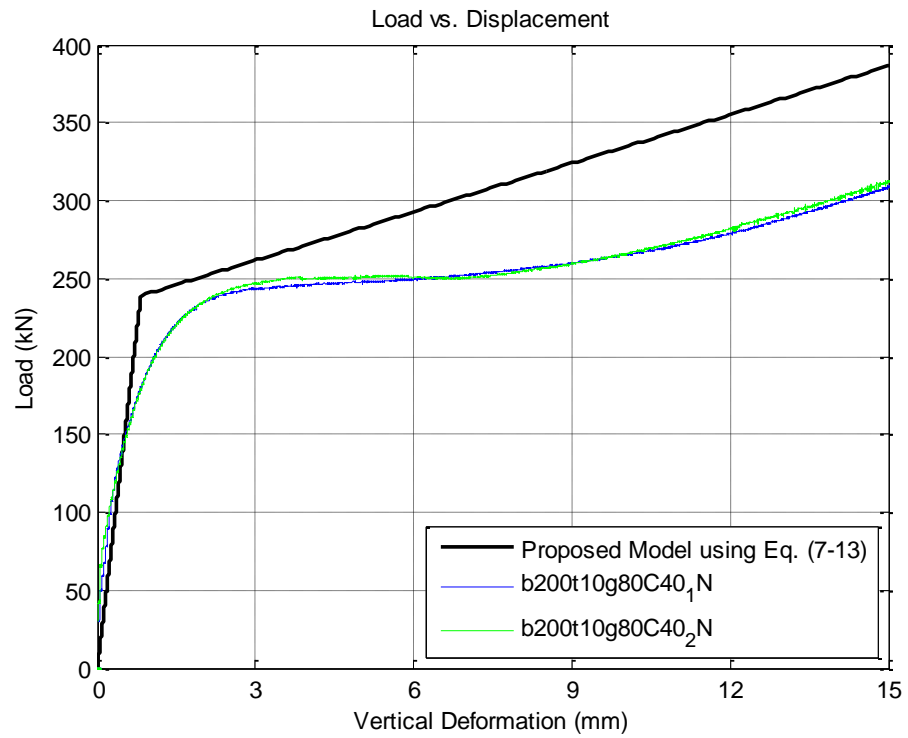


Figure 7.38 Proposed Model using Eq. (7-13) for b200t10g80C40-1&2

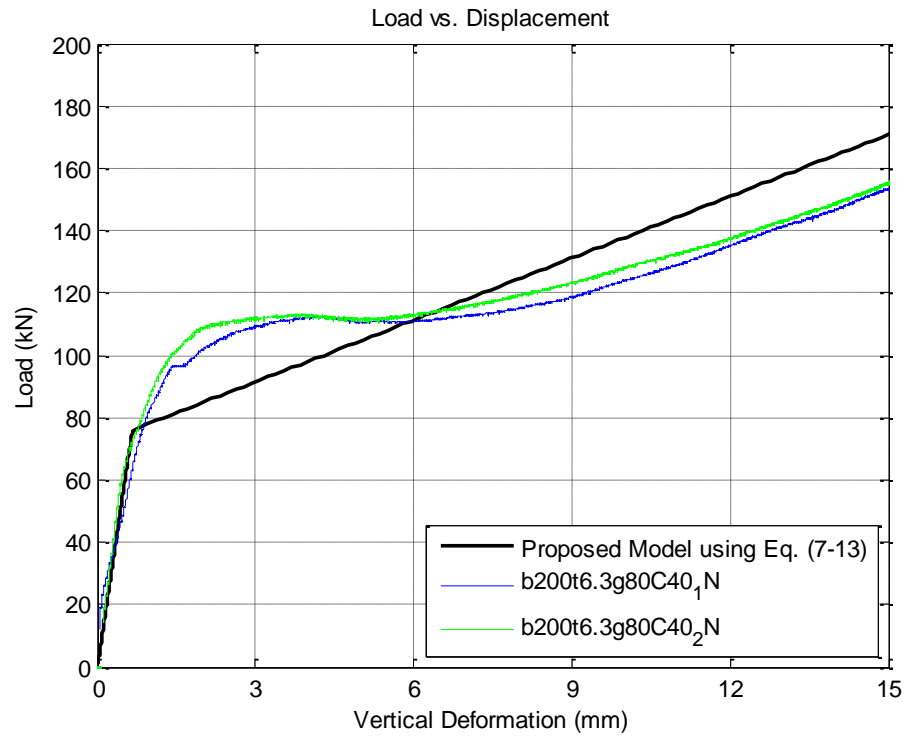


Figure 7.39 Proposed Model using Eq. (7-13) for b200t6.3g80C40-1&2

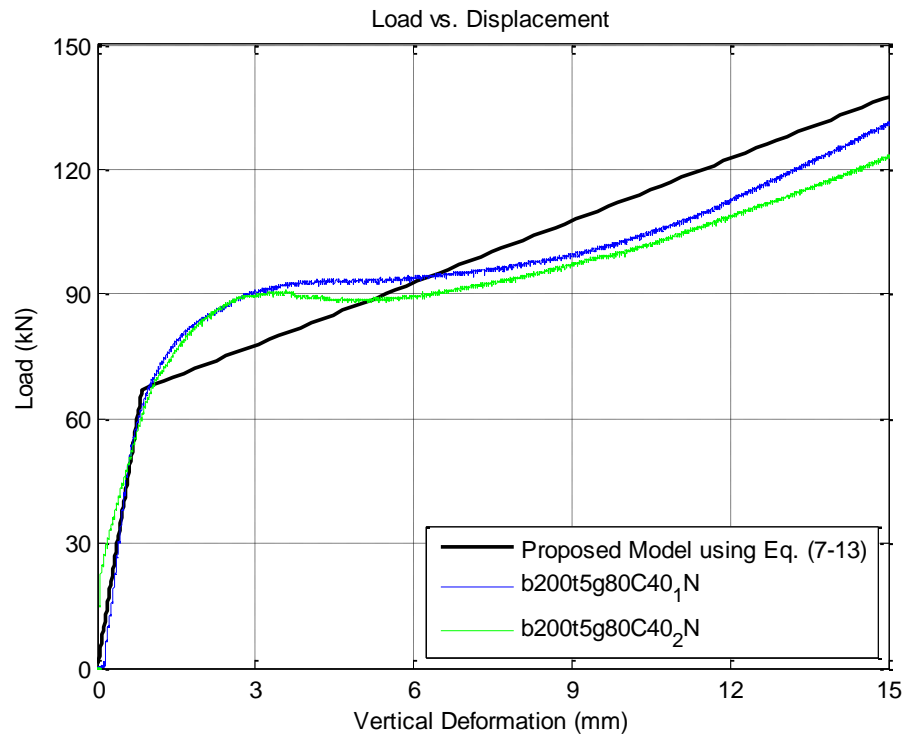


Figure 7.40 Proposed Model using Eq. (7-13) for b200t5g80C40-1&2

7.8 Proposed Semi-Analytical Model limitations

The proposed Semi-Analytical Model of the face bending behaviour of concrete-filled SHS (described in section 7.5) is limited to the following parameters:

- SHS 200x200 in which one row of two bolts is in tension.
- HB16 with minimum clamping thickness.
- SHS face slenderness ratio between 20 and 40.
- Bolt gauge to SHS width ratio of 0.3, 0.4 and 0.5.
- Concrete in-fill compressive strength: 20 and 40N/mm².

Also, the statistical analysis done here in this chapter assumes that the data are normally distributed hence the use of standard t values in the calculation of the prediction lines.

Likewise, appropriate safety factors are to be considered when the proposed model is used for Hollo-Bolted connection design.

7.9 Summary

The experimental results were analysed in this chapter. The results were used to develop design charts for k_{is} , k_{yf} and Post-Yield Stiffness ratio. The charts were used to calibrate the Analytical Model previously proposed in Chapter 3 resulting in a Semi-Analytical Model of the face bending behaviour of concrete-filled SHS. Prediction intervals were used to compare the model to experimental results. The proposed model is found to predict the face bending behaviour of concrete-filled SHS with acceptable accuracy when a concrete-infill which has a compressive strength within the range 20 - 40N/mm² is used.

The main findings of this study as well as recommendations for further work are presented in next chapter.

Chapter

Conclusions and Recommendations

8.1 Introduction

This research aimed to devise a theoretical model for the structural behaviour of the face bending of concrete-filled Square Hollow Sections when connected to other structural members using Hollo-Bolts. This was done as part of the on-going research of Hollo-Bolted connections at the University of Nottingham. It was focused on end-plate connections where one row of Hollo-Bolts, i.e. two Hollo-Bolts, is subjected to tension.

The set of objectives which were initially agreed to reach the research aim were satisfied as explained below:

- Objective 1 was to study the state-of-the-art of available literature that involves blind bolted connections especially the ones which consider SHS face bending behaviour. The work done to meet this

objective was presented in Chapter 2 which highlighted the gap in knowledge to be filled by this research.

- Objective 2 was to develop a theoretical model for the face bending behaviour of concrete-filled SHS when connected to other structural members using Holo-bolts. As shown in Chapter 3, a theoretical model was developed to predict the force-displacement relation of this behaviour. It consisted of three parts: Initial Stiffness, Yield Force and Post-Yield Stiffness. The expression previously developed by Simões da Silva et al. (2004) was modified to calculate the Initial Stiffness of the model. Yield Line analysis was used to determine the critical failure mechanism and to calculate the Yield Force. Finally, the Post-Yield Stiffness was taken as a percentage of the Initial Stiffness.
- Objectives 3 and 4 were to determine the parameters which may influence the theoretical and design and conduct an experimental programme to evaluate the effect of varying these parameters. This work was presented in Chapter 4. The range, parameters and instrumentations of the Experimental Programme are described in that chapter. The results of the experimental program as well as the effect of varying parameters on the face bending behaviour of concrete-filled SHS were presented in Chapter 5 of this thesis.
- Objective 5 was to develop and validate a finite element model to complement the experimental program outcomes. The model was developed using ANSYS APDL and detailed in Chapter 6. The outcomes of the finite element model including charts describing the face bending behaviour of concrete-filled SHS were shown in the same chapter. The charts were formulated for all SHS 200x200 thicknesses filled with 40N/mm² concrete, and with bolt gauges of 60mm, 80mm and 100mm.

- Objective 6 was to calibrate the theoretical model using the data collected from the experimental programme. The outcomes of the Experimental Programme were used to calibrate the theoretical model. This was done by introducing two calibration factors: k_{is} and k_{yf} to account for the shape of the Holo-Bolts. Charts for these factors were developed leading to the proposed Semi-Analytical model as shown in Chapter 7.
- Objective 7 was to establish a simplified approach from the theoretical model that can be used for connections design. A Semi-Analytical model was proposed and compared to the experimental results as shown in Chapter 7. The proposed model predicted the force-displacement relation of the face bending behaviour of concrete-filled SHS with acceptable accuracy except for the cases where the SHS were filled with 50-80N/mm² compressive strength concrete, and could be used for Holo-Bolted connection design after applying appropriate safety factors.

A summary of the key findings of this research are presented in the next section. This is followed by highlights of the contributions of this work and possible application. At the end of the chapter, recommendations for future work are suggested.

8.2 Observations and Conclusions

The followings were observed during the Experimental Programme conducted during this investigation:

- It was observed that there are some yield lines developed to the SHS edge and even extended to the SHS side walls which contradict with the theory which it only develop until half of the side wall thickness.
- It was observed that the failure in the experiment does not occur due to materials reaching their ultimate strength. Instead failure

occurs due to large deformation of SHS holes which lead to the bolts physically pushed out of the SHS.

- With regard to the SHS face bending, various face bending behaviour was visually observed in the part of SHS face between the bolt holes. Minimal face bending deformation was observed in this part in thick SHS and/or SHS with small bolt gauge. More bending deformation was observed with the decrease of SHS thickness and/or the increase of bolt gauge. An example of this is shown in Figure 5.4.
- It proved to be difficult to cut the SHS face to expose the concrete-infill after the tests without it been disturbed to explore the behaviour of the concrete-infill. In one successful attempt, two patterns of concrete cracks were observed: one at a parameter around the two bolts, and the second at outer parameter restrained by SHS walls. The outer cracks resemble the SHS face bending deformation. It is very difficult to reach any conclusion based on this, however, it does hint to the forming of the assumed theoretical concrete cone.

Furthermore, the following conclusions were found during this investigation:

- When the Yield Line analysis was conducted, possible failure mechanisms were considered as well as idealised mechanism commonly adapted in practice for the loading arrangement considered (as shown in Figure 3.4). Mechanism 3 was found to be less conservative than the idealised mechanism represented by Mechanism 4.
- The force-displacement relation of the SHS face bending observed from experiments was found to consist of three parts: the initial stiffness part where the force increases sharply, the yield force part where there is no or minimal increase in the force magnitude with

the increase of the displacement and lastly the post-yield part where the force undergoes a softer increase with the displacement.

- Across the range considered in this investigation, it was found that the bolt gauge had a significant effect on the magnitude of the yield force. An increase of about 15% of the yield force was observed when the bolt gauge increased from 60mm to 80mm (from $\beta=0.3$ to $\beta=0.4$). Moreover, when the bolt gauge increased from 80mm to 100mm, the yield force increased by more than 25%. The initial stiffness was found to increase with the increase of the bolt gauge. The same conclusion was found from the finite element modelling results. The Post-Yield stiffness was not affected by the change of bolt gauge.
- Similarly, both the Yield Force magnitude and the Initial Stiffness of the bending behaviour were improved with the increase of the SHS thickness (i.e. decrease of SHS face slenderness ratio). Post-Yield stiffness was not affected by any change in SHS face slenderness across the considered range. The same conclusion was found from the finite element modelling results.
- The concrete-infill compressive strength was found to directly affect the general behaviour of SHS face bending. This is seen particularly in the part of the force-displacement curves which represents the face yielding (Yield Force). The initial and post-yield parts of the force-displacement curves were not significantly affected. The magnitude of yield force was improved by the increase of the compressive strength. Nonetheless, in the tests where 80N/mm^2 concrete-infill was used, a drop in force magnitude of about 20% preceded the increase of force after the yielding stage before it climbed again in the post-yield part of the curve. 5% and 0% drop in in the tests where 50N/mm^2 and 20N/mm^2 concrete-infill was used.

- The effect of concrete-infill strength on the SHS face bending behaviour can be described in three stages. The initial stage in which both the SHS face and concrete-infill work together to take loads transferred from the bolt. This stage ends when some deformation occurs on the SHS face i.e. the bolts have to move/displace. This movement cannot take place unless the part of concrete-infill in front of the bolts' sleeves is crushed or separated from the rest of restrained concrete. It is assumed that a concrete cone forms in front of bolts' sleeves at this stage as cracks were observed in some tests. The concrete-infill compressive strength has a direct effect on this stage as it can be seen from the tests that the use of higher strength concrete-infill results in higher yielding force. The contribution of the concrete-infill becomes minimal after this stage. Therefore, in the intermediate stage, the force drops from the yield force magnitude to a level of which the SHS face becomes the main source of resistance. In the final stage the SHS face is the main source of resistance hence the similarity in the post-yield part of the force displacement-curves.
- The calculated Yield Force calibration factor (k_{yf}) was significantly lower (at least 50% less) than its counterpart Initial Stiffness calibration factor (k_{is}). This hints that the concrete in-fill behave differently at each stage of the tests. At the initial stage, more concrete in-fill are involved in the loading mechanism hence the reported higher value of k_{is} . This could be attributed to the fact that the low-magnitude load applied at the initial stage of the test causes low level of stresses in the concrete-infill around the bolts. At the later stage of the tests, the low k_{yf} indicate that less concrete in-fill around the bolt is involved in the loading mechanism. This could be also attributed to the stresses on the concrete in-fill. The magnitude

of the applied force at the later stage of the tests indicates that the stresses at part of the concrete-infill must have exceeded its ultimate capacity. Also, the reported high deformation in the SHS face at the later stage of the tests could not have happened unless part of the concrete in-fill around the bolt breaks from the rest of concrete in-fill. This conclusion could not be fully verified though no significant concrete in-fill crushing was observed in any of the tests.

- The proposed Semi-Analytical model successfully predicted the force-displacement relation of the concrete-filled SHS face bending for SHS 200x200 with acceptable accuracy when 20-40N/mm² concrete-infill were used.
- The proposed Semi-Analytical model failed to predict the force-displacement relation of the concrete-filled SHS face bending for SHS 300x300. This was shown when the model was compared to pilot experiments where the samples were cut from SHS 300x300. The proposed model successfully predicted the Yield Force of the concrete-filled SHS face bending behaviour but failed to capture the Initial Stiffness and the post-yield stiffness.

8.3 Contribution of this work

The main contribution to knowledge of this research is the proposed Semi-Analytical model. The proposed model, which is shown in Section 7.5 of Chapter 7, was found to describe force-displacement relation of the face bending behaviour of concrete-filled SHS with acceptable accuracy within the tested range.

The proposed model provides sufficient understanding of the behaviour and could be used to model and design Hollo-Bolted connections provided that appropriate safety factors are applied. The model was found to fit within 90% prediction lines of all the conducted

experiments with the exception of the ones which utilised high strength concrete-infill.

Also, the validated finite element model was used to formulate charts that describe the force-displacement relation of concrete-filled SHS face bending component. The charts covered:

- All SHS 200x200 thicknesses,
- 40N/mm^2 concrete in-fill compressive strength, and
- Bolt gauges of 60mm, 80mm and 100mm

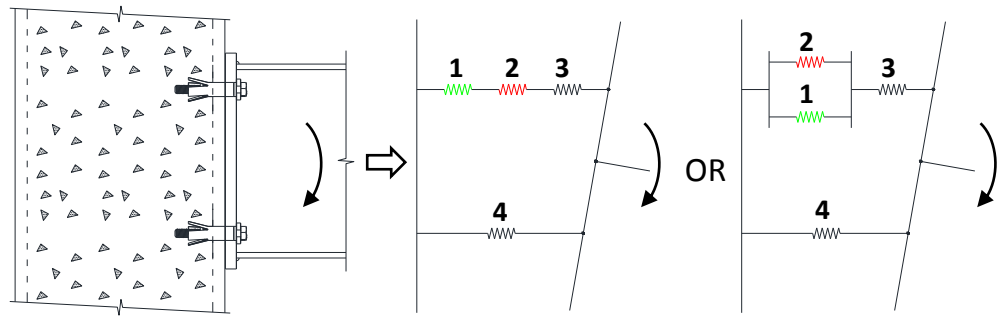
Additionally, this research contributes to knowledge by providing:

- A better understanding of the face bending of concrete-filled SHS of Hollo-Bolted connections.
- A step forward towards the modelling of Hollo-Bolted connections.
- A means for the possible use of Hollo-bolts to produce moment-resisting connections to hollow sections.
- Recommendations for Future Work.

8.4 Application of the proposed Semi-Analytical model

In a beam-to-column connection within the component method framework, the basic components of the connection determine its behaviour. To determine the behaviour of a beam to hollow section column connection utilising the novel Hollo-Bolts, two components are missing: the Hollo-Bolt in tension and the hollow section face bending. The model proposed in this study provides the characteristics of the concrete-filled SHS face bending component for the range specified in previous chapters. This is a step further in the way of determining the behaviour of Hollo-Bolted connections, however, how this component will interact with the other components is yet to be fully investigated

when a model for the Hollo-Bolt in tension exist. Possible component-based model of a Hollo-Bolted connection is shown in Figure 8.1. Two models are shown in this figure in which components are acting together in-parallel and in-series (accurate model cannot be yet investigated as Hollo-Bolt in tension component does not exist to date).



- 1: Concrete-filled SHS face in bending when using Hollo-Bolts (proposed in this work)
- 2: Hollo-Bolt in tension (not known to date)
- 3: End-plate in tension
- 4: Concrete-filled SHS face in compression
- (To consider: Beam flange and web in compression and/or tension)

Figure 8.1 Simple component-based models for Hollo-Bolted connection

8.5 Recommendations for Future Work

The following suggestions are recommended for further research:

- It was observed during the testing program that there are some yield lines extended to the SHS edge and developed on the SHS side walls which contradict with the theory which assumed that these lines only develop until half of the side wall thickness. This should be investigated possibly by using the DIC or stain gauges on the SHS side wall to study the stain distribution along the sides.
- The alignment of Hollo-Bolts sleeves was found to affect the location of the maximum face deformation in few tests. This should be further investigated possibly by means of finite element analysis.

- Weld-seam exists on one the SHS faces from the manufacturing process. This weld theoretically should affect the face bending behaviour and should be investigated further. Testing the welded face of the SHS could be avoided in controlled testing environment however joints where multiple beams are connected to SHS column in the same level are common in reality. Full scale testing is the best way of doing this.
- The finite element model should be used to conduct more experiments on other SHS sections e.g. SHS 250x250 and SHS 300x300 and using various concrete-infill strengths. This was not done during the course of this study due to time constraints.
- The same methodology used in this investigation should be used to develop models for the Extended Hollo-Bolt which is being developed in the University of Nottingham. In theory, the extension of the bolt shank in the extended Hollo-Bolt should lead to similar behaviour to the standard Hollo-Bolt with higher magnitude. This is because more concrete infill will be involved in the force transfer mechanism from the bolts to hollow section face. An example is shown in Figure 8.2.

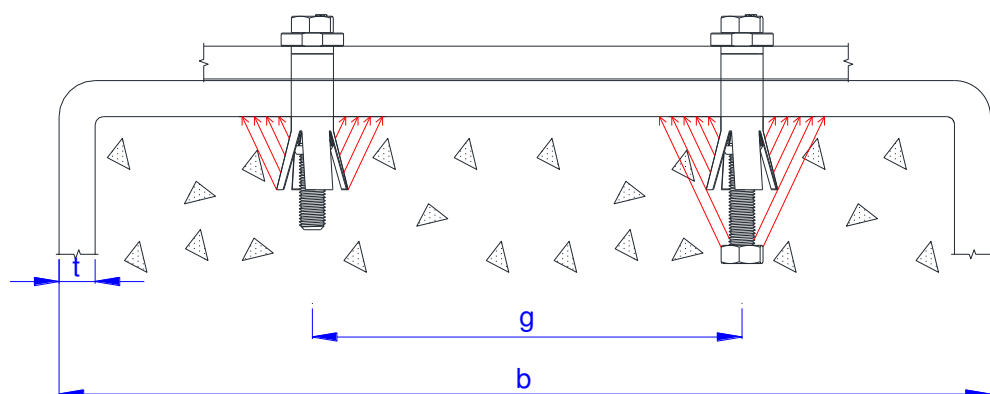


Figure 8.2 Comparison of possible load transfer mechanism of Extended Hollo-Bolt (right) and Hollo-Bolt (left)

- The same methodology used in this investigation could also be used to develop models for connections where multi-rows of Holo-Bolts are subjected to tension. An example of possible failure mechanisms of a connection where two rows of Holo-Bolts are subjected to tension is shown in Figure 8.3. The bolt pitch, denoted p in this figure, should play a role in determining the critical mechanism.

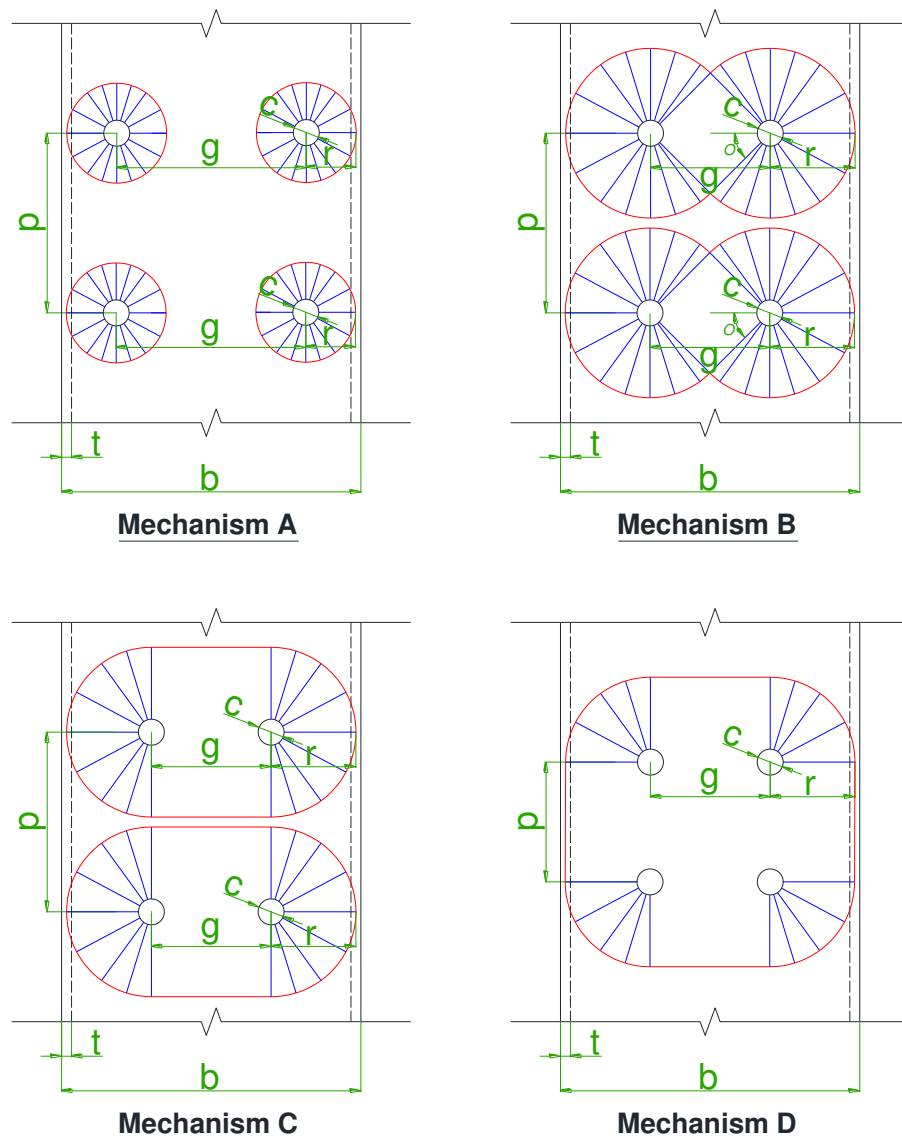


Figure 8.3 Possible failure mechanisms of a two-row connection

- Tri-Linear or Multi-Linear model is more suitable to represent the force-displacement curve when high strength concrete-infill is used. Such model is needed to incorporate the effect of concrete strength on the face bending behaviour and yet to be developed.
- An experimental method is needed to understand the behaviour of concrete-infill throughout the tests, possibly some sort of ultrasound or x-ray scan. This is vital to develop an analytical representation of k_{is} and k_{yf} .
- An experimental programme is needed to investigate the effect of changing the SHS while keeping the same SHS face slenderness and bolts gauge to SHS width ratio (when compared to SHS 200x200 used in this study), and possibly varying same parameters across SHS 300x300 to develop charts of k_{is} and k_{yf} for these sections

Finally, a list of the references cited in this thesis is presented in the next section.

References

- ABD RAHMAN, N. 2012. *Fatigue behaviour and reliability of Extended Hollobolt to concrete filled hollow section*. PhD, The University of Nottingham.
- AL-MUGHAIIRI, A. 2010. *The Behaviour of Moment Resisting Connection to Concrete Filled Hollow Sections Using Extended Hollobolts*. PhD, The University of Nottingham.
- AL-MUGHAIIRI, A., TIZANI, W. & OWEN, J. S. Validation of an FE model for an experimental blind-bolted moment-resisting connection to concrete filled hollow section. *In*: YOUNG, B., ed. *Tubular Structures XIII*, 2010 Hong Kong, China. CRC Press, 45-52.
- ANSYS 2010a. ANSYS Mechanical APDL and Mechanical Applications Theory Reference. ANSYS, Inc.
- ANSYS 2010b. ANSYS Mechanical APDL Contact Technology Guide. ANSYS, Inc.
- ANSYS 2010c. ANSYS Mechanical APDL Element Reference. ANSYS, Inc.
- ANSYS 2010d. ANSYS Mechanical APDL Operations Guide. ANSYS, Inc.
- ANSYS 2010e. ANSYS Parametric Design Language Guide. ANSYS, Inc.
- BAYO, E., CABRERO, J. M. & GIL, B. 2006. An effective component-based method to model semi-rigid connections for the global analysis of steel and composite structures. *Engineering Structures*, 28, 97-108.
- BECKER, T., SPLITTHOF, K., SIEBERT, T. & KLETTING, P. 2006. Error estimations of 3D digital image correlation measurements. *In*: SLANGEN, P. & CERRUTI, C. (eds.) *Speckle06: Speckles, From Grains to Flowers*. Nimes, France: SPIE.
- BOUMERZOUG, Z., DERFOUF, C. & BAUDIN, T. 2010. Effect of Welding on Microstructure and Mechanical Properties of an Industrial Low Carbon Steel. *Engineering*, Volume 2, PP. 502-506.

-
- BSI 1997. Structural Use of Concrete - Part 1: Code of practice for design and construction. BS 8110-1:1997. BSI.
- BSI 2006a. Hot finished structural hollow sections of non-alloy and fine grain steels - Part 1: Technical delivery conditions. BS EN 10210-1:2006. BSI.
- BSI 2006b. Hot finished structural hollow sections of non-alloy and fine grain steels - Part 2: Tolerances, dimensions and sectional properties. BS EN 10210-2:2006. BSI.
- BSI 2009. Metallic materials. Tensile testing. Method of test at ambient temperature. BS EN ISO 682-1:2009. BSI.
- BSI 2012. Hexagon regular nuts (style 1). Product grades A and B. BS EN ISO 4032:2012. BSI.
- BSTP 2003. SHS Jointing: Flowdrill & Hollo-Bolt. *In*: PIPES, B. S. T. (ed.).
- CEN 2004a. Eurocode 2: Design of concrete structures - Part 1-1: General rules and rules for buildings. BS EN 1992-1-1:2004. Brussels: CEN.
- CEN 2004b. UK National Annex to Eurocode 2: Design of concrete structures - Part 1-1: General rules and rules for buildings. NA to BS EN 1992-1-1:2004. Brussels: CEN.
- CEN 2005. Eurocode 3: Design of steel structures - Part 1-8: Design of joints. BS EN 1993-1-8:2005. Brussels: CEN.
- DANTEC. *Digital Image Correlation System (Q-400)* [Online]. Available: <http://www.dantecdynamics.com/Default.aspx?ID=855> [Accessed 12 September 2012].
- DEVORE, J. & FARNUM, N. 2005. *Applied statistics for engineers and scientists*, Thomson Brooks/Cole.
- ELAMIN, A. 2009. *The face bending behaviour of concrete filled structural hollow sections*. MSc, The University of Nottingham.

-
- ELAMIN, A. 2010. The face bending behaviour of concrete filled rectangular hollow sections (1st year report). The University of Nottingham.
- ELAMIN, A. 2012. The face bending behaviour of concrete filled rectangular hollow sections (3rd year report). The University of Nottingham.
- ELAMIN, A., TIZANI, W. & ABD RAHMAN, N. The face bending behaviour of concrete filled structural hollow sections. *In*: TIZANI, W., ed. The International Conference on Computing in Civil and Building Engineering, icccbe²⁰¹⁰, 2010 Nottingham. Nottingham University Press, 511.
- ELGHAZOULI, A. Y., MÁLAGA-CHUQUITAYPE, C., CASTRO, J. M. & ORTON, A. H. 2009. Experimental monotonic and cyclic behaviour of blind-bolted angle connections. *Engineering Structures*, 31, 2540-2553.
- ELLISON, S. & TIZANI, W. 2004. Behaviour of blind bolted connections to concrete filled hollow sections. *Engineering Structures*, 11, 8-16.
- GHOBARAH, A., MOURAD, S. & KOROL, R. 1996. Moment-Rotation relationship of Blind Bolted connections for HSS columns. *Journal of Constructional Steel Research*, 40, 63-91.
- GOMES, F., JASPART, J. & MAQUOI, R. Moment capacity of beam-to-column minor-axis joints. International Colloquium on Semi-Rigid Structural Connections, 1996 Istanbul, Turkey. IABSE, 319-326.
- HUGHES, P. B. 1976. *Limit State Theory for Reinforced Concrete Design*, Pitman.
- IMETRUM¹. *The Video Gauge Options and Specifications* [Online]. Available: <http://www.imetrum.com/products/video-gauge/specifications> [Accessed 10 September 2012].
-

-
- IMETRUM². *Accuracy of Video Gauge for displacement measurement* [Online]. Available: <http://www.imetrum.com/node/50> [Accessed 12 September 2012].
- JASPART, J.-P. 1997. Frame design including joint behaviour. European Coal and Steel Community, Final Report, Contracts 7210-SA/212 and 7210-SA 320 University of Liege.
- JOHANSEN, K. W. 1962a. *Yield-line formulae for slabs*, Cement and Concrete Association.
- JOHANSEN, K. W. 1962b. *Yield-line Theory*, Cement and Concrete Association.
- JONES, S. W., KIRBY, P. A. & NETHERCOT, D. A. 1983. The analysis of frames with semi-rigid connections-A state-of-the-art report. *Journal of Constructional Steel Research*, 3, pp. 2–13.
- KENNEDY, G. & GOODCHILD, C. 2003. *Practical Yield Line Design*, British Cement Association
- KUROBANE, Y., PACKER, J., WARDENIER, J. & YEOOMANS, N. 2004. Design Guide for Structural Hollow Section Column Connections (CIDECT 9), TUV-Verlag.
- LANDAU, L. D. & LIFSHITZ, E. M. 1986. *Theory of Elasticity*, Butterworth-Heinemann.
- LEE, J., GOLDSWORTHY, H. & GAD, E. 2010. Blind bolted T-stub connections to unfilled hollow section columns in low rise structures. *Journal of Constructional Steel Research*, 66, 981-992.
- LI, X. 2012. *Moment - Rotation Behaviour of Universal Beam To Tubular Column Connections Using Reverse Channel*. PhD, University of Manchester.
- LINDAPTER 2013a. *Cavity Fixings: Type HB - Hollo-Bolt* [Online]. Lindapter. Available:
-

http://www.lindapter.com/Products/Cavity_Fixings/2/Type_HB_Hollo-Bolt [Accessed 15 July 2013].

LINDAPTER 2013b. Hollo-Bolt Brochure: The Original Expansion Bolt for Structural Steel. Lindapter.

LINDAPTER 2013c. Lindapter Catalog: Technical Innovation in Steelwork Connections. Lindapter.

LIU, Y., MÁLAGA-CHUQUITAYPE, C. & ELGHAZOULI, A. Y. 2012a. Behaviour of beam-to-tubular column angle connections under shear loads. *Engineering Structures*, 42, 434-456.

LIU, Y., MÁLAGA-CHUQUITAYPE, C. & ELGHAZOULI, A. Y. 2012b. Response and component characterisation of semi-rigid connections to tubular columns under axial loads. *Engineering Structures*, 41, 510-532.

LU, L. H., G.D., W., YU, Y. & WARDENIER, J. Deformation limit for the ultimate strength of hollow section connections. *In*: GRUNDY, P., ed. The 6th International Symposium on Tubular Structures, Tubular Structures VI, 1994 Melbourne, Australia. A A Balkema Publishers, pp. 341-347.

MÁLAGA-CHUQUITAYPE, C. & ELGHAZOULI, A. Y. 2010a. Behaviour of combined channel/angle connections to tubular columns under monotonic and cyclic loading. *Engineering Structures*, 32, 1600-1616.

MÁLAGA-CHUQUITAYPE, C. & ELGHAZOULI, A. Y. 2010b. Component-based mechanical models for blind-bolted angle connections. *Engineering Structures*, 32, 3048-3067.

MOURAD, S. 1994. *Behaviour of blind bolted moment connections for square HSS columns*. PhD, McMaster University.

-
- NETHERCORT, D. A. 1985. Joint action and the design of steel frames. Part A Design and Construction. *Journal of the Institution of Structural Engineers*, pp. 271–279.
- NETHERCOT, D. A. & ZANDONINI, R. 1989. *Methods of prediction of joint behaviour: beam-to-column connections*, R. Narayanan, London (UK), Elsevier Applied Science.
- PACKER, J., WARDENIER, J., ZHAO, X.-L., VAN DER VEGTE, G. & KUROBANE, Y. 2009. *Design Guide for Rectangular Hollow Section (RHS) Joints under Predominantly Static Loading (CIDECT 3)*, LSS-Verlag.
- PARK, A. Y. 2012. *Semi-Rigid Joints to Tubular Columns and their use in Semi-Continuous Frame Design*. PhD, University of Manchester.
- PARK, A. Y. & WANG, Y. C. 2012. Development of component stiffness equations for bolted connections to RHS columns. *Journal of Constructional Steel Research*, 70, 137-152.
- PITRAKKOS, T. 2012. *The Tensile Stiffness of a Novel Anchored Blind-bolt Component for Moment-resisting Connections to Concrete-filled Hollow Sections*. PhD, The University of Nottingham.
- PITRAKKOS, T. & TIZANI, W. 2013. Experimental behaviour of a novel anchored blind-bolt in tension. *Engineering Structures*, 49, 905-919.
- RICHARDS, J. 2009. *Performance of Blind-Bolt Fasteners to Concrete Filled Columns*. MEng, The University of Nottingham.
- SCI/BCSA 2002. Joints in Steel Construction: Simple Connections. Steel Construction Institute and the British Constructional Steelwork Association (P212).
- SCI/BCSA 2005. Joints in Steel Construction: Moment Connections. Steel Construction Institute and the British Constructional Steelwork Association (P207).

-
- SCI/BCSA 2011. Joints in Steel Construction: Simple Joints to Eurocode 3. Steel Construction Institute and the British Constructional Steelwork Association (P358).
- SIEBERT, T., BECKER, T., SPILTTHOF, K., NEUMANN, I. & KRUPKA, R. 2007. High-speed digital image correlation: error estimations and applications. *Optical Engineering*, 46, 051004-051004.
- SIMÕES DA SILVA, L., COSTA-NEVES, L. F. & GOMES, F. C. T. 2003. Rotational Stiffness of Rectangular Hollow Sections Composite Joints. *Journal of Structural Engineering*, 129, 487-494.
- SIMÕES DA SILVA, L., COSTA-NEVES, L. F. & VELLASCO, P. C. G. D. S. 2004. Design procedure for I-beam to concrete filled column and Minor axis joints; Characterization of the component "Column web loaded in out-of-plane bending". Brugge: ECCS Technical Committee 10 "Connections".
- SIMÕES DA SILVA, L., SANTIAGO, A. & VILA REAL, P. 2001. A component model for the behaviour of steel joints at elevated temperatures. *Journal of Constructional Steel Research*, 57, 1169-1195.
- SIMÕES DA SILVA, L., SANTIAGO, A. & VILA REAL, P. 2002. Post-limit stiffness and ductility of end-plate beam-to-column steel joints. *Computers & Structures*, 80, 515-531.
- TATA-STEEL 2010. SHS Jointing: Structural & Conveyance Business. In: STEEL, T. (ed.).
- TIMOSHENCKO, S. & GOODIER, J. N. 1952. Theory of Elasticity, McGraw-Hill Books.
- TIZANI, W., AL-MUGHAIIRI, A., OWEN, J. S. & PITRAKKOS, T. 2013a. Rotational stiffness of a blind-bolted connection to concrete-filled tubes using modified Holo-bolt. *Journal of Constructional Steel Research*, 80, 317-331.

-
- TIZANI, W. & RIDLEY-ELLIS, D. J. The Performance of a new blind-bolt for moment-resisting connections. *In: JAURITTA, M. A., ALONSO, A. AND CHICA, J.A. , ed. Tubular Structures X, 2003 Madrid, Spain. 395-400.*
- TIZANI, W., WANG, Z. Y. & HAJIRASOULIHA, I. 2013b. Hysteretic performance of a new blind bolted connection to concrete filled columns under cyclic loading: An experimental investigation. *Engineering Structures, 46, 535-546.*
- WALES, M. W. & ROSSOW, E. C. 1983. Coupled Moment-Axial Force Behavior in Bolted Joints. *Journal of Structural Engineering, 109, 1250-1266.*
- WANG, J.-F., HAN, L.-H. & UY, B. 2009a. Behaviour of flush end plate joints to concrete-filled steel tubular columns. *Journal of Constructional Steel Research, 65, 925-939.*
- WANG, J. & CHEN, L. 2012. Experimental investigation of extended end plate joints to concrete-filled steel tubular columns. *Journal of Constructional Steel Research, 79, 56-70.*
- WANG, J., HAN, L. & UY, B. 2009b. Behaviour of flush end plate joints to concrete-filled steel tubular columns. *Journal of Constructional Steel Research, 925-939.*
- WILLAM, K. J. & WARNKE, E. D. Constitutive Models for the Triaxial Behavior of Concrete. *Proceedings of the International Association for Bridge and Structural Engineering, 1975 Bergamo, Italy. 174.*
- WILSON, W. M. & MOORE, H. F. 1917. Tests to determine the rigidity of riveted joints in steel structures. University of Illinois. Engineering Experiment Station.
- WOOD, W. & MARTIN, D. 1974. *Experimental Method*, The Athlone Press.
-

YEE, Y. L. & MELCHER, R. E. 1986. Moment-rotation curves for bolted connections. *Journal of the Structural Division, ASCE*, 112 (ST3), 615-630.